Title
A REAL-TIME SIMULATION METHODOLOGY TO ENABLE SEAMLESS MICROGRID ISLANDING

Author
Gu, Fei

Publication Date
2018

UNIVERSITY OF CALIFORNIA,
IRVINE

A REAL-TIME SIMULATION METHODOLOGY TO ENABLE SEAMLESS MICROGRID ISLANDING

DISSERTATION

submitted in partial satisfaction of the requirements
for the degree of

DOCTOR OF PHILOSOPHY

In Electrical Engineering

By

Fei Gu

Dissertation Committee:
Professor Michael Green, Chair
Professor Mohammad Al Faruque
Professor Scott Samuelsen

2018

DEDICATION

Perseverance.

TABLE OF CONTENTS

LIST OF FIGURES

LIST OF TABLES

ACRONYMS

AC	Alternating Current
BC	Breaker Controller
BES	Battery Energy Storage
BMS	Building Management System
CERTS	Consortium for Electric Reliability Solutions
CHP	Combined Heat and Power
DC	Direct Current
DER	Distributed Energy Resource
DQZ	Direct-Quadrature-Zero
EMS	Energy Management System
EMT	Electromagnetic Transient
FACNET	Facilities Network
FC	Fuel Cell
GC	Generator Controller
GT	Gas Turbine
HMI	Human-Machine Interface
LC	Load Controller
LCOE	Levelized Cost of Electricity
MGT	Microturbine Generator
MMC	Master Microgrid Controller
MPP	Maximum Power Point
MPPT	Maximum Power Point Tracking
PCC	Point of Common Coupling
PEM	Proton Exchange Membrane
PID	Proportional-Integral-Derivative
PLL	Phase-locked Loop
PV	Photovoltaic

RLC	Resistor-Inductor-Capacitor
RT-HIL	Real-time Hardware-in-the-Loop
SC	Storage Controller
ST	Steam Turbine
SOC	State of Charge
SOFC	Solid Oxide Fuel Cell
SSN	State-space Nodal
TCP/IP	Transmission Control Protocol / Internet Protocol
UCI	University of California, Irvine
UCIFM	University of California, Irvine Facilities Management
UCIMG	University of California, Irvine Microgrid

ACKNOWLEDGMENTS

My thanks and appreciation goes to my advisors, Professor Scott Samuelsen, Professor Michael Green, and Professor Jack Brouwer, and the many amazing mentors I have had the good fortune of meeting throughout my academic career. Your guidance has made all the difference along this journey.

Financial support for my program has been provided largely in part by the Advanced Power and Energy Program at the University of California, Irvine and material is based upon work supported the U.S. Department of Energy under Award Number DE-OE0000730. I would like to express my appreciation for providing me with the opportunity to further my education and for funding the research presented here.

And finally I would like to thank my friends, family and colleagues for their unyielding support and encouragement. You have made my experience an unforgettable one.

CURRICULUM VITAE

Fei Gu

Education

University of California, Irvine
Ph.D., Electrical Engineering, 2018
Dissertation: A Real-time Simulation Methodology to Enable Seamless Microgrid Islanding.
Advisors: Dr. Michael Green (EECS) and Dr. Scott Samuelsen (MAE).

University of California, Irvine
M.S., Electrical Engineering, 2013
Thesis: Analysis and Design of a High Efficiency Energy Regenerative Snubber Applied to a Tapped Inductor Boost Converter.
Advisor: Dr. Keyue Smedley

California State University, Fresno, 2008
B.S., Electrical Engineering.
Minors: Mathematics, Business.

Publications

F. Gu, G. Razeghi, P. Dai, M. Nagisetty, R. Costa, M. Green. S. Samuelsen, “Islanding a 20MW-Class Community Microgrid with Sensitive Loads,” Applied Energy, 2018. (Manuscript in Submission).

G. Razeghi, F. Gu, R. Neil, S. Samuelsen, “A Generic Microgrid Controller: Concept, Testing, and Insights,” Applied Energy, 2018.

F. Gu, J. Payne, J. Brouwer, S. Samuelsen, “The Impact of High Penetration Photovoltaic Systems on Electrical Distribution Networks Containing Legacy Voltage Regulation Devices”, Journal of Power Sources, 2015. (Manuscript in Submission).

F. Gu, J. Brouwer, S. Samuelsen, “A Study on the Impact of High Penetration Distributed Generation Inverters on Grid Operation and Stability”, American Institute of Physics, 2013.

Presentations

F. Gu, S. Samuelsen, “UCI Microgrid: Islanding,” Microgrid Global Summit, Irvine CA, 2018.

F. Gu, S. Samuelsen, “The Role of Smart Inverters in Renewable Microgrids,” International Colloquium on Energy Preferred Advanced Power Generation, Irvine CA, 2015.

F. Gu, S. Samuelsen, “Microgrid Global Summit: UCI Microgrid,” World Microgrid Forum, Irvine CA, 2014.

F. Gu, S. Samuelsen, “UCI Microgrid: Dynamic Control and Modeling,” International Colloquium on Energy Preferred Advanced Power Generation, Irvine, 2014.

F. Gu, S. Samuelsen, “A Study on the Impact of High Penetration Distributed Generation Inverters on Grid Operation and Stability,” International Conference on Concentrator Photovoltaic Systems, Miyazaki Japan, 2013.

F. Gu, S. Samuelsen, “Evaluation of High Penetration Photovoltaics on Distribution Circuits,” High Penetration Solar Forum, San Diego CA, 2013.

Teaching Experience

University of California, Irvine
Teaching assistant/lab instructor
EECS 163L – Introduction to Power Systems Laboratory (Spring 2017)

ABSTRACT OF THE DISSERTATION

A REAL-TIME SIMULATION METHODOLOGY TO ENABLE SEAMLESS MICROGRID ISLANDING

By

Fei Gu

Doctor of Philosophy in Electrical Engineering

University of California, Irvine, 2018

Professor Michael Green, Chair

The benefits and rapidly decreasing costs of distributed energy resources (DER) has resulted in such assets becoming swiftly integrated into the current power generation landscape, providing numerous benefits to the end user, system operator, and utility such as lowered of energy costs, increased efficiency, and reduced environmental impacts. As direct coordination of all grid-connected DER is impractical, DER and proximate loads must be partitioned into independent systems, e.g. microgrids, and locally controlled to achieve coordinated and optimized utilization of assets. In this manner, improvement of individual microgrid systems contributes to the enhanced performance of the electrical grid as a whole.

This dissertation advances the understanding of microgrid control and operation via the detailed modeling, real-time hardware-in-the-loop (RT-HIL) simulation, and physical islanding demonstration of a real-world community-scale microgrid system in support of the development of a generic microgrid controller. The primary case study, the University of California Irvine Microgrid (UCIMG), consists of a community-scale system containing a 13MW gas turbine, a 5MW steam turbine, 4MW of photovoltaic generation, and a 2MW battery energy storage system. This microgrid was modeled and simulated using a high-performance real-time hardware-in-the-loop simulator employing a scalable state-space nodal electromagnetic transient program. In the physical space, 140 building-level power meters were deployed across the microgrid, with real-time measurements utilized for state observation, online contingency planning, and controller refinement.

Simulation results were used to inform the development of a generic microgrid controller capable of supporting (1) seamless islanding and reconnection of the microgrid, (2) efficient, reliable, and resilient operation in islanded and grid-connected modes, (3) the ability to provide ancillary services, (4) capability to serve the resiliency needs of participating communities, (5) communication with the utility as a single controllable entity, resulting in the (6) increased reliability, efficiency and reduced emissions of the grid as a whole. Subsequent studies with the developed controller attached to the RT-HIL platform demonstrated proof of concept and allowed for determination of microgrid operational limits and island- and grid-connected transition behavior. Physical demonstration of the controller on the UCIMG was conducted via a live islanding and resynchronization event.

1. INTRODUCTION

Over the last decade, a transformative force in the electrical power industry has taken hold as the evolving consumer and utility mindset -- fueled by the underlying drivers of increased attention to environmental impacts, sensitivity to rising energy costs, and proliferation of the digitization and networking of grid assets -- has fast-tracked the integration of renewable distributed energy resources (DER) into the electrical grid. Since its inception, the electrical power paradigm has remained predominantly static -- large centralized generation sites, primarily powered by fossil fuels, produce electricity that is delivered unidirectionally to numerous dispersed loads via a system of transmission and distribution networks. In recent years, the shift towards the utilization of renewable distributed energy resources such as photovoltaic (PV), fuel cell (FC), wind, and microturbine generator (MGT) systems presents opportunities for a new distributed power framework. With generation assets now becoming co-located with loads, the electrical power system is shifting from a generation-to-load arrangement to a peer-to-peer one, allowing and often necessitating the use of a new power system architecture -- that is, the microgrid.

A microgrid is defined as a localized system of distributed energy resources and loads with the distinction that the system is capable of operating either synchronously connected to, or independent of, the overall electrical grid (U.S. Office of Electricity Delivery & Energy Reliability, 2018). A future power system composed of a network of microgrids offers significant advantages compared to the traditional power generation paradigm such as improvements reliability, resiliency, and efficiency. Integration of DER within microgrids extracts additional value from those distributed energy resources. For example, DER operated in non-microgrid systems provide several direct benefits to the end user, system operator, and utility. These benefits include:

Reduced environmental impact

DERs commonly derive power from renewable energy sources such as wind, geothermal, photovoltaic, and renewable biogas, allowing operators to meet greenhouse gas emissions and criteria pollutants reduction targets.

Reduced costs

The levelized cost of energy (LCOE) provided by DER has been steadily falling with many technologies such as solar, wind, and small hydroelectric currently at parity with or below the LCOE of traditional fossil fuel powered generation plants (U.S. Energy Information Administration, 2018).

Improved unit reliability and resiliency

Due to their size, many DER devices are well-suited for mass production, increasing the availability of replacement units and facilitating the purchase of standby units. Self-containment of many DER devices further accelerates deployment.

However, when DER are integrated into microgrid systems, the resulting coordination of DER assets and loads, coupled with islanding capabilities, achieves additional system-wide benefits. These additional benefits include:

Increased system reliability and resiliency

With multiple interconnected generation sources, the rate of a system-wide failure is no longer predominantly dependent on a single component such as a large generator or critical transmission line, but dispersed jointly over numerous independent devices. The ability to seamlessly island from the main electrical grid in the event of a grid outage provides an additional layer of reliability as DERs, which mandatorily shut down when connected to a de-energized utility grid, may continue to operate within an islanded microgrid, reducing the impact of utility service disruptions.

Increased system performance

The grouping and localization of assets within microgrid boundaries assists in reducing the communications burden of monitoring and controlling numerous devices to levels achievable with current technologies. Reduced network latencies resulting from decreased network traffic and physical proximity improves system responsiveness. Coordination of generation assets allows for optimal economic dispatch within the microgrid.

Ancillary services

Coordination and presentation of all DERs within a microgrid as a single controllable entity to the utility facilities the entry of microgrids into ancillary services markets otherwise unavailable to individual DER. Reactive power, voltage, and frequency regulation, spinning reserve, scheduling, and dispatch services may be provided by the microgrid operator, improving the economic case for microgrids.

The attainment of these benefits, as well as successful operation of a microgrid system as a whole, is conditional on the accurate modeling and study of microgrid systems as unique issues arise in microgrids that are not present in traditional power systems. Several issues that must be addressed include: management of numerous independent DER, system instabilities arising from bidirectional power flow and low system inertia, and the unpredictability and uncontrollability of renewable generation resources. This necessitates the development of adequate microgrid analysis methodologies and effective microgrid controllers.

1.1. GOALS

The goals of this research are to establish a methodology for developing and testing the veracity of a controller to govern the evolution of microgrids responding to the emergence of multiple demands, and thereby provide *(1) a high performing, reliable, islanding-ready asset to the microgrid owner, operator, and customers; and (2) a smart demand and power dispatch asset to the grid.*

1.2. OBJECTIVES

The main objective of this research is to achieve the stated research project goal and apply the knowledge gained via this effort to the University of California, Irvine (UCI) campus and other microgrid partners. To achieve the stated research goal, the University of California, Irvine Microgrid (UCIMG) and partner microgrids were modeled and simulated on a high-performance real-time simulator to which a microgrid controller developed concurrently with this project was interfaced in a real-time hardware-in-the-loop configuration. Via this arrangement, microgrid operation and stability was investigated, yielding insights into microgrid operation. Results were used to guide the further refinement of the generic microgrid controller. Proof of concept was established via a real-world seamless islanding demonstration of the UCIMG. To meet the research goal, six objectives were established:

Objective 1

Survey existing knowledge concerning microgrid systems by reviewing literature pertaining to microgrid controllers, design, operation, and stability and develop an ongoing dialogue with industry leaders to identify deficiencies in the current body of knowledge.

Objective 2

Develop analysis techniques and concepts that expands the existing body of knowledge and apply the lessons learned to examine the UCIMG and partner microgrids.

Objective 3

Collaborate with UCI Facilities Management (UCIFM) and microgrid partners to gather real-world microgrid data and deploy a real-time campus-wide energy monitoring system to enable advanced control strategies and improve overall microgrid performance.

Objective 4

Develop an electromagnetic transient model of the UCIMG and interface a concurrently developed generic microgrid controller in a real-time hardware-in-the loop configuration.

Objective 5

Demonstrate proof of concept operation of the generic microgrid controller and obtain experimental data via a live seamless islanding and reconnect event on the UCIMG.

2. BACKGROUND

The study of microgrid systems is an interdisciplinary field necessitating contributions from various engineering disciplines to appropriately model the wide range of DERs and their interactions within a microgrid; electrical engineering in the analysis of electrical power devices and systems, chemical engineering to understand the reaction dynamics of fuel cell and battery energy storage systems, mechanical engineering in the examination of traditional generation machinery such as internal combustion- and turbine-based generators, and the application of controls engineering to ensure coordinated and optimal operation of the system as a whole. This section is presented to introduce the background of interdisciplinary knowledge utilized in this research.

2.1. TRADITIONAL POWER SYSTEMS

The primary function of an electrical power system is to generate and deliver electrical power to loads. In modern power systems, electrical power is predominantly generated at large centralized production stations and transmitted to end users across a system of networked power lines, transformers, power routing switchgear, and other supporting devices collectively referred to as the electrical “grid”. Due to the requirement of transmitting large amounts of electrical power over long distances, line voltages are raised with electrical power transformers near generation sites, as a linear increase in operating voltage results in a quadratic decrease in the power dissipated within transmission line conductors, and subsequently lowered upon proximity to loads, as illustrated in Figure 1. Line voltages are selected depending on several factors including transmission distance, power carrying requirements, and safety. Typical voltage levels used in modern power systems are summarized in Table 1.

For delivery of large amounts of power across long distances, electricity is transmitted across a “transmission-level network” in which line to line voltages are typically operated at 115 kV and higher to reduce line conduction losses. Presence of electrical power at these voltages is often a hazard near population centers and must first be reduced before delivery to end users. In North America, there exist five major independent transmission-level systems; the Eastern Interconnect, the Western Interconnection, the Texas Interconnection, the Quebec Interconnection, and the Alaska Interconnection and are shown in Figure 2. Regulatory standards for these networks are coordinated by the North American Electric Reliability Corporation (North American Electric Relibility Corporation, 2017). Electrical power networks at the transmission interconnection level are topologically meshed with multiple branches connecting major nodes within the system. While these networks are electrically isolated, there exist several high-voltage direct current (DC) and variable-frequency transformer links between them (Koropatrick, 2012) to allow for inter-network power exchange.

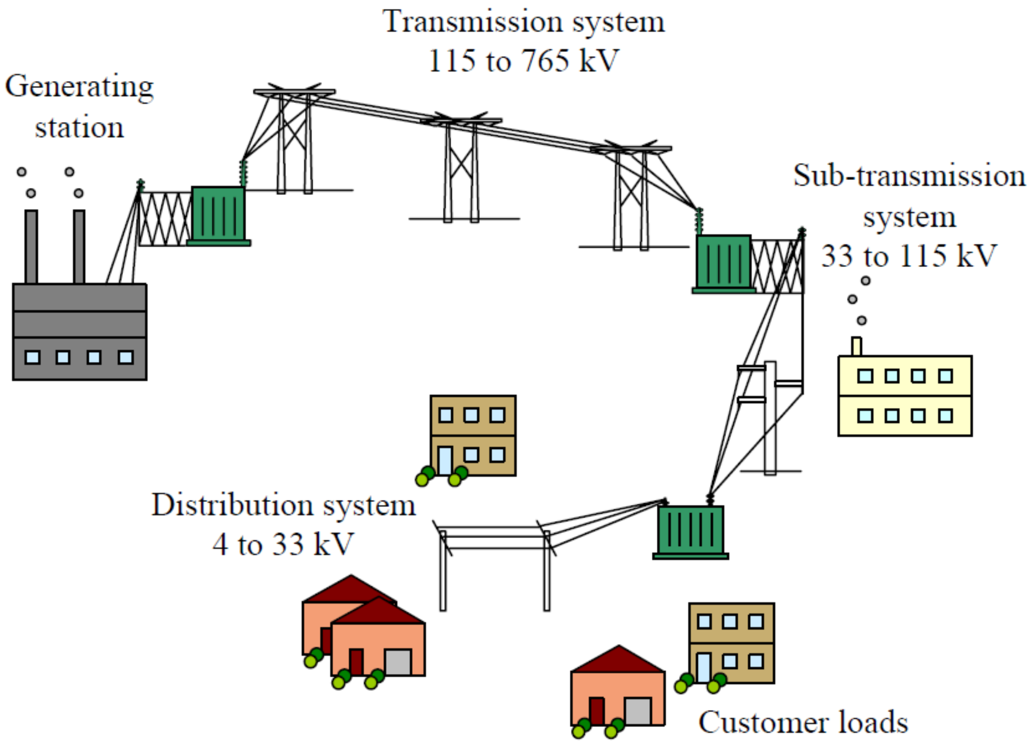

Figure 1. Traditional electric generation model (Auld, 2010).

At points along the transmission-level network, branches connect the network to substations where the high line voltages are reduced to "subtransmission" levels of approximately 34-115 kV via step-down transformers. From these substations, electrical power is similarly routed along subtransmission networks. In North America, subtransmission circuits are usually arranged in a looped configuration for increased reliability via redundancy, although radial and meshed networks are also utilized. Once close to the intended destinations, the electrical power is once again directed to substations and transformers again lower the voltage to a "distribution-level" range of 2-35 kV from which power is delivered via local distribution-level networks (Kaplan, 2009).

Distribution-level power is carried from substations to customer sites via primary distribution lines. Once at the electrical service customer site, a final distribution transformer reduces the line potential to “utilization-level” voltages in the range of 120-480 V. Customers with higher electrical demand may be connected directly to the primary lines, or in some cases the subtransmission networks. Distribution networks utilize either radial or networked configurations -- radial networks are arranged in a trunk-and-branch topology and are used in rural and suburban areas while networked systems are similar to the transmission and subtransmission-level meshes (Sallam, 2011).

Traditional power systems are designed around power flow that is unidirectional, with power being generated at large power plants delivered downstream to end-user loads. Many load-flow solvers used in the modeling of power systems can only simulate systems with unidirectional power flow, and modern power system protection coordination practices are based upon unidirectional power flow to a large degree. Additionally, the relatively few number of large centralized power plants enables the direct coordination of grid-connected generation assets, facilitating grid operations activities such as resource scheduling, power flow optimization, and system maintenance and expansion planning. However, with current renewable energy trends forecasting the integration of a rapidly increasing number of DER into the electrical system (Aguero, 2018) at the distribution level, this model may soon be challenged, requiring new technologies capable of accommodating the bidirectional flow of power.

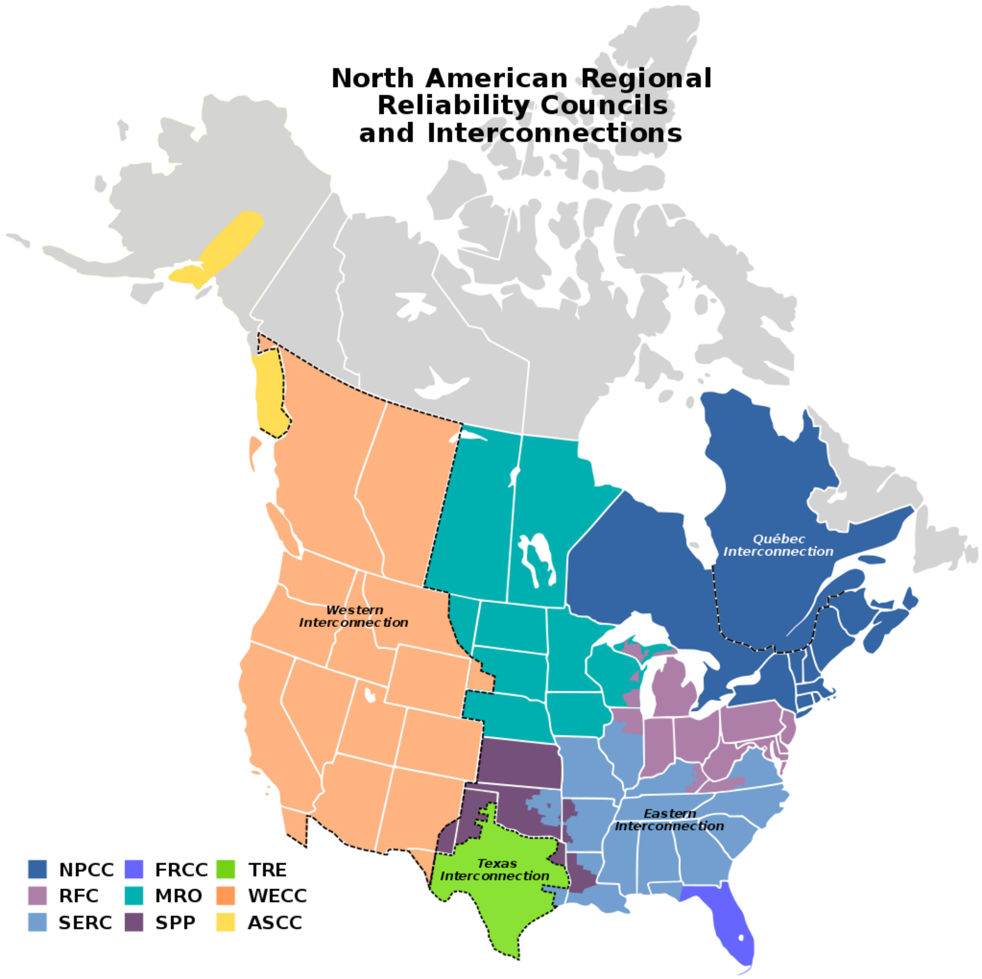

Figure 2. North American interconnection regions (Messerly, 2009).

Level	Total U.S. Conductor Length (Miles)	Voltages (kV)
Ultra-High Voltage Transmission	4,065	>765
Extra-High Voltage Transmission	154,503	345, 500, 765
High Voltage Transmission	89,857	115, 138, 161, 230
Medium Voltage Subtransmission	520,730	34, 46, 69
Low Voltage Distribution	6,020,730	< 34

Table 1. Transmission line voltage categories and distances in the continental U.S. (American Society of Civil Engineers, 2017) (U.S. Energy Information Administration, 2006).

2.2. MICROGRIDS

The global paradigm for electrical generation and distribution is currently undergoing a transformation as distributed generation assets based on renewable resources such as photovoltaic, fuel cell, wind, and small hydroelectric is presenting low-carbon and low-pollutant emissions generation options alongside traditional generation assets. As these devices are typically installed near demand sites, the integration of these technologies is shifting the energy model from a centralized scheme to a distributed one and the resulting coordination of these numerous and often intermittent energy resources has presented a challenge to system operators (Painuly, 2011).

A proposed solution to these challenges is the *microgrid* -- a localized, integrated power system consisting of DER, dispatchable loads, and associated monitoring and automation systems. An example of a microgrid system, the UCIMG, is illustrated in Figure 3. Geographic localization of microgrid components and the accompanying coordination benefits enables microgrids to address many of the challenges presented by the integration of DER at the grid-scale. For example, the use of microgrids assists in preserving the unidirectional nature of power flow throughout the larger power grid by providing a mechanism to eliminate upstream power delivery. Any inadvertent power export through a microgrid PCC due to DER over-production may be removed by generation curtailment and/or disconnecting the microgrid system from the utility entirely, easing the transition into a future grid that more readily supports bidirectional power transfer via smart grid technologies.

As microgrids typically interface to the utility via a single point of common coupling (PCC) and may be operated in either grid-connected or islanded modes, from the viewpoint of the utility, a microgrid manifests itself as a single controllable electrical entity thereby greatly reducing many of the challenges associated with the coordination of large numbers of dispersed, independent, and highly variable distributed energy resources. As such, microgrids provide a single amalgamated smart demand and power dispatch asset to the grid per microgrid system. While connected to the grid, the single unified operational authority of a microgrid system facilitates the provisioning of ancillary services to the utility by presenting a single grouped entity to grid operators as opposed to numerous independent DER. Key advantages afforded by microgrid systems may be summarized as the (1) seamless islanding and reconnection of the microgrid to the utility, (2) efficient, reliable, and resilient operation in islanded and grid-connected modes, (3) the ability to provide ancillary services, (4) capability to serve the resiliency needs of participating communities, (5) communication with the utility as a single controllable entity, resulting in the (6) increased reliability, efficiency and reduced emissions of the grid as a whole.

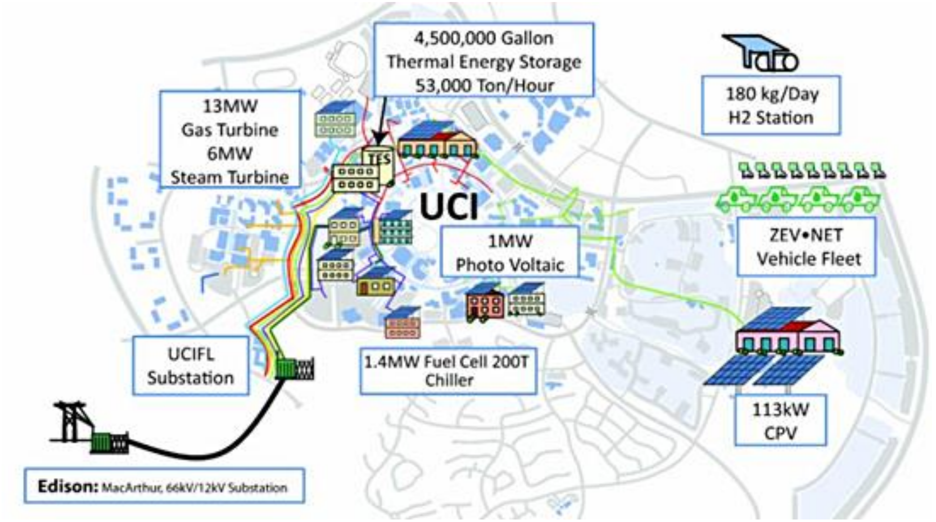

Figure 3. Example microgrid system.

Still, microgrids have several technological challenges to overcome and much research being directed to advance microgrid technologies. The several of the most pressing issues remaining in microgrid systems include:

Internal bidirectional power flow

Existing power systems are largely designed to exclusively support unidirectional power flow from generators to loads, and electrical power equipment such directional feeder relays are designed around this assumption. While the use of microgrids may preserve unidirectional power flow of the overall grid, the presence of rapidly changing bidirectional power flow within microgrid systems, such as the power demand of a PV-equipped building power shifting from export to import as cloud cover reduces PV output results in complications in the coordination of protection equipment and microgrid voltage control, especially in statically configured systems (Colson, 2009).

Low mechanical inertia

Unlike traditional rotating generation devices, most distributed generation sources lack significant mechanical inertia and other energy storage elements, resulting in reduced oscillation damping, disturbance carry-through, and fault current contribution capabilities. Also, DER are commonly interfaced to microgrids via power electronic converters and current DER standards such as the IEEE 1547 (Basso, 2004) require these interfaces to shut down during grid anomalies. This may result in cascading system failure scenarios in which a disturbance in system frequency or voltage caused by insufficient generation further results in the loss of additional online DER generation (Van der Vlueten, 2010).

Power stability

The low inertia of many DER devices, widely varying control mechanisms, unpredictability in DER output, and high dynamic response of power electronic converters often result in undesired power and voltage oscillations within microgrid systems in both grid-connected and islanded-modes (Katiraei, 2006).

Load and generation variability

Currently, energy storage systems are not widely deployed in microgrids. The lack of large energy reservoirs coupled with the unpredictability of many forms of DER, especially wind and PV, create difficulties in ensuring reliable microgrid power balance while islanded and negatively impact power quality while grid-connected. This is especially important during islanded-mode operation where the main grid is unavailable to supply a generation deficit or act as a power sink during periods of excess generation, as without a proper power balance mechanism, line voltages and system frequency would quickly drift away from operational limits. In the absence of grid-scale energy storage, the highly variable and unpredictable nature of renewable energy resources can be somewhat addressed with the use of high-speed monitoring and control, forecasting and prediction technologies (Inman, 2013). However, being stochastic in nature, these measures ultimately cannot completely guarantee uninterrupted microgrid performance.

2.3. MICROGRID EXAMPLES

Microgrids have become an active field of research and there exist several experiments and demonstrations around the world exploring an array of microgrid technologies. A chart of several microgrid projects varying in power capacity and node count is summarized in Figure 4. Several prominent projects include:

Consortium for Electric Reliability Solutions (CERTS)

The CERTS microgrid demonstration test bed (Lasseter, 2011) is located in Columbus, Ohio, USA. The test bed includes three 60 kW inverter-coupled generators and a static switch. Two island-capable feeder circuits connect loads to generation sources. This project achieves microgrid control using a decentralized control scheme. While a communications system is in place to allow for monitoring, the CERTS microgrid has no master controller and utilizes a distributed architecture with devices acting autonomously.

General Electric Global Research Microgrid

General Electric has developed a unified control, protection, and energy management platform for a microgrid (Kroposki, 2007). The General Electric Universal Interconnect is a prototype interconnection system that is based on the General Electric G60 Universal Generator protection relay and a General Electric Zenith transfer switch. The General Electric Universal Interconnect is intended to allow for the interconnection of any distributed generation resource to a microgrid.

National Renewable Energy Laboratory

The USA-based National Renewable Energy Laboratory tests various switchgear and other smart grid technologies (Martin, 2010).

New Energy and Industrial Technology Development Organization

The New Energy and Industrial Technology Development Organization in Japan is supporting several microgrid demonstration projects (Morozumi, 2007). The first of these, the Aichi project, a component of the Regional Power Grids with Renewable Resources Project, was established in 2006. The Aichi project demonstrated load/generation balancing to within 3% using a variety of devices including 1.295MW of fuel cell generation, 330 kW of PV, and a sodium sulfur battery energy storage (BES) system.

European Union Microgrids Research Project

Two major microgrid projects led by the National Technical University of Athens, Greece have been developed (Hatziagyriou et al., 2007). The projects aim to study microgrids to increase penetration of renewable generation resources, study the operation of microgrid parallel- and islanded-mode operation, develop control strategies to ensure efficient, reliable, and economic functionality, define appropriate protection and grounding polices, identify and develop the required communications infrastructure and protocols, and simulate and demonstrate microgrid operations.

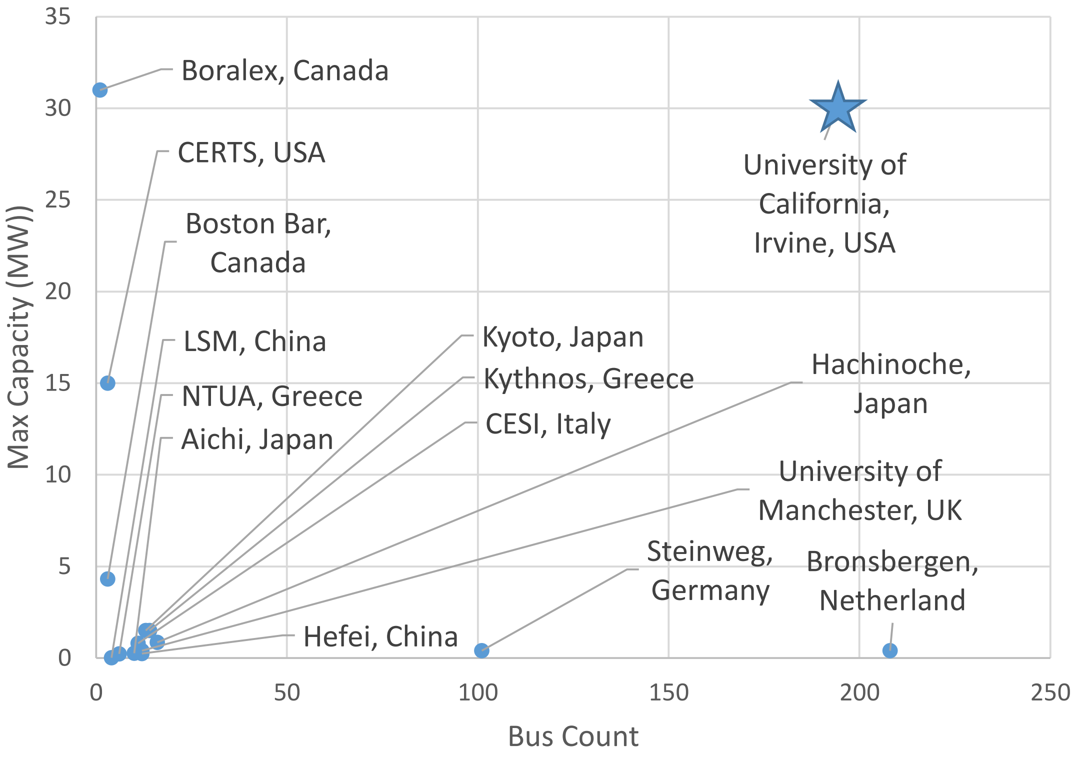

Figure 4. Comparison of various microgrid demonstration projects.

2.4. MICROGRID ARCHITECTURES

Fundamentally, microgrids may adopt any configuration as long as the features of islanding capability and localized containment of DER, loads, and associated communications and control systems are present. However, most microgrid solutions take on a topological structure similar to distribution-level networks, employing a radial layout to support compatibility when interfacing with existing feeder circuits. Such solutions also leverage the economic value of utilizing readily available power systems equipment. In some systems, especially those containing combustion-based generation, proximity between electrical and thermal systems encourages the use of microgrid designs that recover waste heat from DER resources such as in combined heat and power

(CHP) systems. In these systems, electrical and thermal components are interlinked and design of the microgrid system is largely guided by the holistic consideration of the interactions between electrical, thermal, and mechanical systems.

However, a key and necessary characteristic of microgrids, in direct comparison to a traditional electrical system, is its ability to switch between grid-connected and islanded-mode operation. This is typically performed during a utility outage or demand response request, during which the microgrid is electrically isolated from the main grid and operates autonomously. During this period, a microgrid must provide sufficient generation resources to supply, at a minimum, critical loads on the system. When the grid irregularity is resolved, microgrid systems may reconnect back to the main grid via a resynchronization process. The requirement of maintaining islanding and resynchronization capabilities necessitates several topological and control features of microgrids that not required in non-microgrid systems. The requirement of grid separation results in most microgrids employing only one point of common coupling (PCC) to the grid to facilitate reliable disconnection/reconnection to the main utility, and many regulatory agencies require a single PCC (IEEE Std. 2030.7-2017) to conform to microgrid definition standards. The presence of multiple points of common coupling necessitates the simultaneous action of multiple PCC switches, which is difficult to achieve in practice and requires low-latency synchronization between coupling points. Additionally, most commercial load-flow software packages designate the PCC as the exclusive voltage- and phase-angle reference node and will not converge due to over-definition of the system load-flow equations when presented with systems with multiple PCCs. While not widely adopted commercially, several distributed slack bus algorithms based on generator domains have been proposed (Tong, 2005) that do allow for load-flow simulations with multiple PCCs.

Microgrids can be broadly divided into two categories: alternating current (AC) and direct current microgrids, identified by the use of alternating or direct current used to transfer power between microgrid elements. These two configurations each present unique benefits and challenges.

2.4.1. AC MICROGRIDS

Historical precedent, reliability and cost-effectiveness of transformer-based voltage conversion and induction motors, among other attractive properties, have contributed to modern power systems being overwhelmingly based on alternating current power and most microgrid systems mirror this trend. AC-based microgrids, an example of which is illustrated in Figure 5, directly interface to the utility via a PCC and route power within the microgrid in a manner similar to that of a distribution-level network, with power from the PCC distributed downstream throughout the system via a radially configured network. These commonalities enable AC-based microgrids to utilize the same components available to modern power systems such as protection equipment, generators, and electrical cables, reducing costs associated with constructing and maintaining the microgrid system.

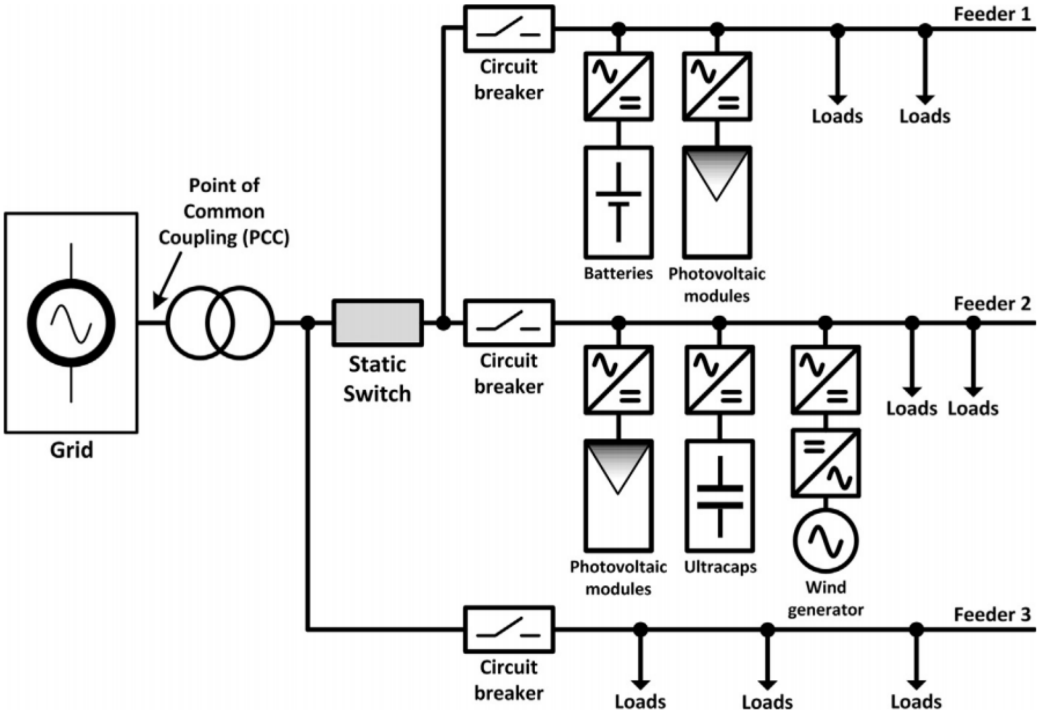

Figure 5. Example AC microgrid (Patrao, 2015).

AC microgrids may also support DC devices. To interface direct current DERs located within AC microgrids such as photovoltaic panels, fuel cells and battery storage systems, devices must be equipped with grid-synchronized DC-to-AC inverters to convert DC power into an AC output. A schematic of the power stage of a three-phase inverter system is shown in Figure 6. Similarly, DC loads designed to accept an AC power input require AC-DC rectifiers, such as in the case of computers, LED lighting and many consumer electronic devices. Lately, traditionally AC-based devices such as induction motors are being equipped with AC-DC-AC converters such as variable frequency drives to increase operational flexibility and mitigate inrush current overloading.

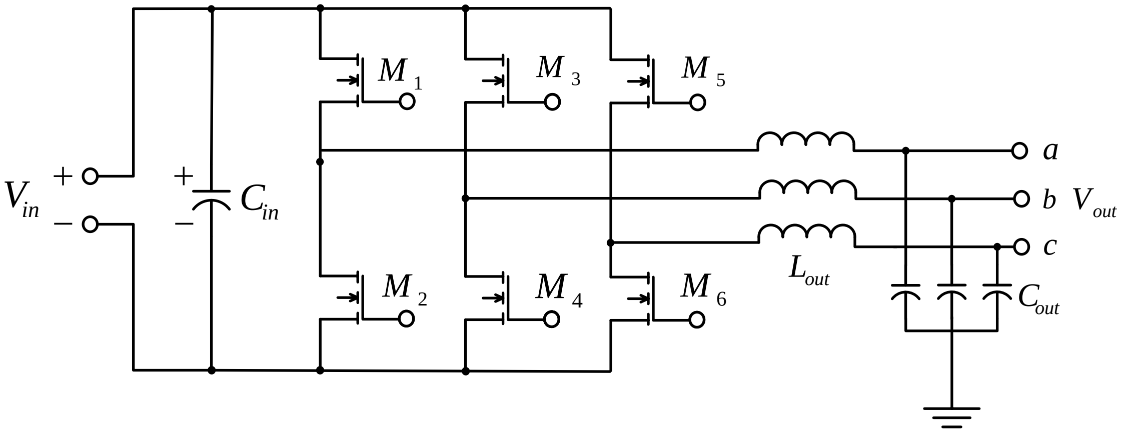

Figure 6. Three-phase DC-AC inverter power stage.

While AC microgrids are currently more cost-effective and widespread, they are inherently more challenging to coordinate than DC-based systems due to the requirement of maintaining line frequency, phase angle, voltage magnitude, and current magnitude across all microgrid elements, as opposed to only voltage and current magnitude in DC systems. Furthermore, during reconnection to the main grid, all DER within the system must be frequency-, phase-, and voltage-matched to the utility grid to achieve synchronized reconnect, which often requires coordinated fine-grained control of DER generators. In systems where the majority of generation and load components are fundamentally DC devices, AC systems are less efficient as the AC-DC rectification and DC-AC inversion processes incur conversion losses through the use of lossy power electronics devices.

2.4.2. DC MICROGRIDS

A majority of modern electronic devices such as computers, phones, televisions and high-efficiency lighting are DC supplied, and an increasing percentage of electrical loads are DC. This trend is amplified considering the potential electrification of the transportation sector with battery electric vehicles being charged with DC fast chargers, introducing a large DC electrical load burden (Liu, 2011). Additionally, existing AC motor loads found with heating, ventilation, and air condition systems and industrial centers are being converted to DC-interfaced devices via the intermediary variable frequency drives which operate using an AC-DC conversion process. Current research suggests that nearly all residential and most industrial loads may be replaced with high-efficiency DC devices, resulting in an efficiency increase of upwards to 30% (Vossos, 2011).

On the supply side, DER generation sources such as photovoltaics and fuel cells are among the fastest growing energy technologies and are fundamentally DC devices that require DC-AC converters to interface to traditional AC systems. Wind turbines and some microturbine systems, despite being rotational devices capable of natively producing AC power, now commonly employ AC-DC-AC converters to match output frequency with the grid and maximize energy extraction via electronic interfaces instead of mechanical gear reduction. Battery energy storage systems, also DC devices, are critical elements of a robust microgrid system as they supply the immediate reserve energy required to compensate for variable generation and load demand during islanded-mode operation. A 2011 study suggests that across the electrical sector, nearly 30% of all AC electrical power is converted into DC at least once along the utilization pathway (Vossos, 2011). With AC-DC rectifiers on average being 80-98% efficient, power is lost in the conversion process and the use of DC-exclusive microgrids may result in efficiency improvements. Table 2 shows typical system efficiencies.

System Description	System Efficiency
AC, baseline efficiency scenario	61%
AC, newer system components	83%
AC, introduction of UPS with high-efficiency mode	87.5%
AC, eliminating the PDU and distributing 480/277 V	89%
AC, eliminating the PDU and distributing 400/230 V	89%
DC, narrow voltage range distribution	86%
DC, wide voltage range distribution	84%

Table 2. Comparison of efficiency enhancements (Johnson, 2012).

As shown in Figure 7, a DC microgrid is topologically identical to an AC microgrid -- i.e., a radial architecture with a single grid interface connected to downstream microgrid devices. Similar to the AC microgrid, the DC microgrid must also connect to the utility via a PCC. However, as the grid is AC, the PCC is typically composed of an antiparallel system of an AC-DC rectifier for delivery of DC power to the microgrid system and a DC-AC inverter for interfacing with the AC grid. While costly, the flexibility afforded by the use of power converters provides numerous operational advantages; islanded-mode DC inverter-coupled microgrid systems can resynchronize with the utility by adjusting the phase, frequency and voltage of a single PCC device as opposed to AC microgrids that require synchronization of all generation components, which are often high-inertia and sluggish rotating machinery. While conversion losses are incurred at the PCC through the AC-DC rectification process for power delivery into the microgrid and the DC-AC inversion process during grid power export, large central power electronic converters are typically more efficient than the numerous smaller units used in many AC microgrids. If the system is operated at zero net import, DC-AC and AC-DC conversion penalties are avoided altogether.

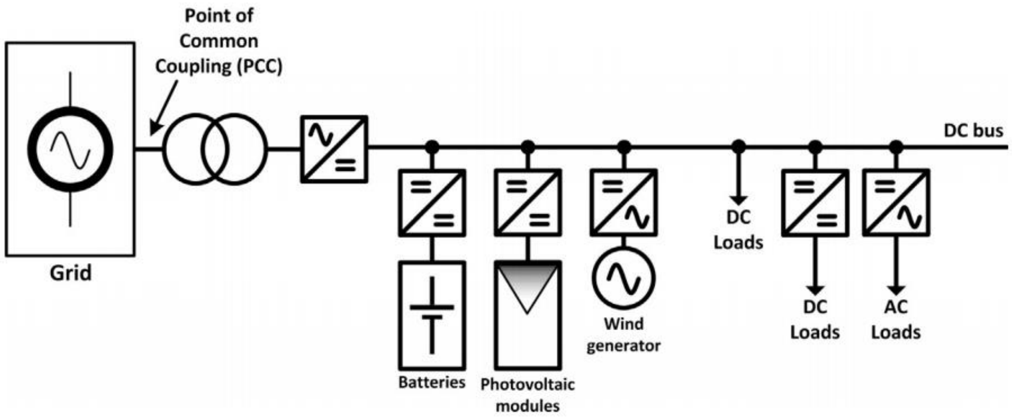

Figure 7. Example DC microgrid (Patrao, 2015).

While DC microgrids provide efficiency and controllability benefits, they do present unique challenges: DC circuit breakers are difficult to implement due to lack of a zero-voltage and zero-current crossing which naturally extinguishes electrical arcs in AC breakers. Also, a scarcity of microgrid components designed for DC systems results in high capital investment requirements, which often outweighs cost savings provided by improvements in efficiency. A lack of well-established regulatory standards further hinders implementation and proliferation of DC microgrid systems.

2.4.3. HYBRID MICROGRIDS

The self-contained feature of a microgrid allows for fractal nesting of multiple microgrid systems. This enables the coexistence of DC and AC microgrid systems within a single point of common coupling to the main utility grid by layering microgrids within the same local system, as shown in Figure 8. These configurations are known as hybrid microgrids. In the case of a typical hybrid system, a parent AC microgrid directly connects to the utility via a PCC. Within this microgrid, a branch of the microgrid circuit equipped with back-to-back DC-AC and AC-DC converters acts as a secondary PCC to a nested DC microgrid. In this manner, a hybrid microgrid is essentially an AC microgrid with a DC microgrid contained within it, and the configuration allows for the partitioning of all DC devices to improve overall system efficiency while allowing AC microgrid components to operate with the existing AC infrastructure.

A practical example of a hybrid microgrid would be the case of a parking structure within a community-scale AC microgrid containing electric vehicle chargers, rooftop photovoltaic panels, and a battery energy storage system. In a strictly AC microgrid system, these devices would require individual power electronics inverters and rectifiers and thus incur conversion losses. In a pure DC microgrid system, parking structure devices could readily share power, but would not easily be able to export power to other AC components within the microgrid system without the costly installation of inverters at each device. Several studies of similar configurations have been presented in research and have shown improved system performance compared to the strictly AC or DC cases (Maclay, 2011).

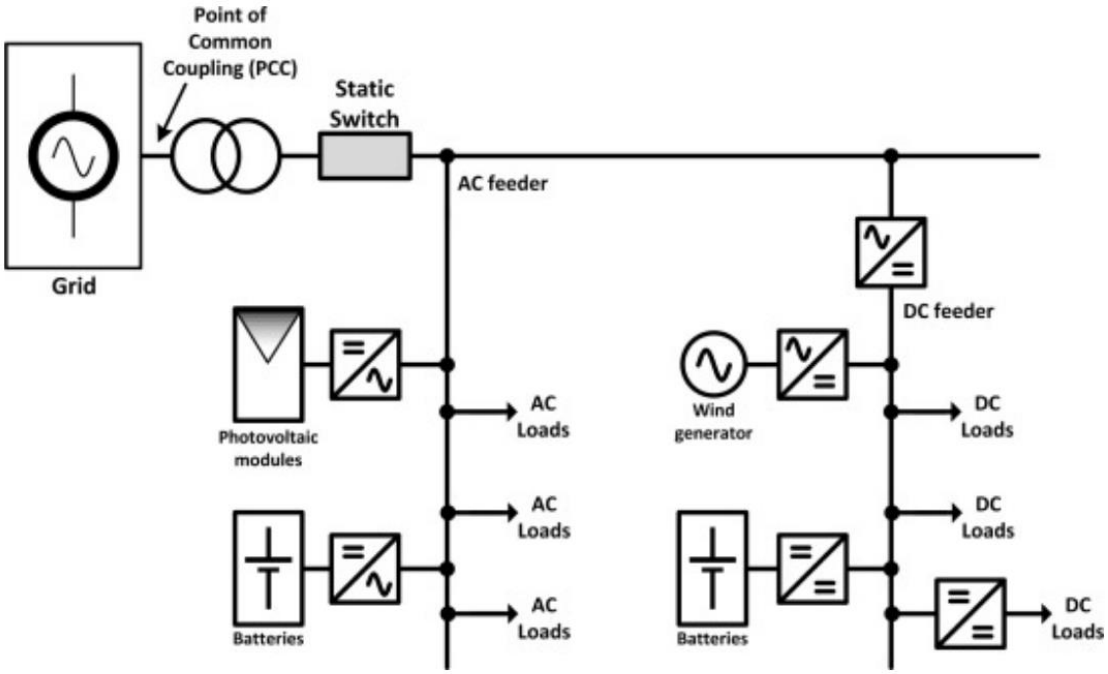

Figure 8. Example hybrid microgrid (Patrao, 2015).

2.5. MICROGRID CONTROL

Microgrid control requirements are vastly different from traditional systems. In grid-connected microgrids, the high degree of coupling between microgrid components necessitates responsive controllers to avoid undesirable phenomena such as power oscillations and poor power quality. Islanded conditions are substantially different from those of the grid-connected scenario as the grid reference becomes unavailable and local voltages and frequency become much more sensitive to generation and load fluctuations (Katiraei, 2006). Existing distribution networks were not designed to tolerate such occurrences and will often fail. Several of the major issues microgrid controllers must be designed to address include:

System protection

With traditional power systems, available fault current contributions are primarily limited by device and line impedances and typically range in hundreds to thousands of amperes in distribution circuits. Rotating generators contain significant kinetic energy and can provide large amounts of fault current to rapidly trigger circuit breakers. DC-AC inverters, by comparison, utilize current-mode feedback which provides inherent overcurrent limiting and the electrical energy stored by inverter filter elements is negligible. Numerous studies demonstrate that these factors result in decreased fault detection rates (Nimpitiwan, 2007) (Kastha, 1994) (Brucoli, 2007) with proposed solutions (Overbeeke, 2009) (Han, 2010) requiring artificial fault current injection or high-speed fault signaling. Additionally, IEEE 929-2000 / UL-1741 compliance requires ground fault detection and grid-connected anti-islanding (UL 1741, 2010) (Basso, 2004) which further reduce available fault current. These differences, along with bidirectional power flow which alters the fault current path, dramatically alter the fault characteristics of the microgrid and the controller must be able to dynamically adjust system protection coordination accordingly.

Dynamic Response

DC-AC inverters are nonlinear and highly dynamic. Unlike power sources which utilize large rotating machines, DC-AC inverters have very little or no electrical inertia and are more sensitive to source, line and load transients. This necessitates high-bandwidth controllers and low-latency communications channels for appropriate control of multi-agent systems.

DER Differences

DERs utilize controllers that are different than those in traditional generators. Prime movers driving synchronous generators are typically controlled with frequency-power droop controllers, which are shown to be intrinsically stable in systems with multiple generation sources, whereas the DC-AC inverters found in many DER systems utilize voltage-tracking or current-mode control. Ancillary control features such as maximum power point tracking (MPPT) found in many DER technologies such as PV, fuel cells, and wind adds further complexity to the control of microgrids containing DERs.

High Generation Variability

Renewable DERs are highly dependent on environmental conditions. Unlike fuel-powered plants, most renewable energy technologies have minimal control over generation availability. In the case of excessive power generation, curtailment methods may be applied, however, very little can be done in the situation where energy demand exceeds supply without an energy storage resource. In these cases, voltage/frequency dips may occur as consequence and must be mitigated via demand response load reduction or the provisioning of adequate energy storage.

In addition to addressing the above issues, microgrid controllers must also be capable of transitioning the system into islanded-mode operation when appropriate and to ensure system stability by balancing load and generation; regulating frequency, phase, voltage, and line current during the standalone duration; provide the ability to supply ancillary services to the main grid; and interface and communicate with the utility as a single controllable entity. Much research has been conducted that investigates microgrid optimization and control, as will be discussed in the following sections. There are two major approaches to the configuration of microgrid control: centralized, and distributed.

2.5.1. CENTRALIZED

Centralized microgrid controllers incorporate a single master controller that is responsible for monitoring the state of all critical components within the microgrid and determines the appropriate control actions necessary to maintain proper system operation such as charging or discharging of energy storage devices in anticipation of future generation mismatch, modifying real and reactive power generation to regulate line voltages, or reconfiguring load-shed and circuit protection coordination plans within the microgrid. The controller transmits the control actions to local devices via a communications network in a master-slave configuration. Such a centralized control scheme necessitates fast, reliable, and low-latency communication links between the master controller and field devices, as a failure or degradation of the communications link often results in the failure the entire microgrid system, especially in islanded-mode operation. The study of microgrid controllers utilizing a centralized controller with a communications link to each DER in small-scale microgrids is well-established (Kim,

2010) (Liang, 2009) (Li, 2004) (Sani, 2010) (Pogaku, 2007) for both grid-connected and island modes (Lopes, 2006) (Katiraei et al., 2008). The communications requirements of larger microgrid systems often presents an upper system size limit when using the centralized approach, with the cost of establishing communications links between microgrid agents becoming prohibitively expensive as the number of microgrid devices increases.

2.5.2. DISTRIBUTED

Distributed systems, in comparison, are built on a collection of independent agents with each device operating autonomously. Controllers in distributed systems may receive varying degrees of information from neighboring devices to assist in their operation, ranging from completely independent agents that collect no information and operate entirely based on local measurements, to fully networked systems where all devices broadcast their status to all other devices on the microgrid. In all cases of distributed microgrid systems, devices do not directly influence the operation of any other devices on the network. Most distributed controllers mirror well-studied droop control strategies developed for the coordination of large power plants equipped with synchronous generators, which themselves could be considered DERs on the very large scale microgrid of an interconnection region. Modern decentralized controllers of this type rely on frequency-power droop control for power sharing and voltage-reactive power droop control for voltage regulation (Kao, 2009) (Guerrero, 2009) (Majumder, 2008) (Katiraei, 2006) (Anh, 2010). This approach lends itself to a “plug and play” approach of microgrid construction and the omission of a single point of control failure increases system reliability.

However, lack of a master controller makes it difficult to manage the operation of the system as a whole for certain tasks, such as the optimization of generation asset dispatch. Similar to centralized systems, in communications-enabled decentralized systems, network requirements quickly become impractical to achieve as the device count increases, especially in complete-graph systems where each microgrid device is updated with the state of the entire system. Recently, much interest has focused to the application of distributed control schemes based on some form of scalable heuristic or machine learning-based control (Parisio, 2014) (Khalghani, 2016) to address these issues.

2.5.3. CONTROL HIERARCHY

In addition to the topologically classifications of centralized and decentralized control, controllers may also be classified by the timeframes in which control action is applied. A control hierarchy may be established to address the unique requirements each timeframe presents. For example, local distributed controllers may be utilized to provide fast-acting transient stability control while a slower centralized controller is used for periodic monitoring and setting steady-state system values. Currently, the prevalent hierarchal approach separates microgrid control into three temporal categories: primary, secondary, and tertiary control, each separated by the distinct time ranges in which they operate, their relative speed of response, and the functionality they provide (Guerrero J. M., 2011) (Bidram, 2012).

Figure 9 shows a typical three-stage framework in which the partitioning of control features begins with individual DERs controlled with device-level “primary control” to provide local device-level stability. As primary-level control devices operate independently, potentially resulting in sub-optimal overall system performance, groups of DER are coordinated at a slower timescale with “secondary control” to correct for deviations in system-wide voltage and frequency. Finally, “tertiary control” sets the long-term operations planning of the entire system by optimizing microgrid asset dispatch and provides a single control interface with external systems. With this structure, microgrid control functions can be abstracted and isolated and communications requirements can be reduced by confining data exchange to involved devices at the appropriate bandwidth and latency requirements particular to the control level. This method addresses many of the scaling challenges of both centralized and decentralized control approaches.

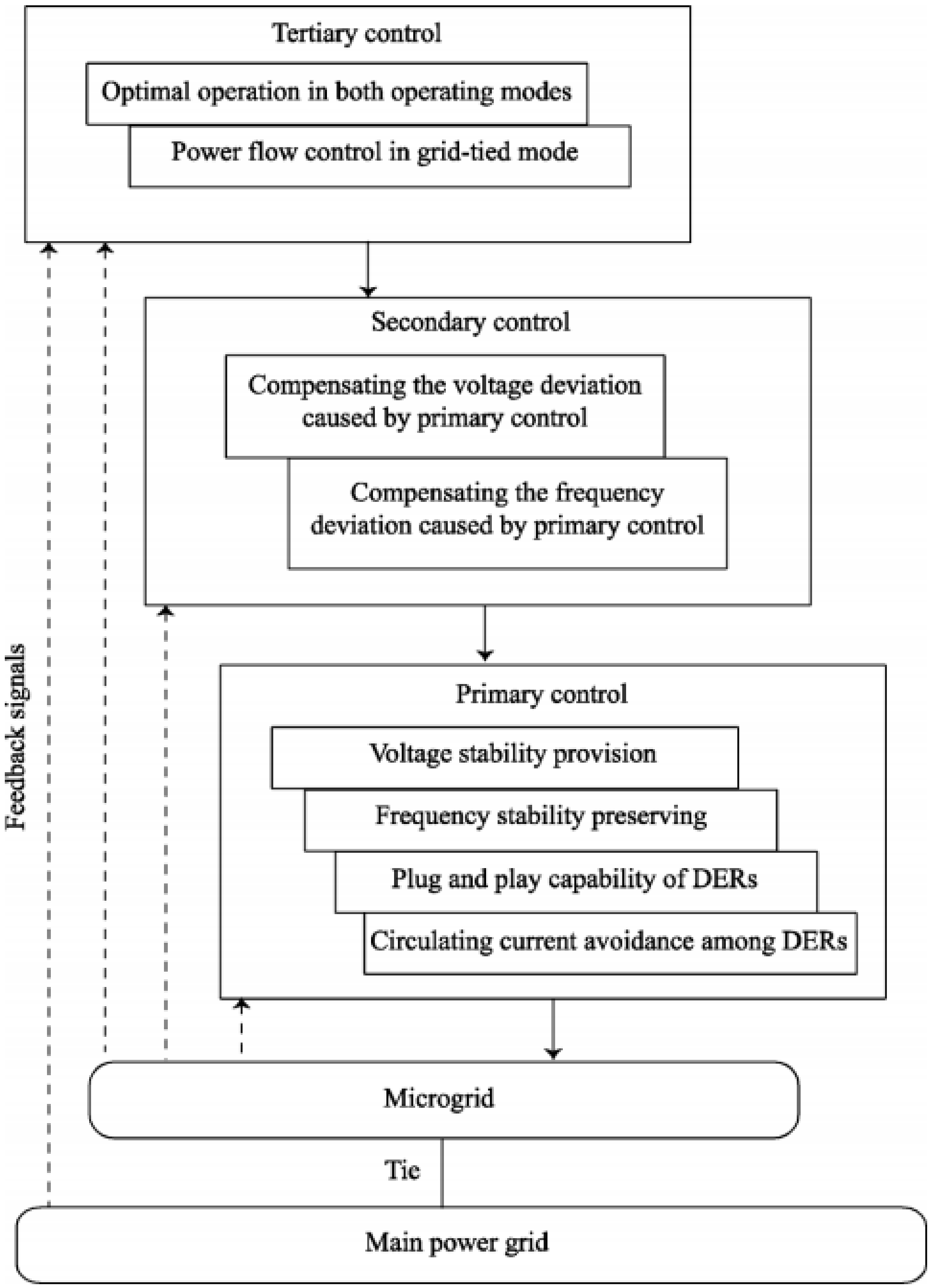

Figure 9. Microgrid controller hierarchical levels (Bidram, 2012).

2.5.4. PRIMARY CONTROL

Primary-level control is responsible for microgrid operation at the transient timescale and provides device-level stabilization and regulation of real and reactive power injections and rejection of external line voltage and current disturbances. Primary control applied to synchronous generator-based devices achieve this by utilizing governor controllers and field winding voltage regulators to adjust real and reactive power outputs, respectively (Kroposki, 2007). DC-based DERs, in comparison, must convert DC power into a grid-compatible AC output prior to power injection and achieve this via the use of grid-tied DC-AC inverters. Instead of governors and field voltage regulators, the primary control in these devices consists of a current feedback controller that trigger sets of semiconductor switches to generate AC and synchronize the inverter output with the grid. Controllers also regulate power output, stabilize the operation of the inverter by dampening power oscillations, and provide additional functions such as such maximum power point tracking, islanding detection, and local reactive power support.

As primary controllers typically only manage local devices, they accommodate coordination commands from agents higher in the control hierarchy such as from secondary control systems that supervise the operation of DER groups. Due to this requirement, primary controllers are equipped with inputs for adjusting setpoints from external systems. In the case of rotational generator controllers, these setpoints adjust frequency and mechanical power generation, often in the form of a frequency-power droop slope provided by a secondary control system, and field excitation current setpoints. Inverter-based devices accept an outer voltage control loop reference to achieve power sharing among multiple devices. Additional inputs include control setpoints for adjusting voltage, frequency, and phase of the inverter output.

2.5.5. SECONDARY CONTROL

Transient-level stabilization of power generation contributions among DER devices is critical in achieving stable system operation in both islanded and grid-connected microgrid modes. While the steady-state power sharing ratios and setpoints are generated by tertiary control, usually as a product of optimal power-flow analysis over a timescale of seconds to minutes, the actual power sharing mechanism is implemented at the secondary control level to achieve the rapid response necessary to compensate for line transients (Rocabert, 2012). In islanded-mode operation, or in grid-connected systems with tightly coupled clusters of DER interfaced to the PCC via a relatively large electrical impedance, it has been demonstrated that secondary-level power stabilization mechanisms installed among parallel-connected DER is required to avoid adverse phenomena such as power oscillations between devices (Coelho, 2002). Modern secondary-level control implementations seek to achieve this by using distributed controllers that emulate the frequency-power droop characteristics of synchronous generators or using a direct control approach and implementing high-speed master-slave control between DERs and a central controller.

2.5.5.1. DIRECT CONTROL

While primary control provides local device stabilization, it is typically neither equipped with the computational capacity nor has access to sufficient system visibility to perform stabilization throughout the entire microgrid. One approach to achieve system-level stabilization is to employ a secondary-level controller that receives system-wide DER measurements of power generation, frequency, voltage, and current and rapidly generates and transmits adjustments to primary-level setpoints to stabilize the overall system. This is distinct from tertiary-level control which provide optimal steady-state operation but does not address transient-level system stability.

While this is the most direct method of control and the also the most resilient to power disturbances (Katiraei, 2006), it relies heavily on a reliable high-performance communications pathway. Loss of the communications link or failure of the secondary controller will result in loss of device coordination and often complete system failure. In systems with a large number of DERs, this solution is size-limited due to high communications network bandwidth and low latency requirements. Several network partitioning configurations have been proposed to address these issues and scalable, low-latency communications technologies are an active area of research (Sortomme, 2005) (Wang, 2012).

2.5.5.2. DROOP CONTROL

Perhaps the most common implementation of secondary-level control, droop control achieves system-level stability via use of linear frequency-power and voltage-reactive power relationships inherent in synchronous generators, an example of which is shown in Figure 10. Several alternative droop relationships are presented in Table 3. By adjusting the relative droop slope between generation assets, coordination of the power-sharing contribution ratio among multiple DER agents may be achieved in addition to system stabilization. Additionally, if droop ratios are pre-determined, a fully decentralized microgrid system requiring only the autonomous operation of individual DER agents may be formed, and the requirement of transmission of measured electrical values between system components is eliminated. Combining this strategy with a centralized system capable of continually updating droop ratios allows for real-time system performance optimization while retaining the resiliency features of a decentralized system, as communication or central controller failure may be remediated by falling back to pre-configured settings.

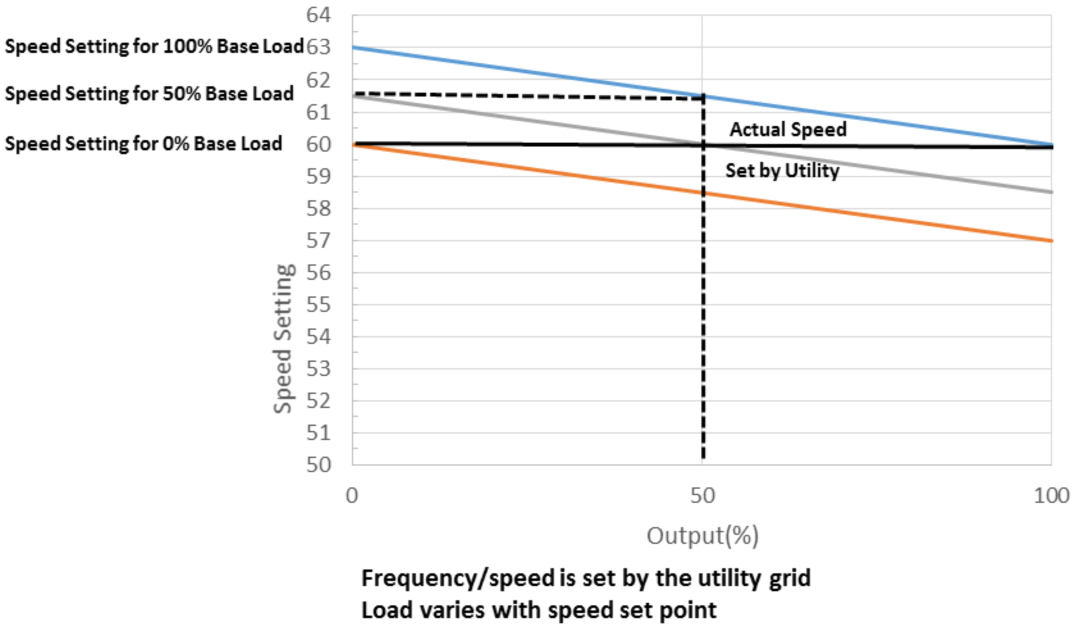

Figure 10. Conventional generator droop curve.

Droop Type	Implementation	Benefits	Disadvantages
Conventional	P/ω and Q/V	• Avoids requirement of a critical communication link • Great flexibility • High reliability	• Slow dynamic response • Poor harmonic load sharing • Line impedance mismatch affects power sharing • Poor voltage regulation • Poor performance with renewable energy resources
Virtual Impedance	Virtual impedance and conventional droop control	• Fast dynamic response • Good power sharing	• Difficult to determine coefficient for integral-derivative term
Adaptive Droop	Integral loop and adaptive droop control	• Good transient response • Excellent power sharing	• Virtual reactance needed to minimize power circulation
Robust Droop	H-infinity synthesis method	• Automatically compensates for voltage drop	• Poor reactive power sharing

Table 3. Comparison of various droop control methods (Tayab, 2017).

Droop control applied to inverter-coupled DER attempts to emulate the droop characteristics of traditional synchronous generator machines. Real and reactive power inverter output are modified with a secondary-level power-tracking loop which introduces an artificial real power-frequency and reactive power-voltage mapping. While droop control applied to inverter-based systems has proven successful and is widely utilized, several issues remain arising from the fundamental differences between rotational generation and inverter-coupled sources:

System response

In single-phase systems, the use of an averaged DC input power measurement to estimate output AC power reduces the overall power control bandwidth and lowers the dynamic response of the system. Several techniques been proposed to address this (Roshan, 2007), such as the use of a virtual voltage and current signal to provide an additional power calculation basis have been proposed.

Black start

Grid-following inverters require an existing AC line voltage source to extract frequency, voltage magnitude, and phase references. In the absence of an energized system many inverter systems will not operate, even with adequate input power, due to anti-islanding regulations (IEEE Standard 1547A - 2014) and the black start of a de-energized electrical system would not be possible. In remote and permanently islanded microgrids, a stable line reference that is invariant to loading conditions is required for both black start and normal microgrid operation.

Design variation

The design of inverter systems is more varied compared to traditional generator systems and may result in large differences in dynamic behavior even among similarly rated systems. In moderate cases, this manifests as modeling uncertainty when analyzing microgrid systems, and in extreme cases may result in systems rendered physically incapable of reaching power sharing and stability targets. To address modeling uncertainty, research has been conducted in the auto-characterization of inverter output impedance via perturb-and-observe methods (Sera, 2013) and online differential impedance measurements (Guerro, 2005).

Harmonics / DC Offset

The high-speed switching of power electronic components introduce voltage and current distortion into the microgrid system if not properly filtered. Additionally, a failed semiconductor device in non-isolated inverters may result in DC being directly injected onto the electrical network, potentially resulting in damage to connected devices and/or incorrect operation of protective devices. Modern electronic loads that rectify AC power will also produce current harmonics that propagate throughout the system without adequate input filters or active power factor correction (Gu, 2013).

To address these issues, several modifications to the traditional droop control scheme have been proposed such as the addition of a frequency restoration loop (Guo, 2015) or use of virtual output resistance to damp power oscillations (Guerrero J. M., 2007). Heuristic power-sharing control mechanisms have also been investigated such as particle swarm (Hassan, 2011) and ant colony inspired approaches (Colson C. M., 2009).

2.5.6. TERTIARY CONTROL

Tertiary control is the highest level of control abstraction and sets the long-term operations trajectory of the microgrid systems and may operate on a time horizon as long as on the order of days. This level usually consists of a communications interface to the regional grid operator so that the entire microgrid system may appear as a single entity within the main grid. This interface allows for microgrids to provide services in grid markets such as the provisioning of ancillary services including scheduling and dispatch, reactive power and voltage support, spinning reserve, and demand response resources. Tertiary control operates by coordinating all devices within the microgrid as a group and provides features similar to energy management systems (EMS) deployed in traditional power systems. As tertiary controllers monitor and communicate with all DER agents on the microgrid, they are appropriate for tasks that operate on long time frames and have the lowest bandwidth requirements. Two of the main tasks at the tertiary control level are real-time optimization and protection coordination. Tertiary control also supervises DERs to ensure that established power quality limits, such as line voltage, system frequency, and line current are respected. If anomalies are detected, the tertiary control system is adjusts the coordination of secondary-level controllers to resolve these issues.

2.5.6.1. REAL-TIME OPTIMIZATION

When operating in grid-connected or steady-state islanded mode, tertiary control dispatches available DER resources such that a particular cost function, typically operational cost, is minimized while subject to constraints such as maintaining adequate energy reserves in energy storage systems to carry through an island transition and maintaining adequate power quality across microgrid busses. Real-time optimization requires computationally intensive optimal load-flow calculations as well as visibility of all power generation and consumption across the system. Many of the optimization techniques used in EMS systems have been directly applied to tertiary-level microgrid control. Optimization routines applied to the energy management and operational planning of a microgrid with PVs are discussed in (Zhi, 2011) (Kanchev, 2011) and optimization of generator dispatch of such systems via techniques such as mixed integer programming and fuzzy logic are presented in (Guan, 2010) (Deng, 2011). Techniques that focus on other optimization criteria such as the minimization of fuel consumption are presented in (Aramburo, 2005), and optimal participation in the energy market has been investigated as well (Celli, 2005).

2.5.6.2. PROTECTION COORDINATION

Tertiary control implements protection coordination via the generation of contingency response plans that are uploaded to secondary-level controllers. These response plans may then be installed within individual DER primary-level controllers to ensure rapid execution of remedial actions when triggered. As protection coordination requires knowledge of the entire microgrid topology and the current load-flow system state, a model of the microgrid system is usually required. Non-model-based approaches such as those utilizing fuzzy logic or artificial neural networks for heuristic system protection are an active area of research (Hatziagyriou, 2014).

An important distinction between traditional and microgrid power systems is the prevalence of bidirectional flow. Power flow reversal is typically rare in tradition power systems but is common in microgrids with high levels of DER penetration and nearly always present in systems switching between operating in grid-connected and islanded-modes (Colson, 2009). A reversal in power flow results in a change in the fault current path, which necessitates re-coordination of protective devices. As such, conventional protection schemes such as static time-grading are incompatible for use in microgrid systems and tertiary control must accommodate changes in power-flow direction via solutions such as the use of differential relay protection devices, protective device communication, and adaptive time-graded protection. More advanced technologies such as zone division (Zamani, 2004) and wavelet transient current analysis for real-time fault location detection have been proposed (Park, 2013).

2.5.7. COMMUNICATIONS

The selection of communications technologies used within the microgrid is heavily dependent on the level in the control hierarchy in which the communications are deployed, as each layer has varying bandwidth, latency, and reliability requirements. At the primary control level, there exists strict requirements for high-bandwidth real-time transmission with low and predictable signal delay, and non-multiplexed single-channel technologies are often deployed such as hard-wired analog and digital input/output lines and single-mode fiber.

Secondary- and tertiary-level communications have relaxed single-device bandwidth and latency requirements but are often required to connect to more devices. While some serial interfaces such as RS-232 and RS-485 are used, it is typically more common to deploy networks utilizing local- or wide-area network-based technologies. The use of the Transmission Control Protocol/Internet Protocols (TCP/IP) implementation of the Open System Interconnection model (International Organization for Standardization, 2010) is widespread in modern communications systems and provides many of the scaling and bandwidth performance attributes required by secondary and tertiary control. Based on the TCP/IP framework, high-performance bus-based protocols such as IEC61850 GOOSE (International Electrotechnical Commission, 2013) and DNP3 (IEEE Power and Energy Society, 2010) are commonly used within the power systems industry. Use of TCP/IP over Ethernet leverages equipment from the information technology industry and allows power systems-specific layer protocols such as IEC61850, DNP3, and MODBUS to be implemented within the TCP/IP stack by modifying only a selection of the stack layers. For example, the DNP3 protocol is composed of the link, transport, and application layers, leaving the remaining physical, network, session and presentation layers of the TCP/IP model unchanged. Table 4 compares common communications protocols.

Protocol	Description	Benefits	Disadvantages
MODBUS RTU	• Established in 1979 • Widely used in industry and accepted by many communicating devices	• Legacy protocol, widely adopted	• Cannot update based on signal changes
MODBUS TCP/IP	• Offers the same functions as Modbus RTU as well as compatibility with multi-master architectures	• Support for TCP/IP	• Slower than MODBUS RTU
DNP3	• Suited for remote control and monitoring of substations in the electric network	• Provides data priority classes • Allows polling at different frequencies • Higher baud rates	• High bandwidth requirements
IEC 61850	• Protocol for communication in electrical substations • Interoperability between multi-vendor devices	• Includes data model • May be mapped to other protocols within data model • Widely implemented at substations	• Requirement of data model complicates initial configuration

Table 4. Comparison of microgrid communications protocols (Schneider-Electric).

2.6. MICROGRID ANALYSIS

Fortunately, similarities between microgrid and non-microgrid systems allows traditional analysis techniques to be directly applied for a large majority of microgrid systems. Depending on the types of phenomena (steady-state or transient) to be simulated, several classical power systems analysis approaches are used.

2.6.1. LOAD-FLOW

Load-flow is a numerical analysis approach used to solve for the steady-state bus voltages and line currents in electrical power systems. It is often used in power system design and optimization tasks such as the allocation of circuit loading distributions, determination of optimal placement of reactive power correction equipment, minimization of real and reactive power transmission losses, and selection of transformer tap settings. Optimal power-flow, an extension of load-flow, is used to determine the optimal economic dispatch of generation units by solving the unit commitment problem via successive load-flow iterations.

Load-flow is generally only applied to grid-connected systems or those with large generation sources, and the absence of these elements in islanded-mode microgrids may render load-flow ill-suited for the study of such systems. The load-flow problem formulation requires the presence of a slack bus, an infinite-capacity power source with a constant voltage magnitude, frequency and phase angle. The slack bus is necessary in solving load-flow studies as this entity provides or absorbs any real and reactive power required to account for line losses, which are unknown quantities until a load-flow solution is determined. When solving load-flow for traditional power systems, it is common to designate the utility connection or the largest capacity generator as the slack bus due their relatively high output capacity and stable frequency and voltage characteristics. In the case of islanded-mode microgrids, the system is disconnected from the utility and it is often difficult to identify the system slack bus as the frequency and voltage at all nodes may vary with changes in system loading. However, load-flow still remains a powerful and widely used tool in both grid-connected and islanded microgrid system design and analysis.

AC circuit analysis for fixed-frequency systems may be simplified by representing time-varying sinusoidal signals with time-invariant phasors, reducing the problem of solving a time-varying system to the following steady-state problem: At each system bus, *i*, either 1) real power, P_i, and reactive power, Q_i, contributions are known or 2) real power and voltage magnitude, $|V_i|$, are known. The first case represents busses with electrical loads or sources operating with a constant real and reactive power values while the second represents busses with generators providing fixed real power and equipped with local voltage regulation. At the slack bus, the voltage magnitude and voltage phase angle, θ_i, are known and held constant. A summary of bus types is presented in Table 5. For an n-bus, r-generator system, a requirement of 2n-r-1 independent equations are required to solve the load-flow problem which are provided by the real power balance (1) and reactive power balance (2) equations at each node. A static admittance matrix (3), Y, where $Y_{ij} = |Y_{ij}|\angle\alpha_{ij}$ representing the electrical admittance between nodes completes the problem formulation. Unlike linear circuit models in which voltage and currents in combination with an admittance matrix may be directly solved with linear algebra techniques, the use of real and reactive power variables results in a nonlinear system that can only be solved with numerical analysis techniques.

$$P_i = \sum_{j=1}^{n} |V_i||V_j||Y_{ij}| \cos(\theta_i - \theta_j - \alpha_{ij}) \tag{1}$$

$$Q_i = \sum_{j=1}^{n} |V_i||V_j||Y_{ij}| \sin(\theta_i - \theta_j - \alpha_{ij}) \tag{2}$$

$$Y = \begin{bmatrix} Y_{11} & \cdots & Y_{1n} \\ \vdots & \ddots & \vdots \\ Y_{n1} & \cdots & Y_{nn} \end{bmatrix} \tag{3}$$

Bus Type	Quantities	Description
Swing/Slack	$\|V\|, \theta$	Reference bus. Voltage magnitude and phase angle are constant. This infinite capacity bus provides real and reactive power to account for line losses.
PV	$P, \|V\|$	Power-voltage busses represent generation sources with active voltage regulation. These busses contribute constant real power and automatically adjust reactive power output to maintain a constant line voltage magnitude. Synchronous condensers and generators are examples of PV busses. Reactive power minimum and maximum limits may be imposed.
PQ	P, Q	The most common bus, load busses source or sink constant real and reactive power.

Table 5. Load-flow bus types.

2.6.1.1. NEWTON-RAPHSON

The Newton-Raphson algorithm is an iterative numerical method for obtaining the roots of nonlinear functions and may be directly applied to solve the load-flow problem. In the Newton-Raphson method, an initial solution is estimated from which a Taylor-series approximation of the load-flow equations is derived. Typically, all higher-order terms are omitted with the assumption that the starting point is sufficiently close to the actual solution, and the resulting linearized equations are solved to yield an updated solution estimate. The updated estimate then becomes the starting point for the next Newton-Raphson iteration and this process is repeated until the difference between consecutive solutions is within an acceptable limit. A flowchart of the Newton-Raphson algorithm is shown in Figure 11.

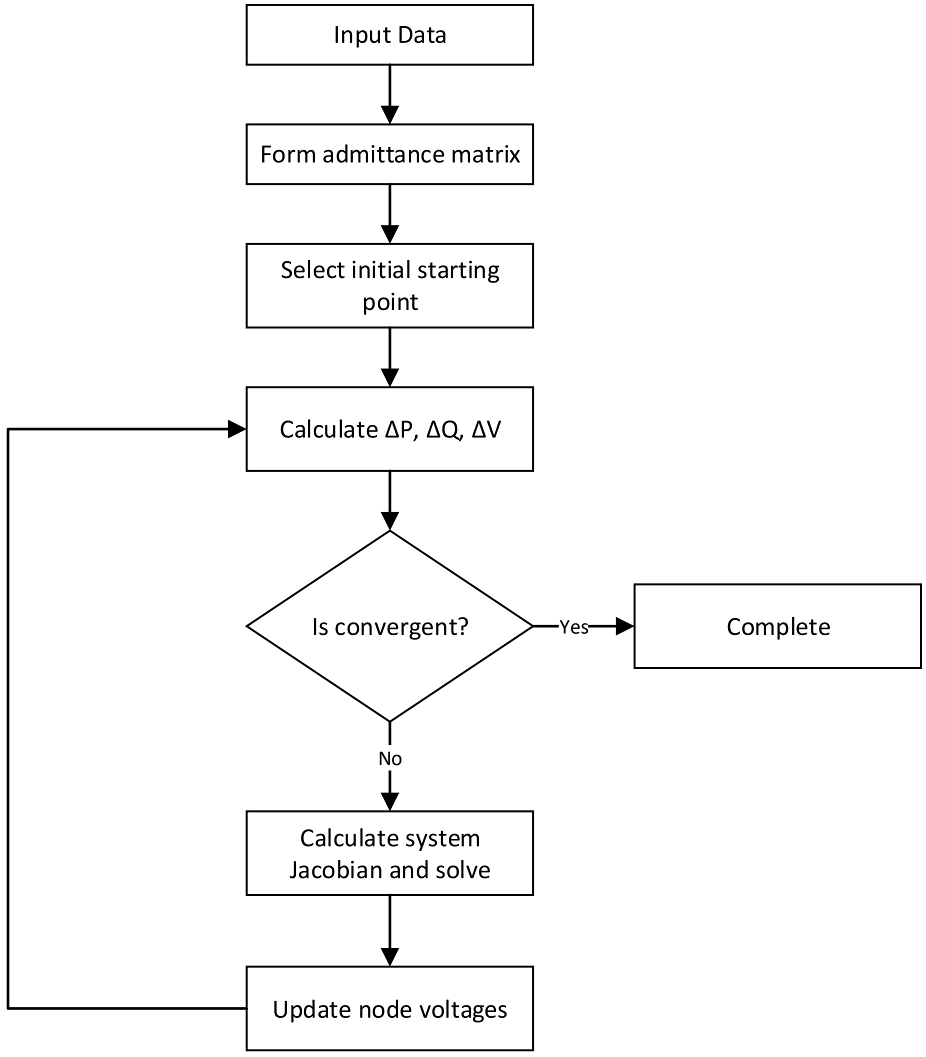

Figure 11. Newton-Raphson algorithm flowchart.

2.6.1.2. GAUSS-SEIDEL

The Gauss-Seidel method or Liebmann method, shown in Figure 12, is an iterative technique that solves the nonlinear load-flow problem via successive estimates of bus voltages. While the convergence time of the Guess-Seidel method is slower in comparison to Newton-Raphson, the method has the advantage of solving load-flow without requiring a direct matrix inversion step, greatly reducing the memory requirements of the algorithm (Bokka, 2010). The method starts with an initial estimate vector containing approximations for all unknown bus voltages. A PQ bus is selected and real and reactive power balance equations (1) and (2) in combination with the remaining estimate vector entries are used to calculate the voltage at the bus. This is also repeated for PV busses with the modification that reactive power values are solved. This step results in a more accurate estimate for the unknown variables and results in a reduction in the voltage, real power and reactive power mismatches in the overall solution set. The process repeats until the change in bus voltage estimates between iterations falls below a pre-specified value, at which point the algorithm is considered to have converged at a solution.

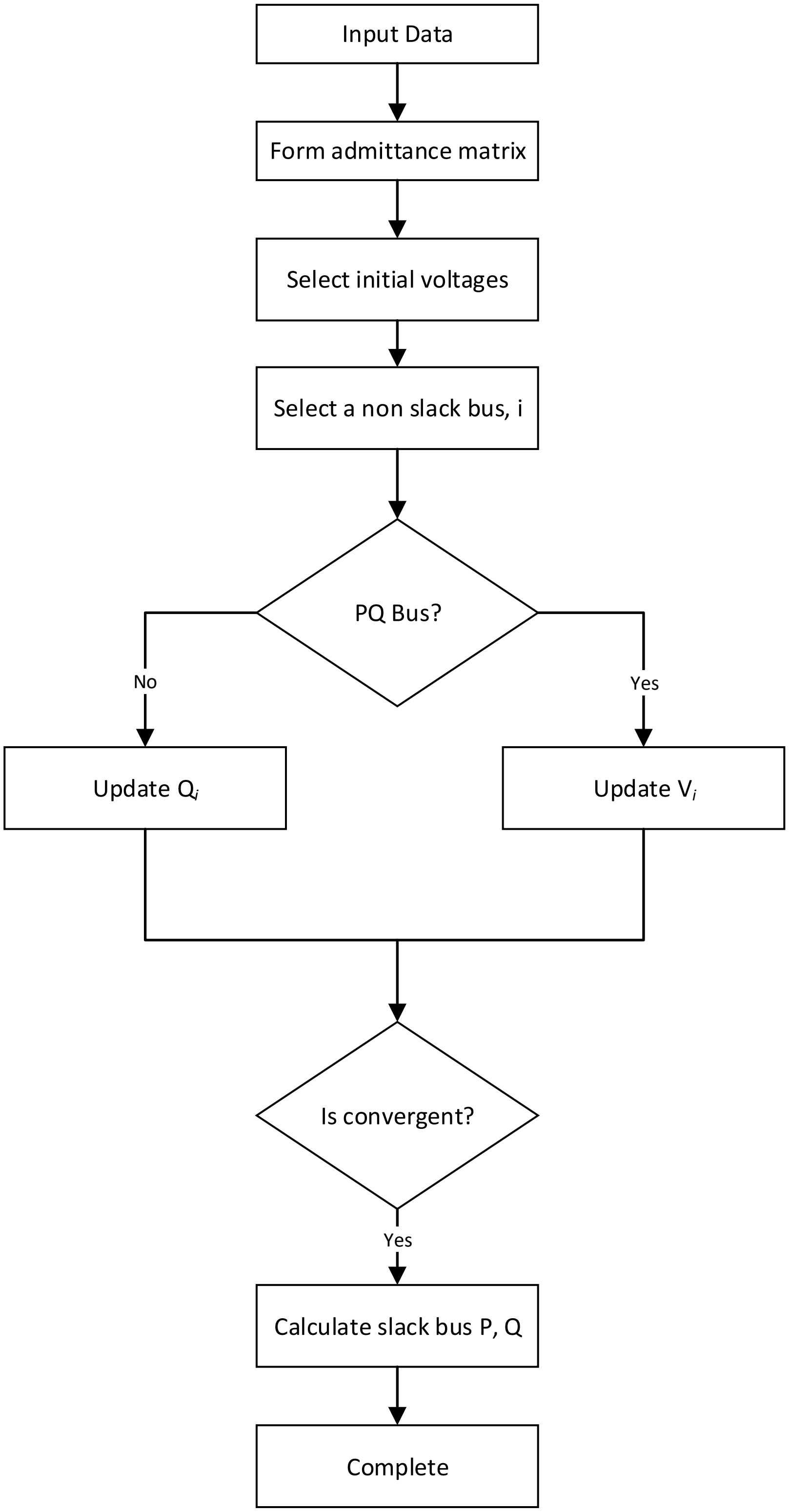

Figure 12. Gauss-Seidel algorithm flowchart.

2.6.1.3. FAST-DECOUPLED

In transmission-level power networks, the coupling between real power/voltage phase angle and reactive power/voltage magnitude is often much more significant than the coupling between real power/voltage magnitude and reactive power/voltage phase angle due to the high reactance-to-resistance ratio of transmission lines. This feature may be exploited to reduce the computational burden of solving load-flow via the Newton-Raphson method by using an approximated load-flow model in which a system Jacobian matrix (4) with $\frac{\partial P_i}{\partial V_j} \approx 0$ and $\frac{\partial Q_i}{\partial \theta_j} \approx 0$ is used. While modern computers can manage solving full load-flow problems with bus counts commonly encountered within microgrid systems, fast-decoupled methods are often necessary when considering load-flow at the subtransmission and transmission levels where upwards of thousands to millions of busses across a regional electrical system may be considered.

$$\begin{bmatrix} \Delta P \\ \Delta Q \end{bmatrix} = \begin{bmatrix} \frac{\partial P}{\partial \theta} & \frac{\partial P}{\partial V} V \\ \frac{\partial Q}{\partial \theta} & \frac{\partial Q}{\partial V} V \end{bmatrix} \begin{bmatrix} \Delta \theta \\ \Delta V / V \end{bmatrix} \tag{4}$$

2.6.1.4. DC LOAD-FLOW

Despite the name, DC load-flow is actually an AC load-flow approximation in which the complete AC load-flow model is further simplified into a fully linear system. The DC load-flow technique assumes negligible line resistance, small phase angle difference between neighboring busses, and a flat voltage profile at all busses across the system resulting in the following linear problem formulation:

$$P = B'\theta \tag{5}$$

where P is the vector of real power contributions at each bus, θ is the vector of bus phase angles, and B’ is modified admittance matrix in which only line susceptances are considered. This allows for the calculation of the problem solution with a single linear matrix inversion step as opposed to the requiring the use of iterative numerical analysis techniques.

DC load-flow only considers real power flow, assumes infinite reactive power capacity at all nodes, and ignores transmission losses. While this method offers an approximation of the actual solution that may be unsuitable for some power systems analysis tasks, it is effectively used in situations where many load-flow case studies must be conducted such as network reconfiguration, system optimization, and line outage contingency planning. For the optimization of very large systems, it is common to conduct preliminary DC-based studies followed by full load-flow iterations once the parameter space has been confined.

2.6.2. ELECTROMAGNETIC TRANSIENT SIMULATIONS

While load-flow techniques are useful for the steady-state analysis of traditional power systems and to some extent microgrid systems, the simulation of microgrids operating within highly dynamic conditions necessitates the use of modeling techniques with the capability to capture transient phenomena. It is often necessary to simulate effects on the timescale of several microseconds per time step to effectively capture transient effects such islanding and DER switching events. Frequency-dependent elements must also be accommodated as the line frequency in islanded systems, especially those without large generation sources, may fluctuate with changes in generation and loading. For these studies, electromagnetic transient (EMT) simulation based on state-space models is used.

2.6.3. STATE-SPACE

A suitable simulation technique to resolve transient effects is state-space modeling. In state-space modeling, microgrid components are mathematically represented with a set of first-order differential equations that relate the system inputs, outputs, and the internal state of the modeled system. State-space models are typically represented with a set of state and output equations presented in (6) and (7), where x(t) is the system state vector, y(t) is the system output vector, u(t) is the input vector, A(t) is the state matrix, B(t) is the input matrix, C(t) is the output matrix, and D(t) is the feedforward matrix. These equations may also be expressed in the discrete-time domain as a set of first-order difference equations, resulting in a system that is well-suited for simulation on computer systems.

$$\frac{dx(t)}{dt} = A(t)x(t) + B(t)u(t) \tag{6}$$

$$y(t) = C(t)x(t) + D(t)u(t) \tag{7}$$

State-space models have been developed for the majority of power system elements (Mathworks, 2003) (Emadi, 2004) and the state-space method readily accommodates the design of microgrid controllers via state feedback.

Discretization of the continuous-time differential equations into state-space difference equations may yield undesirable truncation effects, which may result in simulation instability upon numerical integration (Fernando L. Alverado, 1983). This issue may be remedied by selecting an appropriate integration technique. Several integration solver methods commonly used in practice include forward and backward Euler, Runge-Kutta and Dormand-Prince (Mathworks, 2016), and are selected depending on the performance targets of the simulation as solvers have varying convergence time, numerical stability, minimum and maximum time step requirements, scaling and numerical accuracy tradeoffs. Several solvers are presented in Table 6.

Integration Technique	Order of Accuracy	Numerical Stability	Speed
Direct Euler	1	Low Issues with stiff systems	High
Modified Rosenbrock	2	High Suitable for stiff systems	High
Heun	2	Med	Med
Bogacki-Shampine	3	Med	Low
Fourth Order Runge-Kutta	4	High	Low
Dormand-Prince	5-8	High	Low

Table 6. Comparison of several solver methods.

2.6.4. STATE-SPACE NODAL

Nodal analysis is an electrical circuit analysis method that separates individual circuit elements at connection points, i.e. nodes, and solves for node voltages via the relationship I = V*Y, where I is the current vector obtained by expressing current contributions of each circuit element, V is the unknown vector of node voltages, and Y is the nodal admittance matrix determined by the circuit topology. While this method is typically reserved for the analysis of linear circuits, it may be combined with the electromagnetic transient approach to reduce the total effective node count by partitioning a large circuit into segments which are then represented as individual state-space systems, as illustrated in Figure 13. With this approach the time required to factor the total system admittance matrix is reduced significantly. Furthermore, the resulting state-space partitions may be solved in parallel on multi-core computer systems, extending the upper system size limit. This hybrid state-space-nodal (SSN) (Dufour, 2011) method is useful in the real-time simulation of large EMT systems and is capable of achieving extremely short maximum time steps, often less than a few hundred microseconds.

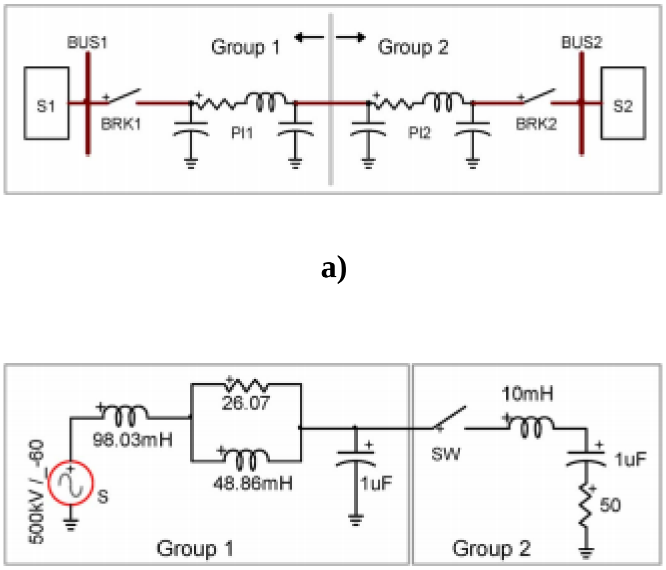

a)

b)

Figure 13. SSN system partitioning example for a) three-phase one-line circuit and b) switched resistor-inductor-capacitor (RLC) circuit (Dufour, 2011).

2.7. MICROGRID ELEMENTS

Common microgrid components include transmission lines, transformers, electrical loads and DER components such as photovoltaics, fuel cells, microturbine generators and inverters. Proper modeling of these elements is critical in the construction of a detailed microgrid system model. Descriptions of these components and their operating principals are presented in this section.

2.7.1. TRANSMISSION LINES

Transmission lines are conductors used to transfer energy between busses across an electrical power network. The most common type of transmission line, aluminum-conductor steel-reinforced, is composed of a strands of aluminum wire for used for electrical power transfer surrounding a steel support core. Several variations of conductors exist such of those composed of entirely of copper, and the addition of an outer insulating sheath. Transmission lines are typically installed along overhead power poles or underground in conduits. The conductor material and length, method of installation, and installation geometry all affect the electrical and thermal characteristics of the line. A transmission line model may be constructed by representing the entire line as a series of infinitesimally short line segments, each composed of four distributed circuit elements: across the transverse length of the segment, a series conductor resistance (ohms/meter) and inductance (henries/meter) appear as a differential series elements dR and dL, respectively, and across the axial direction a shunt capacitance, dC, (farads/meter) and a conductance, dG, (seimens/meter) represent capacitive coupling and leakage between the conductor and the return path. An equivalent schematic is shown in Figure 14.

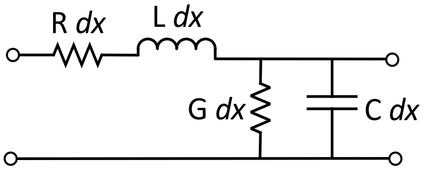

Figure 14. A differential line segment.

To simplify analysis, certain approximations may be made to reduce the complexity of the transmission line model. Considering the model of an entire uniform line segment as a two-port network, shown in Figure 15, a set of ABCD parameters can be derived by relating the sending end voltage, v_S, and receiving end voltage, v_R, with the entering current, i_S, and exiting current, i_R with the relationship expressed in (8). It is common practice to categorize transmission lines using this method into three categories, depending on line length.

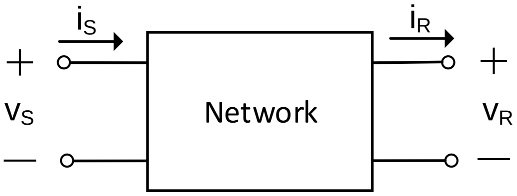

Figure 15. Two-port network.

$$\begin{bmatrix} V_S \\ I_S \end{bmatrix} = \begin{bmatrix} A & B \\ C & D \end{bmatrix} \begin{bmatrix} V_R \\ -I_R \end{bmatrix} \tag{8}$$

2.7.1.1. SHORT LINE MODEL

In the short line approximation (up to 50 miles), shunt resistance and shunt capacitance are assumed to be negligible, and the remaining distributed inductance and resistance elements are approximated as a single lumped complex impedance reducing the entire line model to a linear two-port system, with the sending current equal to the receiving current. This results in two-port ABCD parameters of A = 1, B = R + jωL, C = 0, and D = 1. An equivalent electrical circuit of the short line model is shown in Figure 16.

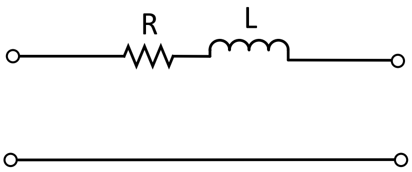

Figure 16. Short line approximation model.

2.7.1.2. MEDIUM LINE MODEL

In the medium length approximation (50-100 miles), the shunt admittance is no longer negligible and an internal shunt current path must be included into the model. The entire line segment may be approximated with the same two-port network as in the short line case, but with the addition of two shunt admittance elements, each with half value of the total line admittance, introduced at the sending and receiving end ports. This is referred to as the “nominal π” medium line model and is shown in Figure 17a. An alternative representation, the “nominal T” model is shown in Figure 17b. Solving for the nominal π model yields the voltage and current relationships in (9) and (10). The ABCD parameters of the nominal π model are: $\mathrm{A} = \mathrm{D} = 1 + \frac{\mathrm{ZY}}{2}$, B = Z, $\mathrm{C} = Y\left(1 + \frac{\mathrm{ZY}}{4}\right)$ where Z = R + jωL and Y = jωC. The voltage and current relationships for the nominal T model are expressed by (11) and (12) and the corresponding ABCD parameters are: $\mathrm{A} = \mathrm{D} = 1 + \frac{\mathrm{ZY}}{2}$, $\mathrm{B} = Z\left(1 + \frac{\mathrm{ZY}}{4}\right)$, $\mathrm{C} = Y$.

$$v_S = \left(1 + \frac{YZ}{2}\right) v_R + Z i_R \tag{9}$$

$$i_S = Y\left(1 + \frac{YZ}{4}\right) v_R + \left(1 + \frac{YZ}{2}\right) i_R \tag{10}$$

$$v_S = v_R + \frac{Z}{2} i_R + \frac{Z}{2}\left[Y v_R + \left(1 + \frac{YZ}{2}\right) i_R\right] \tag{11}$$

$$i_S = i_R + Y\left(v_R + \frac{Z}{2} i_R\right) \tag{12}$$

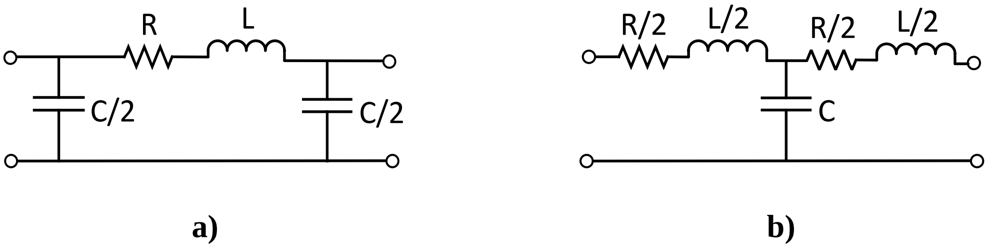

Figure 17. Medium line circuit approximations: a) nominal π, b) nominal T.

2.7.1.3. LONG LINE MODEL

When transmission line lengths exceed 100 miles, lumped element approximations no longer hold and it becomes necessary to consider the contribution of all distributed elements within system model. Considering a long transmission line of fixed length, the steady-state voltage and current at any point, x, along the line may be expressed as (13) and (14), respectively.

$$v(x) = \frac{1}{2}(v_R + Z_0 i_R)e^{\gamma x} + \frac{1}{2}(v_R - Z_0 i_R)e^{-\gamma x} \tag{13}$$

$$i(x) = \frac{1}{2}\left(i_R + \frac{v_R}{Z_0}\right)e^{\gamma x} + \frac{1}{2}\left(i_R - \frac{v_R}{Z_0}\right)e^{-\gamma x} \tag{14}$$

Propagation, γ, and characteristic impedance, Z_0, constants used in (13) and (14) are defined as:

$$\gamma = \sqrt{Z'Y'} \tag{15}$$

$$Z_0 = \sqrt{\frac{Z'}{Y'}} \tag{16}$$

where Z’ and Y’ are the impedance and admittance per unit length, respectively. The steady-state solution for homogenous transmission lines (Grainger, 1994) may be used to derive the ABCD parameters for long lines. Manipulation of (13) and (14) in terms of hyperbolic sine and cosine functions yields the following long line ABCD parameters, where l is the total line length:

$$A = D = \cosh(\gamma l) \tag{17}$$

$$B = Z_0 \sinh(\gamma l) \tag{18}$$

$$C = \frac{1}{Z_0} \sinh(\gamma l) \tag{19}$$

2.7.1.4. EMT LINE MODEL

For electromagnetic transient simulations, the line model is typically directly expressed differential form and numerically integrated to yield a solution or solved via traveling wave techniques. Considering a transmission line composed of an infinite series of the differential line segment presented in Figure 14, the line voltage and current across the entire transmission line may be described via the following Telegrapher’s equations:

$$\frac{\partial V(x,t)}{\partial x} = -L\frac{\partial I(x,t)}{\partial t} - RI(x,t) \tag{20}$$

$$\frac{\partial I(x,t)}{\partial x} = -C\frac{\partial V(x,t)}{\partial t} - GV(x,t) \tag{21}$$

where R is the conductor resistance per unit length, L is the inductance per unit length, G is the conductance per unit length, and C is the shunt capacitance per unit length. Differentiating and rearranging the two linear first-order equations (20) and (21), it is possible to separate voltage and current variables into (22) and (23).

$$\frac{\partial^2 v(x,t)}{\partial x^2} = LC\frac{\partial^2 v(x,t)}{\partial t^2} + (RC + GL)\frac{\partial v(x,t)}{\partial t} + GRv(x,t) \tag{22}$$

$$\frac{\partial^2 i(x,t)}{\partial x^2} = LC\frac{\partial^2 i(x,t)}{\partial t^2} + (RC + GL)\frac{\partial i(x,t)}{\partial t} + GRi(x,t) \tag{23}$$

With most electromagnetic transient simulation programs, (22) and (23) are numerically integrated directly. However, this is computationally intensive and use cases are limited to either small systems and/or short time frames. For analysis of large systems and real-time hardware-in-the-loop (RT-HIL) applications, parallel computation techniques exploiting line propagation delays to partition the system model into smaller, more manageable segments via techniques such as SSN must be used.

2.7.2. INVERTERS

An inverter interfaces a DC source to an AC system. Voltage adjustment and polarity inversion are achieved by pulse-width modulating alternating groups of switches to control the amplitude and direction of the inverter output current. For example, consider the common full-bridge voltage-sourced inverter presented in Figure 18. When switches S2 and S4 are on and S1 and S3 are off, the voltage across the output becomes positive. Similarly, turning on the S1 and S3 pair and turning off S2 and S4 results in a negative output voltage negative. Once a current path has been established, pulse-width modulation of either the high- or low-side switches allows for sinusoidal waveform generation and an output filter stage reduces switching induced ripple.

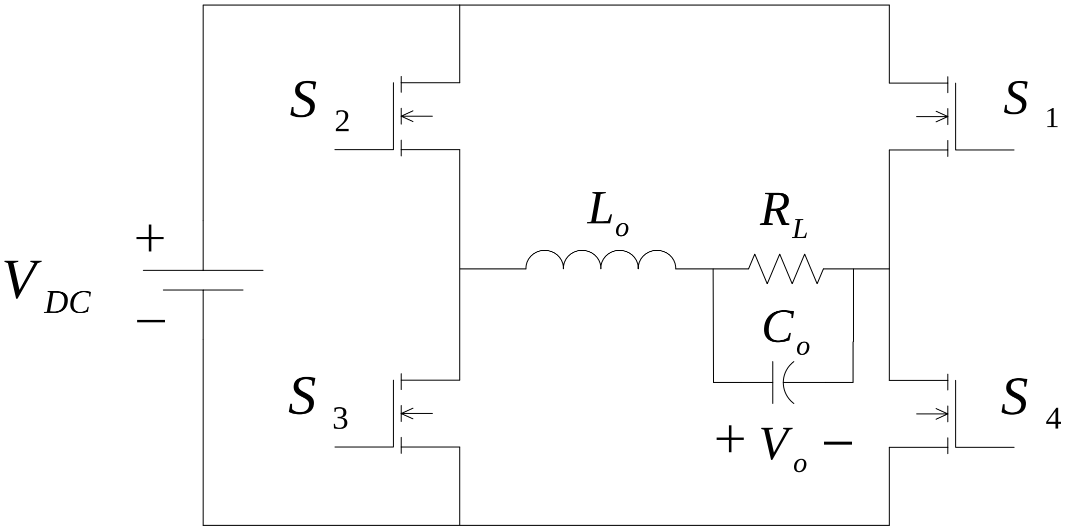

Figure 18. Full-bridge voltage-sourced inverter circuit.

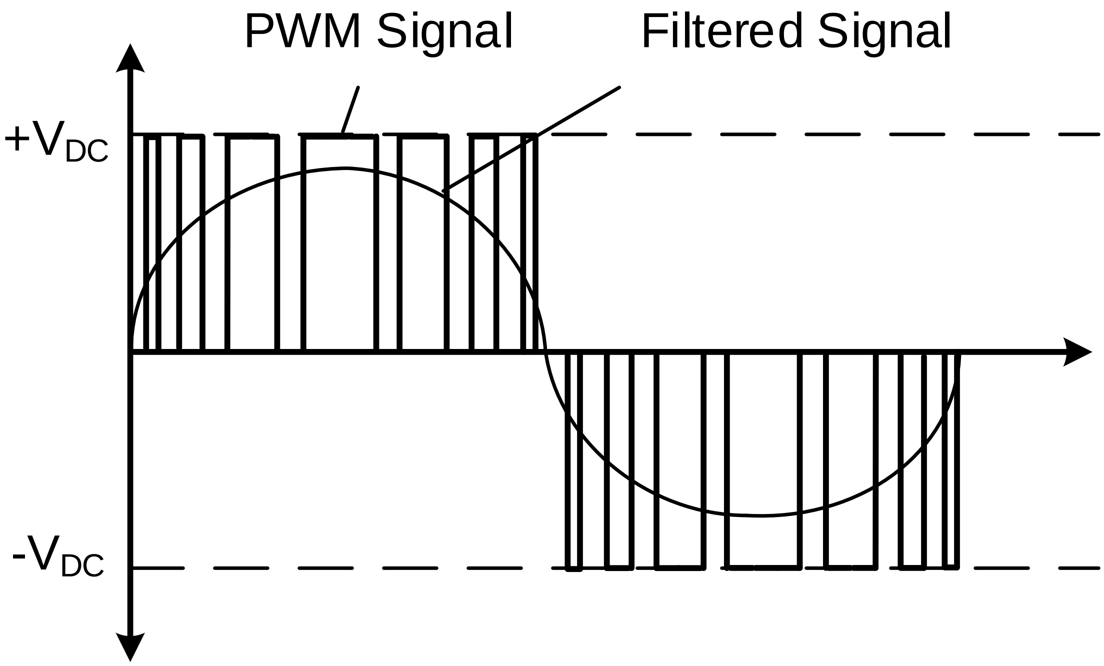

Figure 19. Pulse-width modulation sinusoid generation.

When grid-connected, line-following inverters operate as a grid-synchronized current source. To achieve grid synchronization, a sinusoidal reference signal is extracted from the line voltage via a phase-locked loop which is then tracked by an output power stage controller. Due to the differences in single- and three-phase systems, these inverter types differ greatly in their power-tracking controller design. In the single-phase case, only a single voltage and current measurement channel are available and these inverters must wait for the completion of an entire AC cycle to measure average output power, which greatly increases the power regulation response time of single-phase inverter systems. Alternatively, as the input power conditioning stage in single-phase inverter systems extracts DC power from the underlying generation source at a relatively constant rate, it is possible to approximate the average output power by measuring and averaging the instantaneous input power to achieve closed-loop output power tracking. With this approach, real power input is sensed by measuring the instantaneous power delivered by the source by multiplying the DC input voltage with the DC input current and filtering the result. Typically for 60Hz systems, a 120Hz notch filter or low-pass filter are applied to the input measurements to reduce measurement noise. Reactive power output control is achieved via by adjusting the relative output voltage-current phase angle. The use of this approach avoids many of the complications associated with controller designs based on feedback from instantaneous real and reactive power output measurements, which pulsates at twice the line frequency in single-phase systems, and a block diagram of an inverter based on this approach is shown in Figure 20.

In balanced three-phase systems, instantaneous power does not fluctuate as with single-phase systems, and real and reactive power measurements may be directly used to close the output power feedback loop without the requirement of waveform averaging, enabling significant improvements in power tracking performance. Additionally, as three-phase systems have available a voltage and current measurement pair for each phase, they may employ reference frame transformation techniques such as the direct-quadrature-zero (DQZ) transform to simplify inverter control (Hirofumi Akagi, 2007). In the direct-quadrature-zero approach, the a-b-c reference frame of an input three-phase AC signal, typically line voltage, is transformed via the DQZ transform (24) to produce two steady-state signals in the d-q reference frame. These DC signals, I_d and I_q, are more easily tracked by proportional-integral-derivative (PID) controllers, and control of I_d and I_q directly corresponds to control of the inverter output current amplitude and reactive power output, respectively. To generate the a-b-c frame pulse-width modulated firing pulses to drive the high-speed power electronics switches in the inverter power stage, the output signals from the I_d and I_q PID controllers are remapped back into the a-b-c domain via an inverse DQZ transform (25). A diagram of a typical three-phase inverter employing this control method is shown in Figure 21.

$$\mathrm{K}_{\mathrm{DQZ}} = \sqrt{\frac{2}{3}} \begin{bmatrix} \cos(\theta) & \cos\left(\theta - \frac{2\pi}{3}\right) & \cos\left(\theta + \frac{2\pi}{3}\right) \\ -\sin(\theta) & -\sin\left(\theta + \frac{2\pi}{3}\right) & -\sin\left(\theta + \frac{2\pi}{3}\right) \\ \frac{\sqrt{2}}{2} & \frac{\sqrt{2}}{2} & \frac{\sqrt{2}}{2} \end{bmatrix} \tag{24}$$

$$\mathrm{K}_{DQZ}^{-1} = \sqrt{\frac{2}{3}} \begin{bmatrix} \cos(\theta) & -\sin(\theta) & \frac{\sqrt{2}}{2} \\ \cos\left(\theta - \frac{2\pi}{3}\right) & -\sin\left(\theta - \frac{2\pi}{3}\right) & \frac{\sqrt{2}}{2} \\ \cos\left(\theta + \frac{2\pi}{3}\right) & -\sin\left(\theta + \frac{2\pi}{3}\right) & \frac{\sqrt{2}}{2} \end{bmatrix} \tag{25}$$

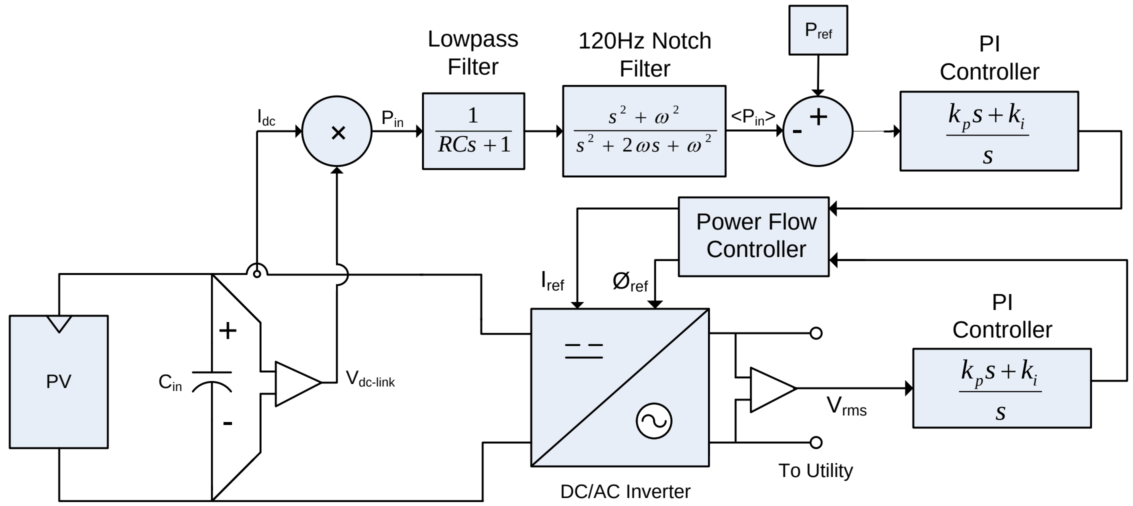

Figure 20. Control block diagram of a single-phase inverter.

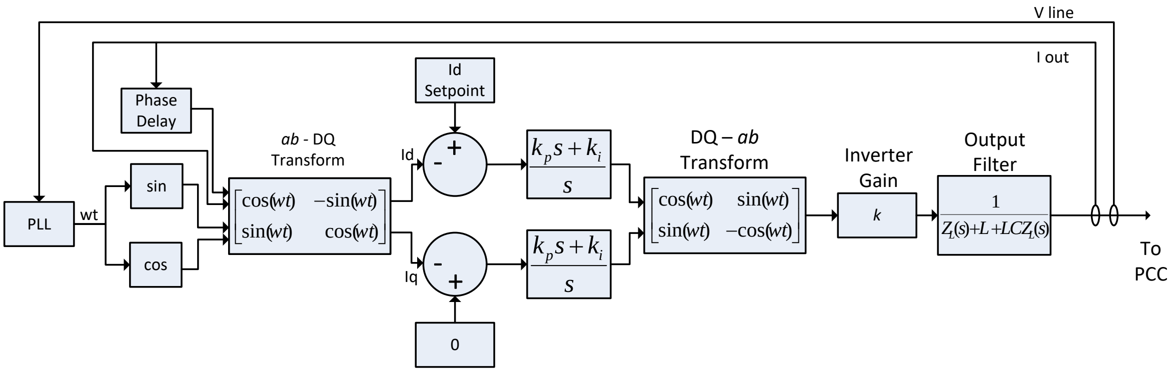

Figure 21. Control block diagram of a three-phase inverter.

While real and reactive power outputs may be adjusted by setting inverter current amplitude and phase references, for the purposes of incorporating inverters into a microgrid controller or EMS it is often more practical to directly set real and reactive power values by implementing a power-flow controller. The inputs of a power-flow controller are the desired real and reactive power outputs, which are then transformed into current amplitude and phase reference values via the following equations:

$$|I_{ref}| = \frac{\sqrt{(P_{ref})^2 - (Q_{ref})^2}}{V_{line}} \tag{26}$$

$$\emptyset_{ref} = \tan^{-1}\left(\frac{Q_{ref}}{P_{ref}}\right) \tag{27}$$

where P_{ref} is the desired real power output, Q_{ref} is the desired reactive power output, V_{line} is the RMS line voltage, and I_{ref} and $\emptyset_{ref}$ are the calculated current magnitude and phase reference values.

2.7.3. TRANSFORMERS

Transformers utilize magnetic coupling between windings around a common magnetic core to transfer electrical energy between two circuits. In electrical power systems, they are typically used to convert from one AC voltage to another. These devices are essential in improving power transmission efficiency as they enable AC transmission lines to raise operating voltages, thereby lowering line currents and associated I^2R conduction losses while not affecting the total amount of transferred power. Single-phase transformers, illustrated in Figure 22, are typically constructed with two windings surrounding a single magnetic core composed of a material with high magnetic permeability such as laminated steel. Three-phase transformers are constructed by packaging three single-phase transformers into a single enclosure, or by winding all six coils onto a single three-legged core as shown in Figure 23. In both single- and three-phase transformers, time-varying current in the primary winding creates a magnetic flux which circulates within the magnetic core. This magnetic flux induces an electromotive force in the secondary winding. By adjusting the number of windings in the primary coil, n_p, and the number of windings in the secondary coil, n_s, the primary winding voltage, V_p, to secondary winding voltage, V_s, ratio may be controlled via the relationship:

$$\frac{V_p}{V_s} = \frac{n_p}{n_s} \tag{28}$$

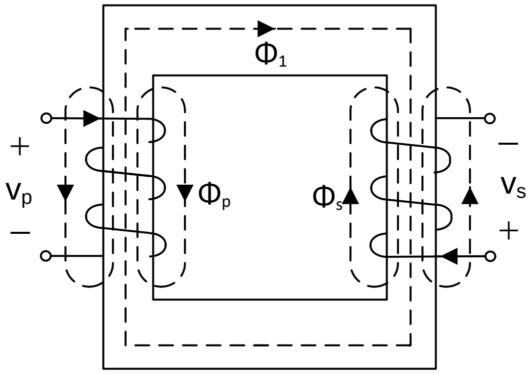

Figure 22. Single-phase transformer.

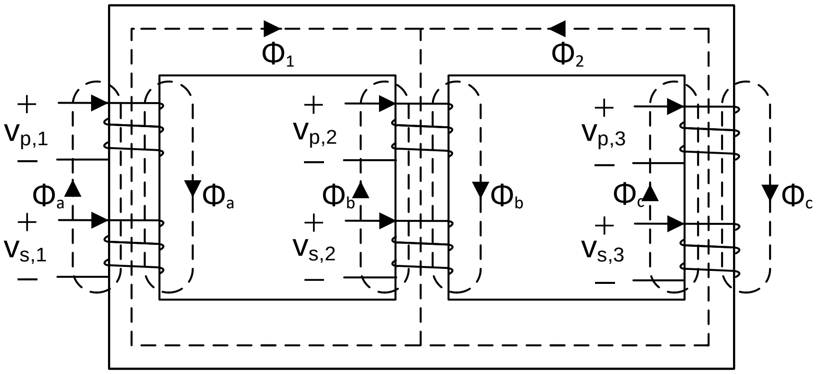

Figure 23. Three-phase transformer.

While (28) holds for ideal transformers, parasitic elements such as winding resistances, stray inductances, and magnetization losses are present in physical devices. To account for the effect of these elements, it is common to represent a non-ideal transformer with the electrical circuit shown in Figure 24, where an ideal transformer is series-connected with a circuit containing elements R, L, R_c, and X_m to account for winding resistance, winding inductance, core or iron losses, and magnetizing reactance, respectively. Secondary-side parasitic elements are reflected onto, and combined with, the primary-side elements. While a more accurate representation of practical devices than the ideal transformer model, this model does not account for non-linear effects such as transformer core saturation and magnetic hysteresis.

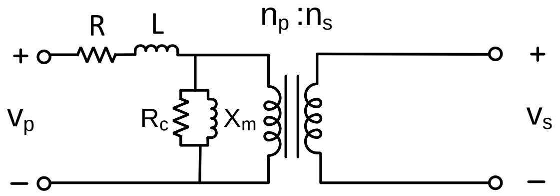

Figure 24. Non-ideal transformer electrical circuit.

The voltage and current relationships of the circuit shown in Figure 24 may be expressed in terms of an ABCD-parameter two-port network similar to that of a transmission line. As the ABCD parameters of a sequence of series-connected ABCD-parameter systems may be derived by multiplying the matrices of each element in the series, the parameters of a non-ideal transformer may be obtained by combining an ideal transformer defined by (28) with an ABCD model that expresses transformer non-idealities. The cascaded two-port equations for the combined system becomes:

$$\begin{bmatrix} V_1 \\ I_1 \end{bmatrix} = \begin{bmatrix} 1 & Z \\ 0 & 1 \end{bmatrix} \begin{bmatrix} 1 & 0 \\ Y & 1 \end{bmatrix} \begin{bmatrix} n & 0 \\ 0 & \frac{1}{n} \end{bmatrix} \begin{bmatrix} V_2 \\ I_2 \end{bmatrix} \tag{29}$$

where Z = R + jωL, Y = 1/R_c – j/X_m, and n = n_p/n_s. The resulting ABCD parameters are:

$$A = n(1 + ZY) \tag{30}$$

$$B = \frac{Z}{n} \tag{31}$$

$$C = nY \tag{32}$$

$$D = \frac{1}{n} \tag{33}$$

For EMT simulations, consideration of nonlinear transformer effects such as core saturation, eddy currents, and magnetic hysteresis are critical for proper transformer modeling, especially for the simulation of large voltage and current transients. Unfortunately, these mechanisms are difficult to model and are often addressed in power systems models via lookup tables generated from device characterization tests. Several modeling techniques based on first principles do exist and fall within five main classifications (Francisco De Leon, 1994):

- Self- and mutual-inductance-based models (Rabins, 1956)
- Leakage inductance-based models (J. H. McWirther, 1963)
- Duality-based models (Cherry, 1949)
- Electromagnetic field-based models (P. Silverster, 1970)
- Measurement-based models (E. P. Dick, 1981)

2.7.4. SOLAR PV

The photoelectric effect was discovered in 1839 by French physicist Edmund Becquerel during an experiment in which silver chloride coated platinum electrodes immersed in an acidic solution was illuminated with ultraviolet light, generating voltage and current. Today, modern photoelectric materials include monocrystalline, polycrystalline, and amorphous silicon. Cadmium telluride and copper indium gallium selenide are also used in high-efficiency cells. Figure 25 shows typical efficiencies for various cell chemistries. Due to economies of scale and technology maturity, silicon is currently the primary semiconductor material used for PV power generation.

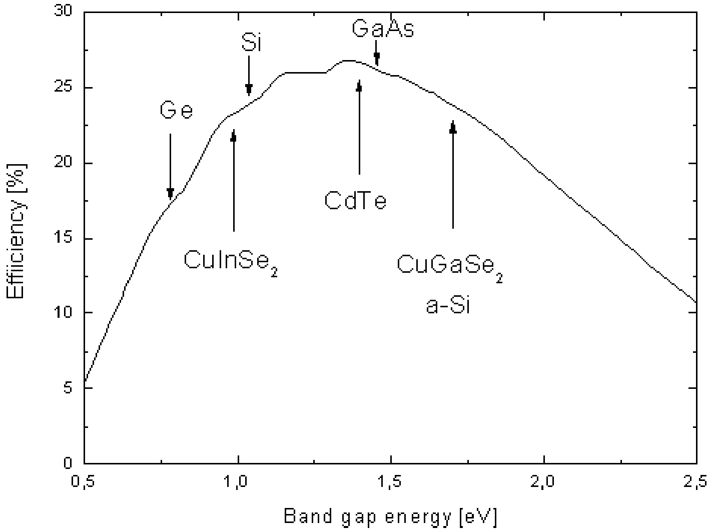

Figure 25. Cell efficiency vs. bandgap for various cell chemistries (G. Martin A., 2012).

As a DER asset, photovoltaic panels are modular, scalable, and rapidly deployable. Recent advances in manufacturing and mass production have resulted in the declining cost of photovoltaic modules (Figure 26) and the increased adoption of PV (Figure 27) as a generation resource.

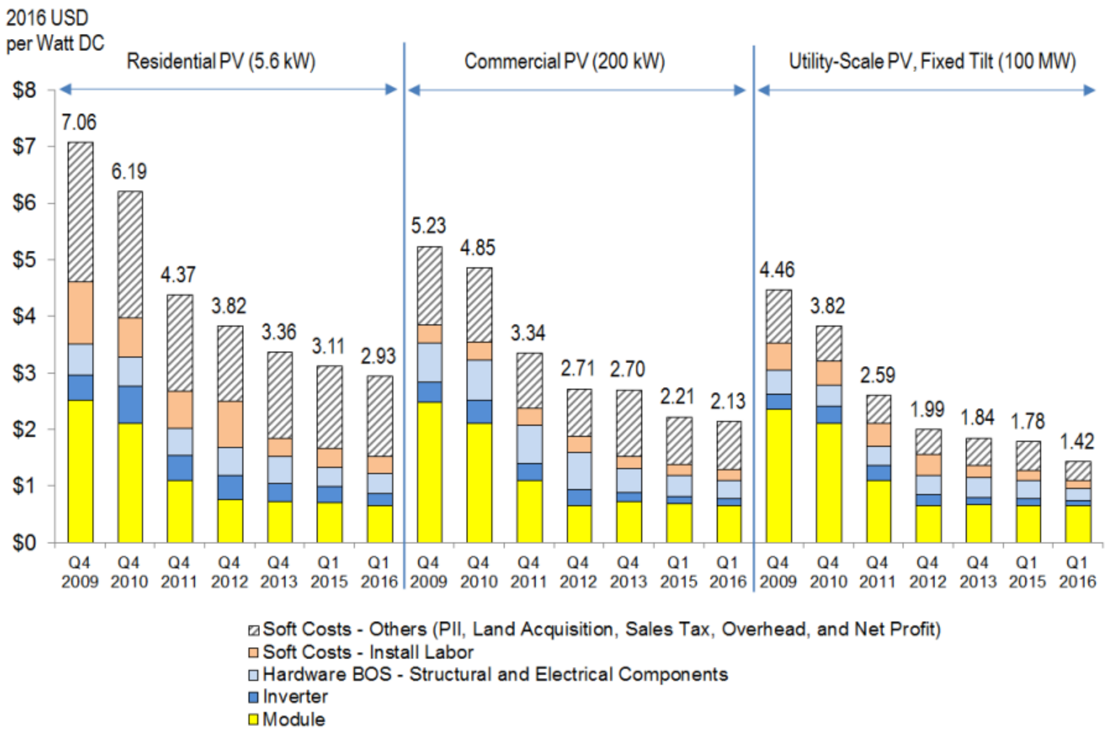

Figure 26. Cost of solar modules (Ran Fu, 2016).

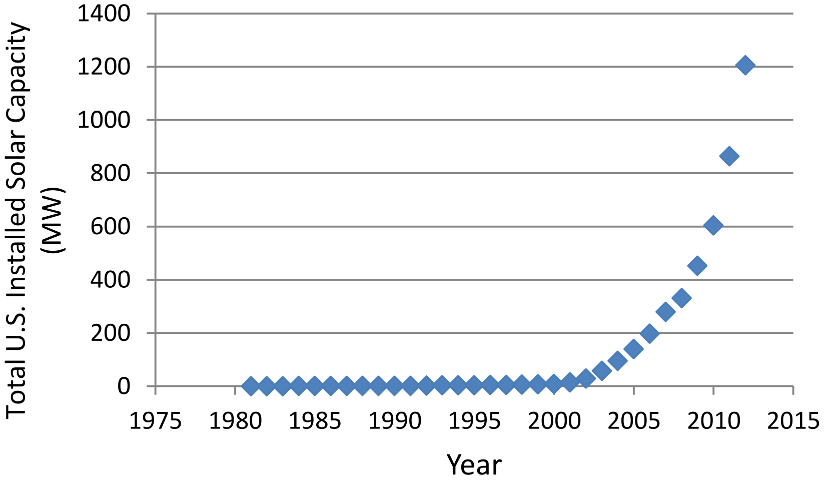

Figure 27. Total installed U.S. solar generation capacity (Ahmad, 2006).

A solar cell can be modeled as nonlinear current source, exhibiting a diode-like voltage-current curve that is dependent on a variety of operating conditions such as temperature, insolation, and cell chemistry (Durand, 1980). A single-junction PV cell may be modeled as a current source in parallel with a diode along with two resistance elements that represent loss mechanisms within the PV cell, as shown in the circuit depicted in Figure 28 .

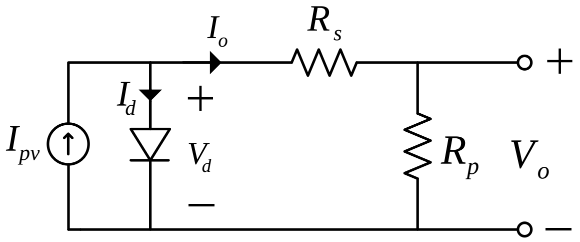

Figure 28. Equivalent circuit model of a single-junction photovoltaic cell.

The current output of a PV cell may be expressed as function of the Shockley diode equation:

$$I_o = I_{pv} - I_s(e^{\frac{V_d}{n_d V_T}} - 1) \tag{34}$$

where I_{pv} is the insolation proportional light-generated current, I_s is the diode reverse saturation current, V_d is the diode voltage, V_T is the thermal voltage, and n_d is the diode ideality factor. The thermal voltage is defined as:

$$V_T = \frac{kT}{q} \tag{35}$$

where k is the Boltzmann constant (1.38 x 10^{-23} J/K), T is the temperature of the panel in degrees Kelvin, and q is the electron charge constant (1.6 x 10^{-19} C).

As the voltages generated by single cells are in the range of 1.5-4 V and are much lower than AC line voltages, multiple cells are connected in series to create a string that achieves a higher output voltage. To increase power output, multiple strings are connected in parallel to form panels, which are then connected to an inverter to generate AC. While effective, the use of series-connected cells introduces a major complication; if a single cell is shaded, the power delivered by the entire string is substantially reduced. A solution to this issue is the use of series-parallel configurations in which DC-DC converters are used to boost the voltage of shorter PV strings. The finer granularity allows for a system that is more robust to partial shading.

Figure 29 shows an example of the voltage-current and voltage-power curves of a single-junction PV cell. The nonlinear output characteristics result in a single point of operation that maximizes power delivery. This point is referred to as the maximum power point (MPP) and varies depending on the operating conditions of both the PV panel and attached electrical loads. Locating and operating at this point is known as maximum power point tracking and is achieved by matching the load impedance to the output impedance of the solar panel. This is typically accomplished with an intermediate DC-DC converter situated between the solar panel and the inverter. In grid-tied solar applications, the grid approximates an infinite load that may accept any amount of power available from a solar panel and continuous operation at the MPP is possible. Islanded-mode operation may necessitate a reduction of PV output to maintain power balance requiring operation of the panel at a non-optimal point along the voltage-current curve. Several control algorithms exist for locating and operating at the maximum power point, with the two most common being the perturb-observe and incremental conductance methods (Ali Reza Reisi, 2013).

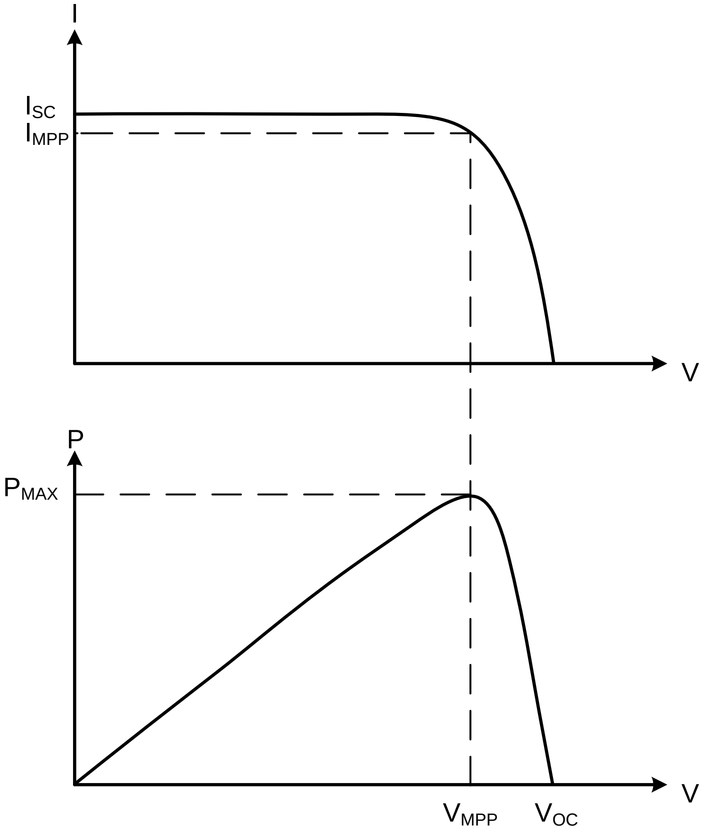

Figure 29. Photovoltaic current-voltage and power-voltage curves.

2.7.5. FUEL CELLS

A fuel cell is an electrochemical device that reacts a fuel with an oxidant, typically hydrogen and oxygen respectively, to generate electricity. Fuel cells as distributed energy resources provide attractive features, especially for deployment in microgrid systems. Several advantages of fuel cell systems include high fuel availability, large fuel storage capacity, high conversion efficiency, scalability and modularity, excellent partial load capabilities, and extremely low criteria pollutant emissions. Some fuel cell technologies may achieve zero greenhouse gas emissions. Currently there are six primary categories of fuel cells based on electrolyte composition; polymer electrolyte membrane (PEM), direct methanol, alkaline, phosphoric acid, molten carbonate, solid oxide, and reversible (Acres, 2001) with varying characteristics such as operating temperatures, efficiencies, power ramping capabilities, and fuel type requirements. Of the current fuel cell technologies, polymer electrolyte membrane and solid oxide fuel cells are the most commonly encountered in DER deployments.

The basic construction of a polymer electrolyte membrane fuel cell, illustrated in Figure 30a), is composed of an anode and cathode electrode surrounding an electrically insulating proton conducting polymer electrolyte membrane. These devices operate by catalytically splitting hydrogen into electrons and protons at the anode (36) and passing the protons through a polymer electrolyte membrane. The separated electrons flow through an external load circuit and into the cathode where they recombine with the conducted protons and oxygen at the cathode (37) to form water and heat. The overall chemical equations for a PEM fuel cell is given in (38). These devices can operate at ambient temperatures resulting in fast warm-up times and due high proton mobility within the electrolyte, are well-suited for applications that require fast power ramp rates such as peak power generation or electric vehicles.

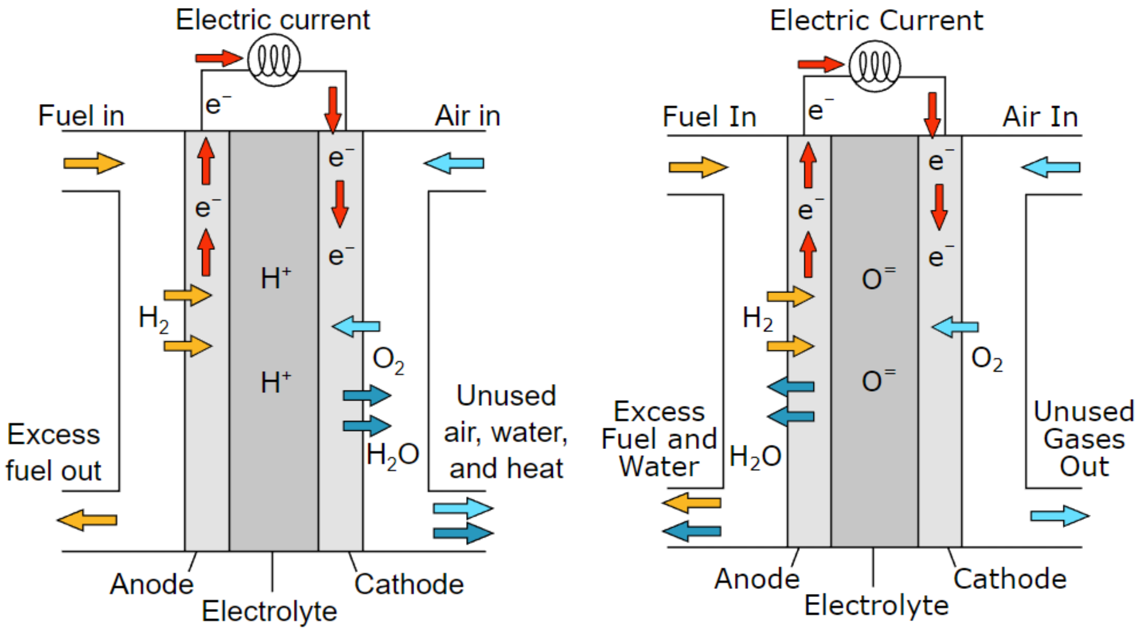

a) b)

Figure 30. a) Polymer electrolyte membrane fuel cell, b) solid oxide fuel cell (Mattuci, 2018).

$$\text{Anode: } H_2(g) \rightarrow 2H^+(aq) + 2e^- \tag{36}$$

$$\text{Cathode: } \frac{1}{2}O_2(g) + 2H^+(aq) + 2e^- \rightarrow H_2O(l) \tag{37}$$

$$\text{Overall: } H_2(g) + \frac{1}{2}O_2(g) \rightarrow H_2O(l) + electric\ energy + \ heat \tag{38}$$

Solid oxide fuel cells (SOFC) are similar in construction to PEMs in that they also use an anode-electrolyte-cathode stack. However, SOFCs conduct oxygen ions through a solid metal oxide electrolyte such as yttria-stabalized zirconia, scandia-stabilized zirconia, and gadolinium-doped ceria, as opposed to protons in polymer electrolyte membrane devices. Equations (39) - (42) express the chemical reactions that occur at the anode and cathode of an SOFC, respectively. The use of an oxygen ion conducting ceramic metal oxide does not require the use of expensive platinum catalysts as in the PEM case, also presents opportunities for fuel flexibility. For example, light hydrocarbons such as methane may be directly used as a fuel via a water-gas shift (40) and internal steam reformation (41) reaction at the device anode. SOFC's are best suited for base load applications as to achieve the required oxygen ion conductance rates for operation SOFCs must operate at high temperatures, typically between 500 and 1000 degrees Celsius, and the prolonged warm-up time requirements combined with the slower oxygen conduction chemical dynamics result in decreased power ramping capabilities. However, SOFC's are currently more cost-effective at scale and long-lived than PEM technologies.

$$\text{Anode: } H_2 + O^{2-} \rightarrow H_2O + 2e^- \tag{39}$$

$$\text{Anode (Water Shift): } CO + H_2O \rightarrow H_2 + CO_2 \tag{40}$$

$$\text{Anode (Steam Reformation): } CH_4 + H_2O \rightarrow 3H_2 + CO \tag{41}$$

$$\text{Cathode: } O_2 + 4e^- \rightarrow 2O^{2-} \tag{42}$$

To improve device performance, several hybrid systems have been proposed such as SOFC-microturbine generator (MGT) (Yi, 2004), SOFC-battery energy storage (BES) (Jinhee Lee, 2006), and SOFC-ultracapacitor (Allie E Auld, 2009) to increase SOFC ramping and load following capabilities.

2.7.6. MICROTURBINE GENERATORS

Microturbine generator systems are miniaturized combustion turbines that are a high power density option for distributed generation applications. Sized from 10-500 kW and with a power density of 2.3-2.7 kW per cubic foot (U.S. Environmental Protection Agency, 2015), MTGs are approximately 1/3 the size of an equivalent diesel generator and provide a compact and rapidly deployable generation asset. Microturbines are also fuel flexible, with options including hydrogen, natural gas, gasoline, diesel, and waste oils making them well-suited for remote microgrid installations.

Microturbine generators, like their much larger turbine counterparts, operate on the Brayton thermodynamic cycle and are composed of the same principal components, as shown in Figure 31. Inlet air adiabatically compressed to which a fuel is introduced. The resulting fuel-air mixture is delivered to an open chamber and isobarically combusted. The resulting hot pressurized gasses then adiabatically drive an expansion turbine which in turn powers the inlet air compressor. Mechanical power is extracted from the output shaft while waste heat is rejected from the turbine. To improve overall device efficiency, waste heat may be recovered through a recuperator to preheat inlet air and/or through a heat exchanger for cogeneration.

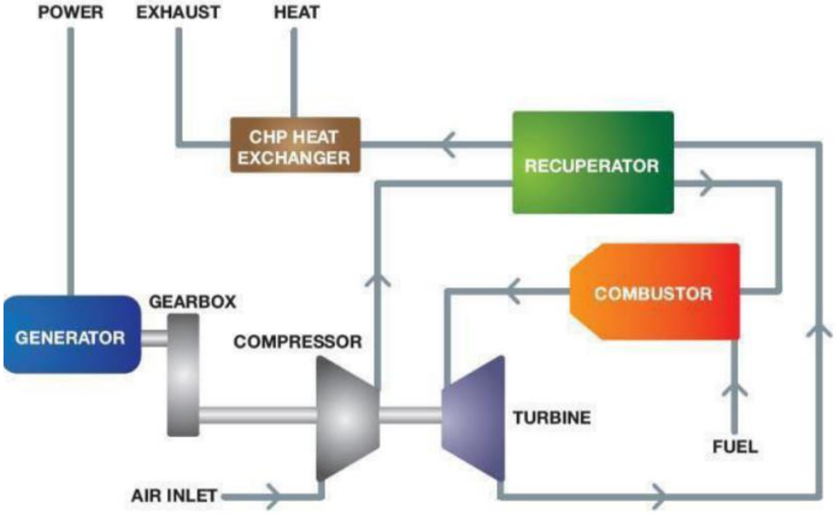

Figure 31. Microturbine CHP system schematic (FlexEnergy).

A key differentiating feature of microturbine generators compared to traditional turbine generators is the use of higher rotor speeds. Unlike larger traditional turbines that typically rotate at 1000-5000 RPM, microturbines operate in the range of 50,000-100,000 RPM. This necessitates the use of direct shaft-coupled generators which use AC-DC-AC converters to reduce the output AC frequency, as opposed traditional gear sets which would wear down at such high speeds. As such, MTGs have much smaller mechanical inertia than standard turbines resulting in increased sensitivity to load changes and reduced carry-through capabilities and MTG rotational shaft speed is physically decoupled from the output power frequency.

Microturbine generators have been studied for use in both stand-alone systems and hybrid configurations with other DER technologies. Roberts and Brouwer (Rory A. Roberts, 2010) developed a simulation model of a Capstone C-60 60kW microturbine for use in the analysis of a 220 kW SOFC-MTG hybrid system. Later, Kaneko et al. (T. Kaneko, 2006) expanded on this model by the addition of a fuel control unit and recuperator and extended the modeling methodology to a second turbine system, allowing for the detailed study of the effects of power ramping on airflow, fuel rate, and recuperator temperature.

2.7.7. GRID ENERGY STORAGE

Particular to microgrids, the issue of generation intermittency of renewable energy assets presents immediate and pressing challenges for the reliable operation of islanded systems. Strategies available to mitigate these issues include: diversification of generation resources, improved renewable energy forecasting, and large-scale interconnection of microgrid systems. Microgrid energy storage presents perhaps the most direct solution to intermittency issues. While several microgrid-scale energy storage technologies are commercially available such as compressed air, batteries, flywheels, hydrogen, and hydroelectric, these technologies currently see limited deployment due cost and/or geographical requirements. Fortunately, the cost of battery energy storage systems has been steadily reducing due to economies of scale driven in part by the increased production of electric vehicles batteries.

Battery chemistries widely vary, but the fundamental mechanism is common across all rechargeable battery types; chemical reactions between an electrolyte, anode, and cathode develops a voltage potential difference between the electrodes. When an external circuit is introduced between the device terminals, a current path is formed and the reduction-oxidization reactions may occur at the electrodes, driving current flow. Charging of a battery system reverses the redox reaction. Energy storage systems have been extensively researched and modeled for use in grid energy storage applications.

Type	Voltage	Specific Energy (Wh/kg)	Energy Density (Wh/L)	Cycles
Lithium sulfur	2.0	400	350	1,400
Sodium ion	3.6	90	30	5,000
Zinc bromide	1.8	34.4-54	15.7-39	2,000
Zinc cerium	2.5	-	-	-
Vanadium redox	1.15	25-35	15-25	100,000
Molten salt	2.58	70-290	160	3,000

Table 7. Comparison of various battery chemistries.

2.8. PRESENT DISSERTATION

The present dissertation seeks to advance the understanding and analysis methodologies of smart microgrids to facilitate their adoption into the electrical power system landscape, thereby progressing the value of DER assets by transforming them from individual assets into a unified system capable of providing a high performing, reliable, islanding-ready asset to the microgrid owner, operator, and customers and a smart demand and power dispatch asset to the grid.

Previous studies on the subject have indicated that the successful implementation of microgrid systems is necessarily reliant on the proper modeling and simulation of the varied interconnected components that compose microgrids. However, documented demonstrations of successfully deployed microgrids, especially those on the community scale, have relied exclusively on independently designed and simulated systems. This ad-hoc engineering approach presents a significant hindrance to the realization of the future smart microgrid framework. Thus a successful microgrid design and analysis approach must be capable accommodating a wide and diverse array of microgrids systems.

3. APPROACH

The approach is structured to outline a task for each of the six objectives. The successful completion of several of these tasks require close collaboration with industry partners and university facilities management.

Task 1. Review the current body of knowledge pertaining to microgrid controllers and identify deficiencies in existing studies.

A comprehensive literature review was conducted to explore existing microgrid modeling and analysis techniques, and microgrid controller technologies. Discussions with partners such as Southern California Edison, ETAP, Schweitzer Engineering Laboratories were held to yield insight from an industry perspective as to the shortcomings of current methods.

Task 2. Collaborate with UCI Facilities Management and microgrid partners to gather real-world microgrid data.

This task involves developing a working relationship with UCI Facilities Management to achieve a coordinated effort that advances the capabilities of the UCI Microgrid from both a research and operations perspective. Close collaboration with UCI Facilities management and corresponding teams of partner microgrids were vital to achieving the information exchange necessary to understand their respective microgrid systems and gain insights into the issues of microgrid operations. The input from these partnerships were used to guide model and microgrid controller development, while results from the research were used to assist facility operators in making microgrid operating and business decisions.

Task 3. Develop microgrid analysis techniques and concepts that expands the existing body of knowledge and provides a high performing simulation tool.

This task advances current microgrid simulation and analysis methodologies. Models of the UCI microgrid and partner microgrids were developed and run on an advanced real-time hardware-in-the-loop simulator and interfaced to a concurrently developed microgrid controller. Recreated in a real-time virtualized environment, the microgrid model simulating variety of synthesized and real-world operating conditions was assessed for performance and stability. This task provided preliminary proof of concept via simulation and analysis, laying the groundwork for a real-world demonstration. Detailed theoretical explanations of microgrid operation and novel control insights were developed in this task.

Task 4. Deploy a real-time campus-wide energy management system to allow for the validation of proposed microgrid optimization strategies.

The University of California, Irvine in collaboration with MelRok, an Irvine-based vendor of high-performance power monitoring equipment, instrumented the campus microgrid with a real-time energy monitoring system. 140 building-level power meters operating at a sampling rate of 1 Hz have been deployed across the UCIMG and combined with existing meters into a unified energy monitoring system, equipping the UCIMG with the real-time metering capabilities necessary to advance the boundaries of current microgrid technologies.

Task 5. Gather experimental data via a seamless islanding and grid resynchronization event.

As part of a real-world islanding demonstration, the UCIMG has been outfitted with an islanding-capable microgrid controller and physically disconnected from the utility via a seamless islanding demonstration. During the island-mode duration, large electrical loads were cycled yielding experimental data on microgrid islanded-mode transient behavior which were used for model validation and analysis. The controller was also tested for the ability to resynchronize the microgrid with the utility via a seamless grid reconnect. Data from high-resolution power meters recording the islanding event were collected during this task.

Task 6. Develop a plug and play test platform to capable of supporting next-generation smart microgrid research activities.

A microgrid test platform was developed to facilitate research on next generation microgrid technologies. The Connectivity Lab at the Advanced Power and Energy Program serves as a dual purpose state of the art power systems research and instruction laboratory. The completed laboratory provide a flexible plug and play environment capable of 1) emulating a large range of AC and DC electrical networks, 2) testing next generation renewable distributed energy resource and power electronics systems, 3) supporting real-time hardware-in-the-loop simulations of existing and future electrical systems, and 4) providing a key teaching tool for the hands-on training of the next generation of power systems engineers.

4. MODEL OVERVIEW

Microgrids are composed of various dynamic components including inverters, PV, fuel cells, gas turbine generators, battery energy storage systems, and electrical distribution, monitoring, and protective equipment, each requiring unique modeling techniques and engineering insight to properly to study the behavior of the microgrid system as a whole. In this dissertation, electromagnetic transient models of the UCIMG and partner microgrids and their associated components are developed and simulated utilizing a real-time state-space nodal engine to investigate the response of these systems to various operating scenarios including planned and unplanned seamless islanding and grid-reconnect transitions. State-space representations of components critical to microgrid dynamic response (e.g. the central plant gas turbine generator, steam turbine generator, electric chiller motors, photovoltaic and battery energy storage systems and their associated inverters, dynamic building loads, and the electrical distribution network) were developed with the Simscape Power Systems/OPAL-RT LAB framework within the MATLAB Simulink platform and compiled to execute on an OPAL-RT OP5600 real-time simulator. A 250 μs maximum simulation time step was achieved enabling real-time hardware-in-the-loop microgrid controller testing. The various microgrid components and their respective modeling efforts are described in the following sections.

4.1. UCI MICROGRID

The University of California, Irvine Microgrid is a community-scale system serving than 50,000 students, faculty, and staff and contains a variety of distributed energy resources including 4MW of flat-plate and concentrating PV, a 4.5 million gallon, 60,000 ton-hr thermal energy storage tank, and a 2MW, 500 kW-Hr lithium-ion battery system. Additional resources include building monitoring and control systems, campus-wide electrical power quality and thermal meters, electric vehicle charging stations, hydrogen fueling stations, a 300 kW electrolyzer, and an integrated PV-battery electric charging installation that supports 20 plug-in electric vehicles. The microgrid is continually monitored with 140 building-level real-time power meters with data utilized for system operation monitoring and optimization. Historical data from the monitoring system are used for scenario generation for islanding simulations. Under normal operation, the majority of UCIMG load is served by a 19MW gas-fired combined-cycle power plant in combination with PV, and any electrical import is received at the UCIMG substation which contains utility protective equipment and switchgear including a ground fault current relay, sync panel, and a utility connection switch that serves as the UCIMG PCC. The UCI microgrid is controlled at the central plant operations room co-located with the combined cycle cogeneration plant. An overview of the UCIMG energy assets and their relative locations is presented in Figure 32.

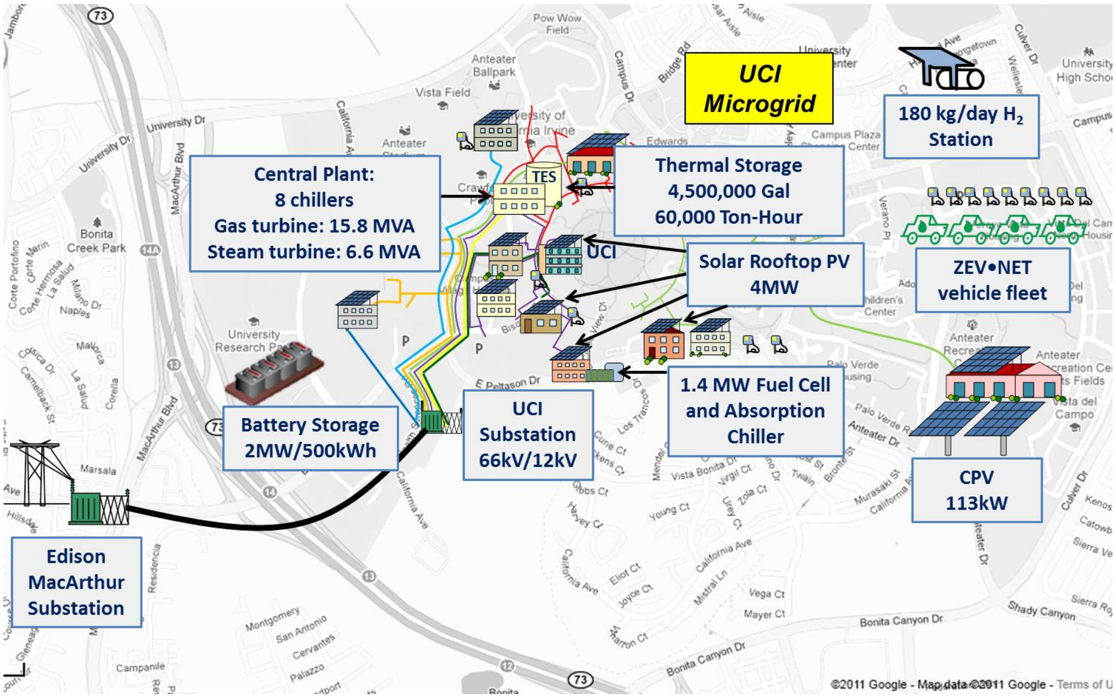

Figure 32. UCIMG energy resources.

4.1.1. ELECTRICAL NETWORK

The UCIMG is connected to the Southern California Edison electrical service at the UCI substation at an incoming line voltage of 66 kV. From the substation, the line voltage is reduced to 12.47kV via one of two redundant 28MVA transformers and distributed to each of the ten UCIMG 12.47 kV circuits that serve separate sections of the UCI campus. Circuits UC-1 and UC-8 power the physical sciences and some biological sciences buildings. The UC-3, UC-4 and future UC-7 circuits connect the substation to the central plant which hosts the gas turbine, steam turbine, and associated balance of plant loads. Chiller, thermal energy storage, cooling tower, and pump motors are also powered by these circuits. UC-4 carries power generated by the gas and steam turbines back to the UCI substation during normal operation for distribution to the remaining circuits and export to the utility. During islanded-mode operation, this circuit acts as a system slack bus and a frequency and phase reference. The UC-2 and UC-5 circuits connect to the health sciences buildings, UC-6 connects to humanities and remaining biological sciences buildings, UC-9 connects to housing and engineering building loads, and UC-10 feeds the Environmental Health and Safety building. A 12 kV system-level one-line diagram illustrating the routing of these circuits can be seen in Figure 33 and a corresponding summary of circuit loading and a one-line color coding description is presented in Table 8.

The UCIMG circuits are arranged in an interleaved radial distribution configuration, with circuits all originating from a single tie-in point at the substation bus and propagating in a truck-and-branch topology to building loads. Crosslinking between circuits at multiple junctions allows loads to be switched from one circuit to another during maintenance and fault remediation events and power routing reconfiguration within the microgrid is controlled via manually operated 12.47 kV switches. A table of circuit interconnections is provided in Table 9. Once circuits arrive at the UCIMG building sites and other campus loads, distribution transformers lower the 12.47 kV line voltage to utilization levels of 120 V-5 kV. Most large buildings are fed with multiple transformers, with each transformer servicing a floor or section of its respective building. Transformers providing power to critical building loads, such as the biological sciences and medical buildings, are connected to the substation via redundant circuits.

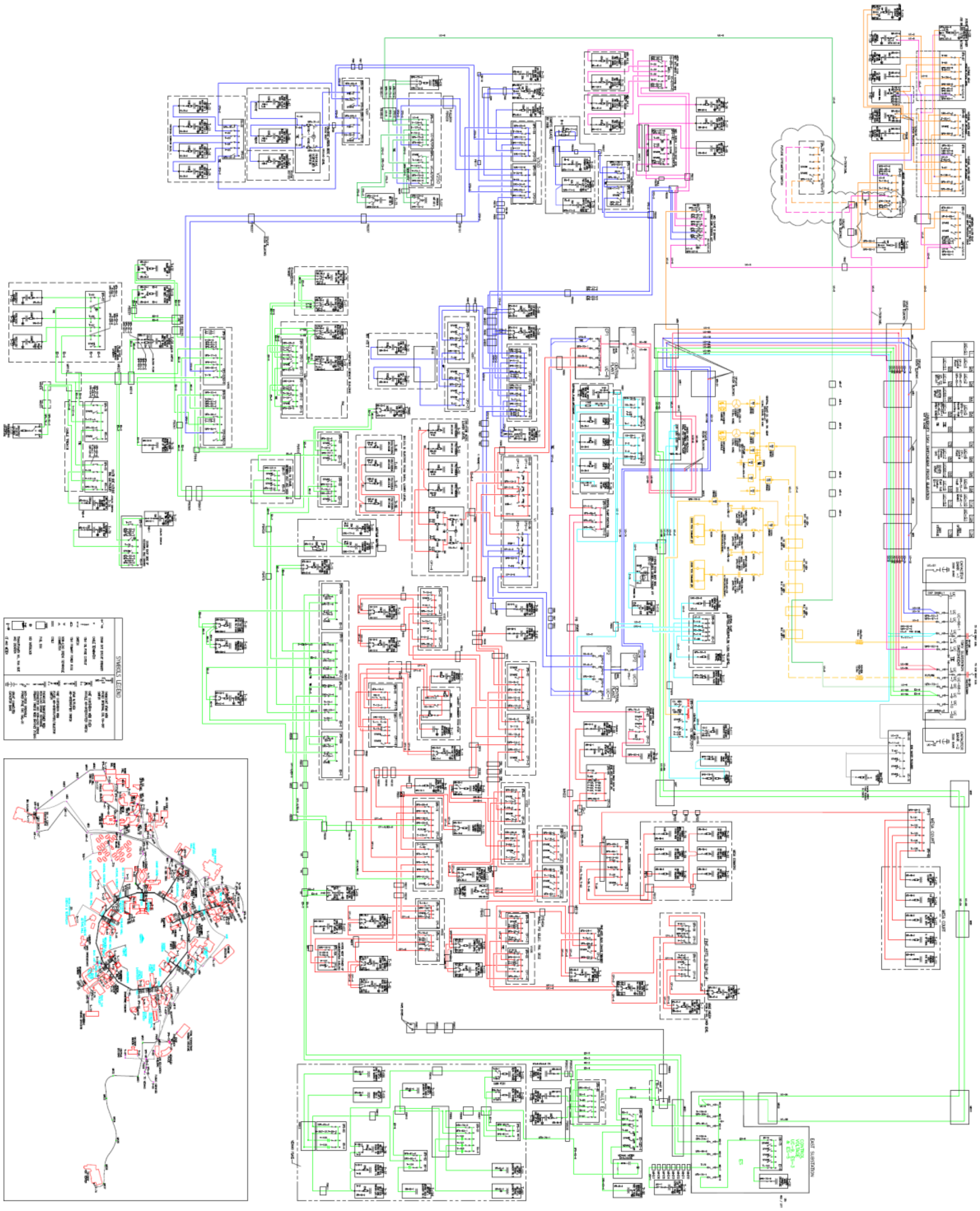

Figure 33. UCIMG 12 kV one-line diagram.

Circuit	Building Count	Max Load (kW)	Color
UC-1	27	4,077	Blue
UC-2	5	755	Orange
UC-3	6	906	Teal
UC-4	16	2,416	N/A
UC-5	7	1,057	Magenta
UC-6	41	6,191	Red
UC-7	4	604	Yellow
UC-8	22	3,322	Dark Green
UC-9	41	6,191	Light Green
UC-10	1	151	Grey

Table 8. Circuit loading and color coding.

	UC-1	UC-2	UC-3	UC-4	UC-5	UC-6	UC-7	UC-8	UC-9	UC-10
UC-1	X	X	X		X	X		X	X	
UC-2	X	X			X					
UC-3	X		X	X		X				X
UC-4			X	X			X			
UC-5	X	X			X					
UC-6	X		X			X			X	
UC-7				X			X			
UC-8	X							X		
UC-9	X					X			X	
UC-10			X							X

Table 9. Circuit interconnection table. “X” denotes a connection between circuits.

A model of electrical distribution network was developed on the MATLAB Simulink platform. Three-phase electromagnetic transient models of cable sections, substation switches, and distribution transformers were created using electrical parameters extracted from a combination of existing load flow-models, nameplate data, and arc flash studies of the campus electrical system. While all UCIMG conductors are less than 50 linear miles in length and fall within the short line category, the majority of line segments were modeled as nominal π segments to improve simulation accuracy. Short-run bus tie conductors and conductors installed between the distribution transformers and building loads were modeled as series impedances. As the UCIMG is relatively small, contained within a circular 2.38 square mile area, no long line segment representations were used. To reduce the size of the simulation model, UCIMG interconnection switches and redundant conductors were omitted, as all circuit interconnection switches are open and only one circuit for parallel-fed transformers is utilized during normal operation. The substation and PCC switches were retained in the system model to allow for simulation of the microgrid utility disconnect and resynchronization responses and the effects of emergency demand response load shedding.

Three-phase breakers and transformers are implemented as a grouped set of single-phase devices. Three-phase breakers are modeled as collection of trigger-coupled single-phase switches. Each switch is represented as a non-ideal switching element that includes a series resistor to simulate static resistance and a parallel snubber resistor and snubber capacitor to account for shunt parasitics. A list of feeder breakers present on the UCIMG and their associated service loadings is presented in Table 10.

Feeder	Feeder Load	Feeder Ampacity	% Loading
UC66-1	1,482	1,710	87
UC-TIE-11/UC-28	948	1,710	55
UC-TIE-12/UC-TIE-20	948	1,710	55
UC-27/ES-8	531	580	92
UC-21/SS-1	531	781	68
SS-8/ES-1	395	758	52
ES-5	268	465	58
ES-4	268	465	58
ES-3	134	414	32
SS-2	113	370	32
ES-2	91	370	26
SF6-75-4	91	370	26
SF6-75-5	22	370	6
ES-6	15	370	4
UC-22/SF6-61A-1	11	465	2
SF6-61/SF-6A TIE	11	465	2
SF6-61-4	8	295	3
SF6-61A-4	3	295	1
SS-3	2	295	1

Table 10. UCIMG primary feeder breaker table (P2S, 2016).

Similar to breakers, transformers are modeled as three separate single-phase transformers. Each phase of the transformer model is independently represented by a linear two-winding transformer. As the majority of UCIMG campus loads are balanced across all three phases, magnetic flux linkage between phases is considered symmetrical and interphase flux is assumed to be negligible. Also, as typical UCIMG loads do not approach transformer power capacity limits during grid-connected or islanded modes, magnetic saturation effects were omitted in the majority of transformer model instances. However, core saturation effects were modeled in the gas turbine, steam turbine, and substation transformers due to anticipation of large inrush currents during grid-resynchronization events and black start energization. Figure 34a) shows a circuit-level schematic of a single leg of the linear transformer model. Similarly, Figure 34b) shows the non-linear version of the transformer model with a saturable core element, L_{sat}, in place of the magnetization inductance element, L_m, in the non-saturable model. In both circuits, R_p, R_s, correspond to primary and secondary winding resistances and L_p, L_s correspond to primary and secondary leakage inductances, respectively. R_m represents core losses. The magnetization curve used for the UCIMG substation transformer is shown in Figure 35 in which several flux vs. magnetization current points taken from manufacturer datasheets (Helix Electric, 2017) are interpolated to produce a piece-wise transformer saturation curve and relevant transformer parameters are presented in Table 11. Residual flux and hysteresis effects were not included in the either version of the transformer models.

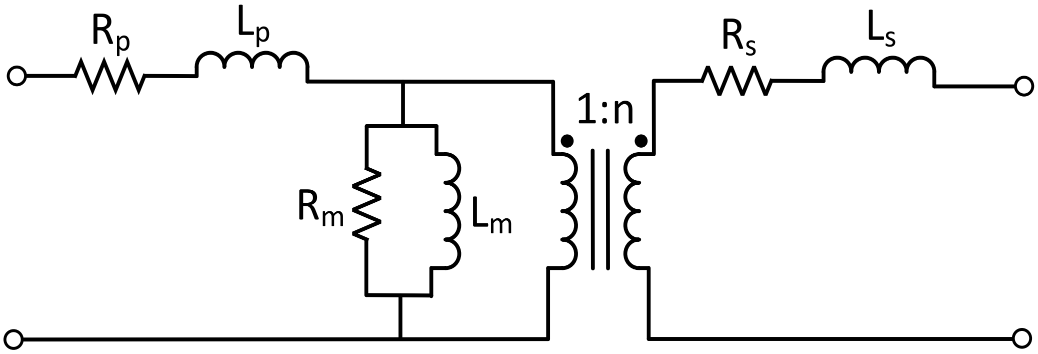

a)

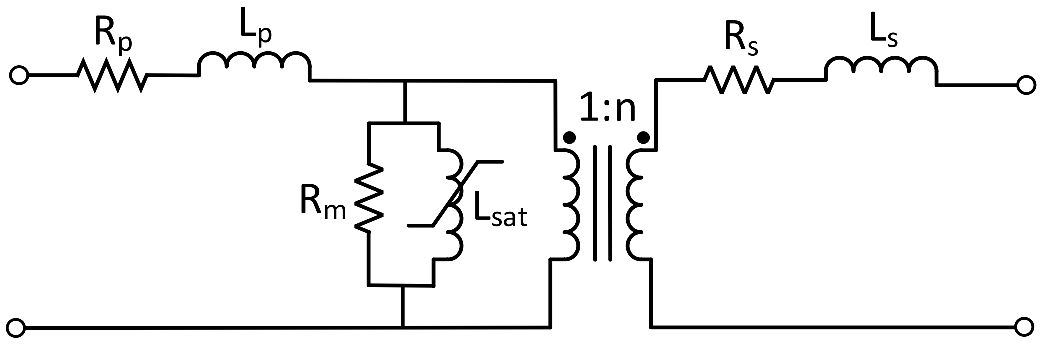

b)

Figure 34. Transformer model circuit: a) linear version, b) non-linear version.

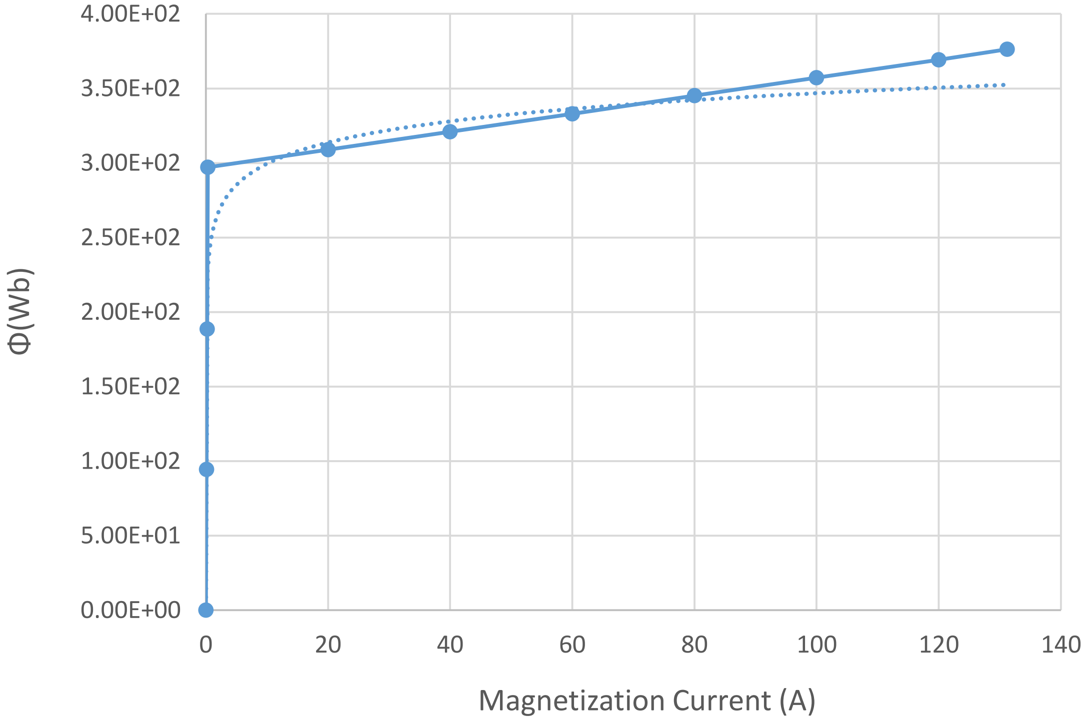

Figure 35. UCIMG main substation transformer core flux vs. magnetization current.

Parameter	Value	Units
Nominal power	1.50E+07	W
Nominal frequency	60	Hz
Primary voltage (phase-phase)	6.60E+04	Vrms (ph-ph)
Primary resistance	2.9621	Ohms
Primary inductance	0.0041321	Henry
Secondary voltage	1.25E+04	Vrms (ph-ph)
Secondary resistance	0.035247	Ohms
Secondary inductance	4.92E-05	Henry
Magnetization resistance	4.36E+05	Ohms
Magnetization inductance	1.16E+03	Henry
Flux base	143.016917	Volt-second

Table 11. Select UCIMG substation transformer nameplate parameters.

In total, approximately 1,300 nodes were included in the EMT system model. In addition to the full electromagnetic transient model designated for simulation on the real-time hardware-in-the-loop platform, a phasor-based model was derived from the full electromagnetic transient model for use with the microgrid controller. This controller model was used to conduct load-flow analysis used to generate a load drop priority list for use in the event of generation-load mismatch while the microgrid was islanded. This model includes all devices present in the EMT model and also restores the redundant conductor paths that were removed during the model simplification process. Simulation complexity reduction resulting from the use of phasor representations of electrical variables as well as an assumption of three-phase symmetry across all microgrid elements allowed the microgrid controller model to be simulated on commodity computer hardware. Validation of the two models was achieved via installation of a campus energy monitoring platform and comparing real-world bus voltage profiles and branch power flow to simulation results from the EMT and controller models. Likewise, the EMT and controller models were directly compared to verify proper model translation. An overview of the UCIMG EMT model and the extracted controller models are shown in Figure 36 and Figure 37, respectively.

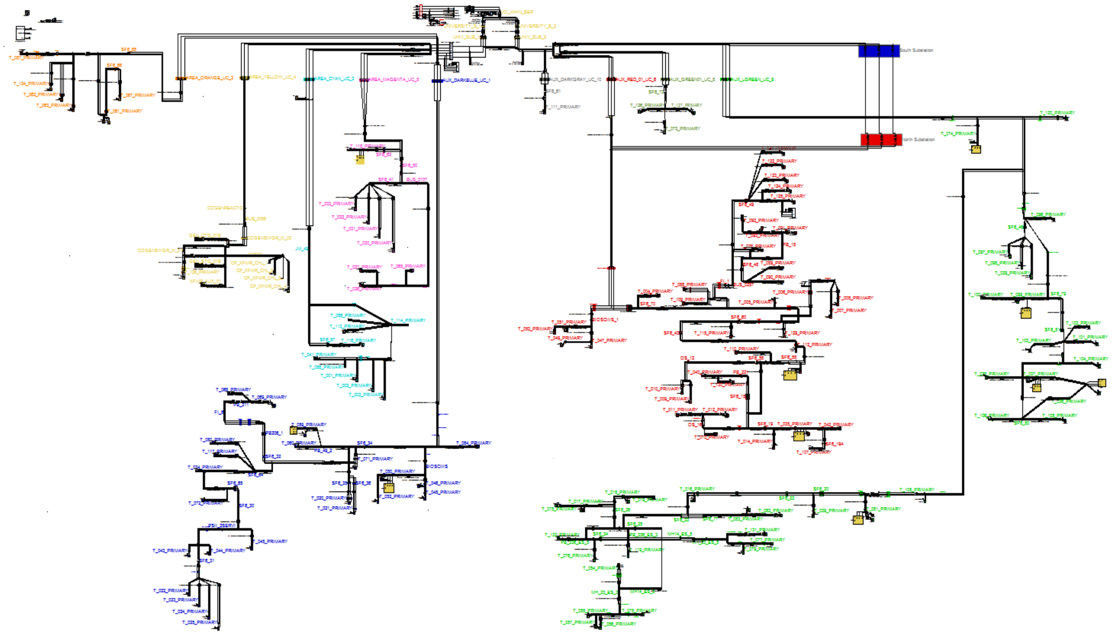

Figure 36. 12 kV-level diagram of the UCIMG EMT model.

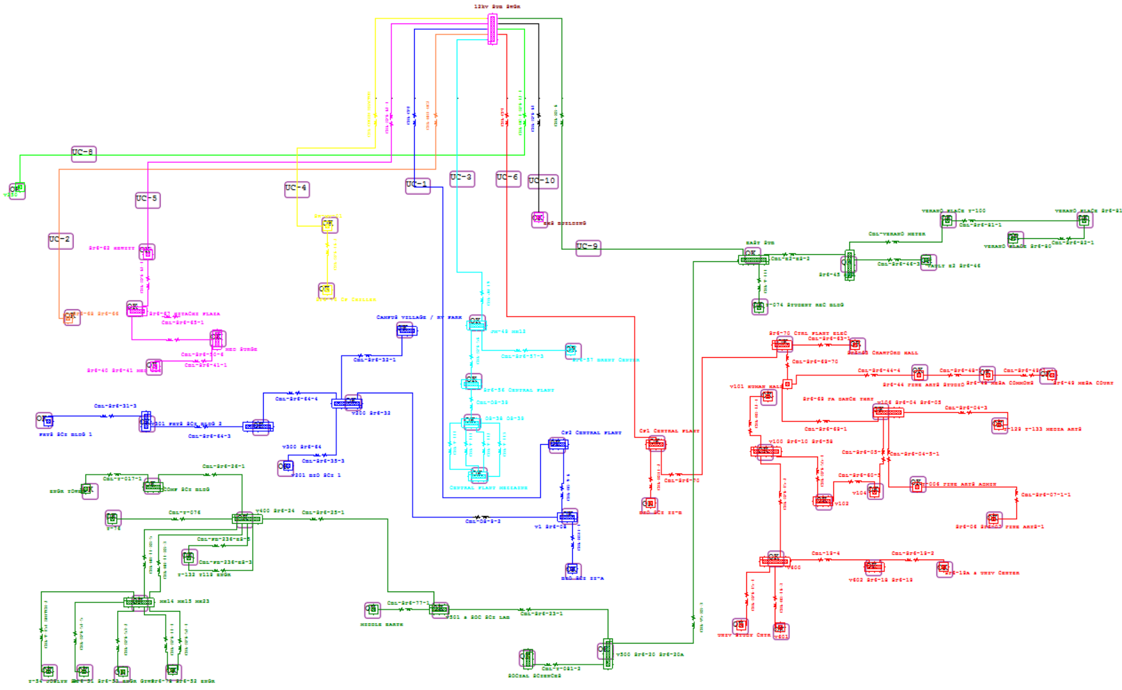

Figure 37. 12 kV-level diagram of the UCIMG controller model.

Time discretization effects were reduced by enforcing an adequately short maximum time step to produce acceptably smooth voltage and current waveforms from the real-time simulator hardware-in-the-loop simulator. A fixed step time of 250 µS was selected, resulting in a resolution of 66.67 simulation points per 60 Hz AC cycle. To achieve this level of performance while simulating the entire UCIMG circuit, the state-space-nodal ARTEMiS solver engine (OPAL-RT, 2013) provided by OPAL-RT was utilized and executed on a high performance OP-5600 digital real-time simulator (OPAL-RT, 2016). The ARTEMiS state-space nodal engine enables segmentation of the entire UCIMG circuit into separate sections which are independently solved in parallel. Current and voltage contributions from each segment at their respective connection nodes to the main model are used at simulation run-time, as opposed to every node within the entire model in the non-SSN case. This improves performance significantly by reducing the computational burden of solving a full system matrix. Additionally allocation of simulation, logging, and external communications tasks across multiple processor cores further improves simulation performance, as show in Figure 38.

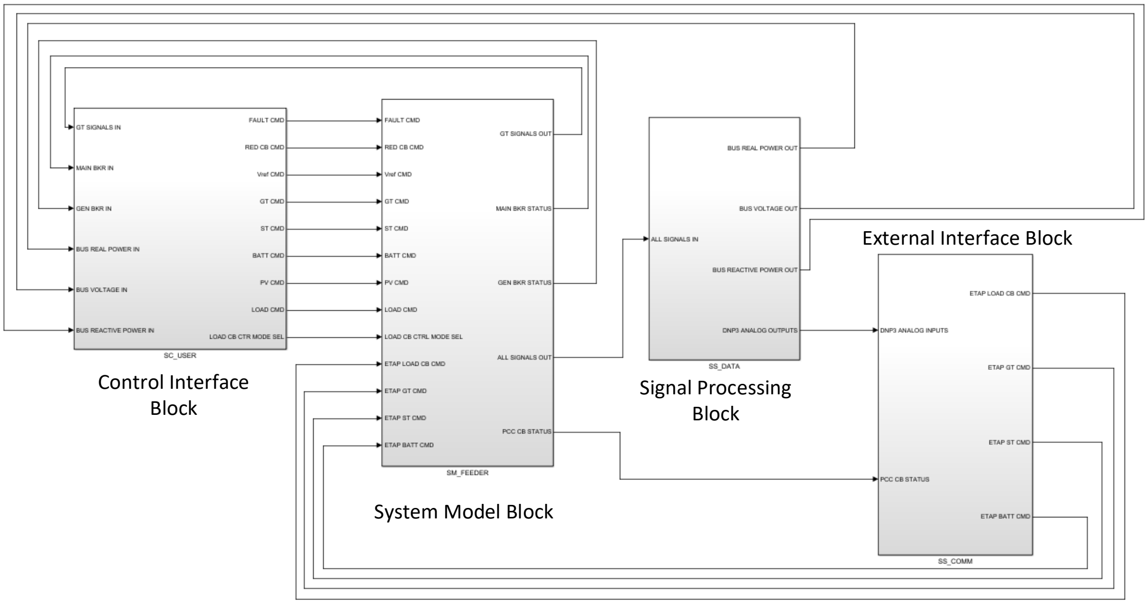

Figure 38. EMT model partitioning.

4.1.2. ELECTRICAL LOADS

Two types of load models were developed to represent major UCIMG loads: transient and adjustable steady-state. For the simulation of scenarios involving large line frequency deviations and voltage/current surges such as islanded-mode and grid-resynchronization switching and microgrid faults, a transient model consisting of a constant impedance parallel RLC load was developed and used due to improved simulation stability characteristics compared to the adjustable steady-state load models. The parallel RLC load is implemented as the circuit shown in Figure 39 with corresponding state-space equations (43) and (44).

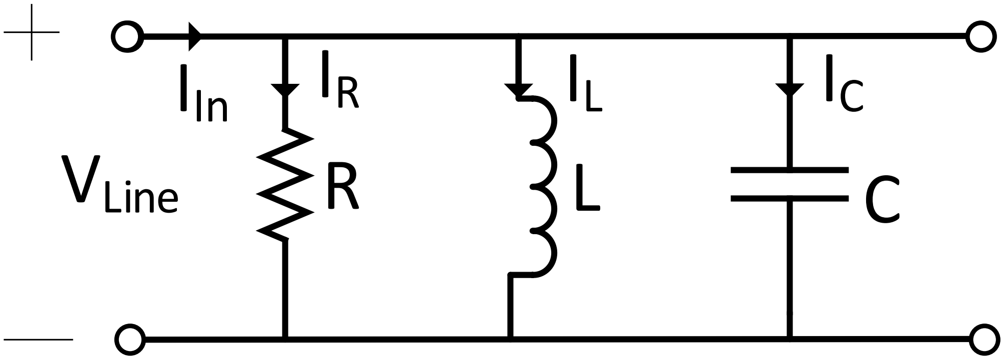

Figure 39. Parallel RLC load.

$$\begin{bmatrix} i'_L(t) \\ v'_C(t) \end{bmatrix} = \begin{bmatrix} 0 & 1/L \\ -1/C & -1/RC \end{bmatrix} \begin{bmatrix} i_L(t) \\ v_C(t) \end{bmatrix} + \begin{bmatrix} 0 \\ 1/C \end{bmatrix} [i_{in}(t)] \tag{43}$$

$$\begin{bmatrix} v_{out}(t) \\ i_R(t) \end{bmatrix} = \begin{bmatrix} 0 & 1 \\ 0 & -1/R \end{bmatrix} \begin{bmatrix} i_L(t) \\ v_C(t) \end{bmatrix} + \begin{bmatrix} 0 \\ 0 \end{bmatrix} [i_{in}(t)] \tag{44}$$

$$P_R = \frac{{V_{Line}}^2}{R} \tag{45}$$

$$Q_L = \frac{{V_{Line}}^2}{2\pi f L} \tag{46}$$

$$Q_C = -{V_{Line}}^2 2\pi f C \tag{47}$$

R, L, and C parameters are derived from an input vector containing the nominal line voltage, frequency, real power, inductive reactive power, and capacitive reactive power ratings based on equations (45), (46), and (47). These values are updated during the model compilation process and remain static throughout the simulation. Initial current and voltages are produced either from a load-flow initialization step based on an estimated system load of 50% of nameplate capacity or directly set as in input vector containing the capacitor initial voltage and inductor initial current depending on the when such data are available.

Simulations that do not involve the activation of switching elements utilize an adjustable steady-state load model (OPAL-RT, 2013) in lieu of parallel the RLC model. Unlike the RLC model used for transient simulations, the real and reactive power loadings of these elements may be adjusted during simulation run-time and are convenient for simulations that investigate the effects of continuously time-varying building load profiles as it eliminates the need to recompile the simulation upon every load change. The dynamic load models are implemented as a current injection source following the transfer functions found in (48) and (49). The discrete-time implementation of these transfer functions is shown in Figure 40 and corresponding parameters are described in Table 12.

$$P(s) = P_o\left(\frac{V}{V_o}\right)^{n_p}\frac{1+T_{p1}s}{1+T_{p2}s} \tag{48}$$

$$Q(s) = Q_o \left(\frac{V}{V_o}\right)^{n_q} \frac{1 + T_{q1}s}{1 + T_{q2}s} \tag{49}$$

$$\begin{bmatrix} d \\ q \\ 0 \end{bmatrix} = \sqrt{\frac{2}{3}} \begin{bmatrix} \sin(\theta) & \sin(\theta - \frac{2\pi}{3}) & \sin(\theta + \frac{2\pi}{3}) \\ \cos(\theta) & \cos(\theta - \frac{2\pi}{3}) & \cos(\theta + \frac{2\pi}{3}) \\ \sqrt{\frac{1}{2}} & \sqrt{\frac{1}{2}} & \sqrt{\frac{1}{2}} \end{bmatrix} \begin{bmatrix} a \\ b \\ c \end{bmatrix} \tag{50}$$

In the discrete-time model, phase-locked loops (PLL) extract a sinusoidal reference signal from the local line voltage measurement for each line phase. These reference signals are then multiplied with the gain terms $P_o \left(\frac{V}{V_o}\right)^{n_p}$ and $Q_o \left(\frac{V}{V_o}\right)^{n_q}$ from (48) and (49) and inputted into a *dq0-abc* (50) transform to produce the *abc* time-domain signals used to drive the current injection sources. Time constant terms $\frac{1+T_{p1}s}{1+T_{p2}s}$ and $\frac{1+T_{q1}s}{1+T_{q2}s}$ expressed in (48) and (49) in represent effects of PLL filter delay. Parameters n_p and n_q control the constant current/constant impedance characteristics of the load where n_p, n_q = 1.0 results in a constant current load and n_p, n_q = 2.0 represents a constant impedance load. Real and reactive power setpoints for adjustable steady-state load blocks are sourced from either measurements from a real-time campus-wide power monitoring system which continually update the real and reactive power demand during online RT-HIL simulations, or from archived demand data used for historical scenario analysis. In both cases n_p, n_q = 1 as exact real and reactive power demands and currents are known. In the absence of historical or real-time measurements, loads were set at a composition of n_p, n_q = 1.5 at a power factor of 0.85, estimated from building load schedule documentation. Figures 41 and 42 show select total building load profiles and load type composition used to produce the building load schedule approximations.

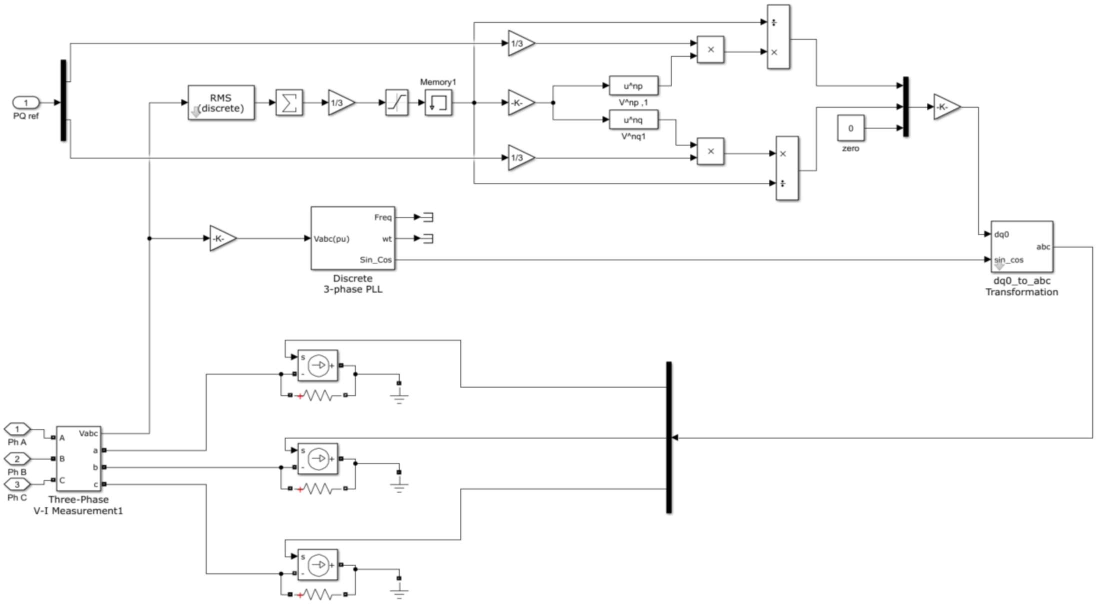

Figure 40. Adjustable discrete-time steady-state load model (OPAL-RT, 2013).

Variable	Description
V_o, V	Initial and current positive sequence voltages
P_o, Q_o	Initial active and reactive power at V_o
n_p, n_q	Load behavior exponents (1 = constant current, 2 = constant impedance)
T_{p1}, T_{p2}	Real power time constants
T_{q1}, T_{q2}	Reactive power time constants

Table 12. Dynamic load parameters.

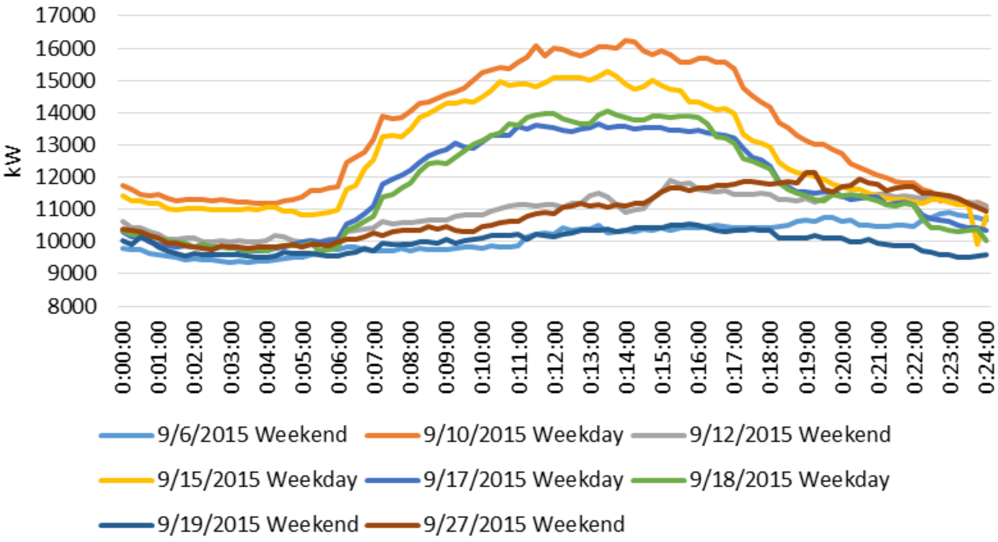

Figure 41. Select total building load profiles.

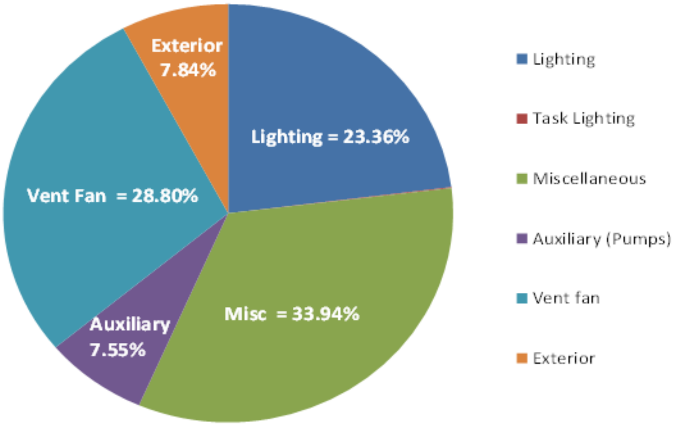

Figure 42. Average building load composition.

4.1.3. PHOTOVOLTAIC GENERATION

Approximately 4MW of flat-panel rooftop PV panels (not shown) and two 74 kW concentrated PV systems (Figure 43) are installed across the campus microgrid. As previous studies demonstrate that the rapid dynamic response of PV-inverter systems combined with the low energy storage capacity of filter elements in modern grid-tied inverters result in negligible power oscillations and fault current contributions, PV systems were modeled as controlled ideal current injection sources as shown in Figure 21. Dynamic models of PV inverter controllers were also developed and included in the model to capture power regulation dynamics. Rather than directly modeling the switching of power electronic devices such as insulated-gate bipolar transistors to inject line current, a linear current source, modeled as an inverter gain, was used to avoid the high computational requirements of simulating the operation of switches. While the resulting current source waveform did not exhibit any ripples, the transfer function of an inductor-capacitor-inductor output filter element found in many inverter systems was retained to account for the influence of filter dynamics on the inverter control loop.

Figure 43. 74 kW concentrated PV systems installed on the UCIMG.

Under/over frequency limit, under/over voltage limit, and time-delay overcurrent elements are used to represent inverter cutout due to UL1741/IEEE 1547 anti-islanding disconnect mechanisms (UL 1741, 2010) (IEEE Std. 1547-2018, 2018). Figure 44 depicts the implementation of the frequency and voltage protective elements.

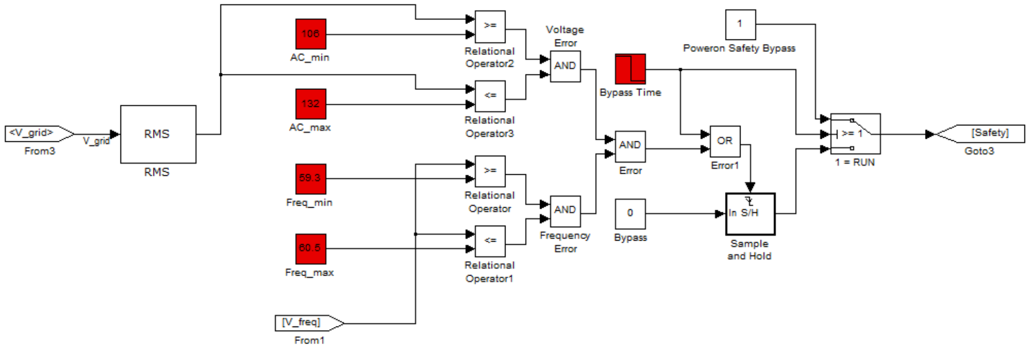

Figure 44. Line voltage and frequency under/over limit protection.

4.1.4. BATTERY ENERGY STORAGE

A 2MW, 0.5MW-Hr battery installed at the UCIMG substation, shown in Figure 45, is modeled as a controlled ideal current source/sink during charging and discharging operation, respectively. Battery state of charge (SOC) is tracked via integration of the net real power flow at the battery coupling point and modification of the integrator gain allows for accounting of systems losses and battery charge cycle nonlinearities. This battery provides a rapid-response power source or sink that is used to support island-mode transitions by temporarily buffering generation-to-load mismatch until either primary generators can adjust output or demand response load shedding can be completed. In the BES model, a line voltage locking phase-locked loop is similar to that of the PV dynamic model is utilized and a direct-quadrature-zero translation with a PID controller is used to achieve real and reactive output power regulation.

Figure 45. UCIMG battery energy storage system.

4.1.5. CENTRAL PLANT

A wide variety of energy resources are available at the UCIMG central plant and integration of these resources within a microgrid provide numerous opportunities for system optimization via improvement of operations strategies. The central plant contains 8 electric chillers with a combined cooling capacity of 14,500 tons along with a supplemental 2,000 ton capacity steam turbine powered chiller. Combined, these units are capable of serving the entire campus cooling load which averages 2,100 tons (74,400 ton-hours/day with a peak demand of 13,900 tons). A chilled water thermal energy storage tank is also available and operates with a 39°F thermocline, allowing shifting of an average of 65% of the campus cooling load to nighttime hours when electricity prices are reduced and lower ambient temperatures result in more efficient chiller operation due to improved heat rejection through cooling towers. The campus heating load averages 44 MMBtu/hr campus with a peak demand 100 MMBtu/hr and is supplied by a 52,000 lb/hr heat recovery steam generator fed from the exhaust of a 13.5MW gas turbine and 5.5MW steam turbine combined-cycle cogeneration system. Supplemental duct burners increase the total steam rate to 120,000 lb/hr.

4.1.5.1. CHILLER MOTORS

The inductive chiller motors at the central plant are located on the same bus as the UCIMG gas turbine, the primary generation and frequency regulation device during islanded-mode operation. Figure 47 shows a one-line diagram of the installation site. As these motors present large electrical loads and may inject substantial voltage and current transients when energized, much attention is afforded to correctly model these components as they may greatly influence microgrid behavior and transition success. As such, while small induction motors are modeled as the aforementioned parallel RLC or adjustable steady-state loads, large electric motors with nameplate capacities greater than 200 kW were modeled as the d- and q-axis referenced circuit shown in Figure 46. Device parameters were determined via nameplate examination. (51) - (61) describe the inductive motor model.

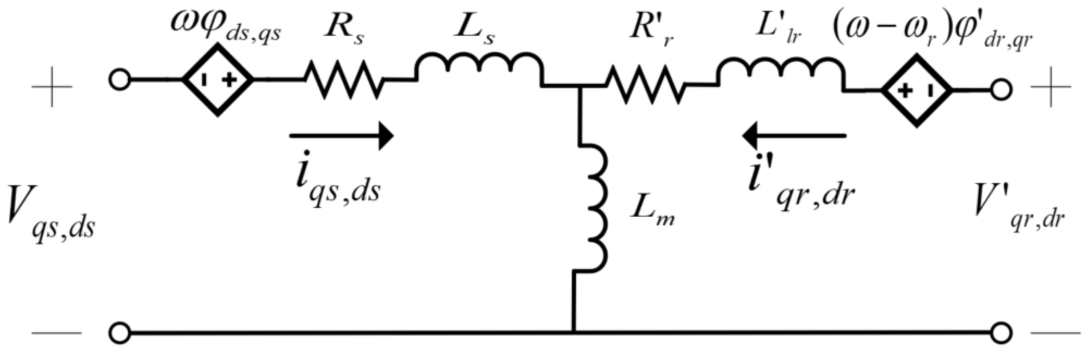

Figure 46. D- and Q-axis referenced induction motor electrical circuit (Mathworks, 2003).

$$V_{qs} = R_s i_{qs} + \frac{d\varphi_{qs}}{dt} + \omega\varphi_{ds} \tag{51}$$

$$V_{ds} = R_s i_{ds} + \frac{d\varphi_{ds}}{dt} - \omega\varphi_{qs} \tag{52}$$

$$V'_{qr} = R'_r i'_{qr} + \frac{d\varphi'_{qr}}{dt} + (\omega - \omega_r)\omega'_{dr} \tag{53}$$

$$V'_{dr} = R'_r i'_{dr} + \frac{d\varphi'_{dr}}{dt} + (\omega - \omega_r)\omega'_{qr} \tag{54}$$

$$T_e = 1.5\mathrm{p}(\varphi_{ds} i_{qs} - \varphi_{qs} i_{ds}) \tag{55}$$

$$\varphi_{qs} = L_s i_{qs} + L_m i'_{qr} \tag{56}$$

$$\varphi_{ds} = L_s i_{ds} + L_m i'_{dr} \tag{57}$$

$$\varphi'_{qr} = L'_r i'_{qr} + L_m i_{qs} \tag{58}$$

$$\varphi'_{dr} = L'_r i'_{dr} + L_m i_{ds} \tag{59}$$

$$L_s = L_{ls} + L_m \tag{60}$$

$$L'_r = L'_{lr} + L_m \tag{61}$$

where d references d-axis variables, q references q-axis variables, r references rotor quantities, s references stator quantities. A table of parameters and their descriptions is given in Table 13.

Parameter	Description
R_s, L_{ls}	Stator resistance and leakage inductance
L_m	Magnetizing inductance
L_s	Total Stator inductance
V_{qs}, i_{qs}	q-axis stator voltage and current
V_{ds}, i_{ds}	d-axis stator voltage and current
φ_{qs}, φ_{ds}	Stator q- and d-axis fluxes
ω_m	Rotor mechanical angular velocity
p	Number of pole pairs
ω_r	Electrical angular velocity
T_e	Electromagnetic torque

Table 13. Description of induction motor model parameters.

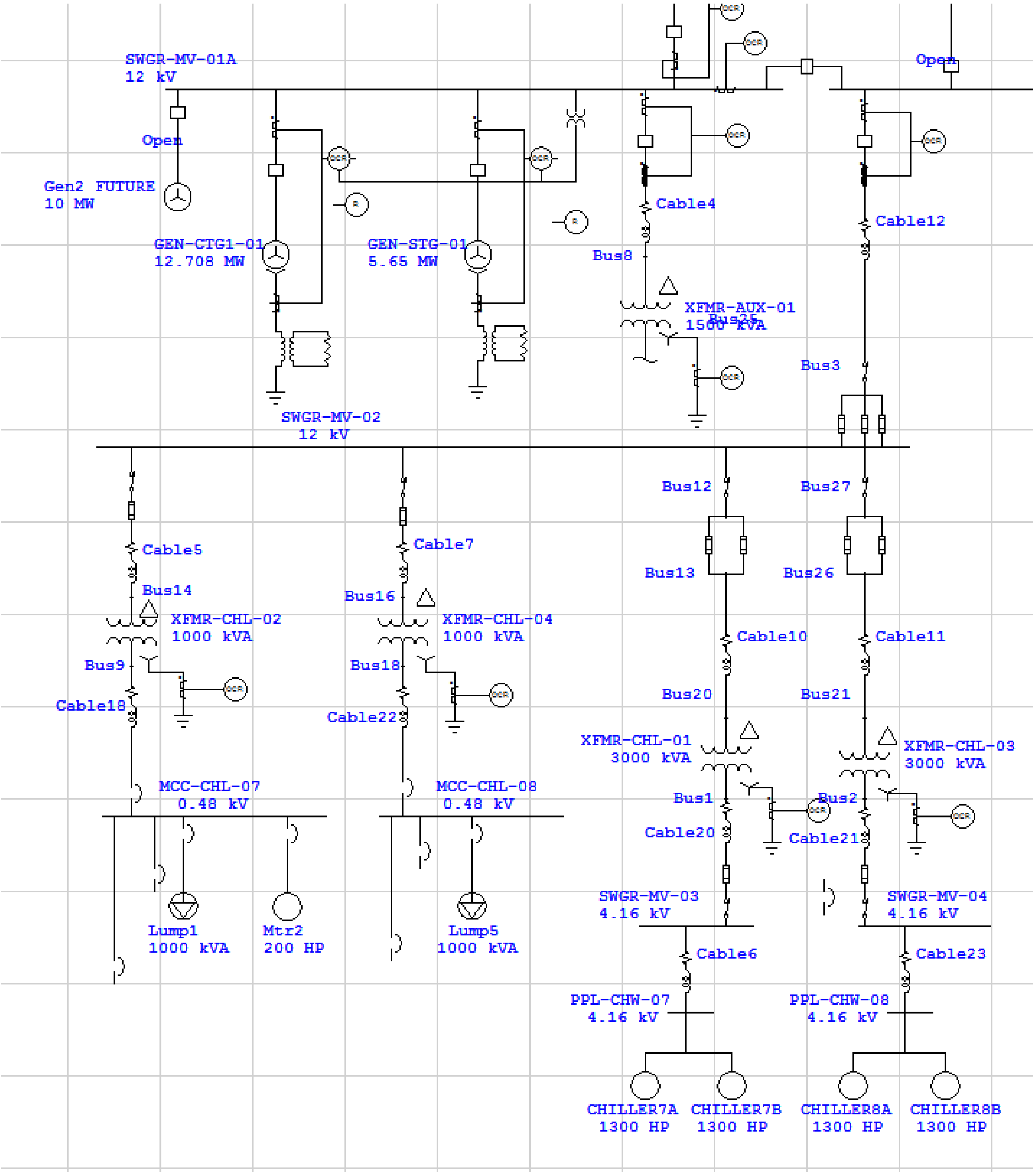

Figure 47. One-line schematic of large chiller motors on the UCIMC.

4.1.5.2. GAS TURBINE

The principal electrical power generation resource on the UCIMG and frequency regulator during islanded-mode operation is a Titan 130 turbine generator set manufactured by Solar Turbines. The system is comprised of a single-shaft natural gas fired turbine coupled to a synchronous generator capable of producing up to 13.5MVA of electrical power at a heat rate of 12380.14 MJ/MW-hr (Solar Turbines, 2018). Waste heat from the Titan 130 exhaust is recovered to provide heating to the campus via a hot water circulation loop. Recuperated heat is also used to produce steam which is used power a 5.65MW steam turbine. As the UCIMG electrical load averages 13.4MW annually with a peak demand of 18.6MW, the gas turbine generator alone is sufficient to power the entire UCIMG while operating in islanded-mode with moderate load demand. While in grid-connected mode, the gas turbine in combination with the steam turbine supply approximately 85% of the full campus electrical demand, with the balance being sourced from microgrid solar resources and utility import.

The gas turbine shaft is mechanically coupled to a synchronous generator in the Titan 130 system and the rotational speed response to sudden changes in turbine loading is critical during the islanded- to grid-connected transition as large deviations may trigger turbine speed protective devices, resulting in a turbine shutdown and a subsequent system blackout. The dynamic response of the governor, exciter, synchronous generator, temperature control, fuel control, combustor, and physical turbine systems were modeled in detail. Inlet air flow, fuel rate, exhaust temperature, exhaust flow rate, mechanical power output, and rotor frequency from the gas turbine were simulated and the synchronous generator voltage and current outputs were coupled to the UCIMG electrical circuit model. Current and voltage output waveforms from the gas turbine synchronous generator along with digital control signals were mapped to the OPAL-RT RT-HIL analog outputs and digital input/output ports for interfacing with microgrid controller systems. An overview of the gas turbine model is shown in Figure 48.

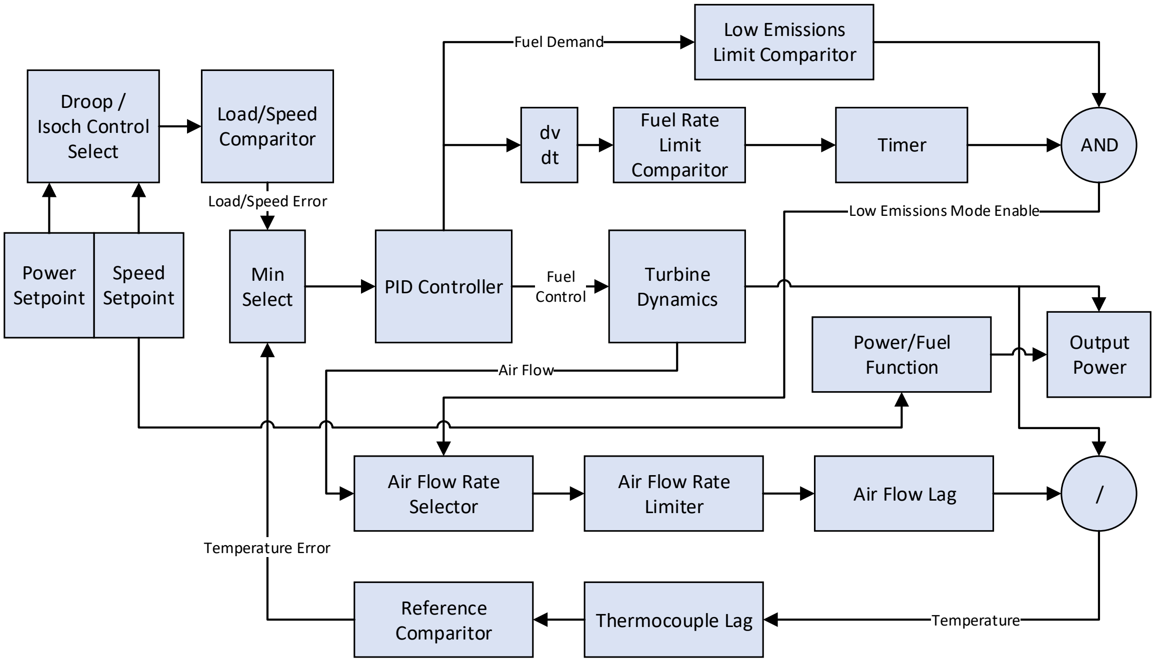

Figure 48. Gas turbine block diagram (Solar Turbines, 2011).

The governor subsystem controls the fuel flow rate based on feedback measurements from the generator electrical power output and turbine shaft rotational speed. The error between the power/speed measurements and their respective reference setpoints are adjusted with an isochronous-mode or droop-mode bias, depending on generator operation mode, and compared with an exhaust temperature limiter reference value. The minimum of these two values is then fed into a saturation-limited PID controller to produce the final fuel flow rate control signal. When operating in isochronous mode, typically used in islanded-mode operation, the governor attempts to maintain the turbine shaft rotational speed at a constant value by adjusting the fuel rate, automatically compensating for any changes in loading. Rotational speed feedback is obtained at the turbine shaft and is tracked against an operator-defined reference constant, typically nominal line frequency scaled to account for turbine to synchronous generator gear reduction, with a PID controller. In power-droop mode, which is normally used while the system is grid-connected, the isochronous control loop is modified with a bias produced by the error between the measured generator output power and a reference setpoint. This bias introduces a linear rotor frequency/output power response and modification of the bias factor is used to adjust the power output of the gas turbine system when grid-connected to allow for the coordination of power sharing between droop-controlled turbine systems. In both isochronous- and droop-control modes, the error signal entering the PID is first compared with a temperature error signal derived from the difference between the measured exhaust temperature and maximum allowable temperature reference value that serves as an over-temperature safety mechanism. The minimum of these two values is then fed into a saturation-limited proportional-integral-derivative controller to produce the fuel valve control signal which sets the fuel flow rate.

The turbine subsystem models the dynamics of the fuel system, turbine combustor, and turbine shaft response. While highly detailed models of these components exist (Maclay, 2011) (Rory A. Roberts, 2010), their dynamic response are primarily attributed to mechanical and thermal inertial effects and occur on timescales far longer than that of the electrical transient phenomena that are of interest during islanding transitions. As such, they are represented with a combined first-order low-pass transfer function with the parameters given in Table 14.

Parameter	Value	Description
R	0.035	Load-speed droop
Mode	2	1 = Droop load/speed control 2 = Isochronous load/speed Control
$\mathbf{L}_{set}$	1	Load/speed control reference set point
$\mathbf{T}_{limit}$	1.05	Temperature limit, per unit power output (temperature control mode)
$\mathbf{K}_{p}$	15	PID control proportional gain
$\mathbf{K}_{i}$	15	PID control integral gain
$\mathbf{K}_{d}$	0.5	PID control derivative gain
Max	1.075	Governor maximum output
Min	-0.07	Governor minimum output
$\mathbf{T}_{gt}$	0.3	Fuel system, combustor, and turbine combined lag time constant (s)
$\mathbf{T}_{tc}$	0.5	Temperature control thermocouple lag time constant (s)
H	4.4	Inertial constant (MW-sec/MVA)

Table 14. Gas turbine subsystem parameters.

The airflow control system of the Solar Titan 130 includes a SoLoNox low-emissions control system that allows the master air flow controller to select between two control modes -- a conventional combustion mode that sets air flow at 1.0 per unit rate and a low-emissions SoLoNox mode that provides a modified air flow rate that results in reduced nitrogen oxide and carbon monoxide emissions. The low-emissions mode setpoint is selected only when the turbine has been operating with a fuel flow rate above 0.5 p.u. with a fuel flow rate of change of less than 3.0 per unit per second within a 20 second window (Solar Turbines, 2011). These mechanisms are shown in Figure 49. While largely inconsequential in the simulation of turbine response to islanding, the inclusion of the low-emissions dropout mechanism is particularly useful for comparing the criteria pollutant emissions performance of microgrid systems operating in grid-connected and islanded modes, as load following requirements in the latter case are typically more dynamic and prone to triggering a departure from low-emissions mode. The remaining air flow dynamics such as transport delay and fluid inertial effects are approximated with a single low-pass transfer function with minimum and maximum saturation limits.

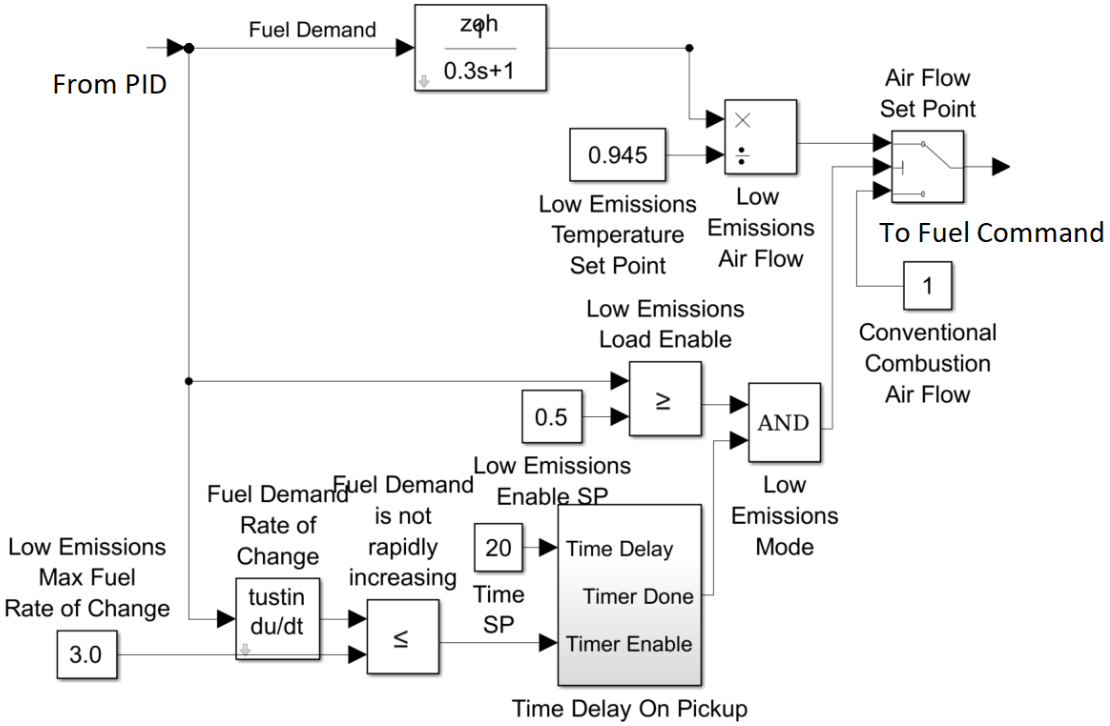

Figure 49. Low emissions control block diagram (Solar Turbines, 2011).

The generator excitation system is based on a Rockwell Automation Combination Generator Control Module and is modeled following the standards established by the IEEE Recommended Practice for Excitation System Models for Power System Stability Studies (IEEE Std. 421.5-2005, 2005). The IEEE AC8B alternator supplied rectifier excitation model (IEEE Std. 1110-2002, 2003) was used with model parameters obtained from a combination of manufacturer design documents and device measurements. The exciter model is shown in Figure 50 and corresponding model parameters are described in Table 15. Values extracted from device nameplate examination are presented in Table 16.

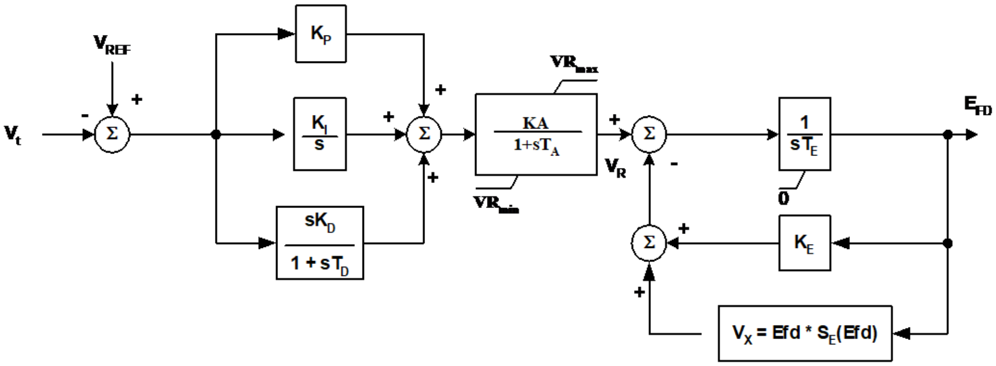

Figure 50. Exciter block diagram (Langenbacher, 2009).

Parameter	**Default Value**	**Definition**
T_E	0.32 s	Exciter field open-circuit time constant
K_P	45 p.u	PID proportional gain
K_I	29 p.u	PID integral gain
K_D	14.5 p.u.	PID derivative gain
K_G	22 p.u.	PID controller gain
T_D	0.01 s	High-pass filter time constant
$S_E[V_{EEF}]$	1.02 p.u.	Saturation function
V_{EFD}	N/A	Exciter output voltage
TA	1 s	Voltage regulator low pass filter time constant
VR_{max}	12.2 p.u	Voltage regulator upper limit
VR_{min}	0	Voltage regulator lower limit
K_E	1	Field voltage feedback gain

Table 15. Gas Turbine exciter model parameters.

Parameter	**Value**	**Units**
Prime Mover Limit	1.35E+07	W
Voltage (L-L)	1.25E+04	V
Frequency	60	Hz
X_d	1.55	Ohms (p.u.)
X_d'	0.28	Ohms (p.u.)
X_d''	0.19	Ohms (p.u.)
X_q	1.55	Ohms (p.u.)
X_q''	0.243	Ohms (p.u.)
X_l	0.18	Ohms (p.u.)
T_d'	6.4	s
T_d''	0.035	s
T_{qo}''	0.035	s
Stator Resistance	0.0035	Ohms (p.u.)

Table 16. Gas turbine generator nameplate ratings.

4.1.6. STEAM TURBINE

Thermally coupled to the exhaust steam of the gas turbine, a 5.5MW steam turbine is powered from both the gas turbine exhaust heat and a natural gas boiler. A four stage tandem-compound prime mover model (IEEE Power Engineering Society, 1973) (IEEE Subsynchronous Resonance Working Group, 1985) was used to model the steam turbine, with a speed governor consisting of a proportional regulator, speed relay, and servo motor controller. Each of the four mechanical stages is represented as a first-order transfer function. Turbine mechanical power is coupled to a synchronous generator model similar to that of the gas turbine generator set and connected to the UCIMG sharing a common connection point with the gas turbine. A block diagram of the steam turbine model is shown in Figure 51.

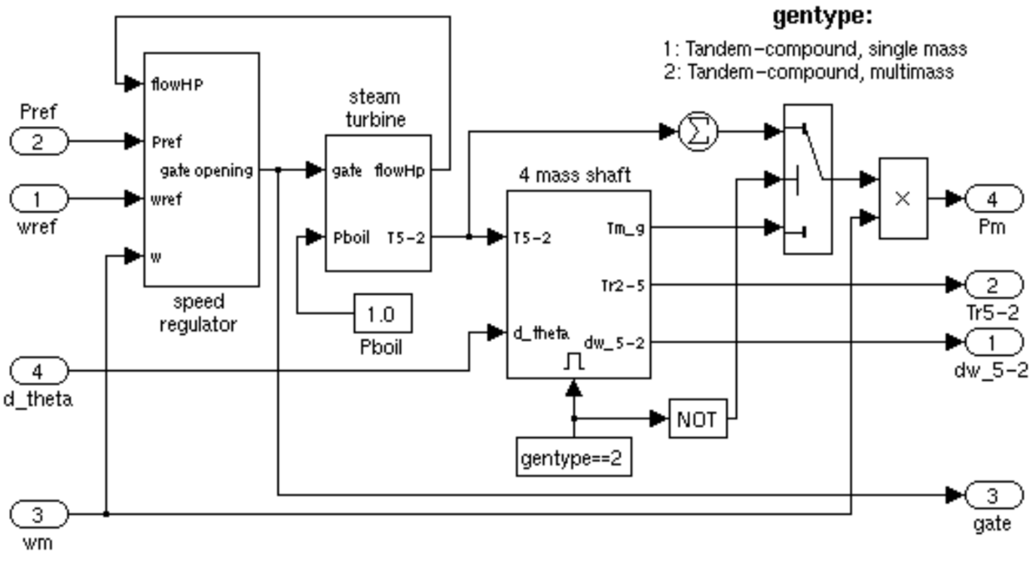

Figure 51. Steam turbine block diagram (Mathworks, 2003).

4.1.7. CONTROLLER

A controller suited for general microgrid systems, including the UCIMG, was developed and designed around a hybrid centralized-autonomous topology. This controller is based on the guidelines set by the IEEE Power and Energy Society Standards for the Specification of Microgrid controllers (IEEE Power and Energy Society, 2017) and consists of a central master microgrid controller (MMC) and four device-specific components: generation controllers (GC), storage controllers (SC), load controllers (LC) and breaker controllers (BC). These elements are responsible for the overall coordination of the microgrid, control of distributed generation devices such as diesel generators and PV, control of storage devices such as batteries, control of dispatchable loads, and control of breakers and switchgear, respectively. Separation of the microgrid controller functions into these component classes allows for autonomous operation of all microgrid elements in the event of loss of communications between components while retaining the optimization and management features of a centralized controller design. The following figure shows the system architecture of the microgrid controller (Razeghi, 2018):

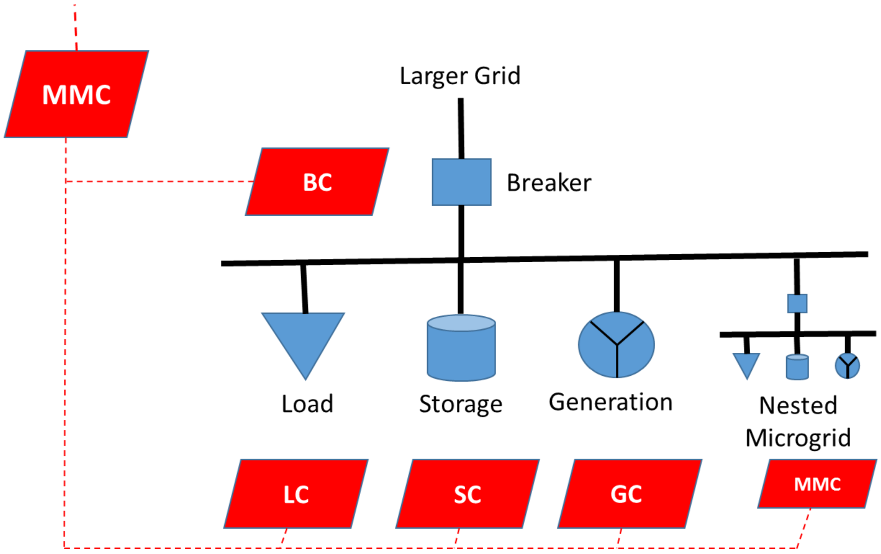

Figure 52. Microgrid controller system diagram.

Each microgrid controller module is responsible for interfacing to and controlling a specific class of devices found within a microgrid system. The master microgrid controller module provides the high-level control functions that allow the microgrid to present itself to the utility as a self-contained system that can manage itself, operate autonomously or grid-connected, and coordinate other controller components to seamlessly connect to and disconnect from the main grid and provide ancillary services. An overview of these high-level functions is presented in Figure 53. This component also coordinates microgrid assets based on real-time power measurements to achieve optimal operation while grid-connected and balance generation to load while islanded. To provide these functions, the primary functions provided by the MMC include:

1) Process load-flow and transient analysis of the microgrid system.
2) Directs microgrid resources to assume grid-forming or grid-supporting roles depending on grid-connected or islanded-mode operation. Figure 54 shows the control flowchart used to provide this function.
3) Directs microgrid generation resources to match frequency, voltage, and phase with the grid upon utility reconnect. Figure 55 shows the utility resynchronization control flowchart.
4) Determine optimal grid-connected generation droop settings.
5) Generate and continually update field devices with a load shed plan in the event of inadequate generation resources.
6) Generate and continually update field devices with an emergency load shed plan in the event of an unplanned islanding event.

7) Determine and maintain the necessary state of charge within energy storage devices to ensure continual island-transition readiness.

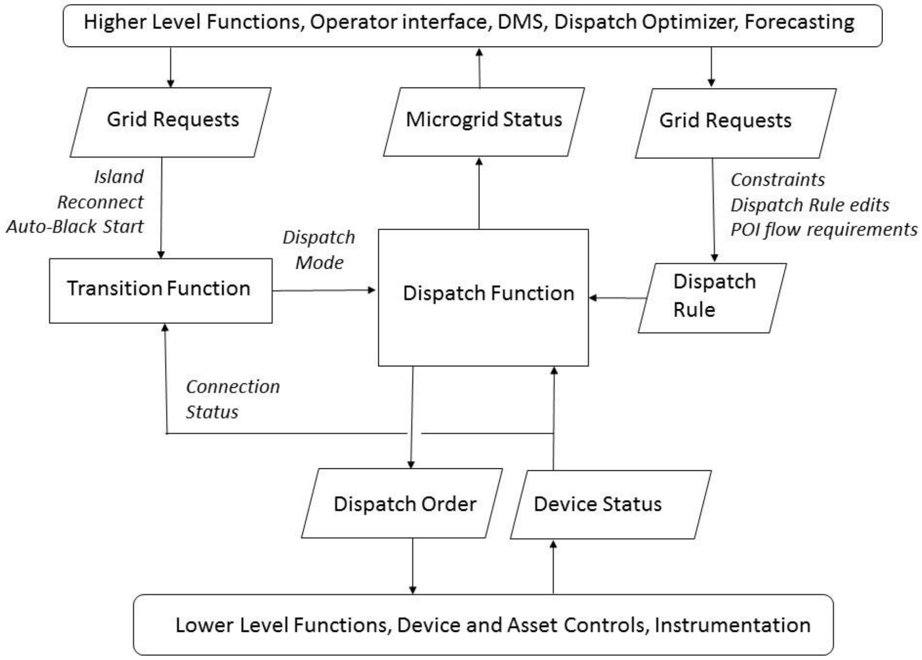

Figure 53. Controller high-level functions (Advanced Power and Energy Program, 2018).

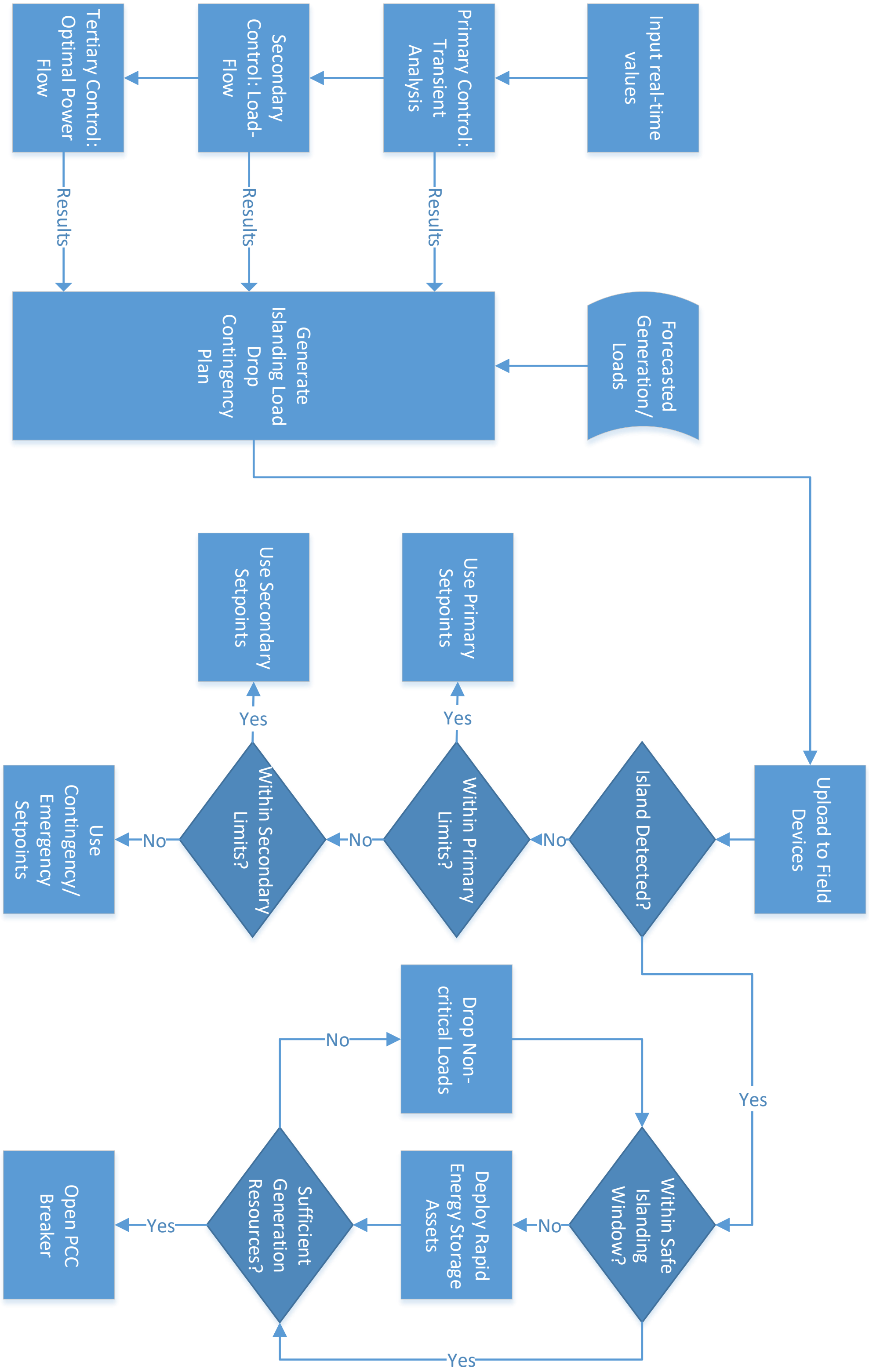

Figure 54. MMC grid-connected and islanded-mode control flowchart.

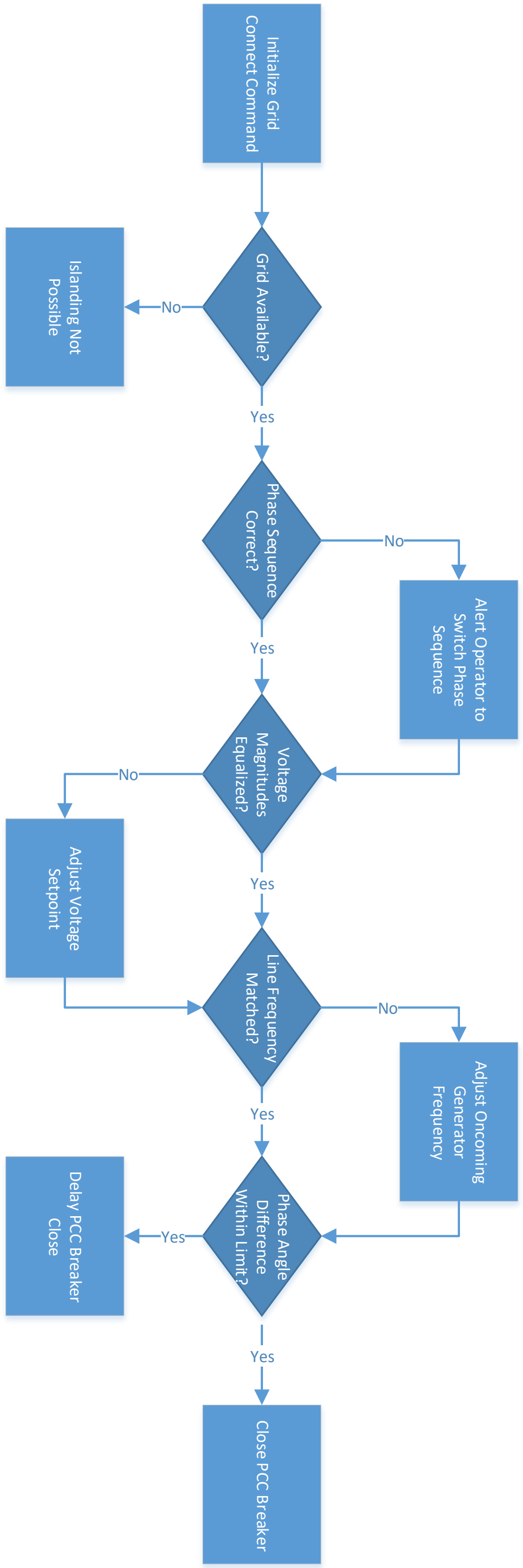

Figure 55. MMC grid resynchronization flowchart.

As the primary microgrid operator interface point, the MMC provides the following user interface functions:

1) Provides a human-machine interface (HMI) to the user(s) for the input of system parameters and allows for manual control of microgrid devices.
2) Provides an interface to display historical, current, and forecasted microgrid operating conditions.
3) Provides a communications interface to the utility.
4) Allows for monitoring and control of downstream microgrid resources connected to generation controllers, storage controllers, load controllers, and breaker controllers. An example of a MMC HMI control and monitoring screen that displays circuit breaker and microgrid islanding status is shown in Figure 56. From this screen, these elements may be directly controlled by a system operator.

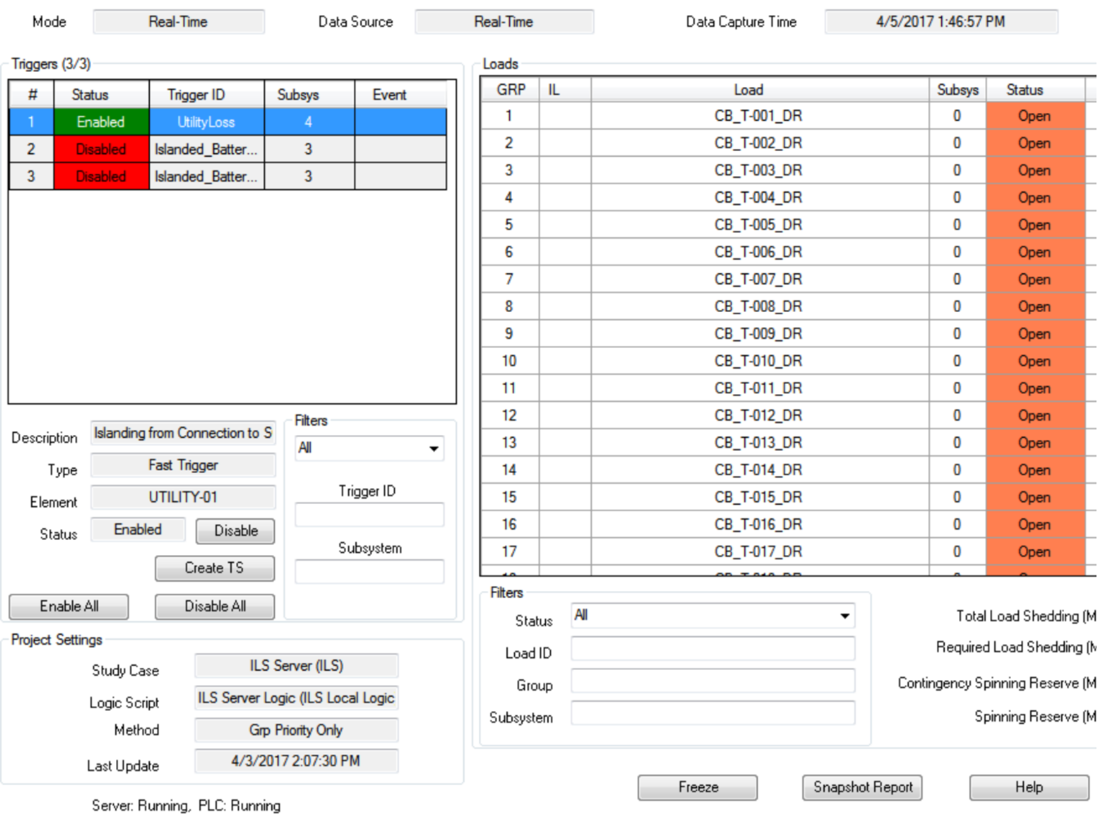

Mode: Real-Time
Data Source: Real-Time
Data Capture Time: 4/5/2017 1:46:57 PM

Triggers (3/3)

#	Status	Trigger ID	Subsys	Event
1	Enabled	UtilityLoss	4	
2	Disabled	Islanded_Batter...	3	
3	Disabled	Islanded_Batter...	3	

Description: Islanding from Connection to S
Type: Fast Trigger
Element: UTILITY-01
Status: Enabled

Filters: All
Trigger ID:
Subsystem:

Loads

GRP	IL	Load	Subsys	Status
1		CB_T-001_DR	0	Open
2		CB_T-002_DR	0	Open
3		CB_T-003_DR	0	Open
4		CB_T-004_DR	0	Open
5		CB_T-005_DR	0	Open
6		CB_T-006_DR	0	Open
7		CB_T-007_DR	0	Open
8		CB_T-008_DR	0	Open
9		CB_T-009_DR	0	Open
10		CB_T-010_DR	0	Open
11		CB_T-011_DR	0	Open
12		CB_T-012_DR	0	Open
13		CB_T-013_DR	0	Open
14		CB_T-014_DR	0	Open
15		CB_T-015_DR	0	Open
16		CB_T-016_DR	0	Open
17		CB_T-017_DR	0	Open

Filters
Status: All
Load ID:
Group:
Subsystem:

Total Load Shedding (M
Required Load Shedding (M
Contingency Spinning Reserve (M
Spinning Reserve (M

Project Settings
Study Case: ILS Server (ILS)
Logic Script: ILS Server Logic (ILS Local Logic
Method: Grp Priority Only
Last Update: 4/3/2017 2:07:30 PM

Server: Running, PLC: Running

Figure 56. Example MMC HMI screen.

Generation controllers monitor and control microgrid distributed generation resources such as diesel generators, wind turbines, PV systems, fuel cells and gas turbine generators and may be implemented natively on generation devices or on external devices such as an industrial programmable logic controller if native implementation of control functions is not possible. These controllers report local bus measurements and device status to the MCC and accept tertiary-level coordination commands including control mode commands (i.e. operating the generation asset in isochronous frequency mode (grid-forming), operating the generation asset to provide a fixed real and reactive power output (grid-feeding), or operating the generation asset with a power or voltage droop response (grid-supporting)) and adjustments to steady-state real power, reactive power, frequency, voltage and droop setpoints.

Load controllers monitor and actuate microgrid loads. These controllers are similar in function to building management systems (BMS) found in many residential and industrial sites and accept load adjustment commands from the MMC while reporting local bus measurements and load status. Examples of devices controlled by LCs include variable frequency drives, lighting systems, electric car charging stations, and electric motors. Load controllers may also be programmed to automatically adjust the operation of connected loads in response to local measurements to decrease system response time and allow for continued operation in the absence of a connection to the MMC.

Similar to the LC, breaker controllers monitor and actuate system breakers as opposed to system loads. A key differentiation is the use of high-speed breaker control signals as opposed the slower communications options commonly used with LCs as switch actuation time is critical to successful microgrid islanding performance. Breaker controllers also report local measurements and breaker status to the MMC. On the UCIMC, BCs are only installed at the substation PCC and gas turbine breakers, although any of the breakers listed in Table 10 can support the installation of a BC.

Storage controllers are a combination of GC and LC units and may be directly implemented as a combination of the two controllers. These controllers provide all of the functions found in both GC and LC systems, but also are responsible for reporting state of charge of the attached energy storage device and maintaining energy reserves to support emergency islanding and/or black start operations. On the UCIMC a storage controller is responsible for monitoring and controlling the BES to provide immediate real power support during an islanding event with high utility import and provide electrical load shifting capabilities.

5. EXPERIMENTAL SETUP

This section describes the experiment setup used in this dissertation. Three major components were developed to support the research effort: 1) a real-time hardware-in-the-loop test setup, 2) an implementation of a UCIMG microgrid controller in accordance to the IEEE Power and Energy Society 2030.7-2017 Standards for the Specification of Microgrid Controllers (IEEE Power and Energy Society, 2017), and (3) deployment of a real-time campus-wide power monitoring system.

5.1. REAL-TIME HARDWARE-IN-THE-LOOP TESTING

The microgrid controller was interfaced to an OPAL-5600 real-time simulation platform for RT-HIL testing. These tests were used to study microgrid islanding response and verify the proper operation of the controller in preparation for a real-world islanding demonstration on the UCIMG and conducted by simulating islanding scenarios derived from online and archived power meter readings. Current and voltage waveforms from the OPAL-5600 low-voltage analog output ports, which were mapped to the simulated UCIMG PCC and gas turbine electrical busses, were interfaced to the controller BC and GC voltage and current sense terminals via a power amplifier. Low voltage digital output signals designated for PCC breaker and gas turbine control were directly connected into the RT-HIL simulation ports. Upon completion of the RT-HIL testing phase, the systems was transferred to the UCIMG substation and central plant where it was connected to field equipment and used to conduct a real-world islanding demonstration. During field deployment, service voltage DC signals were directly applied to gas turbine and PCC breaker control inputs. Remaining control variables such as generator power output, steady-state frequency, UCIMG circuit breaker status, and battery state of charge were transmitted via BACNET, DNP3 and IEC 61850 GOOSE protocols. A picture of the controller interfaced to the RT-HIL simulator is shown in Figures 57 and 58. Figure 59 shows a diagram of the RT-HIL communications setup.

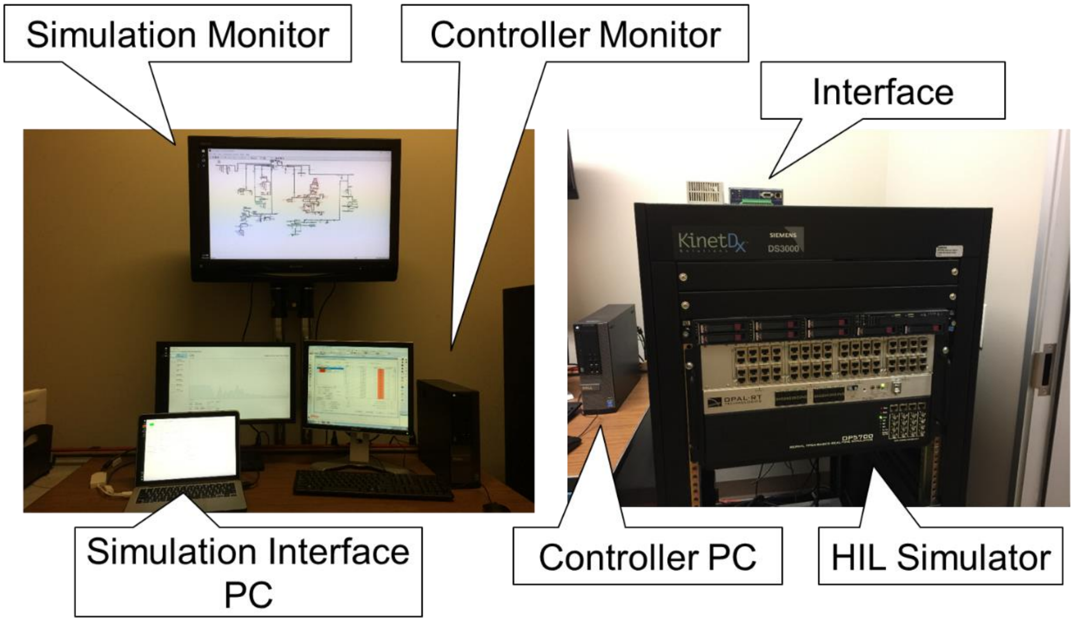

Figure 57. OPAL-RT RT-HIL development and monitoring setup.

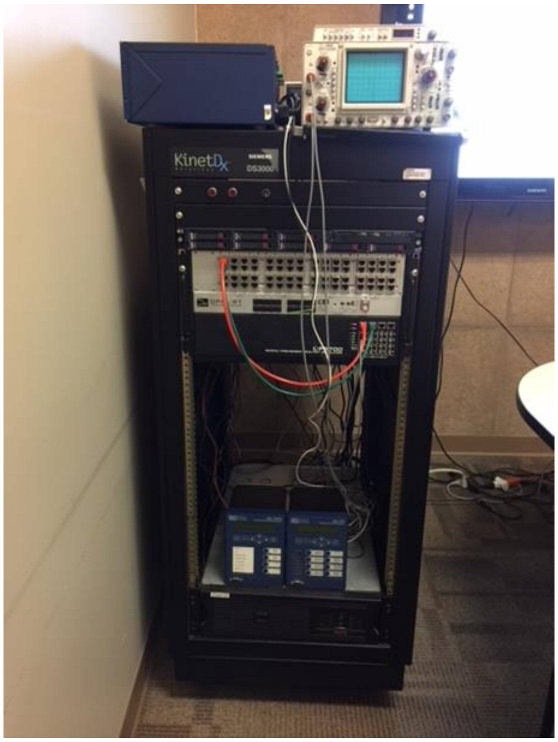

Figure 58. Controller RT-HIL testing setup.

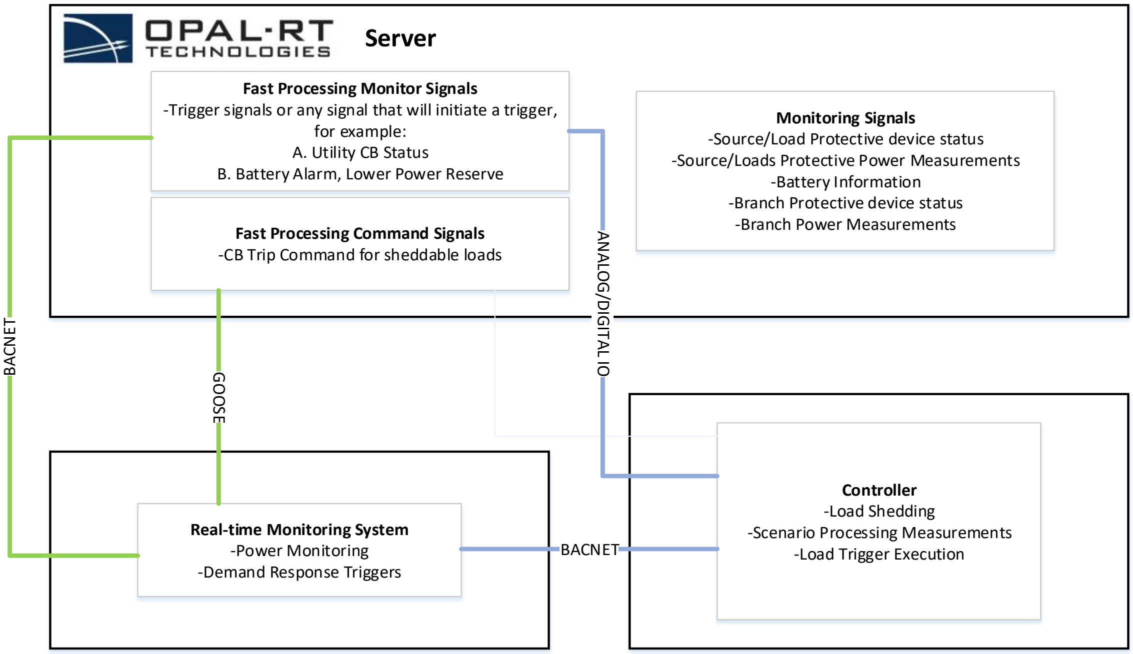

Figure 59. RT-HIL testing communications.

5.2. CONTROLLER IMPLEMENTATION

Due to the physical separation of the UCI substation that contains the PCC breaker and the UCI central plant that hosts the gas turbine generator, the UCIMG controller was implemented with MMC, LC, BC, SC, and GC control functions distributed across a system composed of several Schweitzer Engineering Laboratories (SEL) devices installed across the UCIMG, as shown in Figure 60. The complete system consists of four major components:

1) An SEL 451 Protection, Automation, and Bay Control System that detects the loss of utility power and relays a direct transfer trip signal to a generator protection relay.
2) An SEL 700G Generator Protection Relay interfaced to the gas turbine control system that, upon receipt of a transfer trip from the SEL 451, switches the gas turbine to islanded isochronous mode. This component also adjusts gas turbine frequency and voltage output to achieve resynchronization of the UCIMG to the utility.
3) An SEL 3530 Real-Time Automation Controller that serves as a data acquisition and interface system.
4) An SEL 751 Feeder Protection Relay interfaced to the PCC breaker that issues trip and close commands.

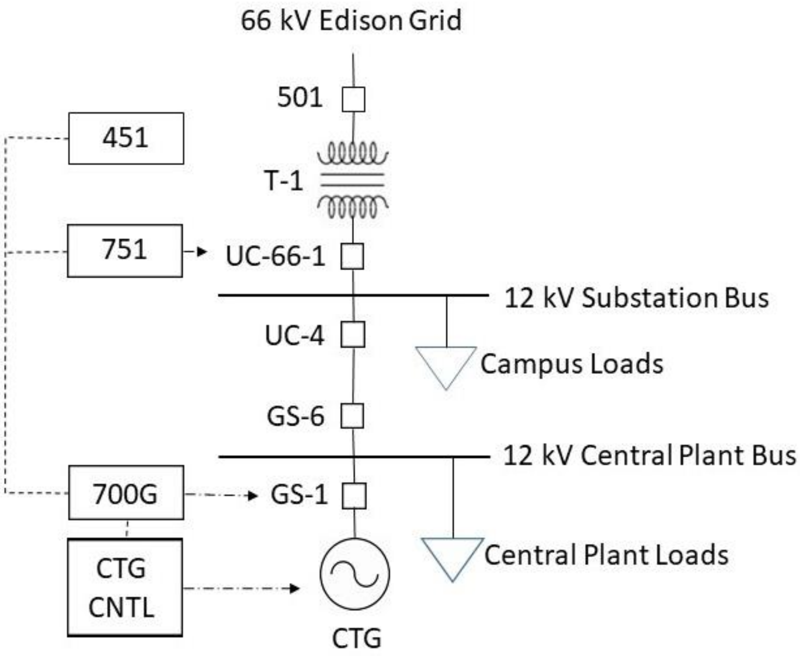

Figure 60. SEL installation locations.

Together, the system of SEL devices provide all of the functions necessary to seamlessly island and reconnect the UCIMG. Individual control routines that provide microgrid controller MMC, BC, GC, LC and SC functions as well as high-level microgrid features were developed in parallel to hasten development and were not confined to individual devices in the final microgrid controller. Therefore, they are allocated across multiple SEL devices. Table 17 and Table 18 detail the allocation of these functions and features.

Function	Device
Master Controller	SEL 451, SEL 3505
Breaker Controller	SEL 751
Generator Controller	SEL 700G
Load Controller	Existing UCI EMS
Storage Controller	N/A

Table 17. Hosting of microgrid controller MMC, BC, GC, LC and SC functions.

Feature	Device
Provide optimal dispatch of resources when grid connected	451, 700G
Provide ancillary services for larger grid	451, 700G
Execute seamless planned separation from the grid	451, 751
Execute seamless unplanned separation from the grid	451, 700G, 751
Execute separation without interruption of power	451, 700G, 751
Maintain voltage and frequency when islanded	700G
Provide prioritized power to loads when islanded	451, EMS
Provide optimal dispatch of resources when islanded	451
Resynchronize and reconnect to grid	451, 700G, 751

Table 18. Hosting of high-level microgrid control features.

5.3. UCIMG INSTRUMENTATION

A campus-wide building power monitoring solution provided by Melrok was installed throughout the UCIMG to supplement the existing low refresh rate (1 sample per 30 seconds) SCADA system with real-time power monitoring capabilities (1 sample per second). Two components from the Melrok system are shown in Figure 61. Data from the system were used for microgrid control and online RT-HIL simulation. The installed system consists of 140 building-level multi-circuit power meters that supplement the existing hot/chilled water temperature and electrical power meters. As the UCIMG campus hosts 183 buildings with substantial electrical loads, a visibility study was conducted to guide the selection of meter deployment locations, taking into account average building electrical load, peak demand, and proximity to sensitive electrical nodes such as the substation and central plant busses. Meter placement was selected with priority given to locations that maximize visibility of total average UCIMG power demand, with exceptions made for locations that exhibit large peak loading or those close to the central plant or critical campus breakers. Table 19 lists the legacy meter inventory and Table 20 identifies the selected installation locations throughout the UCIMG. A map of these locations relative to the campus layout is provided in Figure 62.

Instrumentation			Control Devices		
Meter Type	**Voltage**	**Qty.**	**Device Type**	**Rating**	**Qty.**
ION 7330	12 kV	1	**GT Sync Panel**	12 kV	1
Power Logic 7300	480 V	7	**Switched Capacitor Banks**	6 MVAR	2
Power Logic 7350	480 V	3	**Variable Frequency Drives**	715 kW	12
Power Logic E5600	120-480 V	12	**High-Voltage Synchronizing Breakers**	12 kV	5
Power Logic 7620	66 kV	1	**Replay Panel**	12 kV	2
Power Logic 8600	480 V	2	**Main Breakers**	12 kV	10
Power Logic PM800	480 V	1			
Siemens 9330	480 V	15			
Siemens 9350	480 V	1			
Other Vendors	120-480 V	61			
Total		**105**			**32**

Table 19. Existing meters and control.

a) **b)**

Figure 61. Melrok devices: a) Energy meter, b) IoT router (Melrok, 2018).

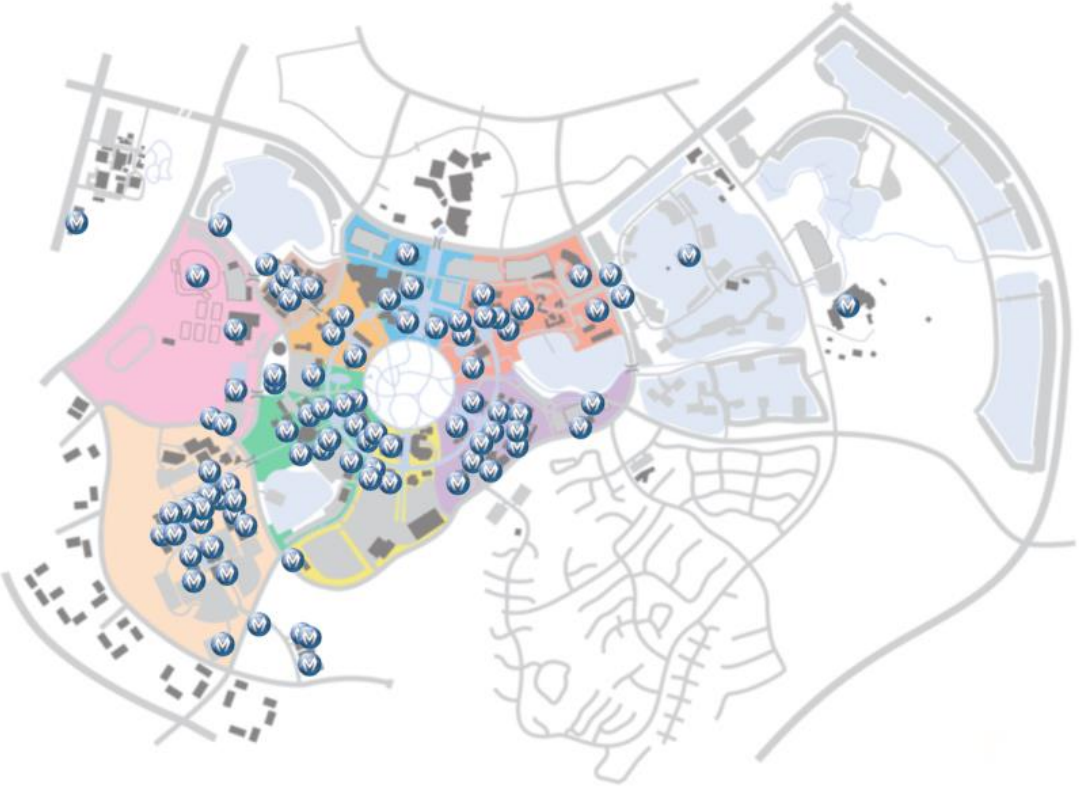

Figure 62. Meter installation locations.

ACE Trailers
Administrative Modular
Administrative Office Building (Aldrich Hall)
Alumni House
Anteater Ballpark (Baseball Stadium)
Anteater Instruction & Research Bldg.
Anteater Parking Structure (571,118)
Anteater Recreational Facility (ARC)
Anteater Recreational Facility (ARC) Expansion
ARC Court Building
ARC Field Building
Art, Culture & Tech
Arts Instructional & Tech. Resource Center (AITR)
ArtsTrailers
B.C.'s Cavern on the Green
Beall Gallery
Beckman Laser Institute
Berk/Alumni Medical Ed. Building
Berkeley Place
Biological Science Lecture Hall (Schneiderman)
Biological Sciences Administration Trailers
Biological Sciences III
Biological Sciences Unit 2 (McGaugh Hall)
Bonney Research Laboratory
Brandywine (Middle Earth)
Bren Center
Building Services Bldg.
Café Med
Calif. Inst. For Telecom. And Info. Tech. (Cal(IT)2)
Campus Village
Central Plant
Children's Care Center
Classroom and Computer Support
Computer Science III (Bren Hall)
Contemporary Art Center
Crawford Clubhouse (Modular Fourplex)
Crawford Hall / Pool
Cross-Cultural Center
Croul Hall
CTB Theater
Dance and Drama Building
Disability Center (Trailer)
Early Childhood Education Center
Engineering and Computing Trailer
Engineering Gateway
Engineering III
Engineering Lab Facility
Engineering Lecture Hall
Engineering Tower
Env. Health & Safety Svcs. Facility
Extended Day Care Center
Fine Arts Orchestra Hall (Choral Studio)
Fine Arts Rehearsal Studio (Smith Hall)
Gateway Study Center
Gavin Herbert Eye Institute
Gillespie Neuroscience Research Fac.
Graduate School of Management (School of Business 2)
Gross Hall Stem Cell Research
Grounds Maintenance Building
Headhouse Greenhouse
Hewitt Hall
High Energy Bay
Hitachi Building (Plumwood House)
Housing Admin. Services
Humanities Classroom Trailer A
Humanities Classroom Trailer B
Humanities Classroom Trailer C
Humanities Gateway
Humanities Hall
Humanities Instructional Building
Humanities Interim Classrom Fac.
Humanities Office Bldg. 2 (Athletics Office)
Humanities Office Building -HOB (Krieger Hall)
Humanities Trailer Complex
ICS Trailers
Infant/Toddler Center
Information and Computer Science
Information and Computer Science 2
Interfaith
Interm Classroom Facility
Irvine Hall
Main Library Building (Langson Library)
Med Sci A Annex
Medical Education Building
Medical Sciences A
Medical Sciences B
Medical Sciences C
Medical Sciences Classroom Facility
Medical Sciences D, Cheney Building
Medical Sciences E
Medical Surge I
Medical Surge II
Mesa Arts Building
Mesa Court
Mesa Office Building
Mesa Parking Structure (325,000)
Middle Earth Phase I
MRI 3T Trailer
MRI Trailer
Multipurpose Academic and Administrative Building
Multipurpose Science & Technology Bldg.
Music and Media Building
Natural Sciences I
Natural Sciences II
Newkirk Alumni Center
Park View Classroom
Phoenix Grille
Physical Science Classroom Building
Physical Sciences I (Rowland Hall)
Physical Sciences II (Reines Hall)
Physical Sciences Lecture Hall
Public Services
Qureshey Lab
Rockwell Engineering Center
Science Library
Social & Behavioral Sciences Gateway
Social Ecology I
Social Ecology II
Social Science Hall
Social Science Lab
Social Science Lecture Hall
Social Science Parking Structure (554,554)
Social Science Plaza A
Social Science Plaza B
Social Science Tower East / West
Social Science Trailer
SOTA Drama Building
SOTA Production Studio
SOTA Sculpture/Ceramic Studio/Nixon Theater
SOTA Studio Art Building
SOTA Studio Four
SOTA Studio Theater and Dance Studio Building
Sprague Hall
Steinhaus Hall
Student Center Building
Student Center Parking Structure (316,800)
Student Health Center
Student Services I
Student Services II
Tamkin Student Lecture Building
Theoretical Neurobiology Facility
University Club
University Extension D
Verano Place
Verano Preschool
Vivarium Administrative Offices
Women's Opportunities Center (University Extension A)

Table 20. List of meter installation locations.

Depending on the Melrok device model version, meters are equipped with 16 or 32 voltage and current measurement channels that interface to potential and current transformers, respectively. Meters also accept inputs via MODBUS, DNP3 or BACNET over Ethernet from third party devices to a facilitate aggregation of monitoring information into a unified monitoring platform. Connectivity is established via the UCIMG Facilities Network (FACNET), an existing wired Ethernet network that spans all campus buildings and is dedicated to facility operations. All campus metering devices including the Melrok system are connected to and communicate over this network. As a security measure, FACNET is maintained as a closed network and any connections to external networks such as the Internet are accomplished via dedicated network gateways. Figure 63 shows a diagram illustrating network zoning.

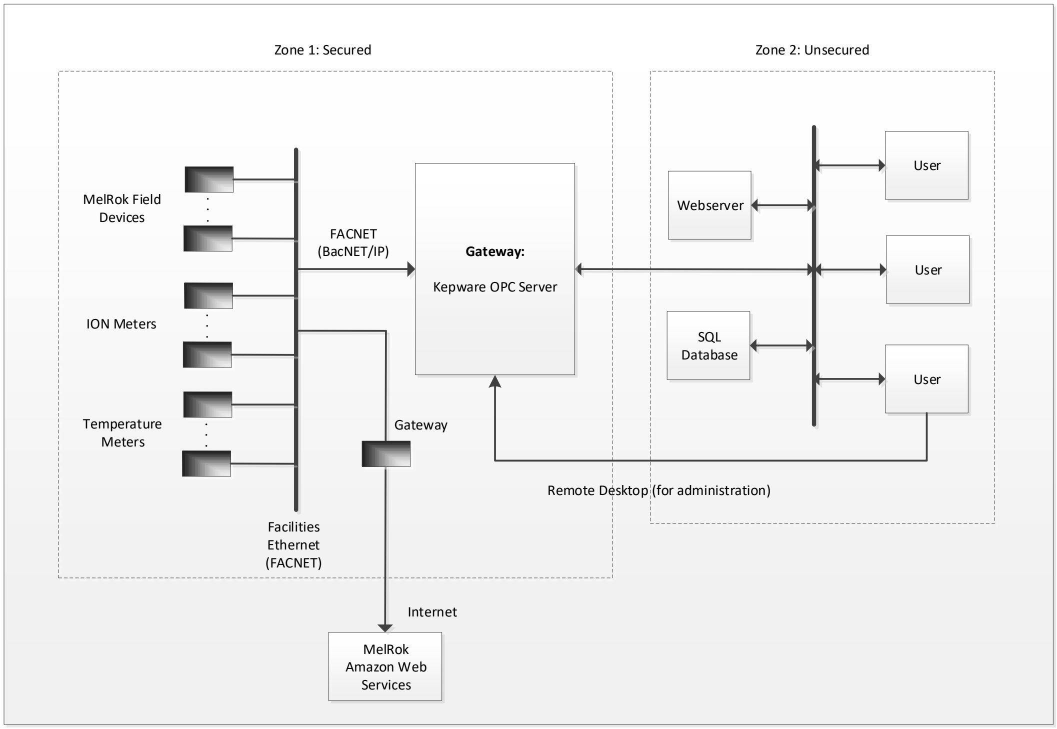

Figure 63. Network zoning.

The collected data are transmitted in real-time by the MelRoK meters through two paths, interfaced by the gateways shown in Figure 63. The primary use path delivers data to a cloud-based server via a FACNET-internet gateway at a maximum refresh rate of one sample per minute across all measurement channels. Meters are equipped with on-board battery backup systems allowing measurements to be buffered locally in the event of a power or network failure and uploaded upon recovery. From a web-based portal, UCIMG users may access stored data. Figure 64 shows an example of a web-based interface screen.

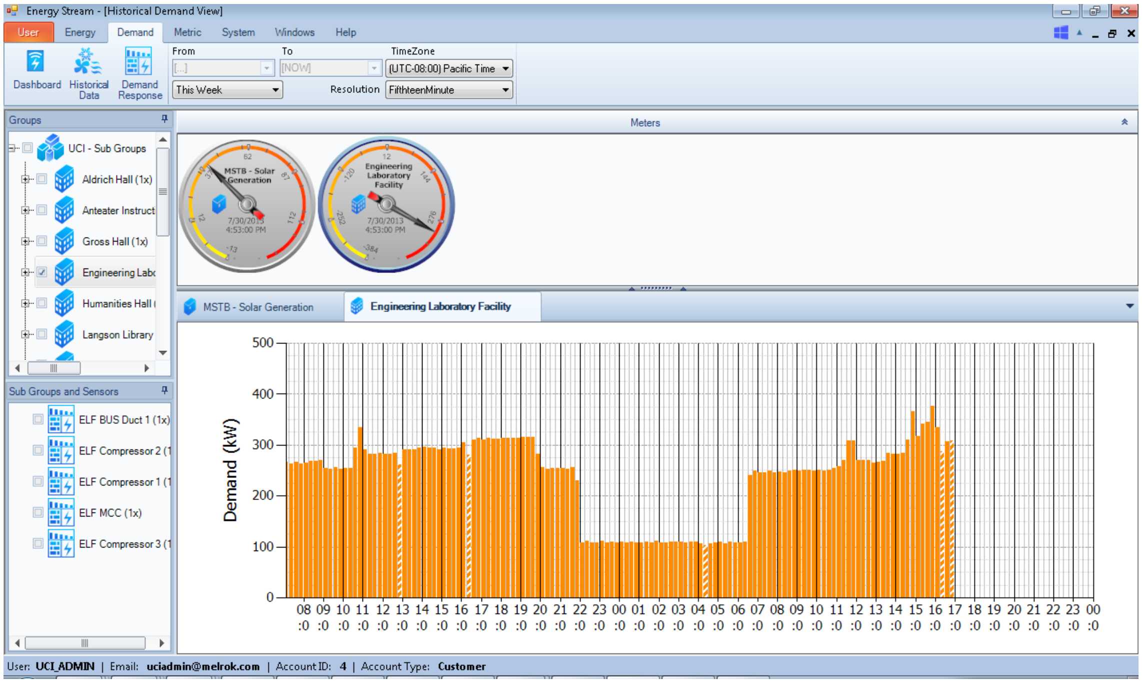

From [...]
To [NOW]
TimeZone (UTC-08:00) Pacific Time
This Week
Resolution FifthteenMinute

User: UCI_ADMIN | Email: uciadmin@melrok.com | Account ID: 4 | Account Type: Customer

Figure 64. Melrok web interface screen.

A secondary data path implemented specifically for RT-HIL use has been established that achieves a 1 Hz sampling rate. This path confines transfer to within the facilities network and routes data to a local dedicated server for archiving and protocol translation for use by other programs. This server also acts as a FACNET gateway to maintain network isolation between FACNET and external users. Clients may connect to this server and receive data via the OPC-UA, MODBUS, DNP3, or BACNET protocols. In the HIL implementation used to test the UCIMC controller, the OPAL-RT RT-HIL simulator accepts real-time data as DNP3 time-stamped values, and the microgrid controller accepts data as BACNET tag-mapped data. Archived data may be accessed via FTP as comma separated values files.

6. SIMULATION RESULTS

RT-HIL simulations were conducted to validate the EMT and controller models, investigate the impact of grid-connected ancillary service dispatch on islanding success, study microgrid islanding behavior, and verify microgrid controller grid resynchronization capabilities.

6.1. MODEL VALIDATION

A series of steady-state and transient simulations were conducted to verify that the controller and EMT models correctly reflect the physical UCIMG electrical network and to confirm simulation stability, especially when simulating large transient events such as step load and inductive motor switching. Circuit feeder points at the UCIMG substation, shown in Figure 65, were used as test points through which total real and reactive power flow were observed as building loads were adjusted. Data sets provided by the Solar Turbines were used to validate the gas turbine dynamic model.

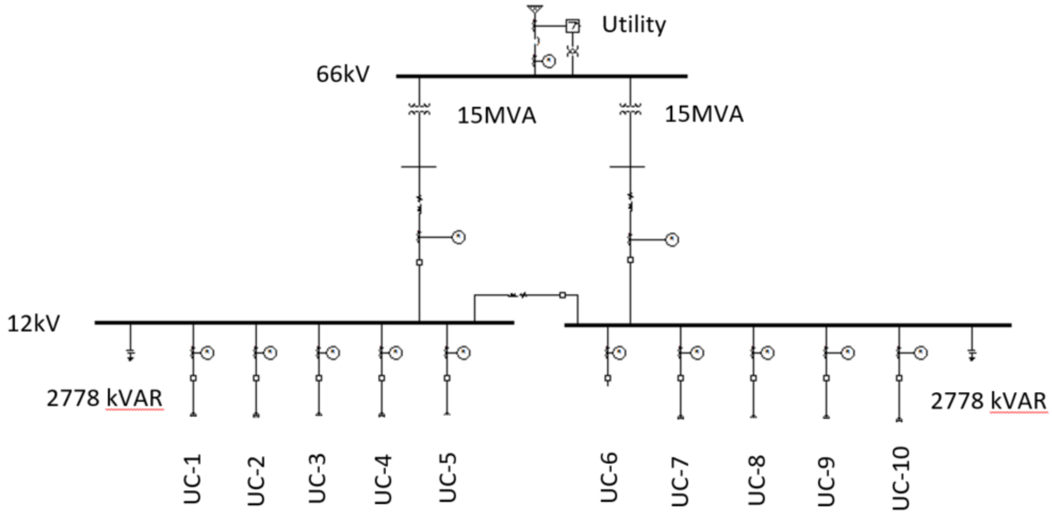

Figure 65. Model validation test points: UC-1 through UC-10.

6.1.1. EMT-CONTROLLER MODEL COMPARISON

The UCIMG controller uses a phasor-based version of the EMT model in which redundant circuit conductors are restored and localized clusters of transformer and building loads were aggregated. Separate load-flow simulations on the two platforms (controller and RT-HIL simulator) with identical building loading values were conducted and compared to ensure that the controller circuit model was properly translated. Total real and reactive power flow through the main switches of the circuit feeder lines, UC-1 to UC-10, were selected as comparison points to verify that electrical parameters were correct and merged loads were connected to appropriate circuits. Figure 66a and Figure 66b show simulation results from a low utility import scenario (4MW) and a high utility import scenario (16MW), respectively. In these scenarios, UCIMG generation was set to zero and total electrical demand was uniformly distributed across all building loads. Figure 67 shows the percent error in load-flow results between the two models across all major circuits as import is varied from the low to high import.

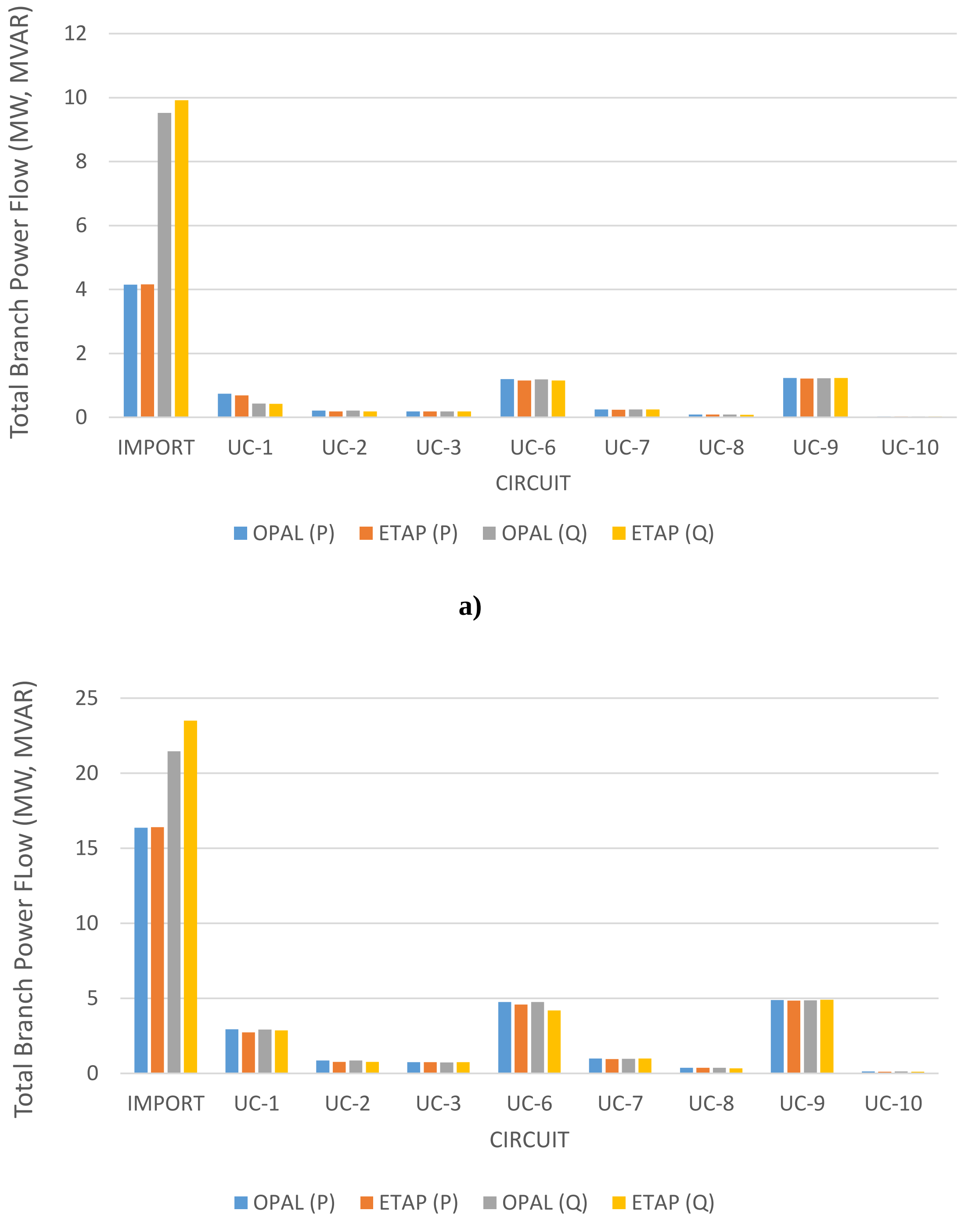

a)

b)

Figure 66. EMT vs. controller branch power load-flow comparison for a) low import (4MW) and high import (16MW) conditions.

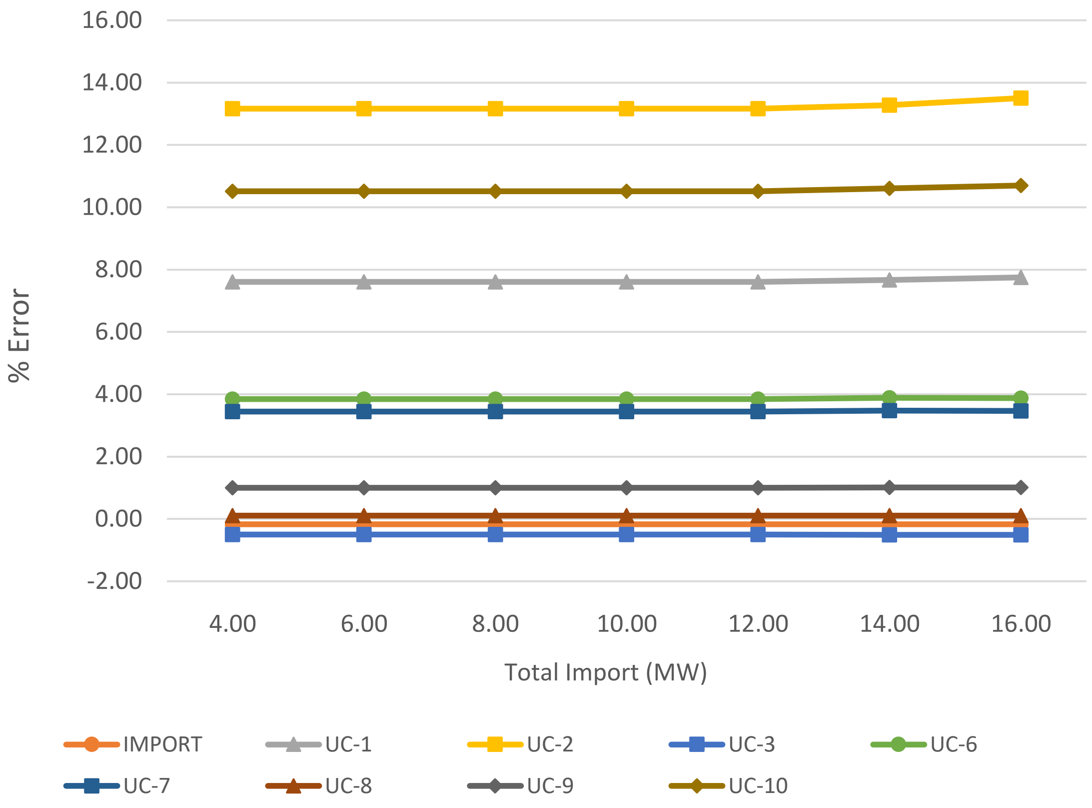

Figure 67. EMT vs. controller load-flow error.

LOAD (MW)	IMPORT (%)	UC-1 (%)	UC-2 (%)	UC-3 (%)	UC-6 (%)	UC-7 (%)	UC-8 (%)	UC-9 (%)	UC-10 (%)
4.00	-0.17	7.61	13.17	-0.50	3.85	3.44	0.11	1.00	10.52
6.00	-0.17	7.61	13.17	-0.50	3.85	3.44	0.11	1.00	10.52
8.00	-0.17	7.61	13.17	-0.50	3.85	3.44	0.11	1.00	10.52
10.00	-0.17	7.61	13.17	-0.50	3.85	3.44	0.11	1.00	10.52
12.00	-0.17	7.61	13.17	-0.50	3.85	3.44	0.11	1.00	10.52
14.00	-0.17	7.67	13.28	-0.51	3.88	3.47	0.11	1.01	10.61
16.00	-0.17	7.75	13.50	-0.51	3.87	3.46	0.11	1.01	10.70

Table 21. EMT vs. controller load-flow error.

The maximum deviation between both models for real power demand were within acceptable limits of 10% with the exception lightly loaded circuits UC-2 and UC-10 at an average of 13.23% and 10.56%, respectively. Increasing the total microgrid loading value had a negligible impact on the comparison error, indicating that electrical parameters between the two models were successfully translated and that the primary source of error was caused by the aggregation of building-level loads. Additionally, reactive power demand in the controller model was consistently higher than in the EMT case, which is in agreement with the anticipated higher reactive power loading due to the reintroduction of idle redundant conductors. This effect is comparatively greater in the low loading case, where the energization of non-load carrying lines results in a larger reactive power demand relative to the high loading case.

6.1.2. STEADY-STATE AND STEP-LOAD RESPONSE

The stability of steady-state adjustable load components in EMT simulation was assessed by introducing 1) real power step load changes distributed uniformly throughout each of the UCIMG circuits and 2) utility voltage step changes at the UCIMG PCC. A series of 10 step load increases were introduced at 0.1 minute intervals across all loads in the EMT model. Similarly, a series of 10 step voltage decreases was introduced at the end loads of each circuit by modifying the ideal voltage source representing the utility grid at the PCC. The total real power profile was observed at each of the circuit entry points as shown in Figure 65 to determine if the simulation converged to steady-state values and line voltages at the end of each UCIMG circuit was observed for stability. Figure 68 shows the response of 10 consecutive real power increases and Figure 69 shows the results from 10 consecutive utility voltage decreases.

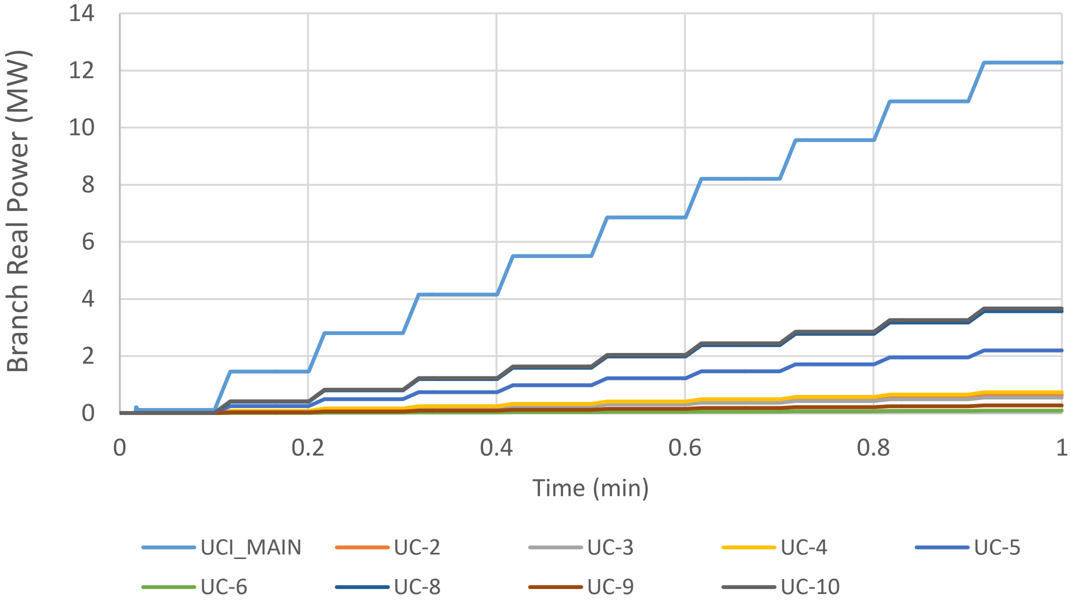

Figure 68. Adjustable steady-state load dynamic power response.

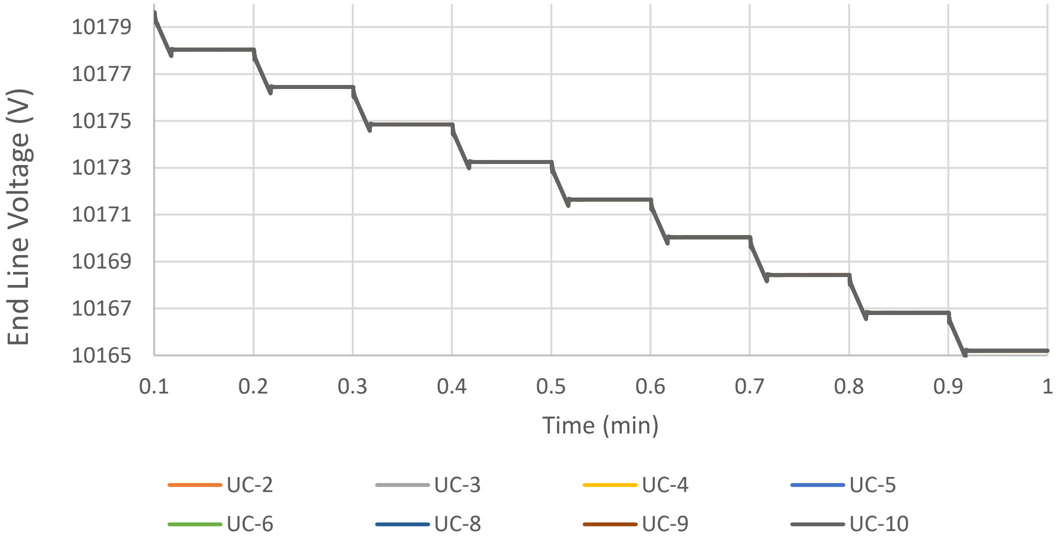

Figure 69. Adjustable steady-state load dynamic voltage response.

In all simulations, EMT simulation profiles converted to steady-state values that corresponded with expected load-flow results and did not exhibit noticeable oscillations or overshoot, even in the presence of step changes. It was noted, however, that despite commanding immediate step increases in real power demand, the adjustable steady-state loads gradually adjusted their local power demand at a ramp rate of approximately 1.76 kW/second. This is due to the power tracking control mechanism implemented in the adjustable steady-state load models. Removal of this feature results in simulation instability with any amount of load change. Related to this, line voltage decreases at the PCC were ramped as sudden voltage changes result in failure of the adjustable steady-state load models. Recognizing this limitation, RLC loads were used in islanding and load-switching simulations. Figure 70 shows a step load three-phase current response of an adjustable steady-state load compared to that of a benchmark RLC load model specifically used for highly dynamic simulations to a step load reference increase.

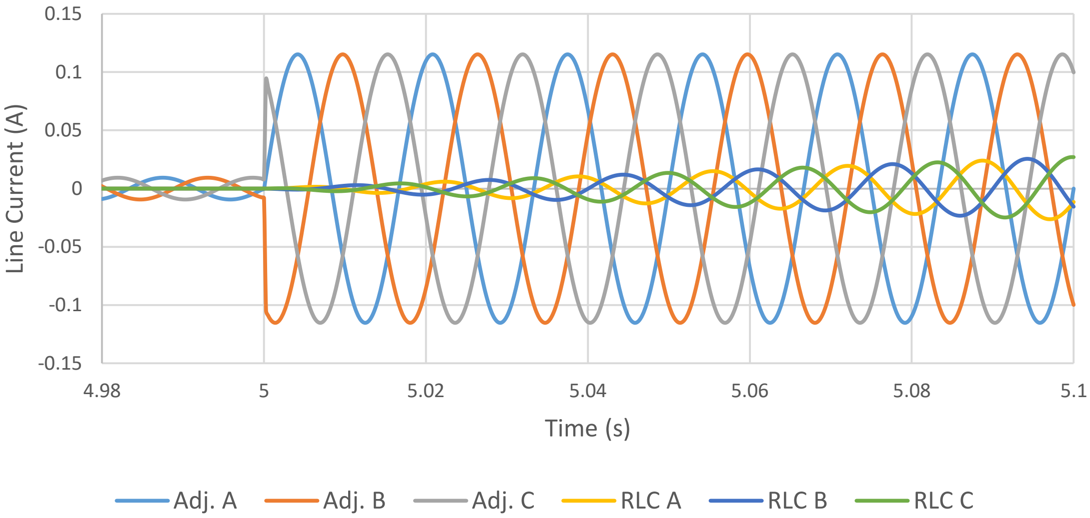

Figure 70. Current waveform comparison of an adjustable steady-state load vs. RLC load.

6.1.3. GAS TURBINE MODEL VALIDATION

Gas turbine dynamic response data provided by Solar Turbines were compared to simulated results. Turbine shaft frequency response to a 60% on-load and 100% off-load step increase while in conventional airflow control mode are shown in Figure 71 and Figure 72, respectively, while the shaft frequency response to a 55% to 85% on-load and 82% to 94% on-load step increase while in SoLoNOx airflow control mode are shown in Figure 73 and Figure 74. In all figures, simulation results are shown in column a) and manufacturer validation data are shown in column b).

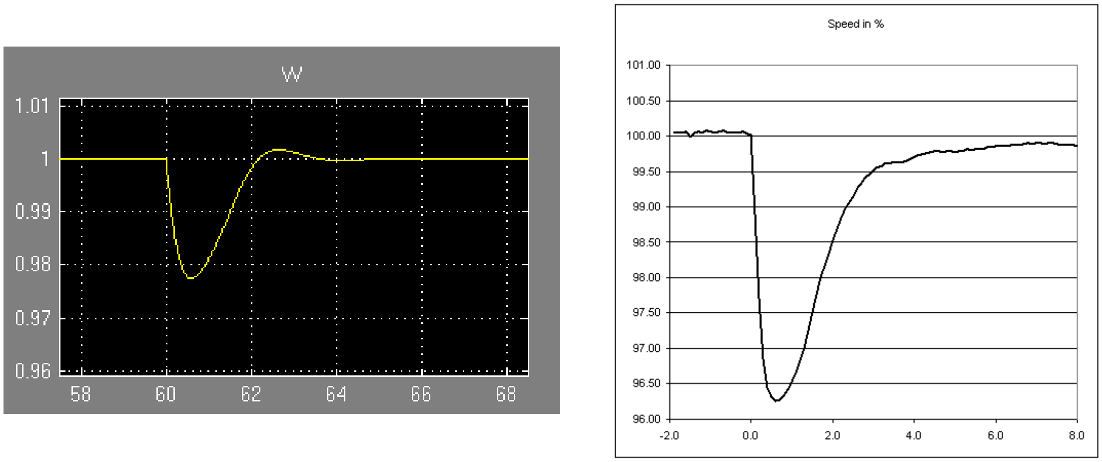

a **b**

Figure 71. 0% to 60% step load gas turbine shaft speed response, conventional airflow (Solar Turbines, 2011).

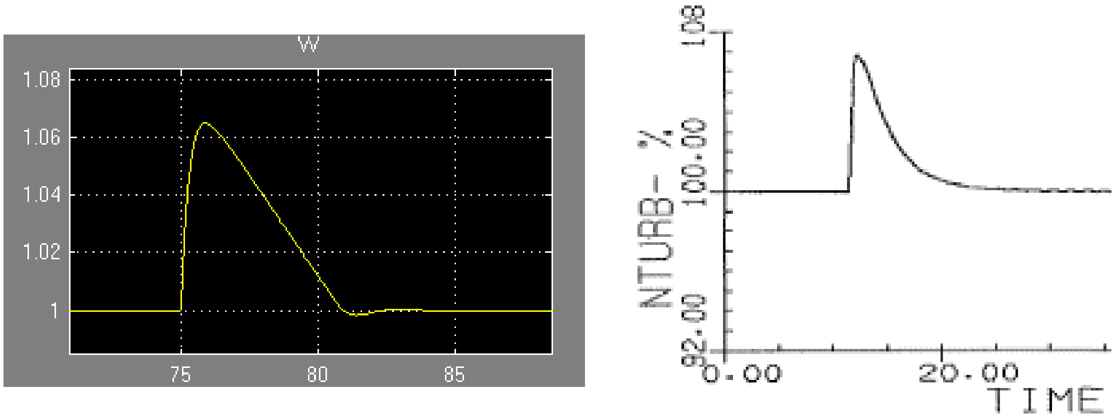

a

b

Figure 72. 100% to 0% step load gas turbine shaft speed response, conventional airflow (Solar Turbines, 2011).

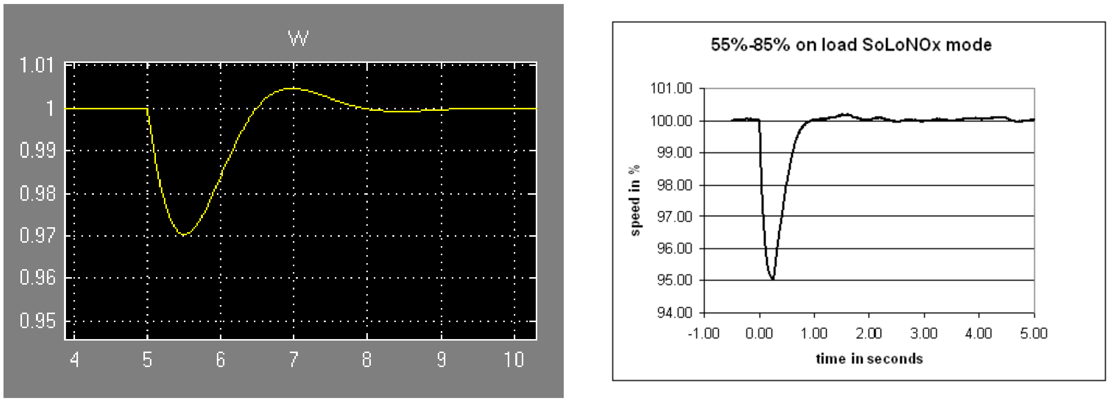

a

b

Figure 73. 55% to 85% step load gas turbine shaft speed response, SoLoNOx airflow (Solar Turbines, 2011).

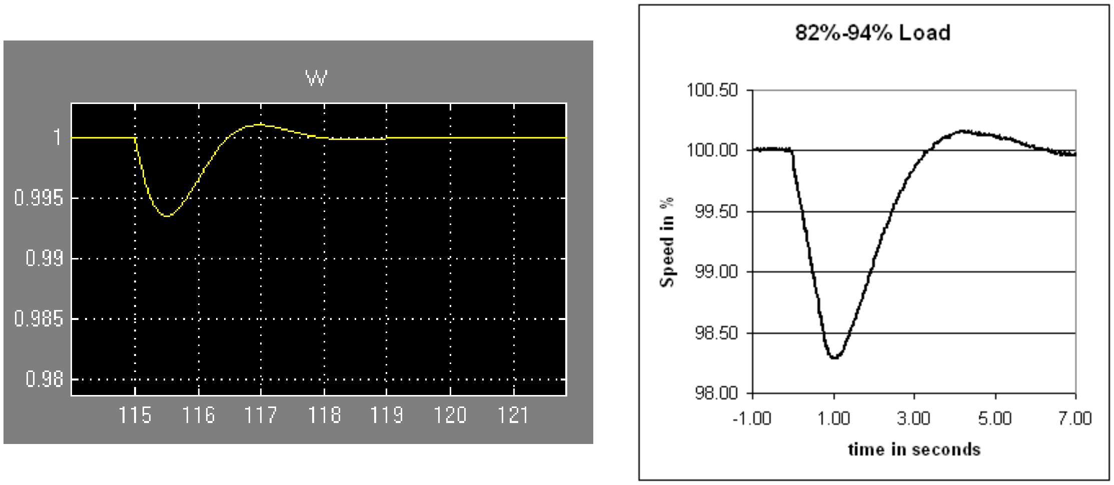

a **b**

Figure 74. 82% to 94% step load gas turbine shaft speed response, SoLoNOx airflow (Solar Turbines, 2011).

6.1.4. DISCUSSION

The model validation effort presented in this section assessed the steady-state and transient performance of the UCIMG EMT and controller models. The translated phasor-based model results appear to be in agreement with the original EMT model when comparing steady-state load-flow simulations, with all major branch power flows matching within 7.75%. A relatively linear correlation between branch power flow mismatch and building loading suggests this error is primarily caused by incorrect load aggregation when reducing the full EMT model and not due to the incorrect transfer of electrical parameters between models. EMT numerical stability also assessed and appeared adequate for the microgrid studies used in the remainder of this research and gas turbine simulations were in close agreement with manufacturer-provided validation data sets.

6.2. GRID-CONNECTED OPERATION

This section focuses on the performance of the UCIMG while grid-connected and assesses the ability of the microgrid to provide ancillary services to the utility and neighboring energy communities while retaining seamless islanding capabilities. These services include real power dispatch, reactive power dispatch, frequency regulation, and spinning reserve. These simulations were conducted using an RT-HIL simulator loaded with an EMT model of the UCIMG and an impedance-coupled voltage source to represent the utility and neighboring energy communities. Service requests and microgrid control were handled by the UCIMG microgrid controller.

6.2.1. REAL POWER DISPATCH

Real power dispatch was controlled by sending dispatch service requests to the UCIMG controller via DNP3 from a remote client. Once received, the controller accounts for real-time generation and microgrid load and adjusts generator output via hardwired digital control lines to achieve the target real power export through the PCC. Power monitoring through current and potential transformers emulated via the analog output ports on the HIL simulator were used as feedback to ensure that the appropriate amount of real power dispatch was provided. In Figure 75, results from real power dispatch tests under controlled load conditions are shown in which the gas turbine generator output was initially set at 9MW while steam turbine output was set at 1MW. The campus load set at a constant 9MW and 1MVAR. Upon a real power dispatch command, the gas turbine power output was increased by (1MW, 1MVAR) to (5MW, 5MVAR) in (1MW, 1MVAR) steps. Simulations setteled to expected steady-state values in all cases with the exception of the (+5MW, +5MVAR) case, in which power output was automatically capped at 13.5MVAR due to turbine limits and thermal management safety mechanism.

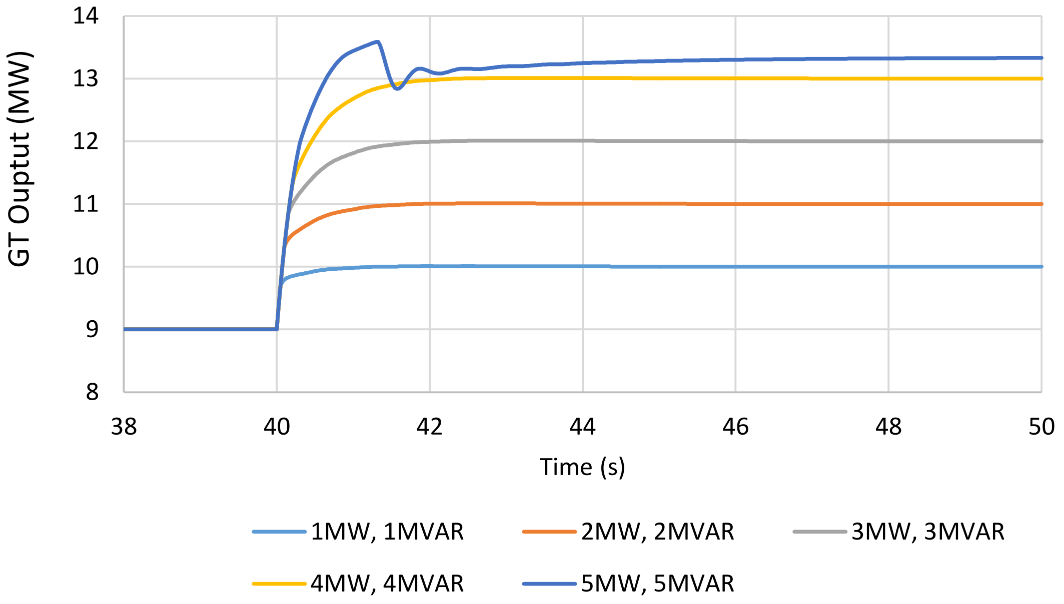

Figure 75. Real power dispatch response under controlled load conditions.

With the performance of real power dispatch under controlled load conditions established, real-world load and generation profiles from select days from historical UCIMG data were simulated with varying amounts of real power dispatch. In the following figure, a fixed amount of real power dispatch (1MW to 5MW) through the UCIMG PCC was requested. The controller was able to automatically adjust UCIMG generation resources to deliver the requested amount of real power to the utility while accounting for varying local load demand and PV generation while maintaining adequate line voltage at all points across the UCIMG.

However, dispatch of real power beyond nominal microgrid load detracts from the generation-to-load margin necessary to support seamless islanding and the export of real power through the PCC imposes an abrupt step load decrease in load when the PCC is closed. These factors may result in the reduced ability of the microgrid to seamlessly island in the event of an unplanned utility outage. To assess the impact of real power dispatch on islanding capabilities, varying levels of real power dispatch were imposed on the grid-connected microgrid operating under a representative low and high load profile conditions acquired from the campus energy monitoring system. At every 5 minute interval, the utility breaker was opened in simulation to determine if the campus was able to successfully transition to islanded-mode operation without an interruption in power. This process was repeated with and without battery support. Figure 76 and Figure 77 show the total campus demand profiles for varying amounts of real power dispatch and the resulting impact on successful microgrid islanding (0 = failure, 1 = success).

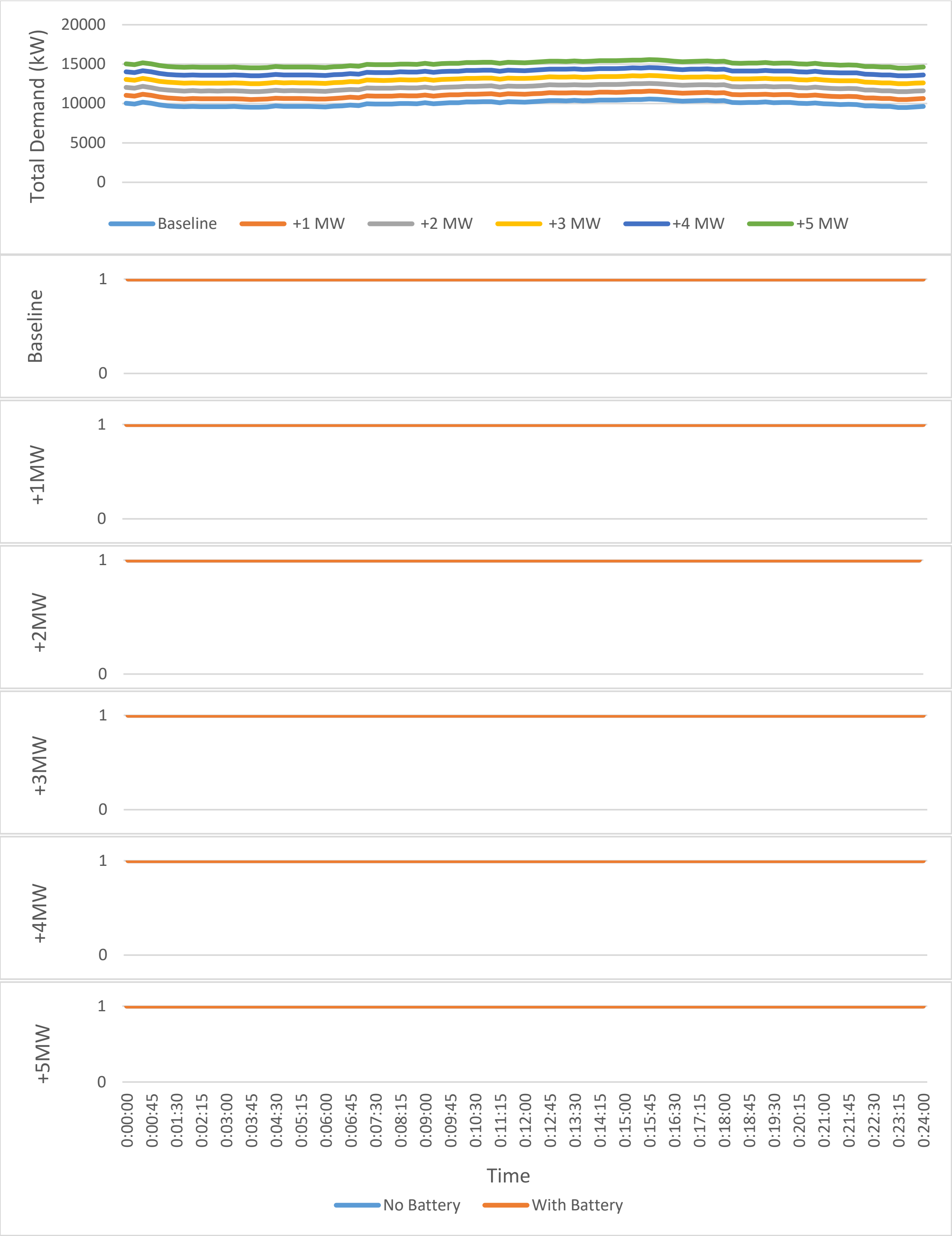

Figure 76. The impact of varying real power dispatch on seamless microgrid islanding success profile, low load conditions (9/19/2015).

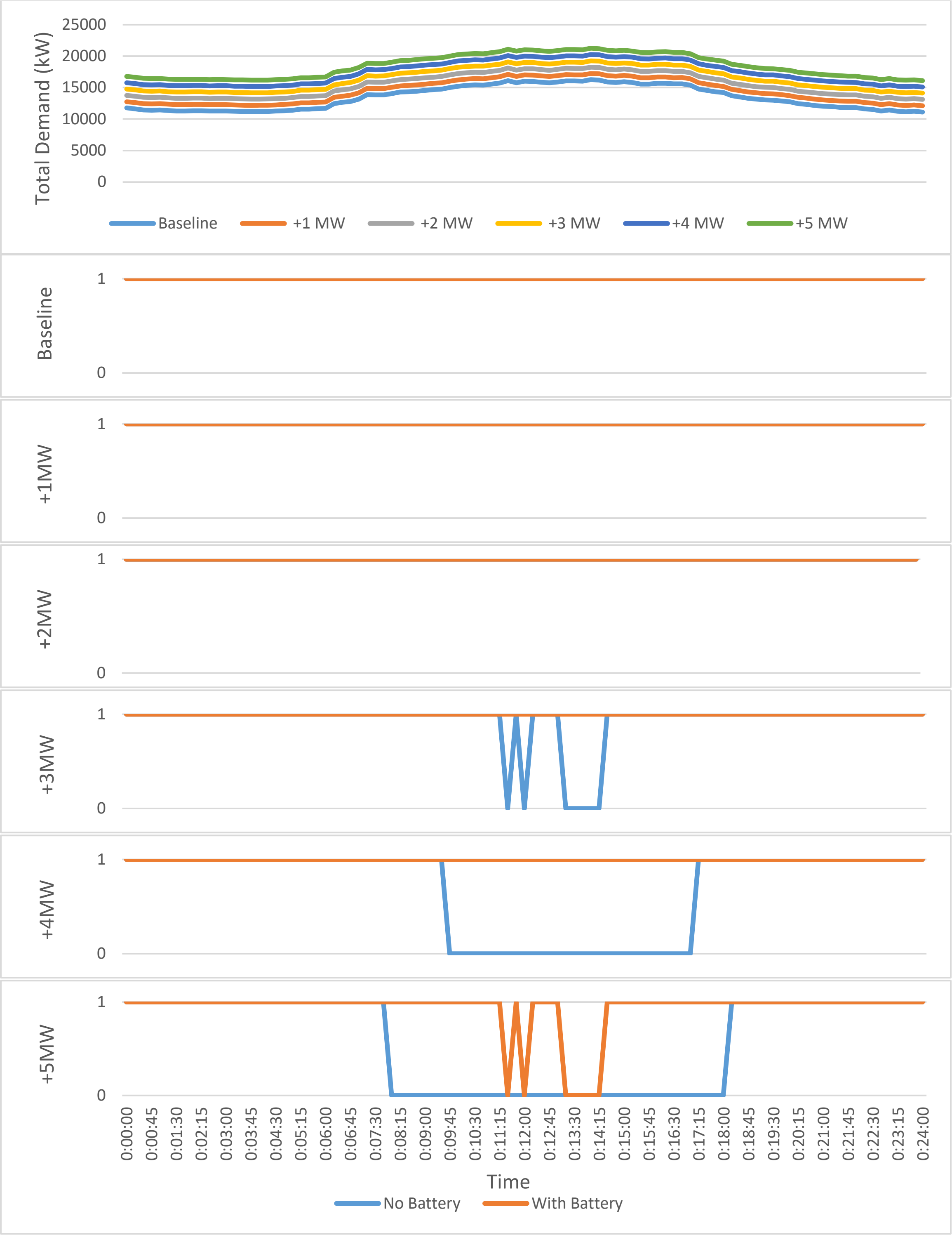

Figure 77. The impact of varying real power dispatch on seamless microgrid islanding success profile, high load conditions (9/10/2015).

As seen in the previous figures, increasing real power dispatch plays a detrimental role in the ability of a microgrid to successfully islanding during an unplanned utility outage due to either excessive voltage or current transients caused by the abrupt halting of real power export or insufficient generation resources during the island transition. The addition of battery energy storage to the microgrid system resulted in a substantial improvement in islanding performance by providing fast-acting an energy buffer, but required the battery storage system to reserve sufficient charge at all times. Figure 78 summarizes the impact of real power dispatch on the islanding success rate for the low and high loading test scenarios. Results suggest that islanding failure primarily results from insufficient generation resources as opposed to sudden export loss, as all test cases were able to achieve islanding in the low loading scenario while islanding failure strongly corresponded with times during which generators were operating near maximum power limits in the high loading scenario.

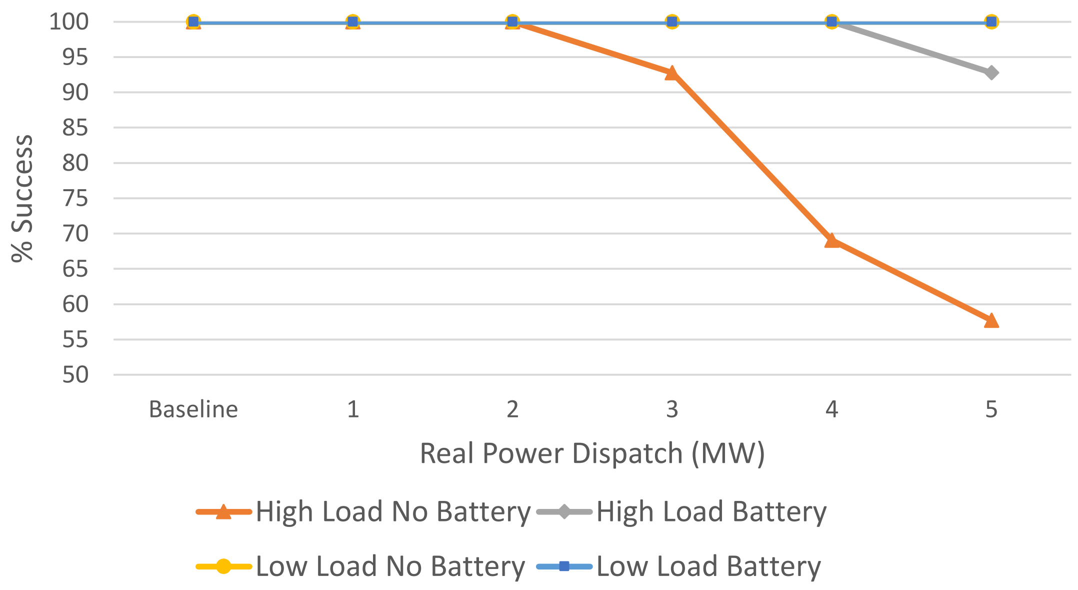

Figure 78. Impact of real power dispatch on islanding success.

6.2.2. REACTIVE POWER DISPATCH

The ability of the controller to direct generation agents to supply reactive power in response to reactive power dispatch requests was tested in the same manner as in the real power dispatch case. Requests were made via DNP3 to the controller and the resulting reactive power and voltage profiles under controlled load conditions were observed. To verify reactive power dispatch capabilities of the UCIMG controller, a series of 10 reactive power dispatch commands were issued. Results were similar to the real power dispatch case with the exceptions that a longer settling time and larger impact on bus voltages were noted. Figure 79 shows the resulting impact on the PCC line voltage as a result of reactive power dispatch.

The impact of reactive power dispatch on real-world islanding success was assesed via a series of simulations in which the gas turbine and steam turbine generators systems were each set with a real power output of 9MW and 1MW, respectively. The gas turbine reactive power output was then increased in 1MVAR increments from the baseline output.

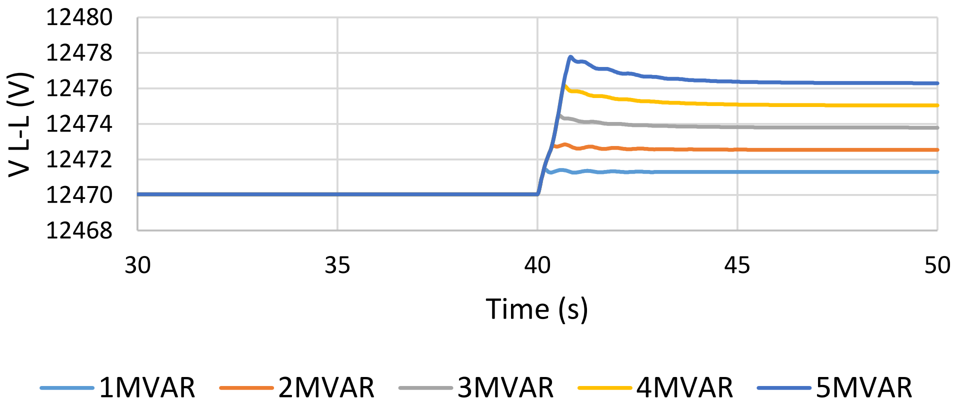

Figure 79. PCC voltage response to reactive power dispatch.

The same loading profiles were simulated as in the real power dispatch case with varying amounts of reactive power dispatch. Results indicate that reactive power dispatch marginally decreases islanding availability and a much lower impact than real power dispatch, with nearly all cases successfully transitioning to islanded mode. As both real and reactive power export results in an increase in current and voltage across the PCC and amplifies transients during PCC switching, this further reinforces evidence that the most significant source of islanding failure on the UCIMG is due to inadequate real power generation.

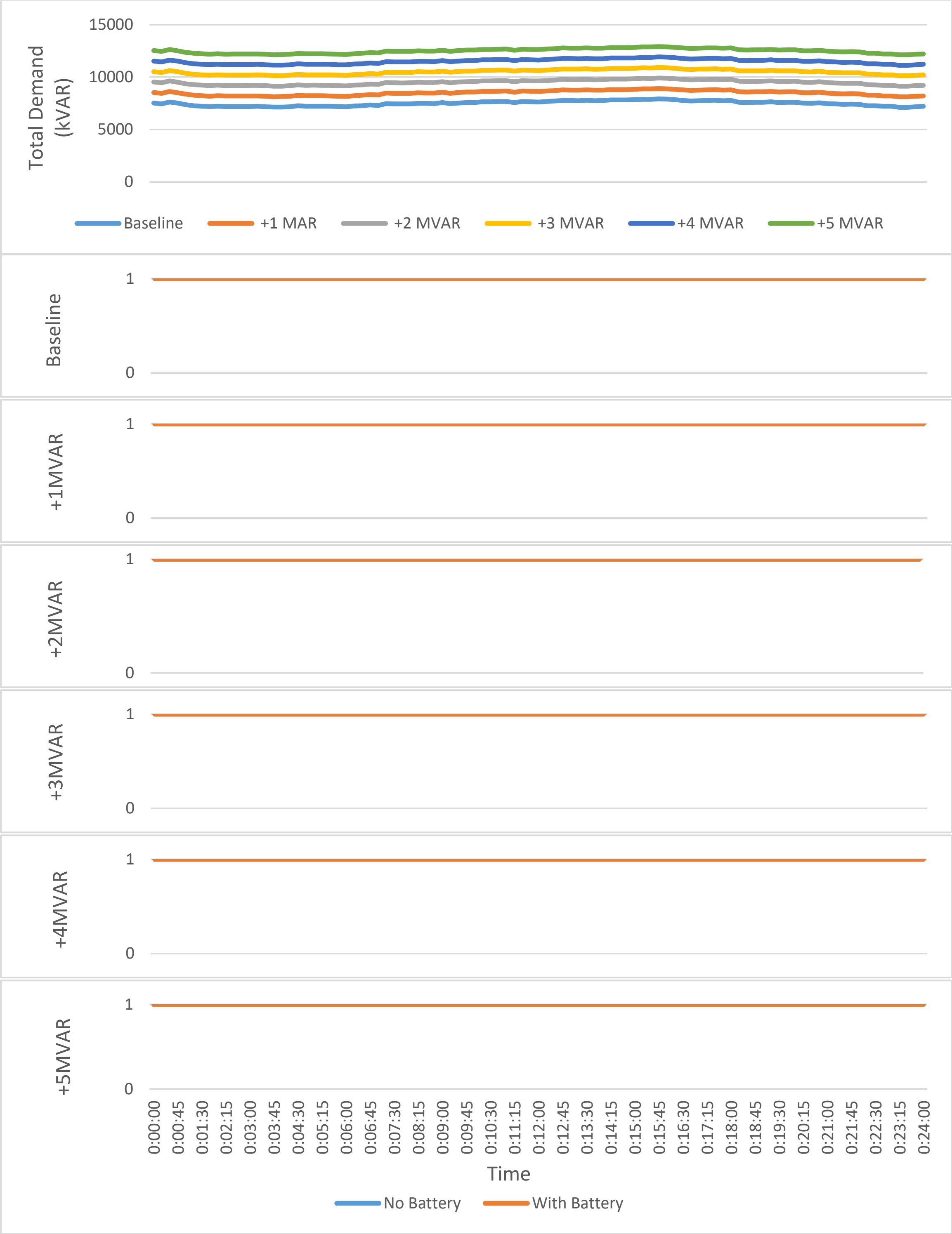

Figure 80. The impact of varying real power dispatch on seamless microgrid islanding success profile, low load conditions (9/19/2015).

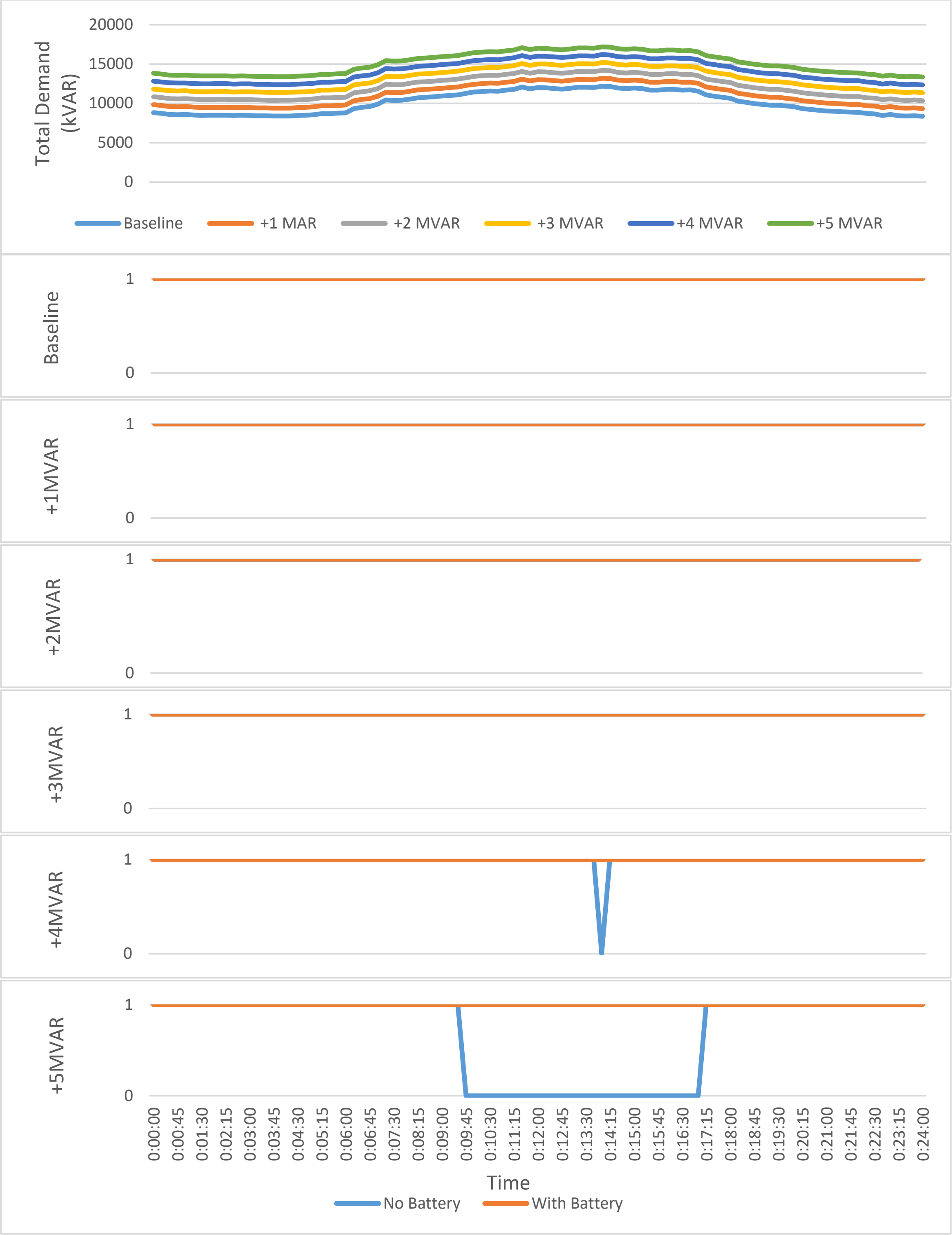

Figure 81. The impact of varying real power dispatch on seamless microgrid islanding success profile, high load conditions (9/10/2015).

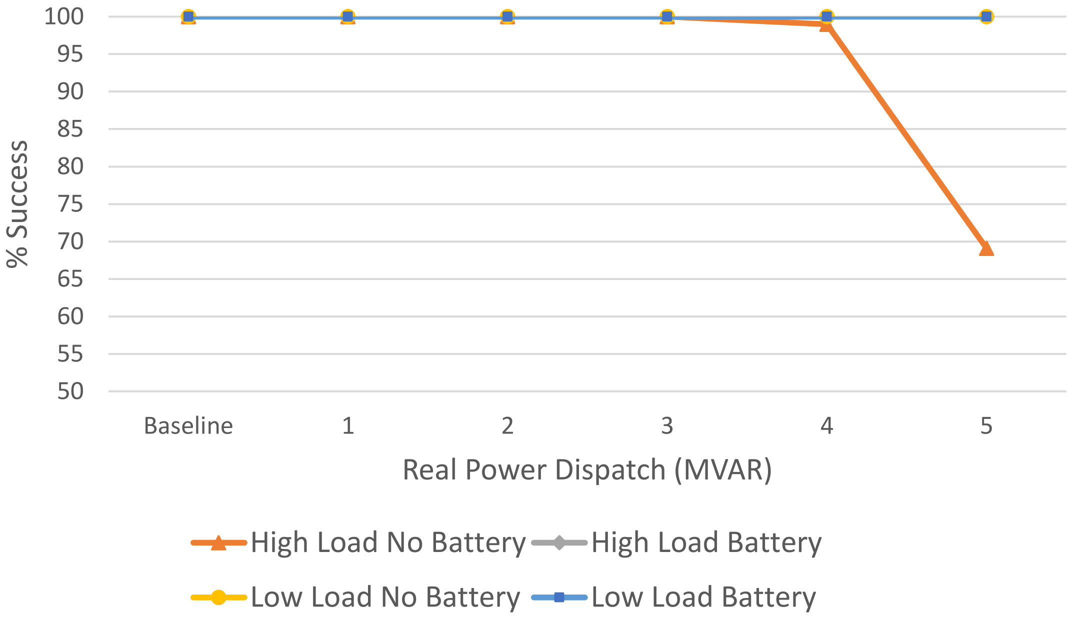

Figure 82. Impact of reactive power dispatch on islanding success.

6.2.3. FREQUENCY REGULATION

Dispatch of frequency regulation services were assessed by testing the ability of the controller to automatically adjust generator real power dispatch based on locally measured line frequency. While operating the microgrid in grid-connected mode, the substation line frequency was increased from 59.95 Hz to 60.05 Hz and ramped back down to 59.95 Hz over a period of 20 seconds in each direction with the campus load set at 10MW and 3MVAR. In these controlled tests, the gas and steam turbine generators were configured to supply 5.5MW and 4.5MW of real power, respectively. Once a frequency regulation service request was detected by the controller, the generator droop bias values were adjusted by the controller resulting in a line frequency-dependent real power dispatch response causing the grid-connected UCI generation to increase from 9MW to 11MW and decrease from 11MW to 9MW based on line frequency. Figure 83 shows the frequency regulation power output response to a controlled decrease in line frequency and Figure 84 shows the frequency regulation power output response to a controlled increase in line frequency.

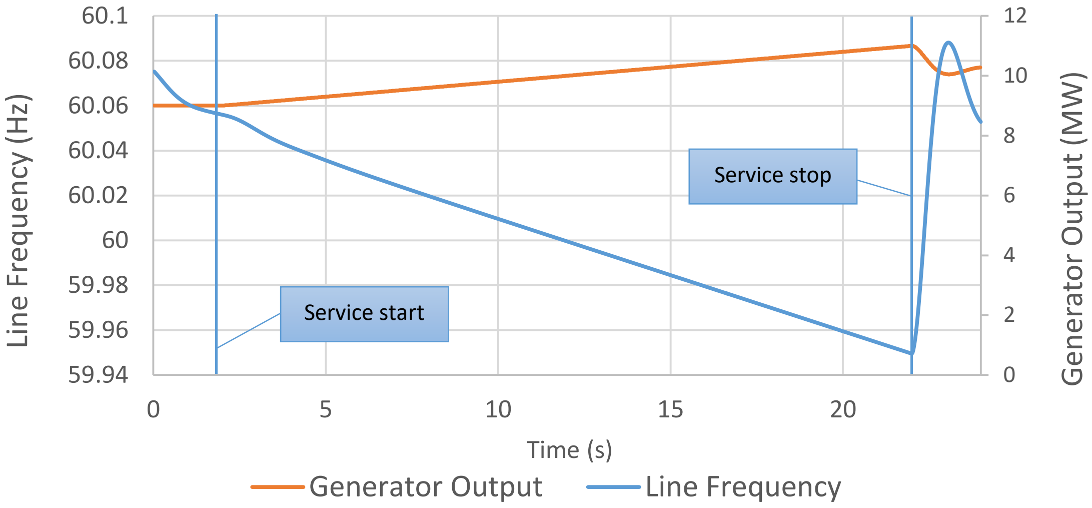

Figure 83. Frequency regulation controlled ramp-down response.

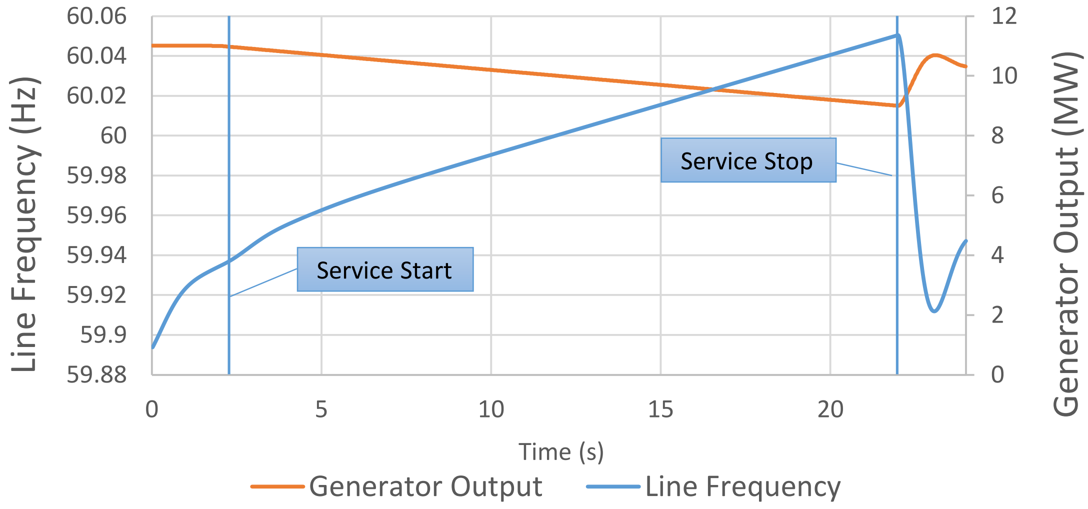

Figure 84. Frequency regulation controlled ramp-up response.

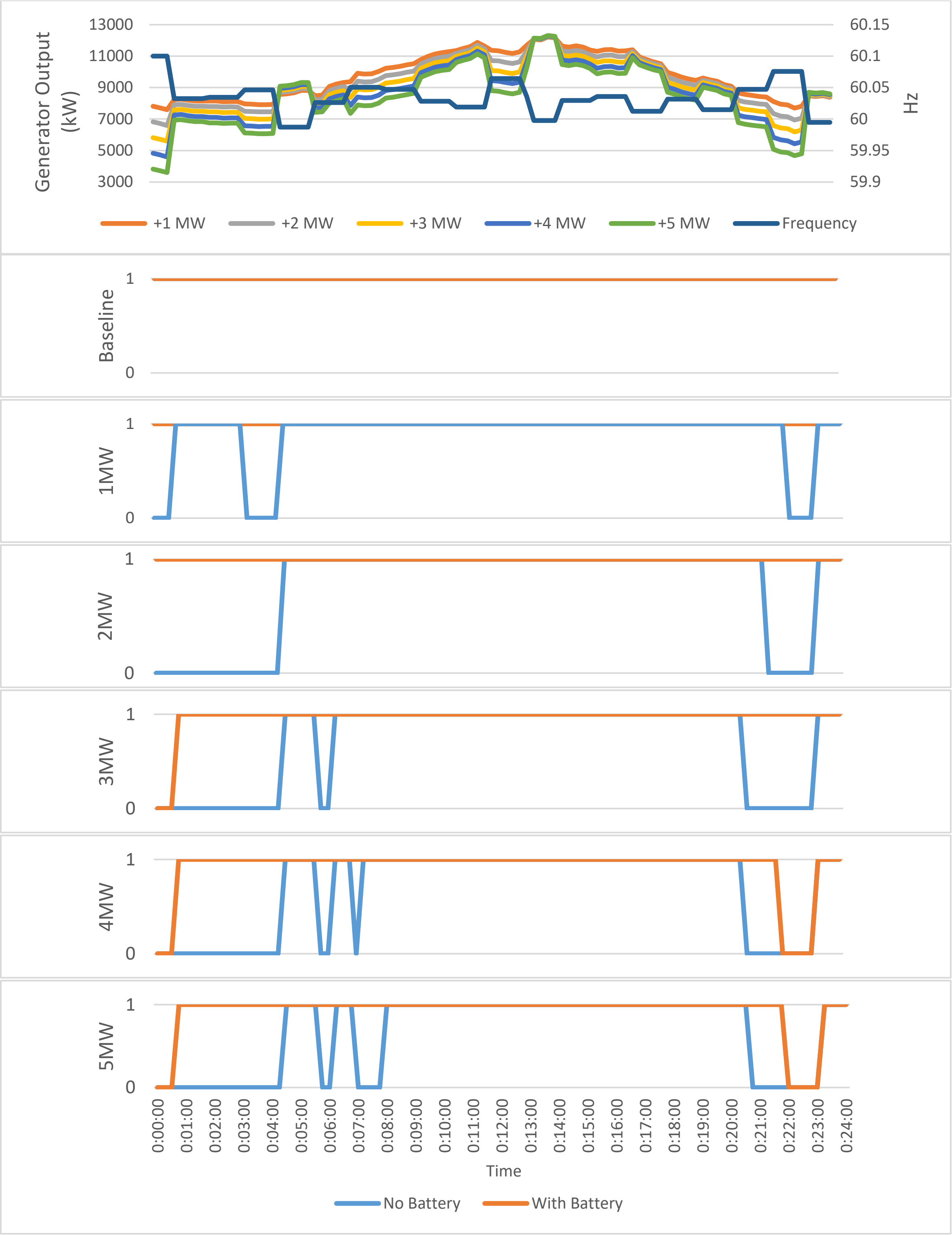

Figure 85. Frequency regulation response, low load conditions (9/19/2015).

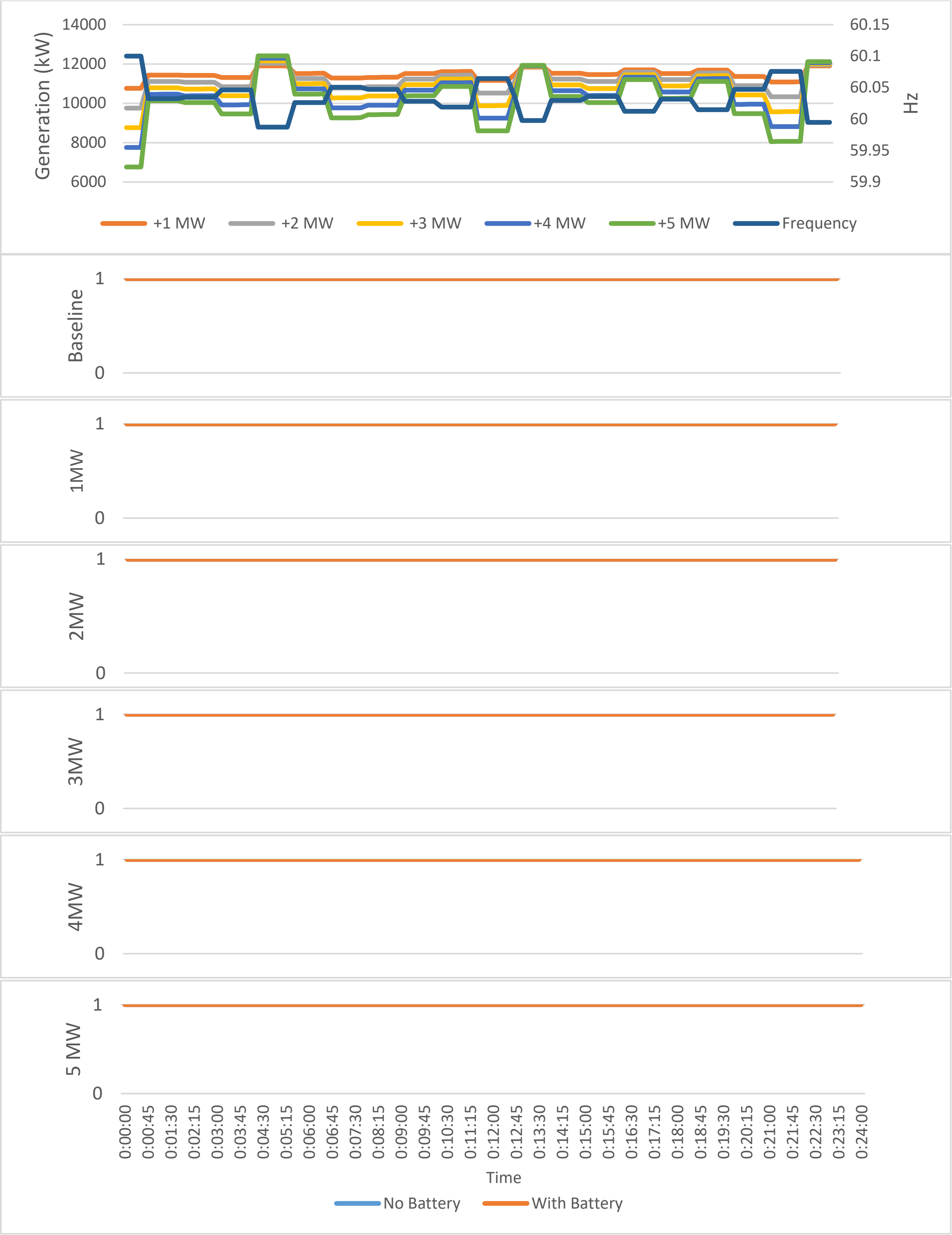

Figure 86. Frequency regulation response, high load conditions (9/10/2015).

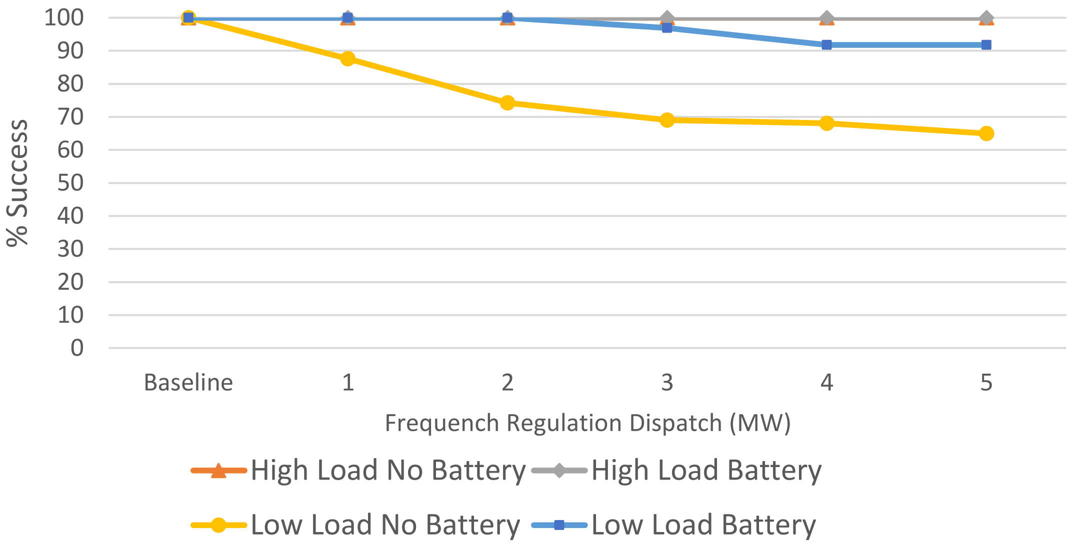

Figure 87. Impact of frequency regulation on islanding success.

6.2.4. SPINNING RESERVE

The ability of the microgrid controller to dispatch internal generation and loads as well as to preserve a prescribed amount of spinning reserve of dispatchable real power was tested and its impact on islanding availability was assessed. In response to a spinning reserve request, the controller automatically implemented any of following three control actions depending on current UCIMG operating conditions:

1) Increase generator power output to meet spinning reserve demand.
2) Discharge battery resources to meet spinning reserve demand.
3) Drop internal campus loads to meet spinning reserve.

To verify the full set of controller responses, three separate operating conditions were simulated on the HIL platform. These scenarios, listed in Table 22, simulate 1) sufficient generation resources without battery support, 2) sufficient generation resources including battery support, and 3) insufficient generation resources, requiring emergency load drop. All three scenarios assume a 1MW spinning reserve requirement with a maximum combined gas turbine (GT) and steam turbine (ST) output of 19MW.

Operating Condition	GT Output (MW)	ST Output (MW)	Campus Load (MW)	Import (MW)	Battery SOC (%)
1	12.5	5.5	18.3	0.3	0
2	13.5	5.5	19.3	0.3	75
3	13.5	5.5	19.3	0.3	10

Table 22. Spinning reserve test conditions.

Three scenarios were tested and passed with no interruption in power quality. Figure 88 through Figure 90 show the generation, load, storage, and import/export profiles for each of the test cases. Figure 88 shows the results from operating condition 1, in which the campus load was set at 18.3MW. The two generators in this case were supplying a combined power output of 18.0MW prior to the dispatch event. Upon receiving the dispatch command, the controller discerned that that was sufficient spare generation capacity in the GT and ST and increased the power output of the generation assets without affecting the operation of any remaining components within the UCIMG.

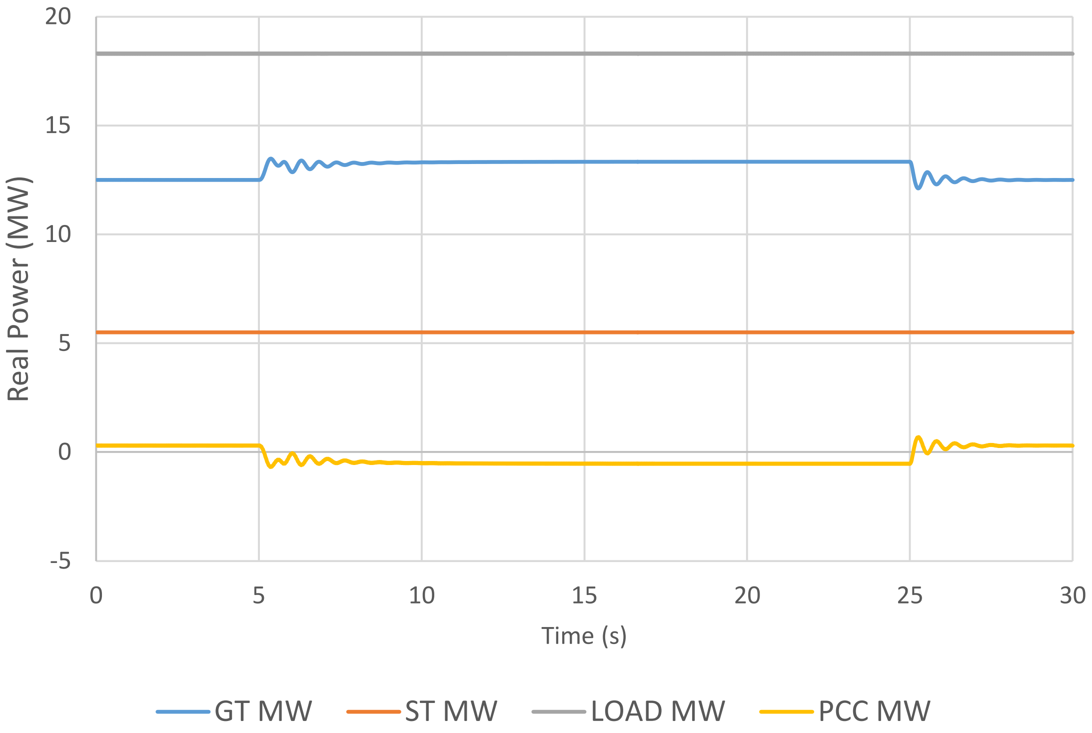

Figure 88. Microgrid response to spinning reserve condition 1 - sufficient generation resources without battery support.

The controller response to scenario 2 is shown in Figure 89. In this case, the campus load and generator output prior to the dispatch event were increased to 19.3MW and 19.0MW, respectively, and the battery energy storage system was initialized with a 75% state of charge. In this case, the controller determined that the generation resources were operating at their peak capacity and opted to command the battery energy system to discharge at a rate of 1MW to meet the spinning reserve request. Remaining components on the UCIMG are unaffected. It was observed that the presence of a battery energy storage system provided significant dampening of power oscillations from the gas turbine during significant power turn-down. It is suspected that this is attributed to the rapid dynamic response of the battery system.

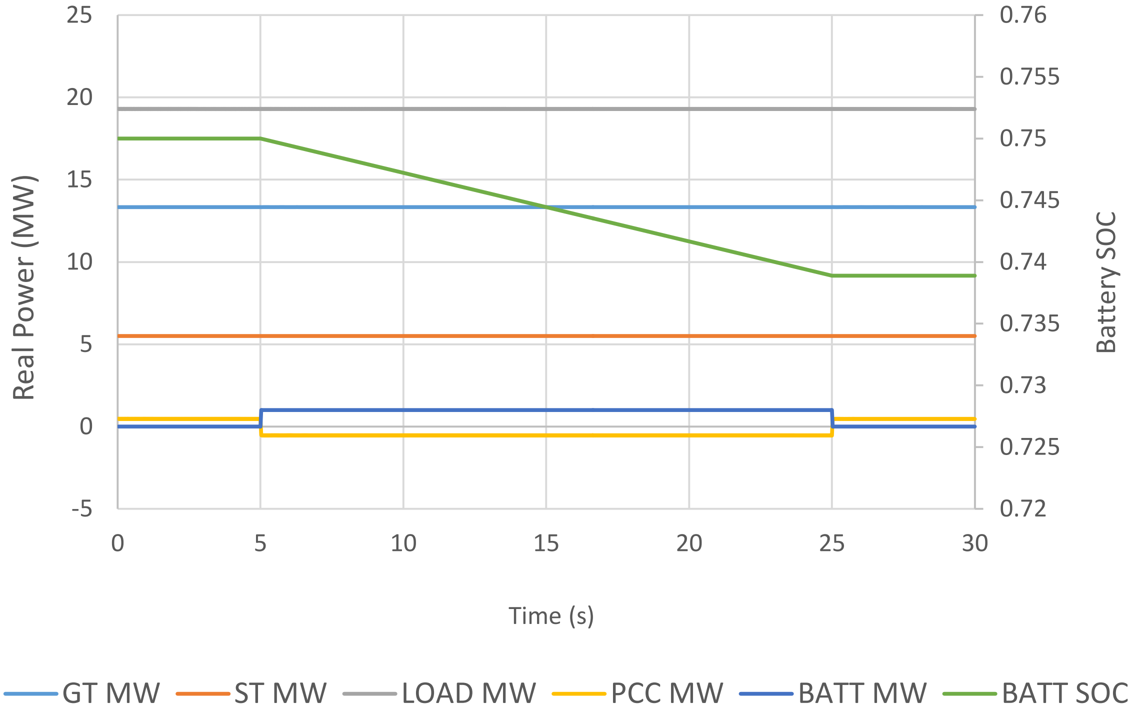

Figure 89. Microgrid response to spinning reserve condition 2 - sufficient generation resources with battery support.

The controller response to scenario 3 is shown in Figure 90. In this case, the campus load and generator output prior to the dispatch event were set at 19.3MW and 19.0MW, respectively, and the battery energy storage system was initialized with a 10% state of change as opposed to 75%. In this case, the controller determined that the generation resources were operating at their peak capacity and detected that the battery contained insufficient SOC to support spinning reserve dispatch. As a measure of last resort, the controller dropped 1MW of non-critical load to meet the spinning reserve request and issued an alert to system operators.

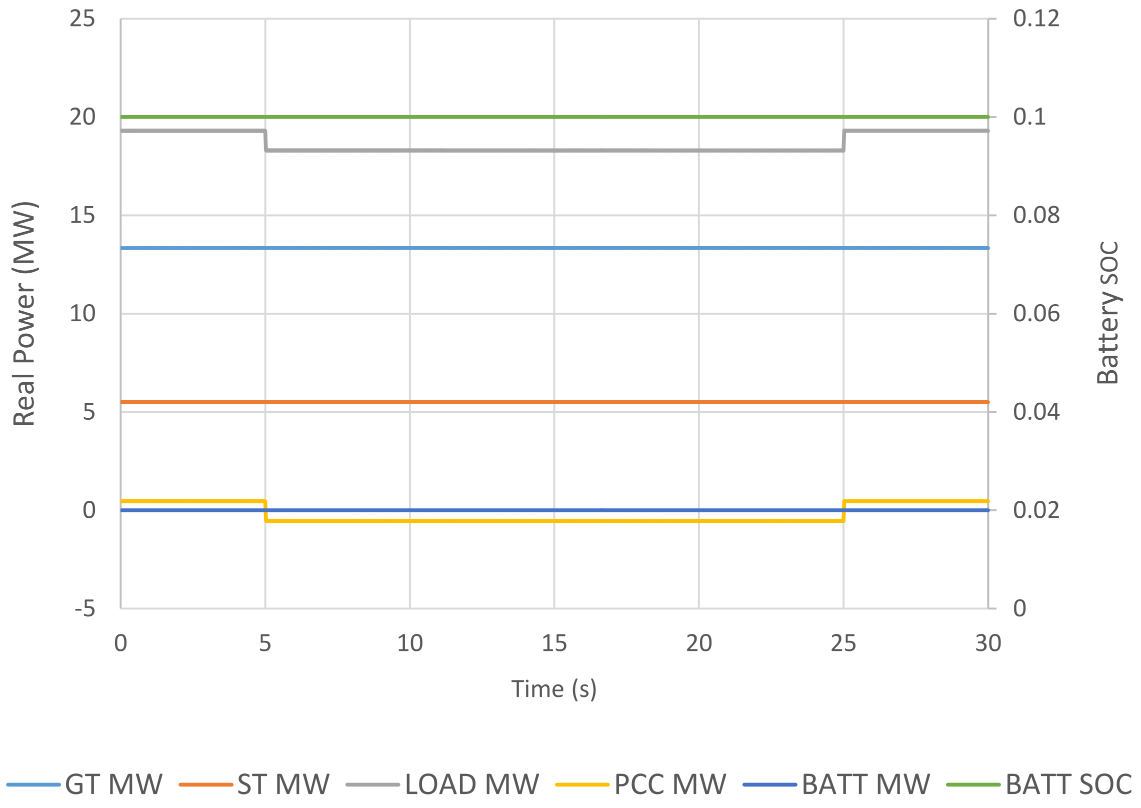

Figure 90. Microgrid response to spinning reserve condition 3 - insufficient generation resources with battery support.

The representative high and low profiles used to assess dispatch and frequency regulation were simulated with varying amounts of spinning reserve dispatch to assess the impact on microgrid islanding availability. As a spinning reserve request does not require immediate deployment of generation resources, there is little impact on the generation to load margin needed to support seamless microgrid islanding and islanding success remains relatively unchanged from the baseline. Furthermore, dispatch of spinning reserve resources may be conducted in a controlled manner as to avoid instances of inadequate generation or excessive load changes. In Figure 91, 1-5MW of spinning reserve in 1MW increments was requested throughout a 24 hour test period and the resulting impact on seamless islanding success was observed. As expected, an increase in the spinning reserve capacity had a negligible effect on islanding success and reduced the success rate by approximately 1% in the high loading scenario.

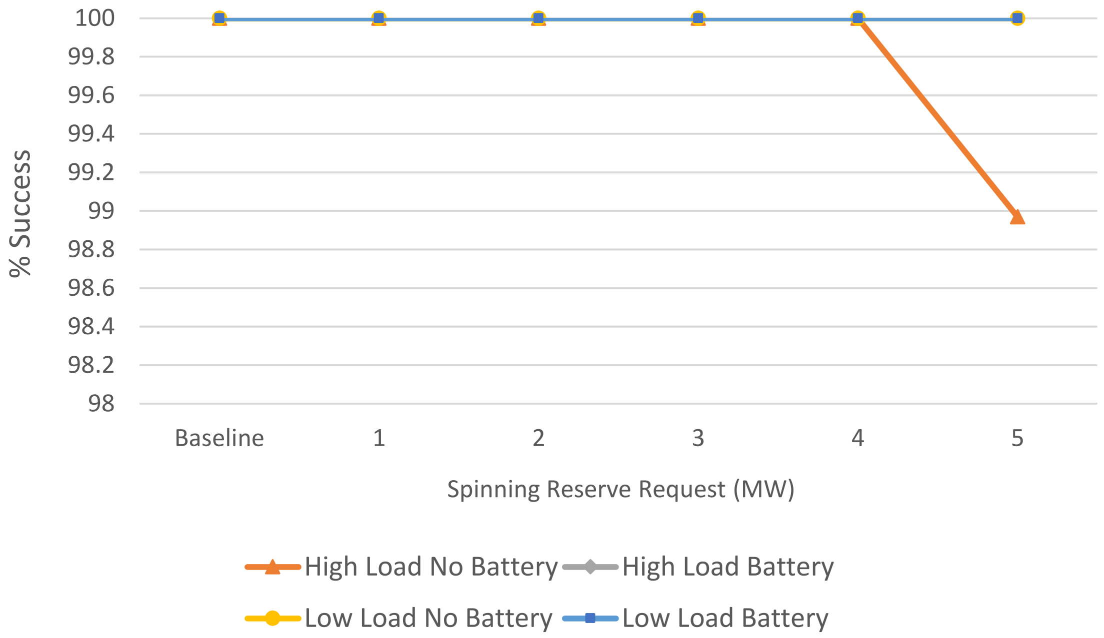

Figure 91. Impact of spinning reserve on islanding success.

6.2.5. DISCUSSION

Grid-connected microgrid ancillary services including real power dispatch, reactive power dispatch, frequency regulation, and spinning reserve were investigated in simulation and their impact on seamless microgrid islanding was assessed. In nearly all cases, the provisioning of ancillary services reduces the generation-to-load margin necessary to support reliable microgrid islanding. In the case of real power dispatch, reactive power dispatch, and spinning reserve, the most common mode of islanding failure was due to insufficient generation relative to microgrid load immediately before the islanding transition. Spinning reserve-induced failure was primarily attributed to the reverse problem, where excessive pre-island turbine turn-down used to reduce line over-frequency resulted in generator shutdown upon an islanding transition. In all cases the deployment of an inverter-coupled battery energy storage system increased the islanding success rate by and also served to greatly reduce islanding-induced power and voltage oscillations. Comparison of various ancillary services impact on islanding success and the maximum allowable dispatch limits on the UCIMG are presented in Figure 91 and Figure 92.

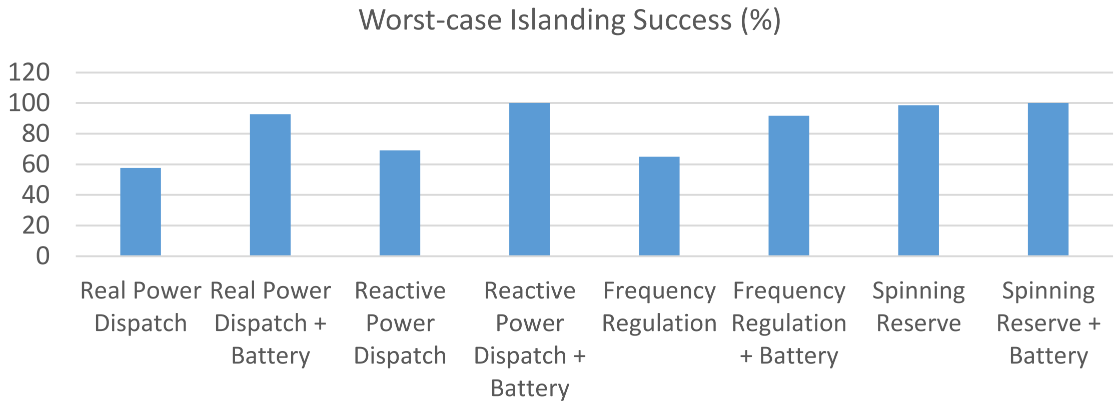

Figure 92. Impact of ancillary services on islanding success.

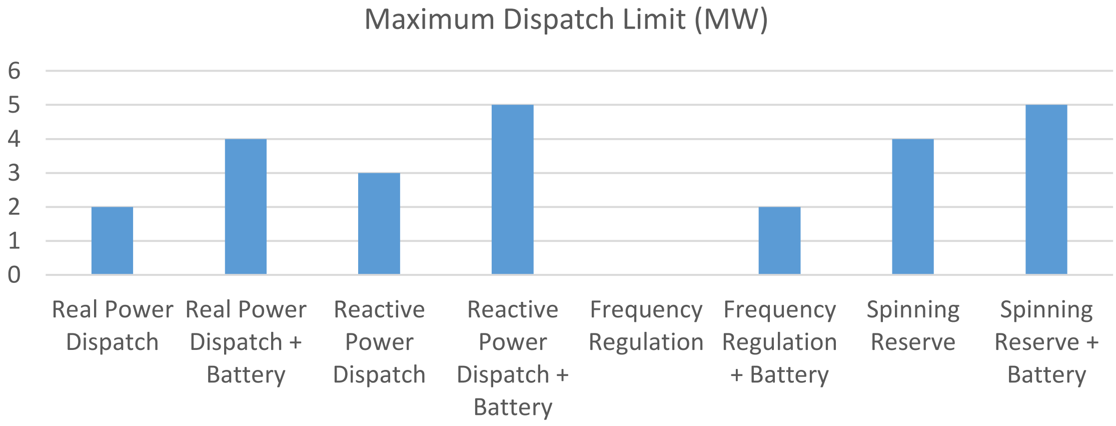

Figure 93. Maximum allowable ancillary service request while retaining island readiness.

6.3. MICROGRID ISLANDING

Model simulation results were used to guide the development a microgrid controller that allows for the continuous and optimal operation of the UCIMG through events including planned seamless microgrid islanding, unplanned seamless microgrid islanding, and utility resynchronization. In this section, microgrid simulations studies conducted with the developed controller attached to a real-time HIL platform allowed for investigation of the UCIMG islanding operational limits. Of particular interest was the classification of microgrid operating conditions into regions of safe and non-safe islanding zones. Simulation-assisted determination of these conditions and their enforcement during grid-connected operation may prove beneficial as a means to ensure continuous microgrid islanding readiness.

6.3.1. PLANNED SEAMLESS ISLANDING

Planned islanding events have been simulated with the following generation and load combinations: (10.3MW load, 10MW generation), (19.3MW load, 19MW generation), and (20.3MW load, 19MW generation). These cases are summarized in Table 23. Upon a planned seamless islanding request, the controller adjusts generation resources to achieve zero net power flow through the PCC. Once established, an “island ready” signal is issued to the operator and islanding is allowed to proceed. In the following case studies, the main utility breaker is opened at t = 40 s with zero import through the PCC. In the 19.3MW and 20.3MW load cases, 0.3MW and 1.3MW, respectively, of non-critical load are dropped prior to islanding to maintain generation balance. Results are identical in both loading cases as the microgrid controller drops non-critical loads to bring the PCC net power flow to zero well before allowing the PCC breaker to open. In all cases disconnection of the microgrid while grid-connected appeared to have negligible effect on line voltage, line frequency, generator output, and generator current transients as the use of a local BC to actuate the opening of the PCC breaker allows for switching at a zero-current crossing, reducing any asymmetrical transient currents that would otherwise be contributed by the untimed opening of the breaker.

Operating Condition	GT Output (MW)	ST Output (MW)	Campus Load (MW)	Import (MW)
1	5.5	4.5	10.3	0.3
2	13.5	5.5	19.3	0.3
3	13.5	5.5	20.3	1.3

Table 23. Planned seamless islanding test cases.

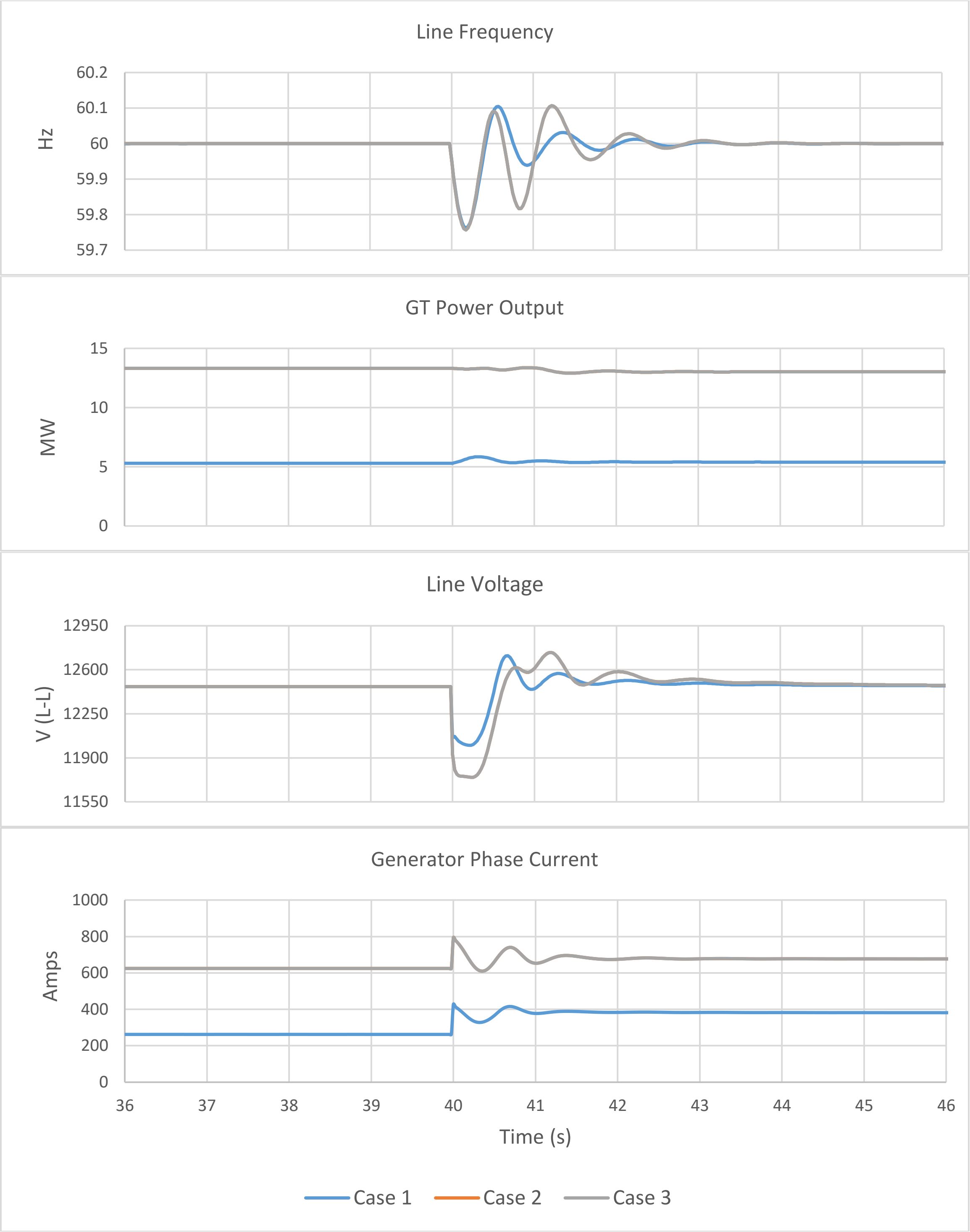

Figure 94. Planned seamless islanding response.

6.3.2. UNPLANNED SEAMLESS ISLANDING

Unplanned islanding differs from planned islanding in that there is often inadequate time to coordinate generation and load assets to achieve a system power balance. Should the PCC breaker open under a mismatch condition, the resulting temporary over- or under-generation may result in excessive frequency and voltage deviations, potentially resulting in a microgrid blackout. In these series of tests, an unplanned island transition, triggered either manually or by a three-phase utility fault, is simulated with varying amounts of utility import. The impact of communications latency and generation-to-load mismatch are also investigated, and the concept of a microgrid “safe islanding zone” is established.

6.3.2.1. MANUAL- VS. FAULT-INITIATED ISLANDING

The following graphs show the direct comparison of manual and utility fault-triggered islanding responses. Several points of interest are revealed in these analyses: First, in manually triggered cases, the amplitude and duration of generation output transients are much larger than in the fault-initiated cases in the import and export scenarios. This may seem counterintuitive as system faults are known for injecting large line transients. However, consideration of the generator current profile transients, which are much larger in the fault-initiated cases, suggests that the presence of a utility fault provides a temporary path for fault energy to leave the microgrid system, rapidly decreasing the inertial energy stored in rotating synchronous generators resulting in the reduced duration of power transients. This does come, however, at an increased risk of triggering a voltage or overcurrent protective relay, potentially de-energizing the entire system. In the manually-initiated case, the synchronous generators must sink excess stored energy through microgrid loads, resulting in a longer system stabilization time. This can be alleviated in the manual case by temporarily switching on large microgrid loads or rapidly turning down generation assets immediately before opening the PCC breaker, as even a manually triggered unplanned event requires an operator initialized signal. Simulation results for generator output, line voltage, and generator current for generation-matched, export, and import conditions are shown in Figure 95, Figure 96, and Figure 97, respectively.

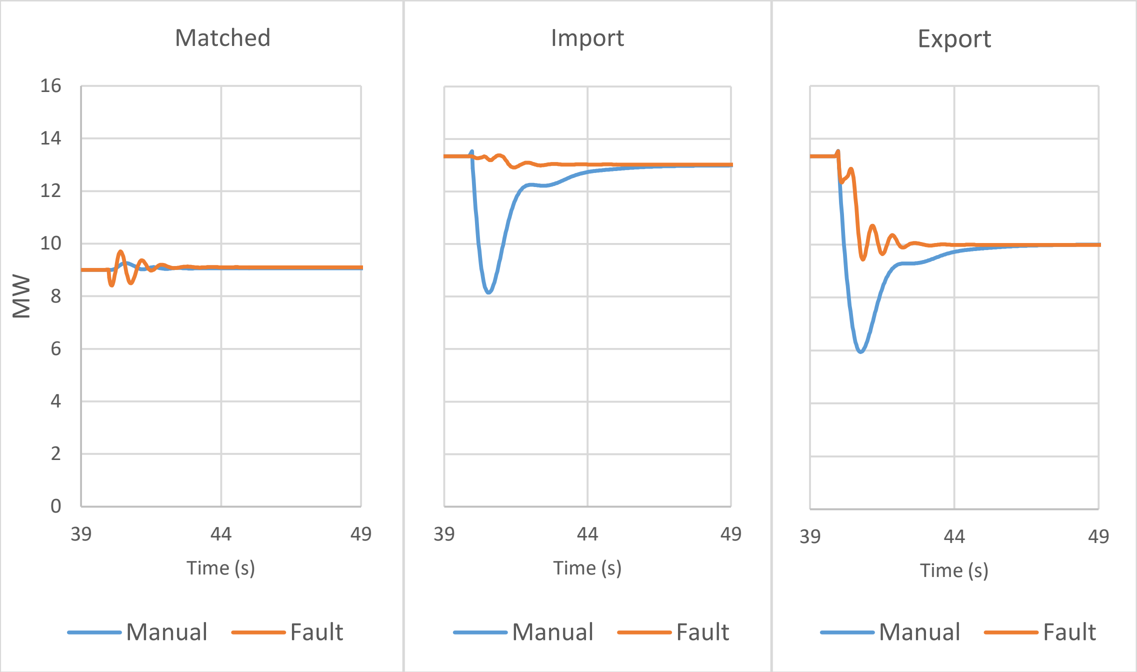

Figure 95. Generation output response for manual- and fault-initiated unplanned islanding.

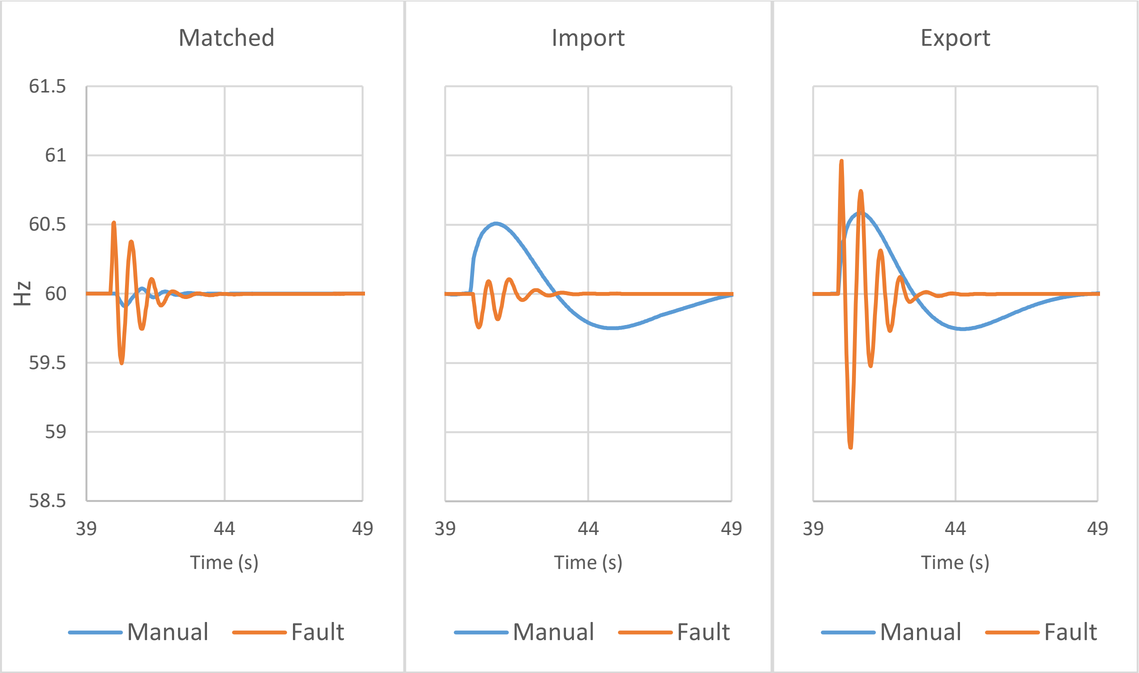

Figure 96. Line frequency response for manual- and fault-initiated unplanned islanding.

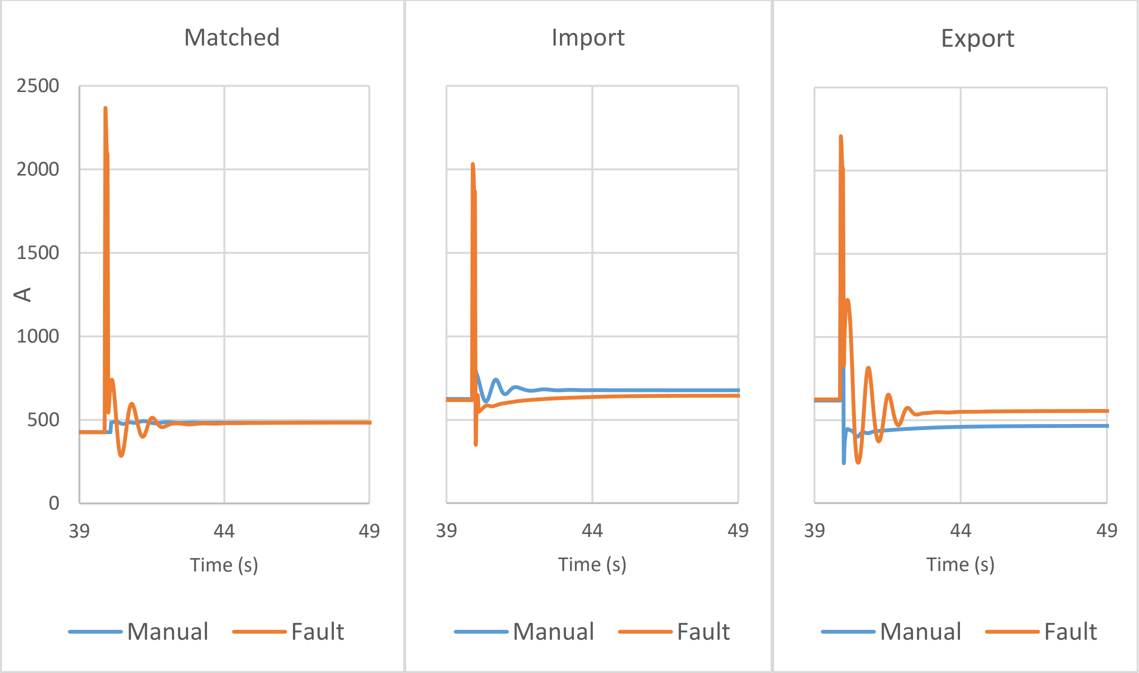

Figure 97. Generator current response for manual- and fault-initiated unplanned islanding.

6.3.2.2. COMMUNICATIONS LATENCY

While the microgrid controller was designed with autonomous control elements installed in close proximity to controlled devices i.e., BCs, LC's, SC's and GCs, the impact of unforeseen communications delays may prove detrimental to successful microgrid islanding. To investigate their potential impact, an artificial communication latency was introduced in HIL simulation between the controller and the OPAL-RT platform to determine the maximum permissible communications latency before the performance of the system was impacted (mean failure rate increased by 1 standard deviation above baseline).

Source	MMC	OPAL	MMC	MMC	MMC	MMC	MMC
Dest.	OPAL	MMC	BC	MMC	RTAC	GMC	CP
Channel	DIO	DIO	61850	TCP/IP	61850	61850	61850
Limit	127ms	176ms	N/A	N/A	N/A	N/A	203ms

Table 24. Maximum allowable communications latencies.

It was noted in this test that for many communications pathways, the system could tolerate any amount of latency including loss of the channel itself. This is due to the autonomous operation capabilities of the microgrid controller components, in which the loss of a direct communication channel results in the devices operating based on the last known good configuration. The only latency-sensitive pathways were found to be the circuit breaker control lines which provide time-critical circuit breaker operation signals. The results are summarized in Table 24.

6.3.2.3. SAFE-ISLANDING ZONE

In addition to the limits on real and reactive power flow through the microgrid PCC established by the grid-connected ancillary services results, operation of the microgrid PCC in response to an islanding event may trigger protective relays within the microgrid system. To complete the assessment of microgrid islanding success, simulated line frequency, generator current, and bus voltage profiles were compared against protective relay response curves for the various instantaneous overcurrent, time-delay overcurrent, phase current unbalance, under-over voltage, and over-under frequency, and rate of change of frequency devices installed on the UCIMG. Several of these settings listed in Table 25. This allowed for identification of additional microgrid operating scenarios that would result in a failed islanding transition. Repeating this process with variations in generator and load real and reactive power in simulation allowed for determination of a range of pre-island conditions capable of consistent islanding capabilities. This range, referred to as the “safe islanding zone” was used to guide microgrid operations to ensure an island-ready system. Figure 98 shows the line frequency response to varying levels of real and reactive power import pre-island, with simulations that exceeded protective device limits highlighted.

Device	Phase Setting	Ground Setting
GEN-CTG-01 RELAY	Phase OC Pickup 1.29 (1290A) ANSI Ext Inverse 1.5; 1 High-Set OC Pickup 5.1 (5100A) High-Set OC Delay 0.05	-
GEN-STG-01 RELAY	Phase OC Pickup 1.4 (560A) ANSI Ext Inverse 2; 1 High-Set OC Pickup 15 (6000A) High-Set OC Delay 0.01	-
UC-1 RELAY	Tap (1-12A) 6 (720A) Time Dial (0.5-11) 5.0	Tap (1-12A) 1.5 (180A) Time Dial (0.5-11) 4.0
UC-2 RELAY	Tap (1-12A) 6 (720A) Time Dial (0.5-11) 5.0	Tap (1-12A) 1.5 (180A) Time Dial (0.5-11) 4.0
UC-3 RELAY	Tap (1-12A) 6 (720A) Time Dial (0.5-11) 5.0	Tap (1-12A) 1.5 (180A) Time Dial (0.5-11) 4.0
UC-4 RELAY	Tap (1-12A) 8 (1920A) Time Dial (0.5-11) 2.5	Tap (1-12A) 1 (240A) Time Dial (0.5-11) 4.0
UC-5 RELAY	Tap (1-12A) 6 (720A) Time Dial (0.5-11) 5.0	Tap (1-12A) 1.5 (180A) Time Dial (0.5-11) 4.0
UC-6 RELAY	Tap (1-12A) 6 (720A) Time Dial (0.5-11) 5.0	Tap (1-12A) 1.5 (180A) Time Dial (0.5-11) 4.0
UC-7 RELAY	Tap (1-12A) 8 (1920A) Time Dial (0.5-11) 2.5	Tap (1-12A) 1 (240A) Time Dial (0.5-11) 4.0
UC-8 RELAY	Tap (1-12A) 6 (720A) Time Dial (0.5-11) 5.0	Tap (1-12A) 1.5 (180A) Time Dial (0.5-11) 4.0
UC-9 RELAY	Tap (1-12A) 6 (720A) Time Dial (0.5-11) 5.0	Tap (1-12A) 1.5 (180A) Time Dial (0.5-11) 4.0
UC-10 RELAY	Tap (1-12A) 6 (720A) Time Dial (0.5-11) 5.0	Tap (1-12A) 1.5 (180A) Time Dial (0.5-11) 4.0

Table 25. Select UCIMG protective device settings.

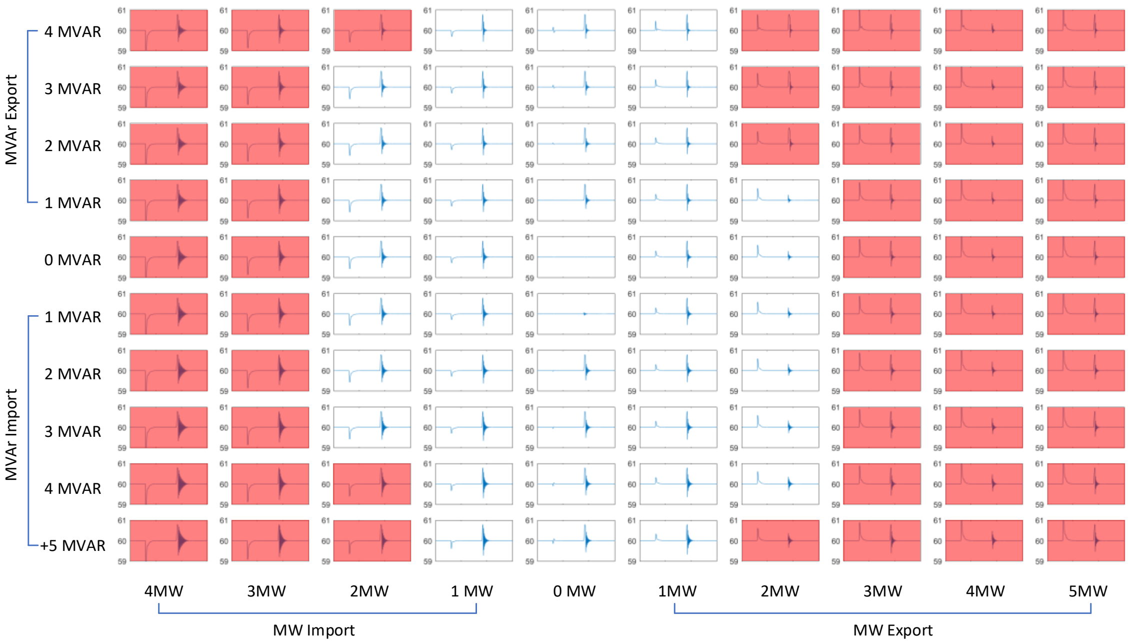

Figure 98. Line frequency induced safe islanding zone.

6.3.3. DISCUSSION

Unplanned islanding scenarios are shown to be more demanding compared to planned islanding scenarios, with failure modes potentially caused by protective devices installed within the microgrid itself. However, it is possible to predetermine a safe islanding zone for any combination of microgrid load and utility import/export. Research on the UCIMG suggests that the safe islanding zone is for the UCIMG is reached at approximately 2.5MW real power import demand. Interestingly, this coincides with the real power import/export limits established in the planned islanding studies. The safe islanding zone is found to far less sensitive to reactive power import than real power import with real power export limits approximately twice that of reactive power import limits. Among phase and ground current differential, phase instantaneous and time delay overcurrent, phase unbalance, under/overvoltage, and over/under/rate of change frequency protective elements, simulations suggest instantaneous overcurrent and reverse power/negative sequence detection play the most critical role in determining microgrid islanding success.

6.4. GRID RESYNCHRONIZATION

Grid reconnect capabilities were evaluated by interfacing the microgrid controller with an OPAL-RT HIL simulator via analog and digital control lines. Simulated microgrid line voltage and PCC current signals were buffered with power amplifiers and connected to the BC voltage and current sense terminals. Similarily, digital control lines signaling breaker status and operation were also connected in an HIL configuration. As the implementation of the grid resynchronization process within the controller operates the PCC breaker once line voltage and phase are within preset range, it was not possible to deterministically recreate grid-resynchronization profiles. However, varying pre-reconnect line voltage and line frequency scenarios were evaluated with a static load to evaluate utility reconnect success. In all cases, the controller appropriately identified voltage and frequency mismatch and controlled the generators to adjust real and reactive power output to allow for resynchronization to the simulated grid source. Once phase and voltage were matched within tolerance, the BC closed the circuit breaker with the utility, completing the resynchronization process. Figure 99 shows a typical grid resynchronization profile and Figure 100 shows the resulting profiles under low-voltage and low-frequency conditions prior to resynchronization.

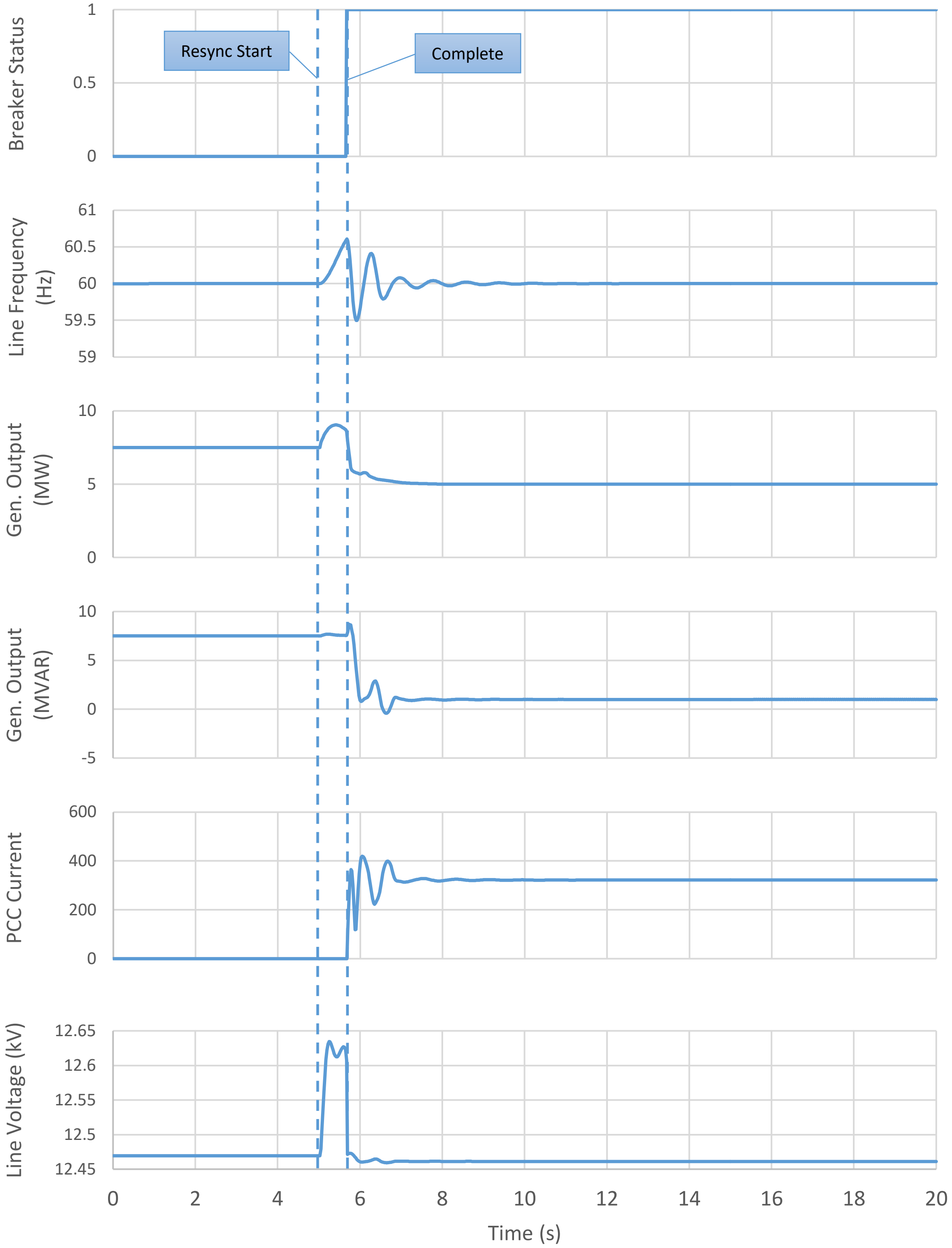

Figure 99. UCIMG grid resynchronization response.

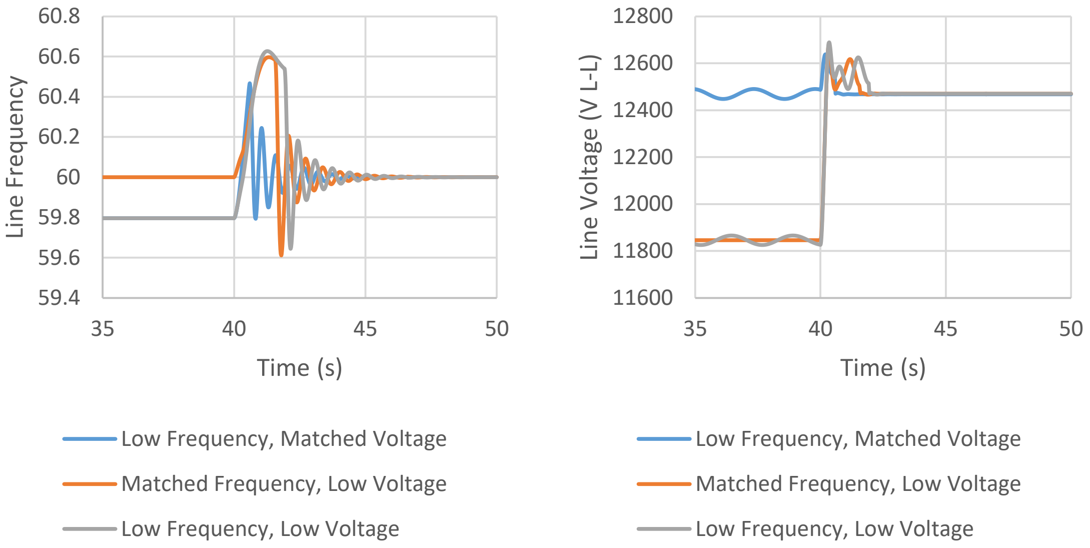

a) **b)**

Figure 100. Low voltage and low frequency resynchronization profiles.

7. CASE STUDIES

For the purposes of testing, evaluation, and verification, the microgrid controller was applied to two community-scale microgrids: the 20MW UCI Microgrid, and the 10MW UCI Medical Center Microgrid (UCIMC-MG). Both microgrid systems play an indispensable role in supplying essential services to their respective communities and serve critical loads, emphasizing the necessity and importance of a reliable and resilient power system. As these two systems are quite distinct in their generation and load features, with the UCIMG primarily powered by two large mechanical generator systems and the UCIMC-MG importing most of its power from the utility but equipped with a fuel cell cluster and several small backup diesel generators, these two case studies showcase the flexibility of the microgrid controller in its ability to accommodate a wide range of microgrid systems.

a) b)

Figure 101. Campus maps of the a) UCIMG and b) UCIMC-MG.

7.1. UNIVERSITY OF CALIFORNIA, IRVINE – MAIN CAMPUS

After the controller was successfully tested with the UCIMG EMT model running multiple scenarios in a RT-HIL environment, the controller was deployed to the UCIMG central plant and substation to demonstrate campus islanding capabilities for a 75 minute duration via a live campus islanding event. During the event, operators initiated the demonstration by manually triggering a loss of utility power via a direct transfer trip signal originating at the substation breaker which activated the controller's automated islanded-mode transition control response, separating the campus from utility power and setting the gas turbine to operate in islanded isochronous speed control mode. During the next 75 minutes, campus loads operated per business as usual but within an islanded system, with the gas turbine automatically responding to load demand changes and maintaining nominal line frequency. Several chiller motors and fans were manually brought online and disconnected from the system to test the dynamic response of the system to step loads during this period in addition to normal load demand variations. After the 75 minute island period, operators issued a grid-reconnect request command and the controller adjusted the voltage and frequency of the gas turbine generator to match utility voltage and phase angle. Once synchronized, the PCC breaker was closed by a signal from the BC and a seamless utility reconnect was achieved. The real power profiles of the UCIMG PCC and gas turbine generator during the campus islanding event is shown in Figure 102 and a corresponding sequence of events is given in Table 26.

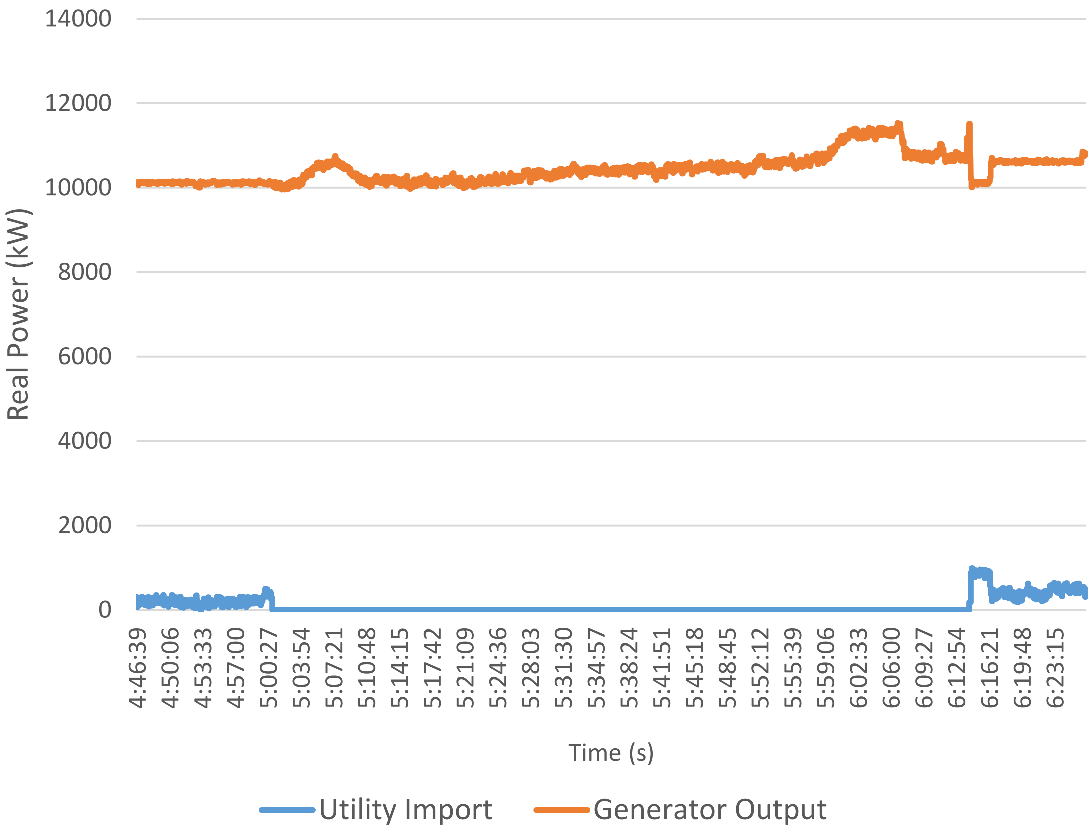

Figure 102. PCC and generation power profiles during the UCIMG islanding demonstration.

The entire demonstration was conducted on 02/21/2018 without interruption to campus power or requiring the deployment of emergency load shed. In addition to the real-time campus power monitoring system, a waveform-level oscillograph event capture system was temporarily installed to augment data collection capabilities. Closer inspection of the grid-disconnect and resynchronization stages and comparison to simulation results are provided in the following sections.

Time	Event
02:55 AM	<REDACTED> Load in campus running at 9.8MW with only Chiller No. 1 running. STG offline and disassembled with damage to diaphragm blades noted. Boilers warmed but offline. Plan to email and notify campus as well as phone SCE at 04:30. Operator will open UC66-1 breaker at 05:00. A final tailboard scheduled at 04:30.
04:30 AM	Final tailboard conducted in control room. Email notice to campus and phone call to SCE completed.
04:50 AM	Substation bus voltage observed at 12.2 kV. Import approximately 200 kW and 2200 kVAR fluctuating.
05:00 AM	UC66-1 opened from UC66-1 SEL-751 relay front panel push button. Separation appears bump-less in substation. Voltage at substation was 11.7 kV. Governor reported in isochronous mode. AVR in standard island droop mode with setpoint of 12,180 V.
05:01 AM	Three 200 HP pumps started one at a time. Frequency and voltage behavior stable. Noted brief fluctuation of frequency down to 59.95 Hz at substation.
05:15 AM	Initiated autosynch at SEL-451 relay. CTG did not appear to respond to pulses. Autosync process timed out at 300 seconds. Troubleshooting began. (For this test, the SEL-451 was configured to remain in lockout following a timeout. Resetting required use of a connected PC. The final full PowerMax configuration may allow for remote resetting in this condition.) Over the next hour campus load grew from 9.8MW to 10.8MW. At that point Chiller No. 1, 589 kW, was stopped. A persistent ‘GEN VOLT LO’ light was on SEL-451. Campus voltage at 11.7 kV is 600 V or 4.9% below SCE voltage of 12.3 kV. (Normally acceptable gen volt with respect to bus voltage to begin autosynch is 85% to 110% and acceptable reclose voltage is 95% to 105%. For this test the SEL-451 relay was configured to allow reclosing only between 0% - 5% to preclude large reactive power flows after reconnecting)
06:00 AM	Persons in Central Plant discovered Solar Turbine controls had “speed and voltage external controls” disabled at the local HMI. They took steps to enable the external controls from local HMI to allow Solar turbine to accept external pulses for speed and voltage control.
06:14 AM	Operators raised CTG voltage to its high limit, reducing voltage difference until SEL-451 GEN VOLT LO light goes out. Another attempt of autosynch at the SEL-451 relay was performed. This time the autosync was successful and UC66-1 breaker closes. Reconnection appeared bump-less in substation.
06:30 AM	Email and other required notifications of end of test were made.

Table 26. UCIMG islanding demonstration sequence of events (Schweitzer Engineering Laboratories, 2018).

7.1.1. PLANNED SEAMLESS ISLANDING

Immediately prior to the opening of the PCC breaker, the campus gas turbine was operating in grid-connected droop mode with a real power output of 10.093MW and the campus import was 284 kW. The gas turbine and battery energy storage systems were unavailable during the islanding demonstration due to planned maintenance and PV systems were inactive during the 5:00AM - 6:15AM window, leaving only the gas turbine available as the islanded microgrid generation source. Table 27 lists the microgrid operating conditions at the time of grid-disconnect. Real and reactive power from both the gas turbine generator and PCC as well as generator current were collected using a real-time monitoring system, with measurements acquired at 1 second intervals throughout the islanding event. The oscillograph system was configured to trigger upon operation of the PCC breaker. Figure 103 shows the PCC and generator real power output during the time period immediately surrounding the opening of the grid breaker.

Power System Element	Expected Value	Actual Value
UC66-1 P	0.25MW	0.22MW
UC66-1 Q	0.25MVAR	2.2MVAR
UC66-1 P + GS-1 P	10.0	10.1
UC66-1 Q + GS-1 Q	3.0	2.9
CTG mode	DROOP	DROOP
CTG mode	VAR CTRL	VAR CTRL
GS-2 CB	OPENED	OPENED
UC66-1 CB	CLOSED	CLOSED
UC66-2 CB	OPENED	OPENED
UC-23 CB	CLOSED	CLOSED
GS-7 CB	CLOSED	CLOSED

Table 27. Pre-island UCIMG conditions.

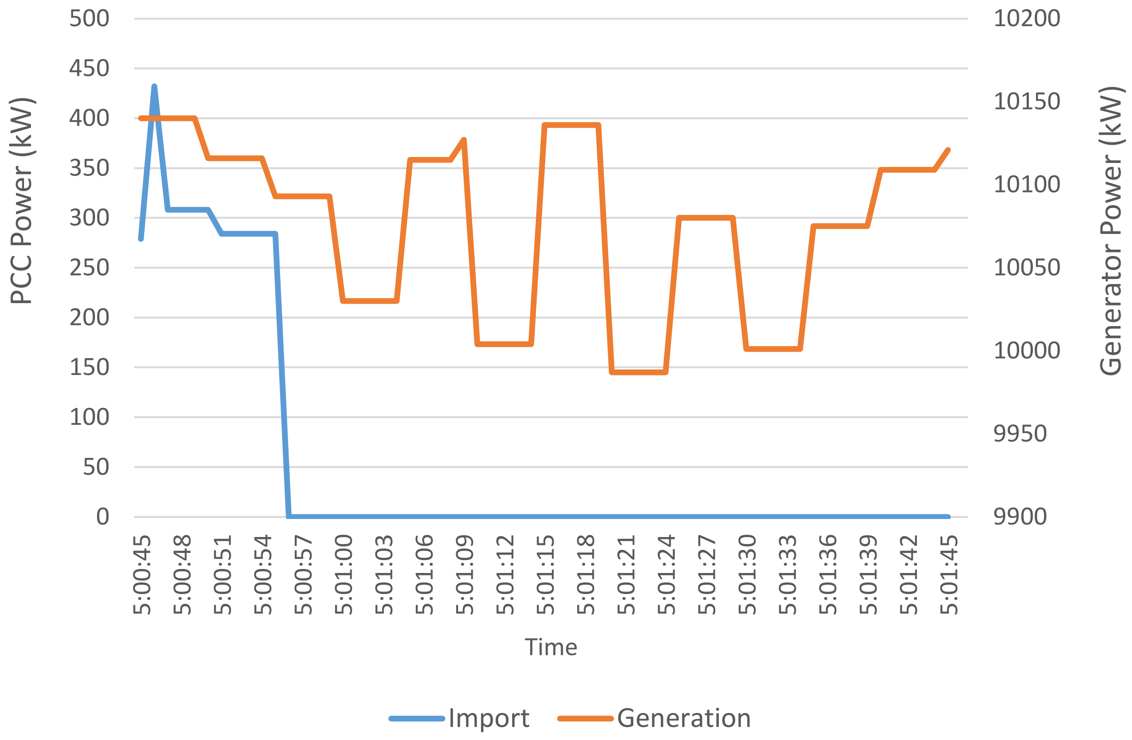

Figure 103. UCIMG import and generation real power profiles during grid disconnect.

It can be observed that upon islanding, the PCC power reduces to zero and slight power transients and oscillations were present in the system from t = 5:01:03 to 5:01:36. It is unclear if these transients were induced by the operation of the PCC breaker or from switching of the generator operation mode from droop control to isochronous speed control. Figure 104 shows a snapshot of the UCIMG operator circuit breaker status screens immediately before and after the islanding transition.

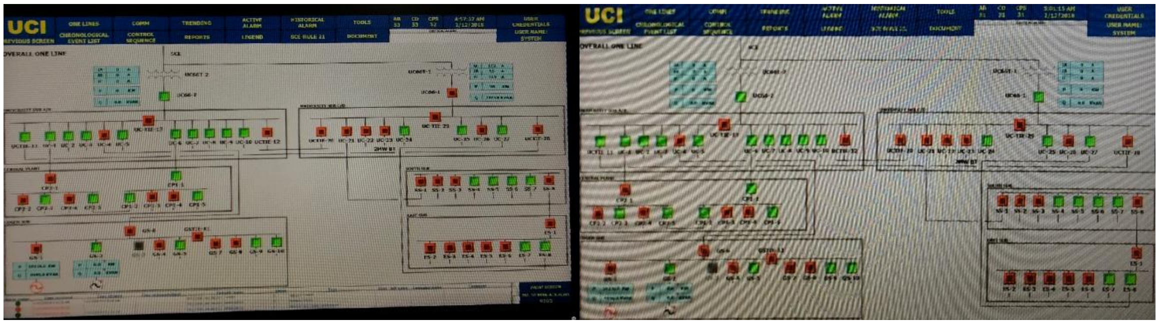

a) b)

Figure 104. Operator circuit breaker HMI: a) pre-island and b) post-island (Green = CB Closed, Red = CB Opened).

After the islanding demonstration was completed, the recorded power, voltage, and current data were replayed in simulation using the OPAL-RT HIL platform to validate model results against event measurements. Comparisons are shown in Figure 105 and shows good matching between simulated results and experimental data. Also, while the real power import during the time of grid-disconnect was low, it is of interest to consider the impact of increasing the pre-island PCC power flow on the islanding transition response. Figure 106 shows an example of the generator power profile when pre-island import power is modified. To investigate islanding success, RT-HIL simulations were again conducted while replaying the recorded islanding transition data with an additional 1-3MW of import superimposed onto the baseline. Load was uniformly distributed across all building load elements and Figure 107 shows resulting load demand and islanding success profiles from these simulations where islanding was attempted at every 1 second interval during the 75 minute dataset. The resulting impact on islanding success is summarized in the graph presented in Figure 108.

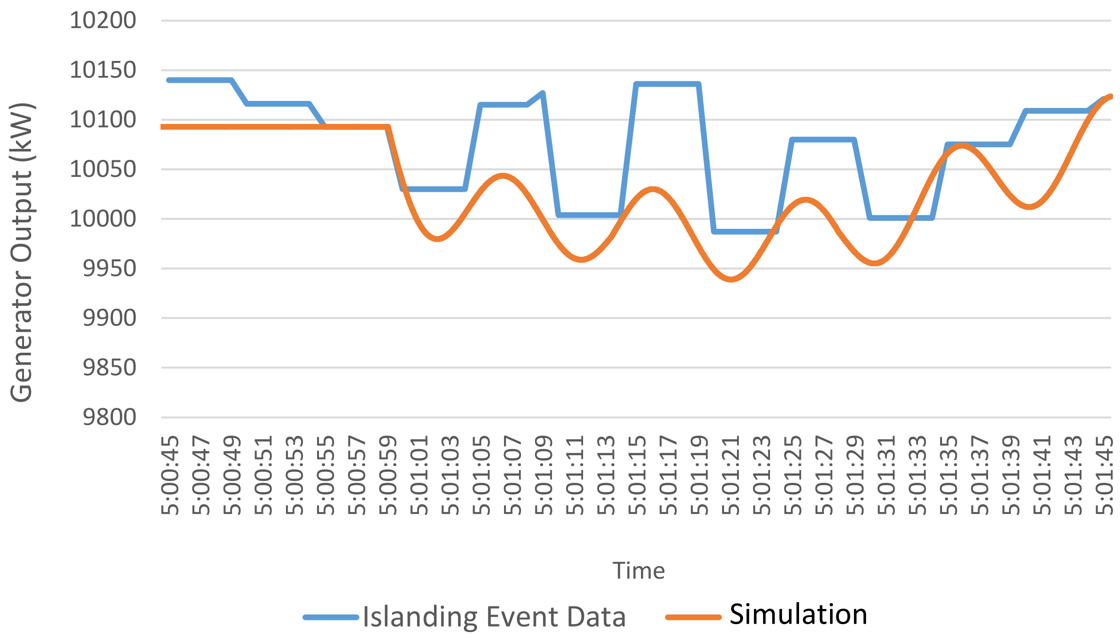

Figure 105. Comparison of simulated islanding vs. experimental data.

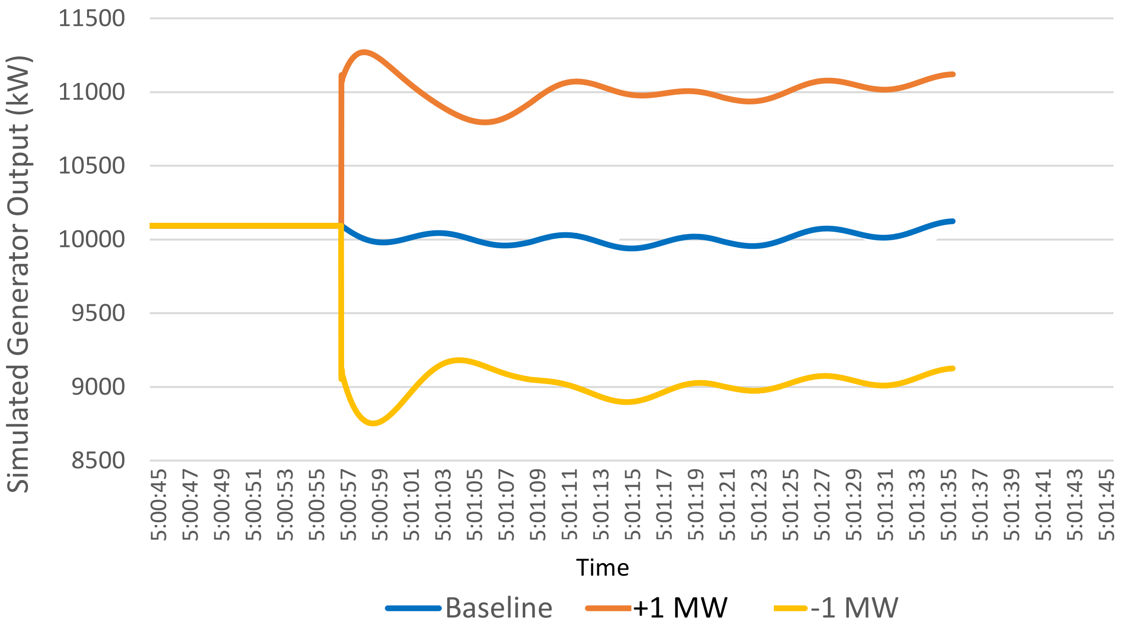

Figure 106. Effect of varying pre-island PCC real power import and export on generator output.

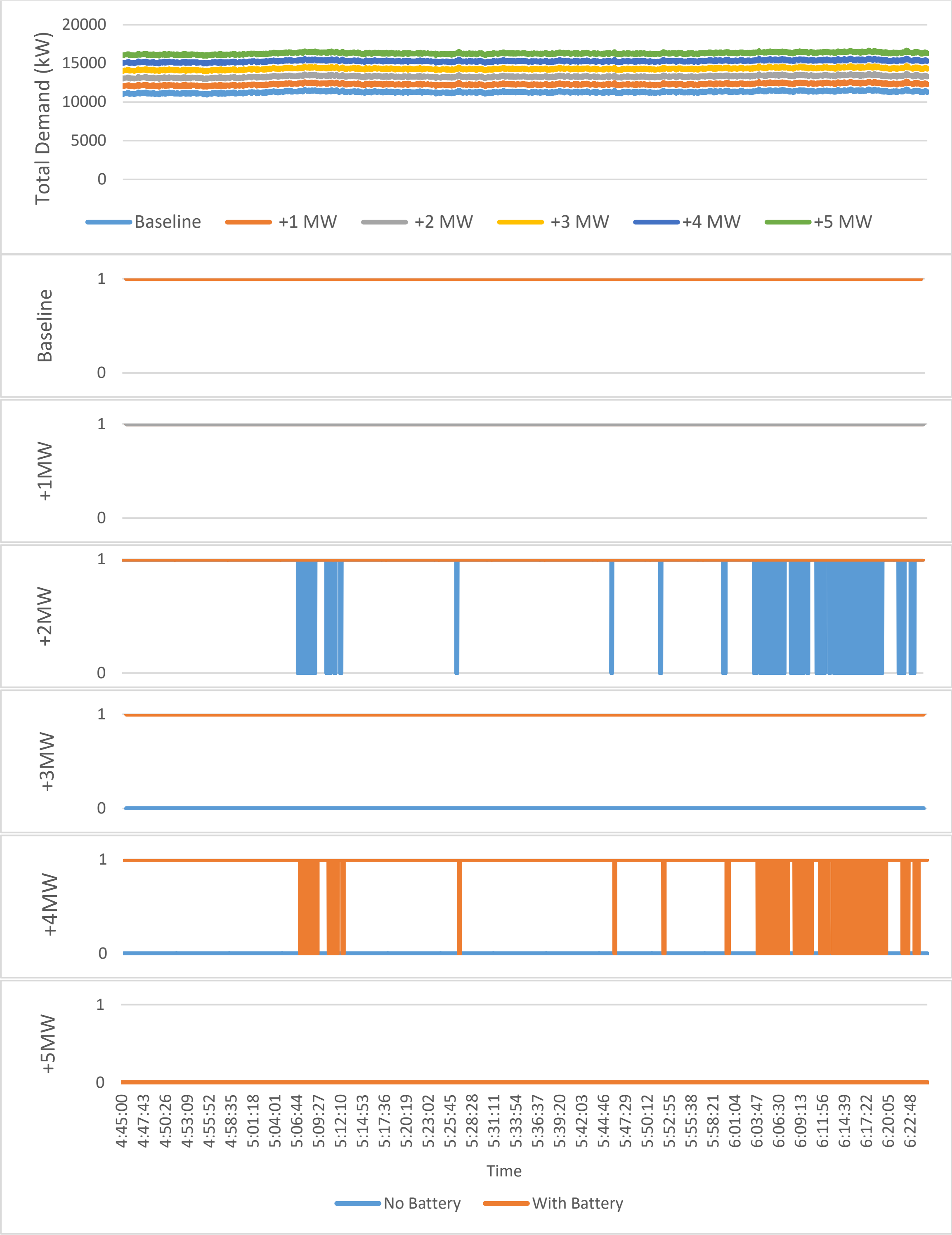

Figure 107. The impact of varying real power import on seamless microgrid islanding success, demonstration conditions (2/21/2018).

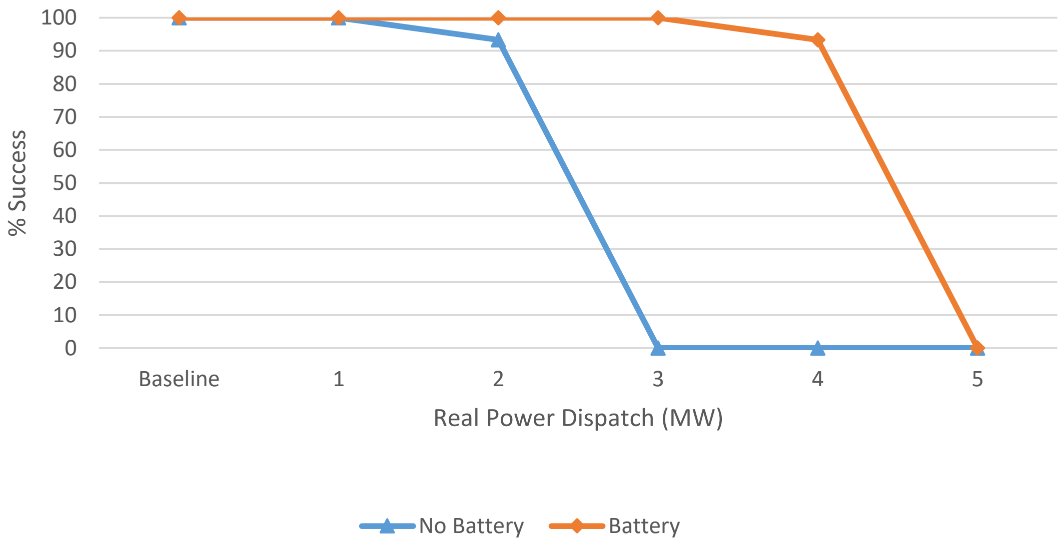

Figure 108. Impact of varying real power import on the islanding success rate.

Results suggest that with the loading and generation profiles experienced by the campus during the islanding event, the UCIMG may have supported an additional 1-2MW of electrical import while reliably supporting seamless islanding. Integration of the 2MW, 0.5MW-hr battery system would have increased this margin to 3-4MW of additional import.

7.1.2. GRID RESYNCHRONIZATION

Reconnection of the microgrid to the utility was carried out by using the automated resynchronization feature provided by the microgrid controller. Upon an operator-initiated grid-reconnect request command, the controller adjusted the generator real power output and voltage to match with the utility. PCC and generation real power profiles collected using the campus power monitoring system during the resynchronization windows are shown in Figure 109 and microgrid conditions at the beginning of the reconnect process are presented in Table 28. No noticeable power oscillations after closure of the PCC breaker were observed. After closing the PCC breaker, the generator was returned to droop control mode and set to the pre-island power output value of 10MW. As the campus load had been increasing throughout the islanding demonstration, the resulting in a utility import after closure of the PCC breaker was approximately 900kW.

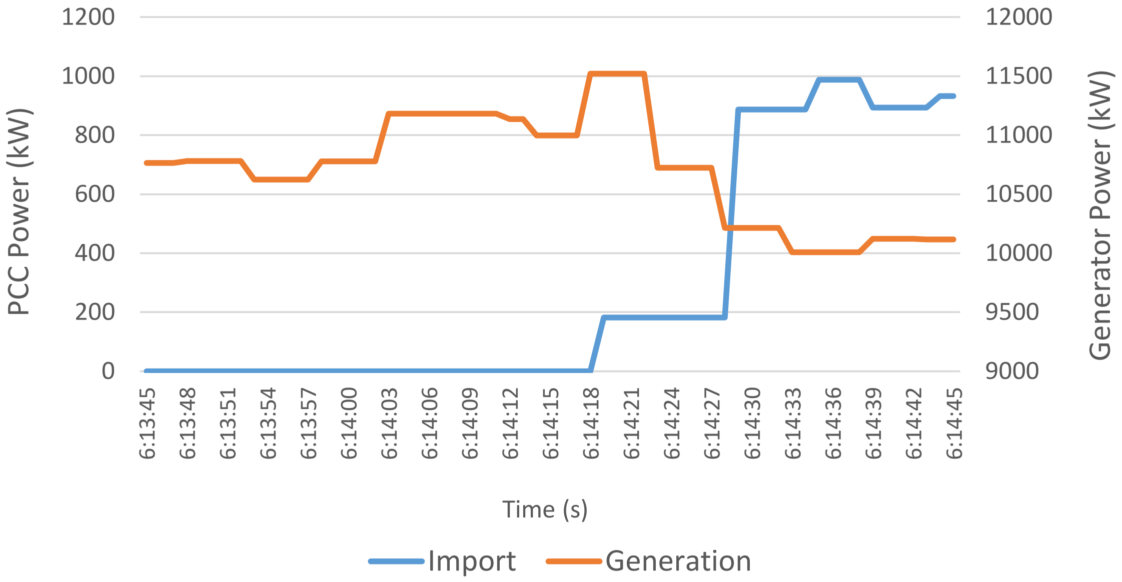

Figure 109. UCIMG import and generation real power profiles during grid reconnect.

Power System Element	Expected Value	Actual Value
CTG Aux mode	FALSE	FALSE
SEL-451 CB CLOSE status	FALSE	FALSE
UC66-1 SEL-751 CB CLOSE status	FALSE	FALSE
UC66-1 SEL-751 CB CLOSE status	FALSE	FALSE
GS-1 SEL-700G operational	TRUE	TRUE
CTG mode	ISOC	ISOC
CTG mode	Volt CTRL	Volt CTRL
Frequency range	Nominal	Nominal
Voltage range	Nominal	Nominal

Table 28. Pre-resynchronization UCIMG conditions.

Immediately before resynchronization was achieved, the campus PCC voltage was operating at 4.9% below that of the utility (campus at 11.7kV, utility at 12.3kV). For the demonstration, the acceptable voltage range to initiate an autosynch procedure was set at ±15% while the closure of the PCC breaker was set to trigger only within the range of ±5%. Similarity, the phase angle window was also limited to ±5% (±18 degrees). Figure 110 shows an oscillograph capture triggered by the closing of the PCC breaker. As shown in the capture, the controller was also able to coordinate the closure of the breaker to occur at a zero-voltage crossing point, reducing voltage and current transients.

Figure 110. UCIMG grid reconnect oscillograph capture.

Similar to the islanding transition comparisons, recorded resynchronization power, voltage, and current data were replayed in simulation using the OPAL-RT HIL platform to validate model results against demonstration measurements. However, due to the implementation of the utility resynchronization control routine which relies heavily on voltage and phase match ranges as opposed to deterministic actuation times, it was not possible to recreate the exact resynchronization waveforms.

7.2. UNIVERSITY OF CALIFORNIA, IRVINE – MEDICAL CENTER

The UCI Medical Center Microgrid serves a major research university hospital complex located in Orange, California. As of 2018, the electrical load of the system averages 6MW and the thermal demand, consisting of hot water heating, space heating, humidification, and steam sterilization loads, varies between 15,000-19,000 lb/hr. Natural gas consumption averages 1,650,000 therms/year. With the expansion of the facility to meet increasing load demands, the UCIMC-MG has been renovated to accommodate a fuel cell cluster that will provide sufficient power and heat to serve a projected total electrical of 10MW. The modeling methodology, analysis, and controller RT-HIL simulations used to study the UCIMG were also applied to the UCIMC Microgrid. While the UCIMC Microgrid was not physically islanded, as in the UCIMG case, the RT-HIL studies yielded valuable insights as to the performance of the microgrid controller when applied to other microgrid systems.

Figure 111 shows the EMT model of the UCIMC Microgrid circuit. Line parameters were obtained from existing electrical arc flash studies and building loads were approximated based on maximum transformer capacity ratings. As the entire UCIMC Microgrid circuit contained only 258 EMT nodes, the complete circuit was modeled in full without any load aggregation. Furthermore, elements that were removed due to insufficient computational capacity in the UCIMG case, such as three-phase circuit breakers, were retained in the UCIMC Microgrid model. A phasor-based model was derived from the EMT model for use with the microgrid controller, as the controller only features a phasor-based load-flow solver engine.

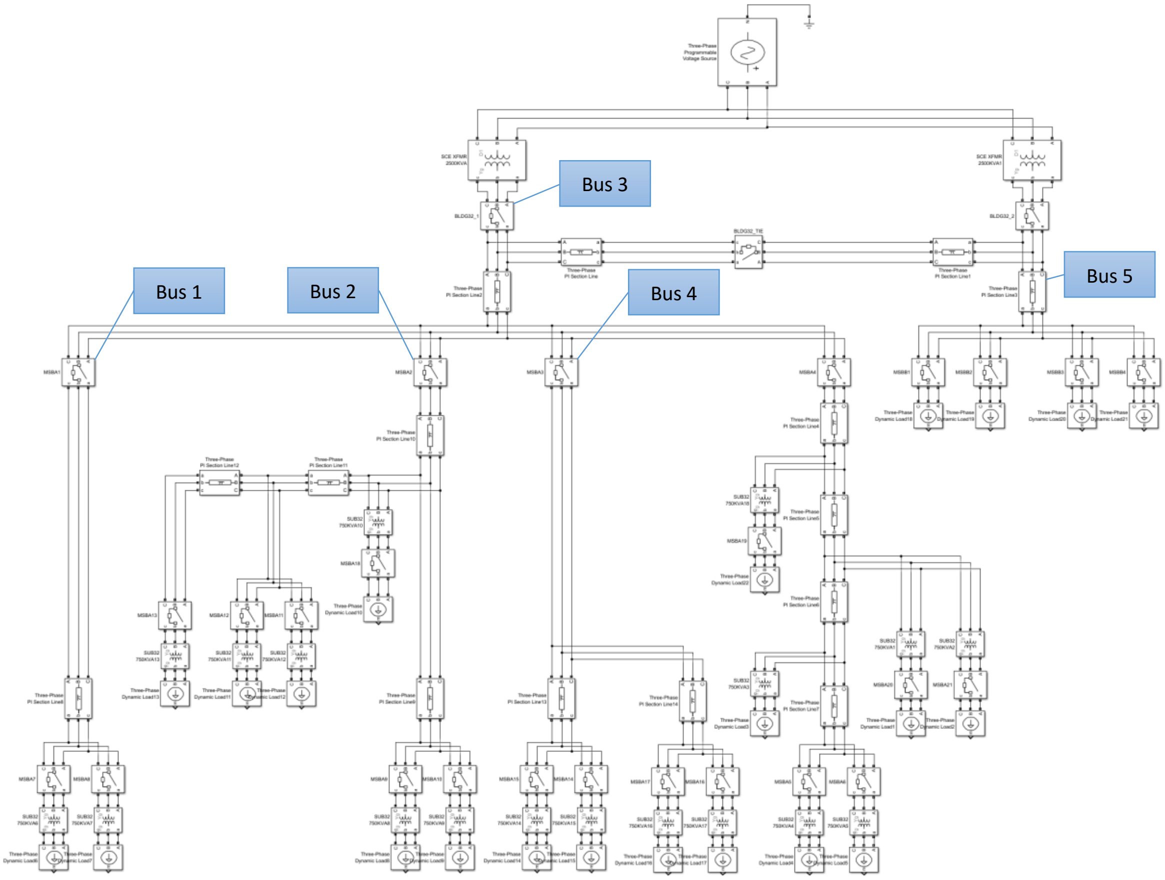

Figure 111. UCIMC Microgrid EMT model.

7.2.1. MODEL VALIDATION

To assess model translation fidelity between the phasor- and EMT-based models and verify EMT simulation stability, 10 consecutive step load increases were introduced into the models and the line voltages at 5 microgrid busses were compared. These busses are identified by the marked locations in Figure 111. Uninterestingly, steady-state load-flow simulations conducted using a traditional load-flow solver were compared to results from the OPAL-RT real-time EMT simulator, and due to direct translation from the EMT to controller models results were exactly identical as shown in Table 29.

Load/Branch	Load / Line Voltage (p.u) Load Flow	Load / Line Voltage (p.u) EMT
PCC	1.0000	1.0000
SCE XFMR 2500KVA	0.9986	0.9986
Load 1	0.9955	0.9955
Load 2	0.9953	0.9953
Load 3	0.9957	0.9957
Load 4	0.9965	0.9965
Load 5	0.9965	0.9965
Load 6	0.996	0.996
Load 7	0.998	0.998
Three-Phase PI Section Line 1	0.0415	0.0415
Three-Phase PI Section Line 2	0.0415	0.0415
Three-Phase PI Section Line 3	0.0415	0.0415
Three-Phase PI Section Line 4	0.0415	0.0415
Three-Phase PI Section Line 5	0.0415	0.0415
Three-Phase PI Section Line 6	0.0415	0.0415
Three-Phase PI Section Line 7	0.0415	0.0415
Three-Phase PI Section Line 8	0.0415	0.0415
Three-Phase PI Section Line 9	0.0415	0.0415
Three-Phase PI Section Line 10	0.0415	0.0415
Three-Phase PI Section Line 11	0.0415	0.0415
Three-Phase PI Section Line 12	0.0415	0.0415
Three-Phase PI Section Line 13	0.0415	0.0415

Table 29. Steady-state UCIMC-MG load-flow and EMT simulation results.

The line voltage transient response to step load increases were also tested and shown to be stable. As shown in Figure 112, EMT simulations exhibited slight overshoot in line voltage upon introduction of a real power step load, but quickly settled to expected steady-state values. Also noted was the lack of power ramping in load components as in the UCIMG case, as the lower node count of the UCIMC Microgrid allowed for the exclusive use of RLC load model components which are numerically stable in the presence of large step load changes as opposed to adjustable steady-state components.

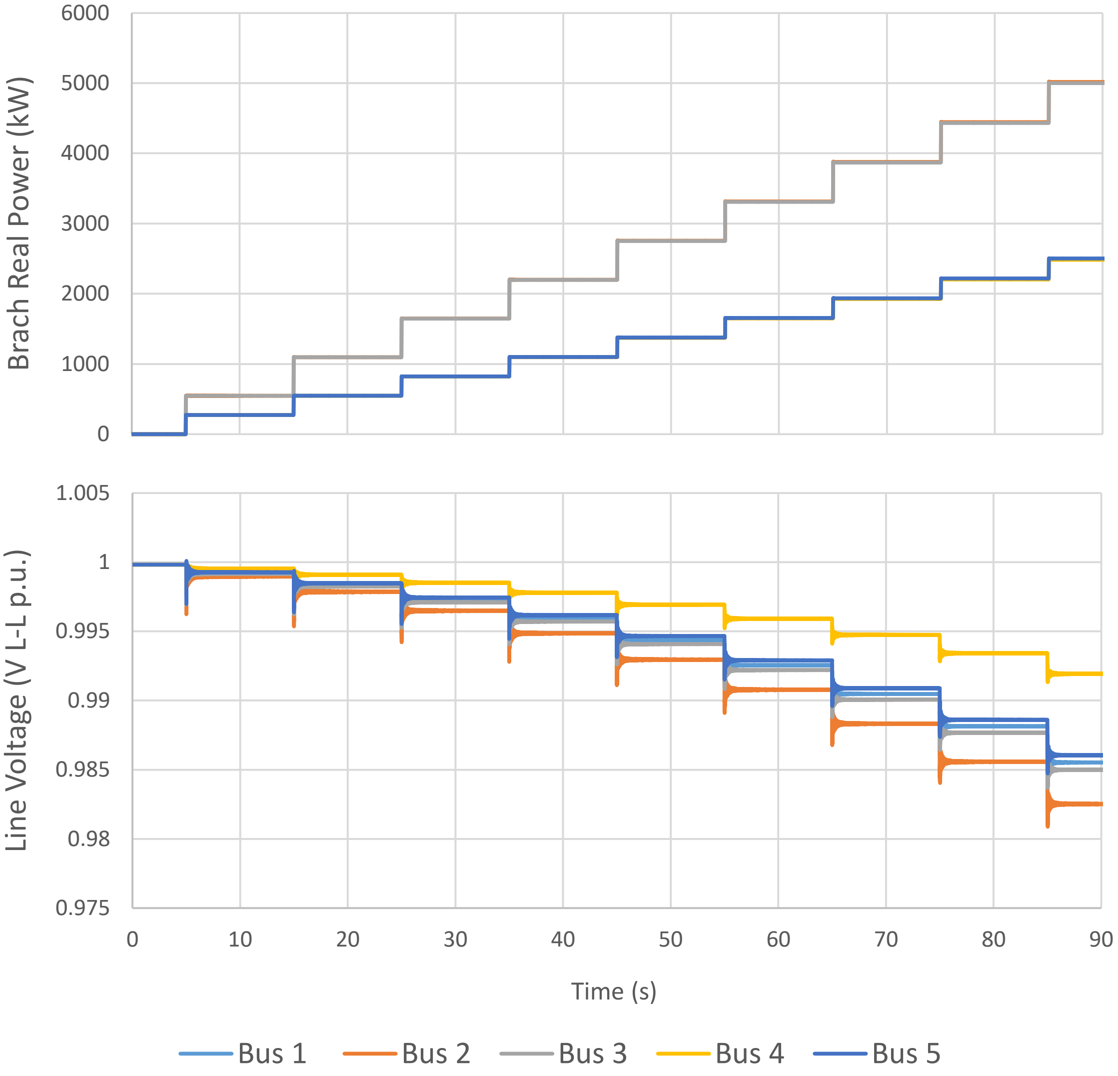

Figure 112. UCIMC Microgrid EMT model power and line voltage step load response.

7.2.2. UNPLANNED SEAMLESS ISLANDING

The ability of the microgrid controller to support unplanned seamless islanding when applied to the UCIMC-MG was investigated in simulation by assessing both manual and fault-initiated microgrid islanding. Three 1MW diesel generators combined with a 2.8MW FuelCell Energy SureSource SOFC system provided islanded microgrid generation. Interestingly, simulated power and current profiles for both scenarios were nearly identical, likely owing to the rapid dynamic response of the inverter-coupled fuel cell and battery energy storage systems used in the UCIMC-MG as opposed to the relatively slower response of the gas and stream turbine generators found in the UCIMG. This is further supported by the results found in the grid-connected ancillary services dispatch simulations of the UCIMG, where the introduction of an inverter-coupled battery energy storage system resulted in significant power oscillation dampening when stepping microgrid building loads.

As seen in the islanding voltage profiles shown in Figure 113 and Figure 114, increases to the pre-island real power import contributed to the resulting islanding-induced voltage transient in both the manual- and fault-initiated cases. Also, when islanding success under scaled loading profiles used in the UCIMG simulations were applied to the UCIMC-MG, findings suggested that the use of inverter-coupled systems will fail under any amount of generation-to-load deficiency. These findings are summarized in Figure 115.

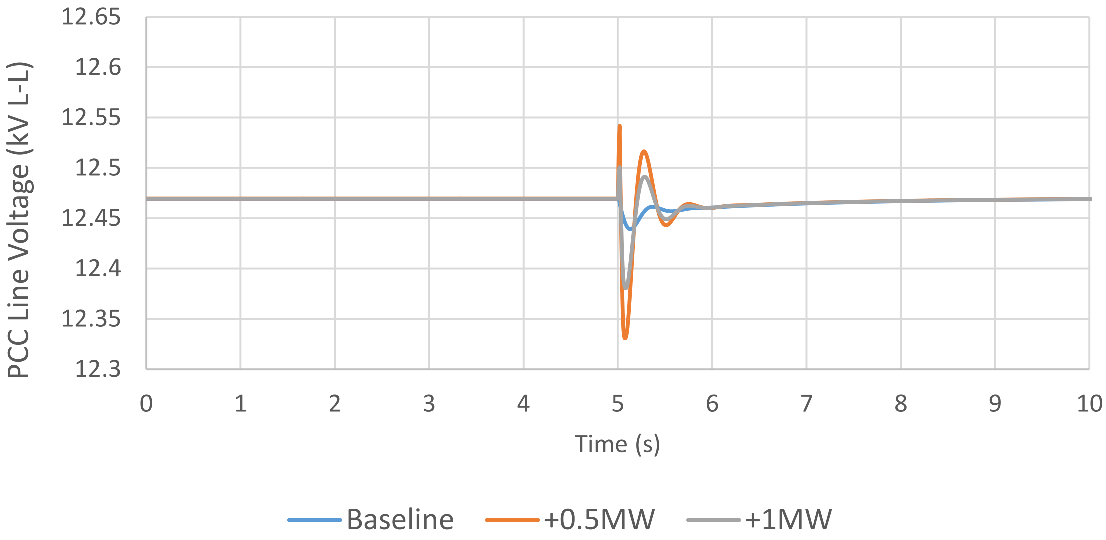

Figure 113. Effect of increasing UCIMC-MG real power import on the fault-initiated islanding voltage profile.

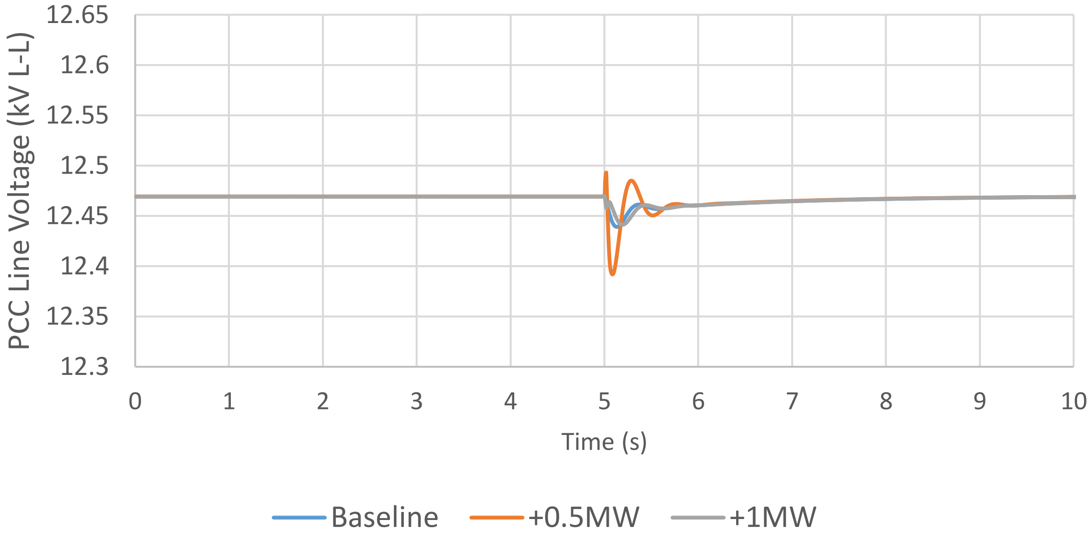

Figure 114. Effect of increasing UCIMC-MG real power import on the manual-initiated islanding voltage profile.

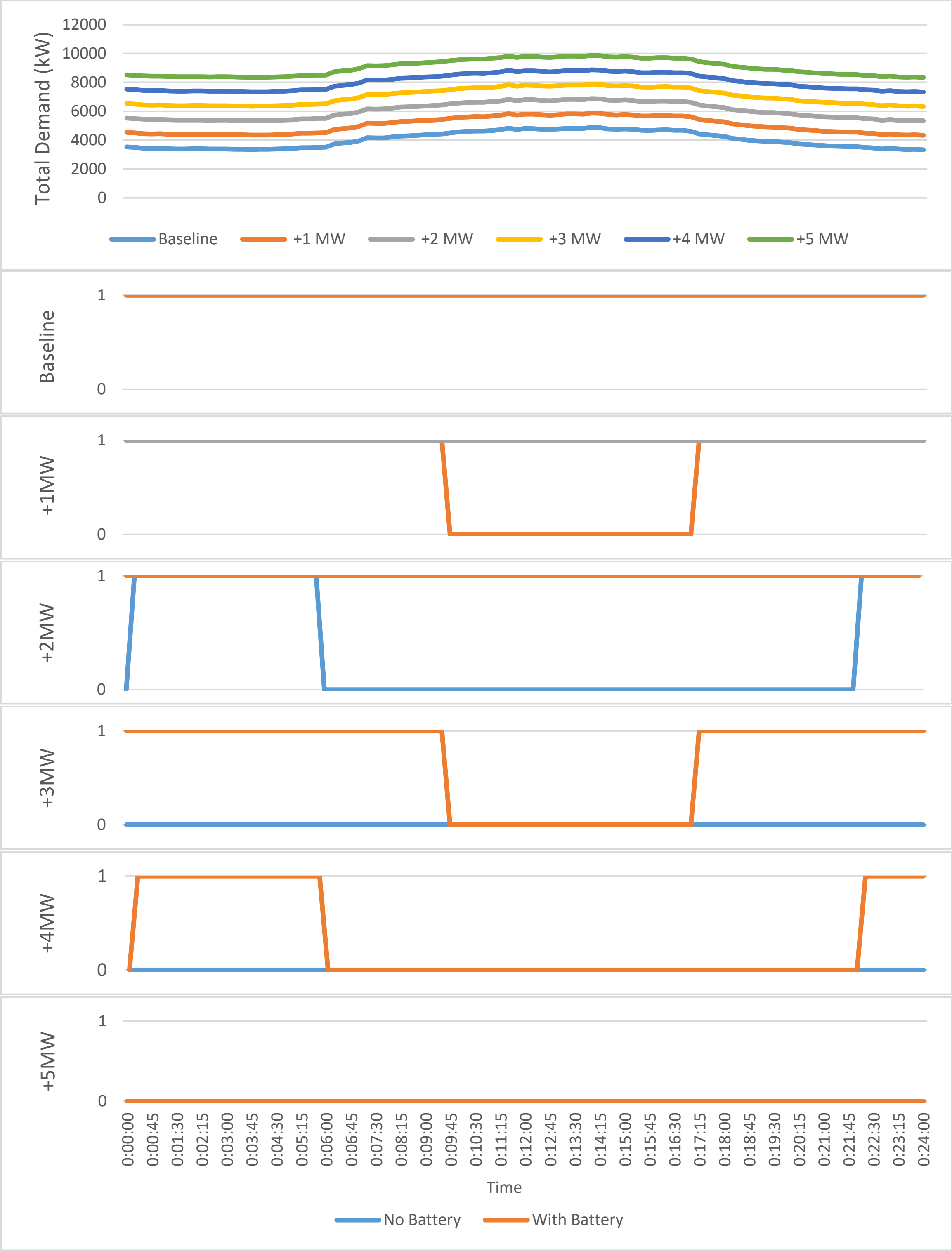

Figure 115. The impact of varying real power import on UCIMC-MG seamless microgrid islanding success profile, high load conditions (9/10/2015).

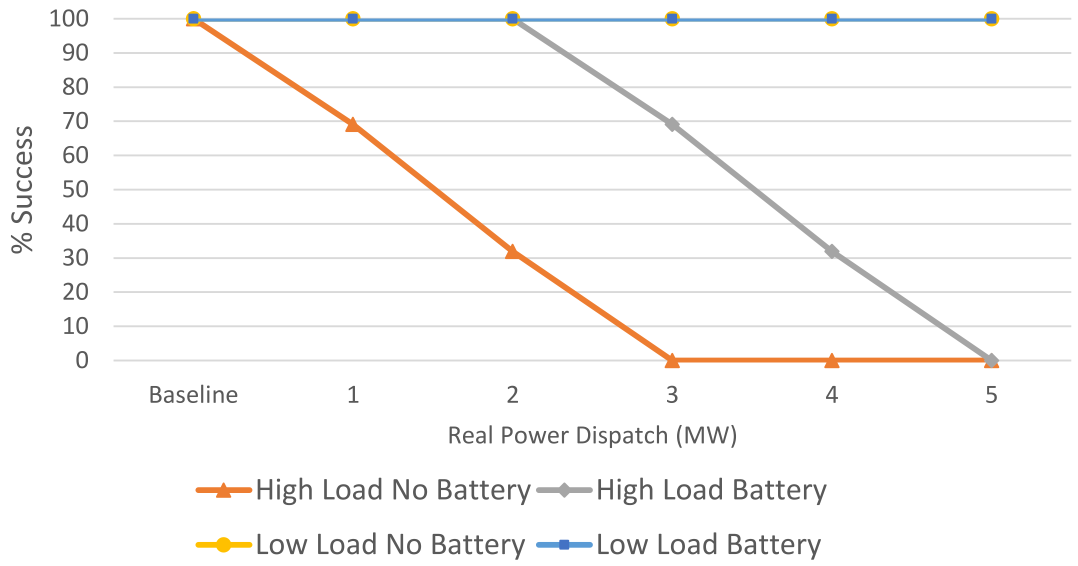

Figure 116. Impact of varying real power import on UCIMC-MG islanding success.

7.2.3. ISLANDED REAL POWER DISPATCH

A series of microgrid load increases were introduced into the islanded system to observe controller and microgrid response and verify proper coordination of generation and load assets. These load increases were designed to present the microgrid with situations that necessitate the deployment of battery storage assets to maintain the operation of critical loads. Loads on the UCIMC-MG differ from those on the UCIMG as, being a medical facility, all loads are considered critical and therefore designated as unavailable for load drop. In Figure 117, the results from a test profile that requires the deployment of the battery energy storage system is presented. In this comprehensive test, the islanded UCIMC-MG is operated with an initial battery state of charge of 75% and a real power demand of 2.7MW, which is entirely provided by the fuel cell cluster. At t = 20s in the simulation, the load was increased by 0.1MW and the controller appropriately increased fuel cell power output. At t = 35s, another 0.1MW load step was introduced, bringing the total load beyond the fuel cell generation limits. In this situation, the controller activated the battery storage system, outputting 0.1MW to avoid any load shedding. At t = 335s, the UCIMC-MG load was increased by another 0.1MW to a total of 3MW, and the battery output was automatically increased. At t = 635s, the load was decreased to 2.8MW at which time the battery system stopped discharging. Upon decrease of another 0.2MW at t = 650, the controller determined that conditions were adequate for battery charging and the battery began to charge at a rate of 0.2MW. A table of these events is presented in Table 30.

Time of Event (MM:SS)	Event	Expected Controller Response
00:00	Initial islanded conditions: Microgrid load: 2.7MW Fuel cell output: 2.7MW + losses Battery state of charge: 75%	None
00:20	+0.1MW load	+0.1MW fuel cell output
00:35	+0.1MW load	0.1MW battery output
05:35	+0.1MW load	+0.1MW battery output
10:35	-0.2MW load	- 0.2MW battery output
10:50	-0.2MW load	Battery charges at 0.2MW
18:20	Battery SOC reaches 75%	Battery stops charging

Table 30. Islanded-mode UCIMC-MG test load profile sequence of events.

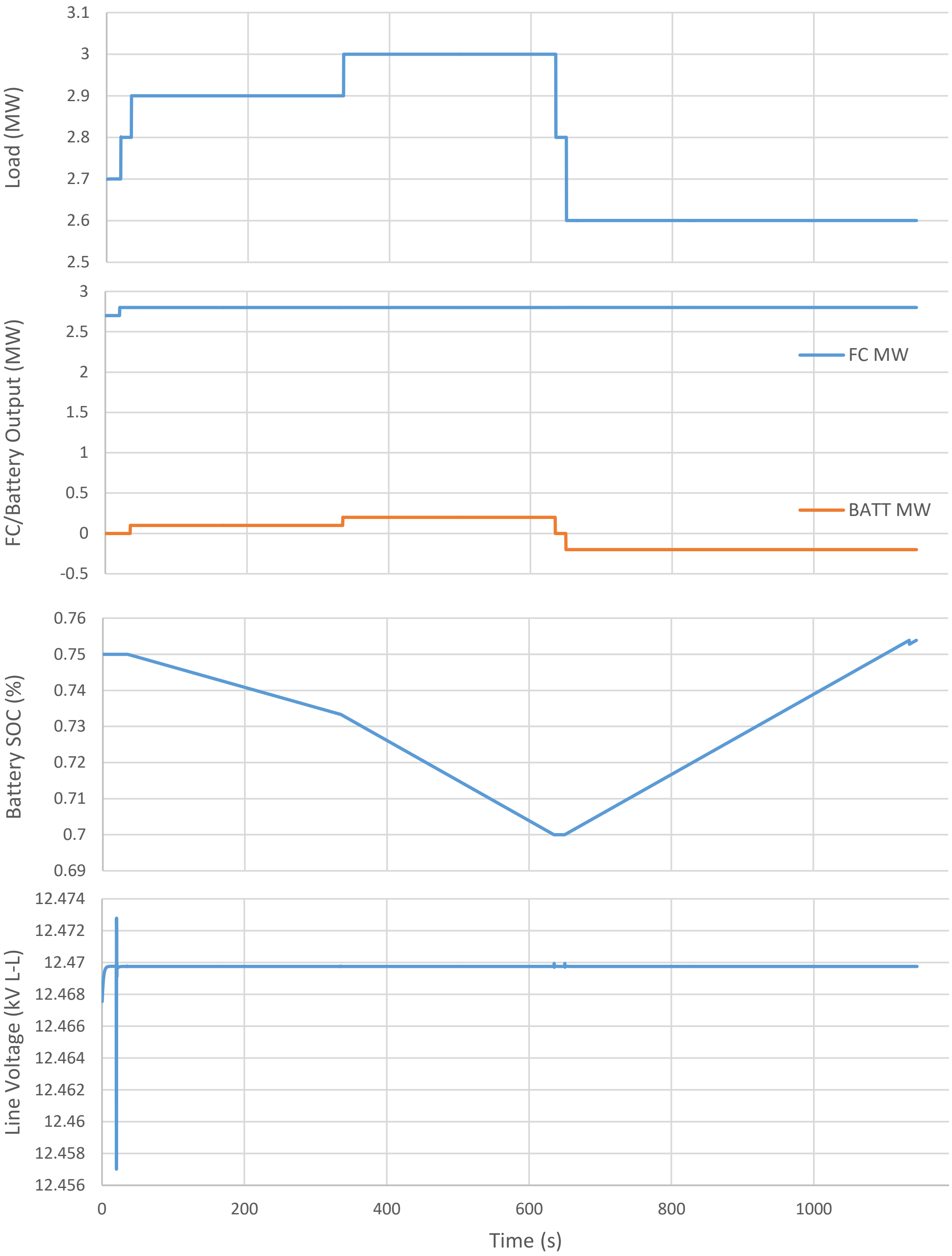

Figure 117. Islanded-mode UCIMC-MG test load profile response.

7.2.4. GRID RESYNCHRONIZATION

Grid reconnect capabilities for the UCIMC-MG system were verified using the same tests as those used to assess the UCIMG. Upon receiving a grid resynchronization command, the controller automatically sent control signals that modified the fuel cell and battery systems to match PCC upstream voltage and phase. Upon matching, the PCC was closed by a BC command and UCIMC-MG power output returned to pre-island values. Figure 118 shows the generation and PCC voltage profiles for one such event.

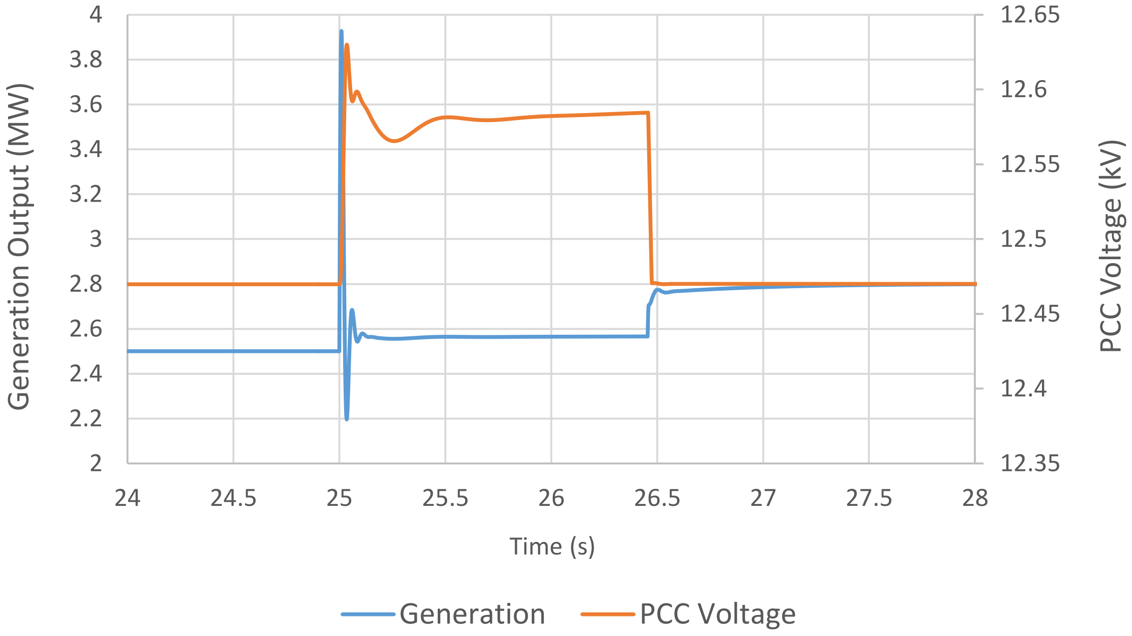

Figure 118. UCIMC-MG utility resynchronization profile.

When compared to the grid resynchronization performance of the UCIMG, a key difference is the speed at which generation assets were able to match utility voltage amplitude and phase. While both systems were capable of completing the resynchronization process within approximately the same time (1.5 – 2 seconds), the high dynamic response of the inverter-coupled generation sources allowed for faster dampening of voltage and power oscillations after closure of the PCC, as shown in Figure 119. This is also seen in the ancillary services dispatch results where the addition of an inverter-coupled generation resource, e.g, the battery energy storage system, provided significant oscillation dampening. Figure 120 shows a comparison of resynchronization profiles of the UCIMG under varying post-island import conditions and indicates an increase in the resynchronization time as the post-island import increases. Table 31 shows the comparison of these utility reconnection process times.

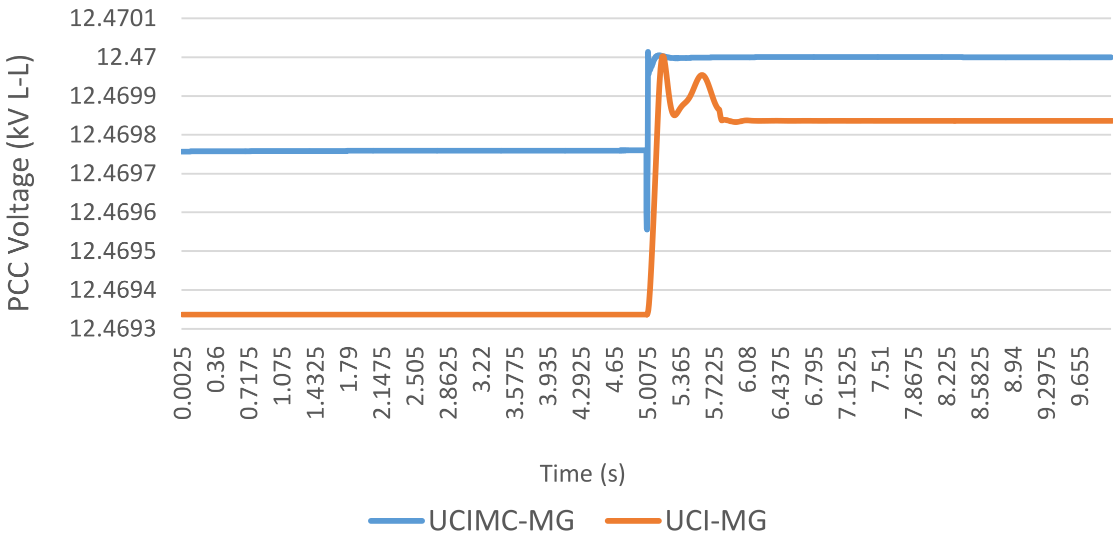

Figure 119. Comparison of UCIMC-MG and UCIMG utility resynchronization PCC voltage profiles.

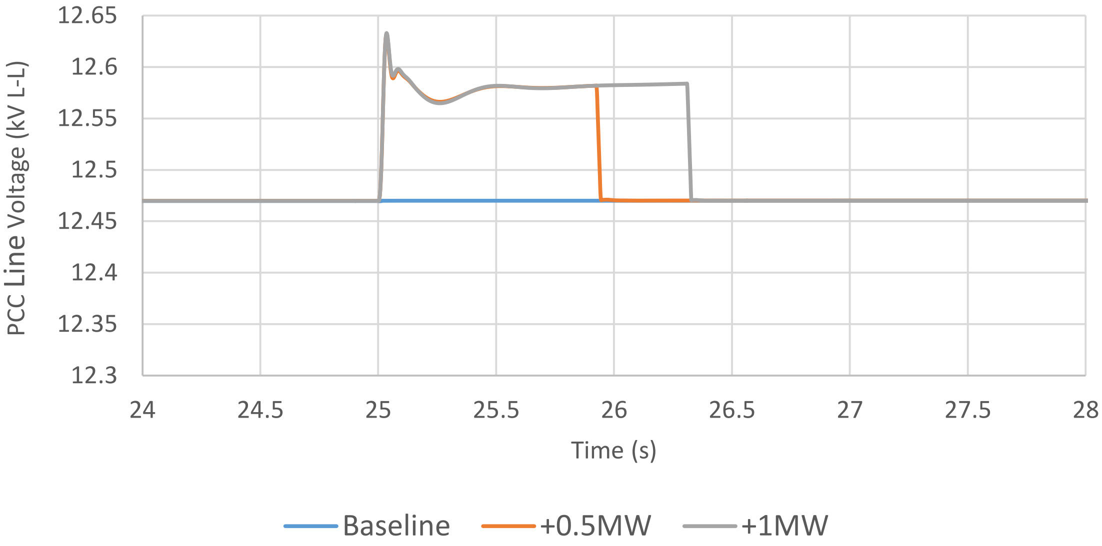

Figure 120. Comparison of UCIMC-MG utility resynchronization profiles under varying post-island import.

Baseline	+0.5MW	+1MW
0.0875s	1.5575s	1.7375s

Table 31. Impact on post-island import on UCIMC-MG utility resynchronization times.

8. SUMMARY, CONCLUSIONS, AND RECOMMENDATIONS

This section concludes this dissertation with a summary of the research effort and highlights several important key findings. Recommendations based on the presented conclusions are also made. It is hoped that they may serve as useful suggestions for the direction of future microgrid research.

8.1. SUMMARY

In this dissertation, the UCI and UCIMC microgrids and their components were modeled using the Simulink platform and run on an advanced real-time OPAL-RT hardware-in-the-loop simulator. Model simulation results based on real-world scenario data were used to inform the development of a controller designed for the uninterrupted operation of a wide range of microgrids through islanding events while supporting ancillary services. Studies conducted with the controller incorporated in a real-time HIL configuration investigated grid-connected and islanded dynamic behavior, the impact of ancillary services on islanding success, and identified the microgrid islanding limits. A real-world demonstration of the controller was performed in which the UCIMG was seamlessly transitioned to islanded-mode operation for a duration of 75 minutes and seamlessly reconnected to the grid.

8.2. CONCLUSIONS

Several important conclusions can be drawn from the research presented in this dissertation and are summarized here.

- **A high-speed demand response system may dramatically increase the safe islanding zone.**

  While most microgrids systems vastly differ in size, topology, power capacity, and even load and generation assets, a safe landing zone can be determined using offline EMT simulations provided an adequate system model exists. Once established, the safe islanding zone may be used to guide microgrid operation to ensure continuous islanding readiness without requiring online transient simulations. This may prove useful in implementing microgrid control based on local distributed controllers that may lack the computational resources to resolve transient simulations.

- **Research suggests that the UCIMG safe islanding zone is reached at approximately 2.5MW real power import demand.**

  Additionally, the safe islanding zone for the UCIMC-MG has been shown to be reached at approximately 0.5MW import demand. The safe islanding zone real power export limits are approximately twice that of real power import limits in both systems and the safe islanding zone has been found to less sensitive to reactive power import/export than real power import/export. Based on these two case studies, it is hypothesized that the safe islanding zone across most community-scale microgrid systems is primarily limited by pre-island real power import at a limit of 10-20% of the total real power capacity of the microgrid system.

- **A high-speed demand response or battery energy storage system may dramatically increase the safe islanding zone.**

  By allowing the immediate reduction of loads to reduce generation mismatch, the real power import may be reduced at the time of grid-disconnect. Simulations have shown that inverter-based systems present in the microgrid such as battery energy storage systems and fuel cell systems may serve to suppress switching-induced voltage and current transients, reducing the possibility of islanding failure due to the activation of instantaneous-trip line protective devices. Actuation delay of the PCC breaker, and by extension load shed breakers, during fault-initiated islanding and utility resynchronization contributes a substantial amount of voltage and line current disturbance. It was also discovered that the delay of switching gas turbine operation mode from grid-connected droop control to islanded-mode isochronous speed control was of negligible impact to both islanding success and line and voltage profiles.

- **Ancillary services negatively impact UCIMG islanding availability.**

  The provisioning of ancillary services such as real and reactive power dispatch, spinning reserve, and frequency regulation reduce the ability of the UCIMG to seamlessly island in both planned and unplanned islanding scenarios. The upper limit of dispatch services while allowing successful microgrid islanding coincides with the limits imposed by the safe-islanding zone, and the type of ancillary service provided plays a significant role in islanding success with frequency regulation resulting in the largest detrimental impact and reactive power dispatch resulting in the least.

- **Instantaneous overcurrent and reverse power line protective devices are the most common source of microgrid islanding failure.**

  Among phase and ground current differential, phase instantaneous and time delay overcurrent, phase unbalance, under/overvoltage, and over/under/rate of change frequency protective elements, simulations suggest instantaneous overcurrent and reverse power/negative sequence detection play the most critical role in determining microgrid islanding success in synchronous generator-powered microgrids whereas inverter-based systems are more sensitive to generation mismatch and under/over frequency.

- **Power electronics-based DER improve microgrid power quality.**

  The addition of inverter-coupled DER agents onto a primarily synchronous generator powered system greatly reduces power oscillations and transients caused by the operation of the PCC breaker or sudden changes in load demand. However, while the introduction of these devices improves both grid-connected and islanded power quality and greatly reduce any line voltage transients during both islanding and utility resynchronization transitions, they are shown to decrease the islanding success rate, failing with any amount of generation deficiency.

8.3. RECOMMENDATIONS

This work provides a methodology to comprehensively assess the islanding response of general microgrid systems, and (2) demonstrates the methodology by applying the approach to two distinct high community impact microgrid systems. While the methodology developed in this research allows for the elucidation of useful microgrid islanding metrics such as the safe islanding zone and power quality impacts, the approach presented relies on the development and validation of EMT models of the microgrid and its associated components in question and also requires access to a high performance EMT simulator, both of which may not be accessible to many microgrid owners. To truly unlock the potential to accelerate the implementation of microgrid systems, the methodology presented in this research should be modified to accommodate commodity-level computational and simulation tools. To this end, it is recommended to develop a comprehensive library of microgrid components that do not rely on full EMT simulations. Phasor- or heuristic based design approaches are suggested.

Also suggested is the integration of microgrid islanding metrics into optimal power flow and other power system optimization studies. For example, consideration of the generation-to-load margin established by the safe islanding zone as a component of an operational cost function may prove to be of value when assessing the true operational cost of operating a microgrid system with reliability factors considered.

Finally, the UCIMG was islanded during a live test during which the controller successfully and seamlessly transitioned the UCIMG from grid-connected to islanded mode, maintained island-mode operation for 75 minutes, and automatically and seamlessly reconnected to the utility upon the conclusion of the test. The test provided a valuable dataset useful for validating the developed UCIMG EMT model. It is recommended to expand the data available via additional islanding events and to obtain data from other islanded microgrid systems. It is also recommended to establish an islanding report data format standard and develop a repository for islanding data similar to the IEEE Power Systems Test Case Archive.

9. REFERENCES

Acres, G. J. (2001). Recent advances in fuel cell technology and its applications. *Journal of Power Sources*, 60-66.

Advanced Power and Energy Program. (2018). DOE Contract DE-0E0000730 Final Report. *A Generic Microgrid Controller*. Irvine, CA: University of California, Irvine.

Aguero, J. R. (2018). Grid Modernization, DER Integration & Utility Business Models - Trends & Challenges. *IEEE Power and Energy Magazine, 16*(2), 112-121.

Ahmad, Z. (2006). Solar photovoltaic (PV) energy; latest developments in the building integrated and hybrid PV systems. *Renewable Energy*, 711-718.

Ali Reza Reisi, M. H. (2013). Classification and comparison of maximum power point tracking techniques for photovoltaic system: A review. *Renewable and Sustainable Energy Reviews*, *19*, 433-443.

Allie E Auld, e. a. (2009). Load-following strategies for evolution of solid oxide fuel cells into model citizens of the grid. *IEEE Transactions on Energy Conversion*, 617-625.

American Society of Civil Engineers. (2017). *2017 Infrastructure Report Card.* American Society of Civil Engineers.

Anh, S. J. (2010). Power-Sharing Method of Multiple Distributed Generators Considering Control Modes and Configurations of a Microgrid. *IEEE Transactions on Power Delivery, 25*(3), 2007-2016.

Aramburo, C. T. (2005). Fuel Consumption Minimization of a Microgrid. *IEEE Trans. on Ind. App, 41*(3), 673-681.

Auld, A. E. (2010). An Asset-Based Interconnection Paradigm For Distribution System Energy Resources. Irvine, CA: UMI.

Basso, T. S. (2004). IEEE 1547 series of standards: interconnection issues. *IEEE Transactions on Power Electronics, 19*(5), 1159-1162.

Bidram, A. a. (2012). Hierarchical Structure of Microgrids Control System. *IEEE Transactions on Smart Grid, 3*(4), 1963-1976.

Bokka, N. (2010). *Comparison of Power Flow Algorithms for inclusino in On-line Power Systems Operation Tools.* New Orleans, Louisiana: University of New Orleans ScholarWorks.

Brucoli, M. T. (2007). Modelling and analysis of fault behaviour of inverter microgrids to aid future fault detection. *IEEE International Conference on System of Systems Engineering.*

Celli, G. F. (2005). Optimal Participation of a Microgrid to the Energy Market with an Intelligent EMS. *The 7th International Power Eng. Conf*, (pp. 663-668).

Cherry, E. C. (1949). The Duality Between Interlinked Electric and Magnetic Circuits and the Forrmation of Transformer Equivalent Circuits. *Proc. of the Physical Society*, 101-111.

Coelho, E. A. (2002). Small-signal stability for parallel-connected inverters in stand-alone AC supply systems. *IEEE Transactions on Industry Application, 38*(2), 533-542.

Colson, C. M. (2009). A review of challenges to real-time managment of microgrids. *PES'09 IEEE.*

Colson, C. M. (2009). Ant colony optimization for microgrid multi-objective power management. *Power Systems Conference and Exposition.* IEEE.

Deng, Q. X. (2011). System Modeling and Optimization of a Microgrid Using Genetic Algorithm. *2nd Int. Conf. on Intelligent Control and Info. Processing*, (pp. 540-544).

Dufour, C. J. (2011). A combined state-space nodal method for the simulation of power system transients. *IEEE Transactions on Power Delivery, 26*(2), 928-935.

Durand, H. (1980). Present status and future prospects of silicon solar cell arrays and systems. *Philosophical Transactions of the Royal Society of London*, 435-443.

E. P. Dick, W. W. (1981). Transformer Models for Transient Studies Based on Field Measurements. *IEEE Transactions on Power Apparatus and Systems*, 409-418.

Emadi, A. (2004). Modeling of power electronic loads in ac distribution systems using the generalized state-space averaging method. *IEEE Transactions on Industrial Electronics, 51*(5), 992-1000.

Fernando L. Alverado, R. H. (1983). Testing of trapezoidal integration with damping for the solution of power transient problems. *IEEE Transactions on Power Apparatus and Systems*, 3783-3790.

FlexEnergy. (n.d.).

Francisco De Leon, A. S. (1994). Complete transformer model for electromagnetic transients. *IEEE Transactions on Power Delivery, 9*(1), 231-239.

G. Martin A., K. E. (2012). Solar cell efficiency tables (version 39). *Progress in photovoltaics: research and applications, 20*(1), 12-20.

Grainger, J. J. (1994). *Power Systems Analysis.* McGraw-Hill.

Gu, F. J. (2013). A study on the impact of high penetration distributed generation inverters on grid operation and stability. *AIP Conference Proceedings, 1556.*

Guan, X. Z. (2010). Energy-Efficient Buildings Facilitated by Microgrid. *IEEE Trans. on Smart Grid, 1*(3), 243-252.

Guerrero, J. J. (2009). Control Strategy for Flexible Microgrid Based on Parallel Line-Interactive UPS Systems. *IEEE Transactions on Industrial Electronics, 56*(3), 726-736.

Guerrero, J. M. (2007). Decentralized control for parallel operation of distributed generation inverters using resistive output impedance. *IEEE Transactions on industrial electronics, 54*(2), 994-1004.

Guerrero, J. M. (2011). Hierarchical control of droop-controlled AC and DC microgrids—A general approach toward standardization. *EEE Transactions on industrial electronics, 58*(1), 158-172.

Guerro, J. M. (2005). Output impedance design of parallel-connected UPS inverters with wireless load-sharing control. *IEEE Transactions on industrial electronics*, *52*(4), 1126-1135.

Guo, F. (2015). Distributed secondary voltage and frequency restoration control of droop-controlled inverter-based microgrids. *IEEE Transactions on industrial Electronics, 62*(7), 4355-4364.

Han, Y. X. (2010). Study of adaptive fault current algorithm for microgrid dominated by inverter based distributed generators. *IEEE International Symposium on Power Electronics for Distributed Generation Systems.*

Hassan, M. A. (2011). Optimal design of microgrids in autonomous and grid-connected modes using particle swarm optimization. *IEEE Transactions on Power Electronics*, *26*(3), 755-769.

Hatziagyriou et al. (2007). Microgrids. *IEEE power and energy magazine, 5*(4), 78-94.

Hatziagyriou, N. (2014). *Microgrids: architectures and control.* John Wiley & Sons.

Helix Electric. (2017). *Utility Transformer Factory Test Report Spec. Section 33 7313.1.3.B.* Helix Electric.

Hirofumi Akagi, E. H. (2007). *The instantaneous power theory.* John Wiley & Sons.

IEEE Power and Energy Society. (2010). *IEEE Std 1815-2010.*

IEEE Power and Energy Society. (2017). *P2030.7-2017 – IEEE approved draft standard for the specification of microgrid controllers*. Retrieved from https://standards.ieee.org/findstds/standard/2030.7-2017.html

IEEE Power Engineering Society. (1973). Dynamic models for steam and hydro turbines in power system studies. *IEEE Transactions on Power Apparatus and Systems*, 1904-1915.

IEEE Standard 1547A - 2014. (2014). IEEE Standard 1547A - 2014. *New Interconnection Requirements for Distributed Energy Resources*.

IEEE Std. 1110-2002. (2003). IEEE Guide for Synchronous Generator Modeling Practices and Applications in Power System Stability Analyses. *IEEE*.

IEEE Std. 1547-2018. (2018). IEEE Standard for Interconnection and Interoperability of Distributed Energy Resources with Associated Electric Power Systems Interfaces. *IEEE Std. 1547-2018*.

IEEE Std. 2030.7-2017. (2017). *IEEE Standard for the Specification of Microgrid Controllers.* IEEE.

IEEE Std. 421.5-2005. (2005). IEEE Recommended Practice for Excitation System Models for Power System Stability Studies. *IEEE*.

IEEE Subsynchronous Resonance Working Group. (1985). Second Benchmark Model for Computer Simulation of Subsynchronous Resonance. *IEEE Transactions on Power Apparatus and Systems*, 1057-1066.

Inman, R. H. (2013). Solar forecasting methods for renewable energy integration. *Process in energy and combustion science, 39*(6), 535-576.

International Electrotechnical Commission. (2013). *IEC 61850:2013.*

International Organization for Standardization. (2010). *ISO/IEC 7489-1.*

J. H. McWirther, C. F. (1963). Determination of Impulse Stresses within Transformer Windings by Computers. *AIEE Transactions on Power Apparatus and Systems*, 1028-1031.

Jinhee Lee, e. a. (2006). A 10-kW SOFC low-voltage battery hybrid power conditioning system for residential use. *IEEE Transactions on Energy Conversion, 21*(2), 575-585.

Johnson, R. W. (2012). *AC Versus DC Power Distribution.* Eaton.

Kanchev, H. D. (2011). Energy Management and Operational Planning of a Microgrid With a PV-Based Active Generator for Smart Grid Applications. *IEEE Transactions on Power Systems, 58*(10), 4583-4592.

Kao, Y. L. (2009). An Accurate Power Control Strategy for Power-Electronics-Interfaced Distributed Generation Units Operating in a Low-Voltage Multibus Microgrid. *IEEE Transactions on Power Electronics, 24*(12), 2977-2988.

Kaplan, S. M. (2009). Smart Grid. Electrical Power Transmission: Background and Policy Issues. In *The Capital.Net, Govermnment Series* (pp. 1-42).

Kastha, D. a. (1994). Investigation of fault modes of voltage-fed inverter system for induction motor drive. *IEEE Transactions on Industry Applications, 30*(4), 1028-1038.

Katiraei et al. (2008). Microgrids management. *IEEE Power Energy Magazine, 6*(3), 54-65.

Katiraei, F. a. (2006). Power managment strategies for a microgrid with multiple distributed generation units. *IEEE transactions on powr systems, 21*(4), 1821-1831.

Khalghani, M. R. (2016). A self-tuning load frequency control strategy for microgrids: Human brain emotional learning. *International Journal of Electrical Power & Energy Systems, 75*, 311-319.

Kim, J. J. (2010). Cooperative control strategy of energy storage system and microsources for stabilizing the microgrid during islanded operation. *IEEE Transactions on Power Electronics, 25*(12), 3037-3048.

Koropatrick, R. L. (2012, March). *HVDC Projects Listing.* Retrieved from HVDC and Flexible AC Transmission Subcommittee of the IEEE Transmission and Distribution Committee.

Kroposki, B. e. (2007). Microgrid standards and technology development. *Power Engineering Society General Meeting*.

Langenbacher, F. (2009). *Instructions for Using the IEEE AC8B AVR/Exciter Model for Analysis of Solar Turbines Generators Using CGCM.* Solar Turbines.

Lasseter, R. H. (2011). CERTS microgrid laboratory test bed. *IEEE Transactions on Power Delivery, 26*(1), 325-332.

Li, Y. D. (2004). Design, analysis, and real-time testing of a controller for multibus microgrid system. *IEEE Transactions on Power Electronics, 19*(5), 1195-1204.

Liang, C. Y. (2009). Design of parallel inverters for smooth mode transfer microgrid applications. *Applied Power Electronics Conference and Expo*, 1288-1294.

Liu, R. L. (2011). A survey of PEV impacts on electric utilities. *Innovative Smart Grid Technologies*.

Lopes, J. L. (2006). Defining control strategies for microgrids islanded operation. *IEEE Transactions on Power Systems, 21*(2), 916-924.

Maclay, J. D. (2011). Experimental results for hybrid energy storage systems coupled to photovoltaic generation in residential applications. *International Journal of Hydrogen Energy*, 12130-12140.

Majumder, R. A. (2008). Load Sharing and Power Quality Enhanced Operation of a Distributed Microgrid. *IET Renwable Power Generation, 3*(2), 109-119.

Martin, B. K. (2010). Hybrid renewable energy and microgrid research work at NREL. *Power and Energy Society General Meeting*.

Mathworks. (2003). *SimPowerSystems User's Guide.* Natick, MA: Mathworks.

Mathworks. (2016, 5 21). *Mathworks Documentation: Chose a Solver*. Retrieved from https://www.mathworks.com/help/simulink/ug/types-of-solvers.html

Mattuci. (2018, May 28). *Wikipedia Common.* Retrieved from https://en.wikipedia.org/wiki/Proton-exchange_membrane_fuel_cell#/media/File:Proton_Exchange_Fuel_Cell_Diagram.svg

Melrok. (2018). *Melrok Energy IoT Platform*. Retrieved from Touch|Touch Pro: https://melrok.com/#/pages/platform_landing.html

Messerly, J. (2009). *NERC Map.*

Morozumi, S. (2007). Micro-grid demonstration projects in Japan. *Power conversion conference-Nagoya*.

Nimpitiwan, N. e. (2007). Fault current contribution from syncrhonous machine and inverter based distributed generators. *IEEE Transactions on power delivery, 22*(1), 634-641.

North American Electric Relibility Corporation. (2017). *North American Electric Relibility Corporation*. Retrieved from Key Players, Regions.

OPAL-RT. (2013). Opal-RT User Manual and RT-LAB Block Library Reference Guide.

OPAL-RT. (2016). *OP5600 v2 User Manual.* Montréal, Québec, Canada: OPAL-RT Technologies.

Overbeeke, F. V. (2009). Fault current source to ensure the fault level in inverter-dominated networks. *20th Int. Conf. Electricity Distribution.* Prague, Czech Republic.

P. Silverster, M. C. (1970). Finite Element Solution of Saturable Magnetic Field Problems. *IEEE Transactions on Power Apparatus and Systems, 89*(7), 1642-1651.

P2S. (2016). *UCI Primary Electrical Improvements Step 4.* Long Beach, CA: P2S Engineering.

Painuly, J. (2011). Barriers to Renewable Energy Penetration; A Framework for Analysis. *Renewable Energy, 24*, 73-89.

Parisio, A. E. (2014). A model predictive control approach to microgrid operation optimization. *IEEE Transactions on Control Systems Technology, 22*(5), 1813-1827.

Park, J.-D. e. (2013). DC ring-bus microgrid fault protection and identification of fault location. *IEEE transactions on Power delivery, 28*(4), 2574-2584.

Patrao, I. E.-M. (2015). Microgrid architectures for low voltage distributed generation. *Renewable and Sustainable Energy Reviews,* 415-424.

Pogaku, N. M. (2007). Modeling, analysis and testing of autonomous operation of an inverter-based microgrid. *IEEE Transactions on Power Electronics, 22*(2), 613-625.

Rabins, L. (1956). Transformer Reactance Calculations with Digital Computers. *AIEE Transactions*, *75*(1), 261-267.

Ran Fu, D. C. (2016). *U.S. Solar Photovoltaic System Cost Benchmark: Q1 2016.* Golden, CO: National Renewable Energy Laboratory (NREL).

Razeghi, G. F. (2018). A generic microgrid controller: Concept, testing, and insights. *Applied Energy*, 660-671.

Rocabert, J. e. (2012). Control of power converters in AC microgrids. *IEEE transactions on power electronics, 27*(11), 4734-4749.

Rory A. Roberts, J. B. (2010). Fuel cell/gas turbine hybrid system control for daily load profile and ambient condition variation. *Journal of engineering for gas turbines and power*.

Roshan, A. e. (2007). A DQ frame controller for a full-bridge single phase inverter used in small distributed power generation systems. IEEE.

Sallam, A. A. (2011). Electric Distribution Systems. *IEEE Computer Society Press*, 21.

Sani, A. a. (2010). Potential-function based control of a microgrid in islanded and grid-connected modes. *IEEE Transactions on Power Systems, 25*(4), 1883-1891.

Schneider-Electric. (n.d.). Communication networks and protocols. (M. Gerin, Ed.)

Schweitzer Engineering Laboratories. (2018). *Decoupling/Autosynchronization Test Report.* Pullman, WA: Helix Electric, Inc.

Sera, D. e. (2013). On the perturb-and-observe and incremental conductance MPPT methods for PV systems. *IEEE journal of photovoltaics, 3*(3), 1070-1078.

Solar Turbines. (2011). Preferred Governor Models for Solar Turbines Generators.

Solar Turbines. (2018, 8 26). *Gas Compressor Packages - Titan 130*. Retrieved from https://www.solarturbines.com/en_US/products/gas-compressor-packages/titan-130.html

Sortomme, E. S. (2005). Microgrid protection using communication-assisted digital relays. *IEEE Transactions on Power Delivery, 25*(4), 2789-2796.

T. Kaneko, J. B. (2006). Power and temperature control of fluctuating biomass gas fueled solid oxide fuel cell and micro gas turbine hybrid system. *Journal of Power Sources*, 316-325.

Tayab, U. B. (2017). A review of droop control techniques for microgrid. *Renewable and Sustainable Energy Reviews*, 717-727.

Tong, S. M. (2005). A distributed slack bus model and its impact on distribution system application techniques. *IEEE International Symposium on Circuits and Systems*.

U.S. Energy Information Administration. (2006). *Delivery to Customers.* U.S. Energy Information Administration.

U.S. Energy Information Administration. (2018). *Levelized Cost and Levelized Avoided Cost of New Generation Resources in the Annual Energy Outlook 2018.* U.S. Energy Information Adminstration.

U.S. Environmental Protection Agency. (2015). *Catalog of CHP Technologies.* Combined Heat and Power Partnership.

U.S. Office of Electricity Delivery & Energy Reliability. (2018, 05 13). *Energy.gov*. Retrieved from The Role of Micorgrids in Helping to Advance the Nation's Energy System: https://www.energy.gov/oe/activities/technology-development/grid-modernization-and-smart-grid/role-microgrids-helping

UL 1741. (2010). *Inverters, Converters, Controllers and Interconnection System Equipment for Use With Distributed Energy Resources.* UL.

Van der Vlueten, E. a. (2010). Transnational infrastructure vulnerability: The historical shaping of the 2006 European "Blackout". *Energy Policy, 38*(4), 2042-2052.

Vossos, V. K. (2011). Energy savings from direct DC appliances and power systems. *Lawrence Berkeley National Laboratory*.

Wang, B. M. (2012). Intelligent DC microgrid with smart grid communications: Control strategy consideration and design. *IEEE transactions on smart grid, 3*(4), 2148-2156.

Yi, Y. e. (2004). Analysis and optimization of a solid oxide fuel cell and intercooled gas turbine (SOFC–ICGT) hybrid cycle. *Journal of Power Sources*, 77-85.

Zamani, M. A. (2004). A communication-assisted protection strategy for inverter-based medium-voltage microgrids. *IEEE Transactions on Smart Grid, 3*(4), 2088-2099.

Zhi, N. H. (2011). Overview of Microgrid Management and Control. *Int. Conf. on Elec. and Control*, (pp. 4589-4601).